Numerical Modelling of Sediment Delivery from Tidewater Glaciers to the Marine Environment

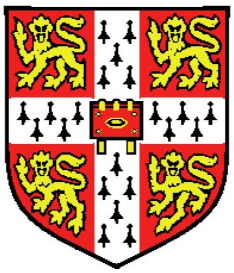

Ruth Mugford

Scott Polar Research Institute

Jesus College

University of Cambridge

This dissertation is submitted for the degree of

Doctor of Philosophy

2008

This dissertation is the result of my own work and includes nothing which is the outcome of collaboration. The length of this dissertation is within the 225 page limit.

Acknowledgements

While I have been working on this thesis, I have had the pleasure of meeting a great number of people who deserve recognition for their assorted contributions to my research and personal life. First and foremost I offer my sincerest gratitude to my supervisor, Prof. Julian Dowdeswell, who has supported me throughout with his patience and knowledge whilst allowing me the space to work in my own way. I really appreciate your tireless reading of this thesis and returning corrections at a phenomenal rate. Also, thank you for the opportunities to visit INSTAAR and to participate in two incredible cruises to the Arctic.

James Syvitski, John Andrews, Irina Overeem, Albert Kettner, Eric Hutton and the rest of the 'Delta Force', thank you for welcoming me so warmly to INSTAAR — it was a pleasure to join the team. I would like to express my gratitude to the crew of the R.R.S. James Clark Ross, whose staunch professionalism and hard work, as well as their great sense of fun and our shared joy at seeing polar bears, left me with experiences I will treasure for a lifetime.

In my daily work I have been lucky to share workspace with a friendly and cheerful group of fellow students — Anna Nelson, Kelly Hogan, Steve Palmer, Cameron Rye and Narelle Baker. Ian Willis offered a friendly ear and good advice when it was needed. Bob Hawley has been particularly generous with his time and knowledge of Unix, Matlab and Latex and very graciously volunteered the use of his workstation for running the models. Toby Benham showed me the art of ERDAS IMAGINE, without him I may still be foundering in the mire of satellite image processing.

I feel extremely fortunate to have made some wonderful friends during my time in Cambridge, many of them through the Graduate Society at Jesus College, who have made my time here full of fun and fond memories. A special mention to: Tess McCabe, Martyn Frampton, James Loxam, Chris Akerman, Julia Vaca, Dan Vaca, Francesa Bolognini, Ken Sutherland, Ed Martin, Laurie Shaw, Enrico Magnani, Jacques Boppe, Stephanie Bunt, Tobias Locsei and Tom Greggs. To all the above individuals, and to several

colleagues whose names I cannot continue listing and who have assisted me one way or another, I feel very much indebted.

The Scott Polar Research Institute has provided me with vital support, a comfortable working environment and the privilege of being a part of the diverse and charming community. Financial support from NERC and the Autosub Under Ice Program is gratefully acknowledged.

My family deserves a special mention for their support: my Mum, the first person to point out a glacial valley to me and who is a constant inspiration; my Dad, who taught me to chose a job you love; my sister, Emily, and my brothers, James and Harry. Finally, Rich, I couldn't have done this without you: your counsel on mathematical issues in this thesis has been invaluable and your unwavering encouragement, humour and emotional support have kept me going to the end.

Abstract

Glaciated fjords are dynamic sedimentary environments with high deposition rates, thus providing high-resolution sedimentary records of deglaciation. This thesis introduces two numerical models, *SedBerg* and *SedPlume*, developed to simulate marine sedimentation from tidewater glaciers for the dominant transport processes of iceberg-rafting and glacial meltwater plumes.

Icebergs calved from tidewater glaciers contain sediment, which is released as the icebergs melt. The *SedBerg* Model utilises Monte Carlo based techniques to simulate the formation, drift and melt of a population of icebergs, and the subsequent deposition. Subaqueous and subaerial melt of the icebergs result in a continuous rainout of sediment with occasional sediment dumping from overturning events. Underlying the model are a number of parametric probability distributions to describe the stochastic behaviour of iceberg formation and dynamics. Parametric values of the probability density functions are found using maximum likelihood estimation from field observations.

Turbid meltwater emerging from beneath a glacier into a fjord rises as a buoyant forced plume due to salinity and temperature contrasts with the ambient fjord water. The *SedPlume* Model utilises an integral model formulation for the conservation of volume, momentum, buoyancy and sediment mass along the path of a turbulent, entraining plume injected into stably stratified ambient fluid. The resulting system of non-linear ordinary differential equations are solved numerically using an adaptive stepsize fourth-order Runge-Kutta method. When the plume reaches the surface, it is treated as a radially spreading surface gravity current, for which exact solutions exist for the mass flux of sediment deposited.

A case study is examined for each model. The *SedBerg* Model is applied to Kangerdlugssuaq Fjord in East Greenland, as an example of an iceberg-dominated depositional environment. The sedimentation rate due to iceberg rafting is simulated for Kangerdlugssuaq Fjord over the last 1500 years, with climatic, oceanographic and glacial conditions estimated from a mixture of present day measurements and inferences from the sedimentary record. The *SedPlume* Model is applied to McBride Inlet in Alaska, as an example of a glacial meltwater-dominated sedimentary environment, with input data and ice-proximal sedimentation rates taken from published data.

The influence of various parameters on sediment deposition is investigated for each of the two models. For the *SedBerg* Model, the parameters considered are: iceberg size; temperature and depth of thermocline; and seeds of the random number generator for water and wind velocities. For the *SedPlume* Model, the parameters studied are: subglacial conduit radius and initial meltwater velocity; initial sand fraction; and ambient density gradient. The *SedBerg* and *SedPlume* Models enable quantitative assessments of the role and importance of different environmental and climatic conditions on the rate of deposition and the formation of distinctive marine deposits by tidewater glaciers.

Contents

List of Symbols

Constants

c_p	Specific heat capacity of water (at $15°C$)	$4.1855\ J\,g^{-1}\,°C^{-1}$
g	Gravitational acceleration	$9.81\ m\,s^{-2}$
Γ_i	Latent heat of fusion of ice	$3.34 \times 10^5\ J\,kg^{-1}$
κ_a	Thermal diffusivity of air at 283K	$2.160 \times 10^{-5}\ m^2\,s^{-1}$
κ_w	Thermal diffusivity of seawater:	
	$T_w = 0°C$, $S = 35\,gkg^{-1}$, P $= 1\,atm$	$1.37 \times 10^{-7}\ m^2\,s^{-1}$
k_a	Thermal conductivity of air	$2.49 \times 10^{-2}\ W(m\,°C)^{-1}$
k_w	Thermal conductivity of sea water:	
	T $= 0°C$, S $= 35\,gkg^{-1}$, P $= 1\,atm$	$0.563\ W\,(m\,°C)^{-1}$
μ_w	Dynamic viscosity of water at $277K$	$1.567 \times 10^{-3}\ kg\,m^{-1}s^{-1}$
μ_w	Dynamic viscosity of water at 283K	$1.307 \times 10^{-3}\ kg\,m^{-1}s^{-1}$
ν_a	Kinematic viscosity of air at 283K	$1.460 \times 10^{-5}\ m^2\,s^{-1}$
ν_w	Kinematic viscosity of water	$1.826 \times 10^{-6}\ m^2\,s^{-1}$
$\mathbf{\Omega_0}$	Angular velocity of the Earth	$7.27 \times 10^{-5}\ rad\,s^{-1}$
π	$\simeq 3.14159265\ldots$	
ρ_i	Density of iceberg	$850\ kg\,m^{-3}$
ρ_{ice}	Density of ice	$917\ kg\,m^{-3}$

Roman Symbols

A	Archimedes buoyancy index	
A_{bas}	Area of the iceberg face containing basal sediment	m^2
A_{dep}	Area of the fjord floor over which sediment is deposited	m^2
A_{eng}	Area of the iceberg face containing englacial sediment	m^2
A_m	Area of iceberg face undergoing melt	m^2
$A_\perp$	Cross sectional area of the side of the iceberg normal to the stressing force	m^2
a_s	Area of the marine basin	m^2
A_T	Amplitude of the tidal water velocity	$m\,s^{-1}$
a_{wv}	Wave amplitude	m
b	Calving rate coefficient	yr^{-1}
b	Scale parameter of Laplace distribution $b = \sigma/\sqrt{2}$	

B	Buoyancy Flux	$\frac{L^4}{T^3}$
b_v/b	Radial dimension where velocity is reduced to e^{-1} of centreline value	L
b_{scalar}	Radial dimension where scalar quantities (density and sediment concentration) are reduced to e^{-1} of centreline value	L
C	Form drag coefficient	
$\overline{c}_d$	Mean percentage debris content by volume of the basal layer	%
C_{si}	Sea ice concentration	%
d	Characteristic length of boundary layer for convective processes	m
d_{cc}	Distance from glacier front where critical crevasse forms	m
D_{gc}	Deposition rate from a gravity current	$kg\,m^{-2}\,s^{-1}$
d_s	Sediment grain diameter	L
$E\left(A_{bas_i}\right)$	Expectation of iceberg cross-sectional area for population of icebergs	
$E\left(V_i\right)$	Expectation of iceberg volume for population of icebergs	
$E(Y)$	Expectation of Y	
E_k	Ekman depth: iceberg draught or $90\,m$, whichever is shallower	m
f	Coriolis parameter $= 2\Omega_0 \sin\theta$	$rad\,s^{-1}$
$f(Y)$	Probability Density Function	
$\mathbf{F}_a$	Wind drag	N
f_{bas}	Volume fraction of sediment in basal ice	
f_{eng}	Volume fraction of sediment in englacial ice	
$\mathbf{F}_p$	Horizontal pressure gradient force exerted on the water volume displaced by the iceberg	N
$\mathbf{F}_r$	Wave radiation force	N
F_{sol}	Solar radiation flux	Wm^{-2}
$\mathbf{F}_w$	Water drag	N
Fr	Local densimetric Froude number	
G	$\frac{g}{\rho_{ref}}\frac{d\rho_a}{dz}$	
g'	Reduced buoyancy $= g\left(\rho_a\left(z\right)-\rho_p\right)/\rho_{ref}$	
Gr	Grashof number: approximate ratio of the buoyancy to viscous forces acting on a fluid	
h	Height of gravity current	
$\overline{h}$	Average heat transfer coefficient	$J\left(s\,m^2K\right)^{-1}$
H_m	Metacentric height - vertical distance between centre of gravity and the metacentre	m
h_b	Mean thickness of the debris-rich basal layer	m
h_{cc}	Layer thickness of convection cells	m
h_g	Glacier ice thickness	m
h_r	Roughness height of the iceberg surface	m
h_w	Water depth	m

h_{wv}	Mean height of waves	m
i	Magnitude of impulse	$kg\,m\,s^{-1}$
$\hat{\mathbf{k}}$	Unit vector in the z-direction	
L_i	Iceberg size calculated from log-normal distribution	m
$L_\perp$	Length of the berg normal to incident waves	m
L_x	Iceberg length (along long-axis)	m
L_y	Iceberg width	m
L_z	Iceberg height	m
M	Momentum Flux	$\frac{L^4}{T^2}$
$\overline{m}_g$	Mean advance or retreat of the ice front over a given time period	m
M_i	Iceberg mass	kg
$\hat{\mathbf{n}}$	Unit normal vector to fjord wall or ice front	
N	Number of samples	
n_b	Number of icebergs containing basal sediment	
n_M	Manning coefficient of roughness	$\frac{T}{L^{1/3}}$
n_{tot}	Total number of icebergs	
N_{tot}	Total number in the sample	
Nu	Nusselt number: ratio of convective to conductive heat transfer	
P	Pressure	$dbar$
P_c	Probability of calving in each time step	
P_h	Horizontal pressure field	Pa
P_w	Mean period of waves	s
Pr	Prandtl number: ratio of momentum diffusivity and thermal diffusivity	
q	Heat flow rate	W
Q	Volume Flux	$\frac{L^3}{T}$
Q_0	Meltwater flux from subglacial conduit	$\frac{L^3}{T}$
Q_ϕ	Sediment Mass Flux	$\frac{M}{T}$
Q_{scalar}	$\left(\frac{\lambda^2}{1+\lambda^2}\right)\pi b^2 V_c$	
r	Radial coordinate	
$\mathbf{r}$	Vector from centre of iceberg to corner in contact with fjord wall (Figure 2.7)	
R	Radius of plume	m
R_0	Subglacial conduit radius	m
R_a	Total subaerial melt rate of ice without debris layer	
R_{bc}	Melt rate due to buoyant convection	$m\,day^{-1}$
R_{dl}	Melt rate of ice with debris layer	
R_{fc}	Melt rate due to forced convection	$m\,day^{-1}$
R_h	Hydraulic radius	m

r_h	Radial horizontal distance from the point where the plume reaches the surface ($r_h = x - x_s$ on plume centreline)	
$\overline{r}_s$	Mean iceberg sedimentation rate over the basin area	m
R_{sh}	Melt Rate due to convective or sensible heat exchange with the air	$m\,s^{-1}$
R_{spread}	Plume spreading radius	
R_{sr}	Melt rate due to solar radiation	$m\,s^{-1}$
R_s	Plume radius at the surface	L
R_{tot}	Total melt rate of the iceberg face	$m\,hour^{-1}$
R_{we_1}	Melt rate due to wave erosion	$m\,s^{-1}\,{}^{\circ}C^{-1}$
R_{we_2}	Melt rate due to wave erosion	$m\,day^{-1}$
Ra	Rayleigh number	
Re	Reynolds number: ratio of inertial to viscous forces	
Rs	Salinity Rayleigh number	
S	Salinity	PSU
S_0	Slope of the subglacial conduit ($\tan\theta_0$)	
S_E	Standard error of the mean of a sample from a population	
S_{gc}	Sedimentation from a gravity current	$kg\,m^{-1}\,s^{-1}$
S_s	Sea state according to the Beaufort Scale	
S_{ws}	Slope of the water surface	
$SD(Y)$	Standard deviation of Y	
t	Time	s
T_a	Air temperature	${}^{\circ}C$
T_d	Thermal driving temperature (elevation of seawater temperature above freezing point)	${}^{\circ}C$
t_d	Thickness of the debris layer	
T_{face}	Sediment thickness deposited for iceberg face per time step	
T_{fp}	Freezing point of seawater	${}^{\circ}C$
T_{gc}	Thickness of sediment deposited from the gravity current per unit time	$m\,s^{-1}$
T_i	Ice temperature	${}^{\circ}C$
T_T	Period of the tidal oscillation (12 hours)	
T_w	Seawater temperature	${}^{\circ}C$
u	Velocity of gravity current	
U	z-component of velocity (vertical)$= V\sin\theta$	$m\,s^{-1}$
V	Velocity along the path of the plume	$m\,s^{-1}$
V_0	Initial velocity of glacial meltwater emerging from conduit	$m\,s^{-1}$
$\mathbf{v}_a$	Air velocity	$m\,s^{-1}$
V_a	Annual volume of icebergs calved from glacier	m^3
v_c	Iceberg calving rate	$m\,yr^{-1}$

$\overline{v}_g$	Mean velocity at the tidewater glacier margin	$m\,s^{-1}$
$\mathbf{v}_i$	Iceberg drift velocity	$m\,s^{-1}$
$\mathbf{v}_{i_1}$	Iceberg velocity before collision with fjord wall or ice front	$m\,s^{-1}$
$\mathbf{v}_{i_2}$	Iceberg velocity after collision with fjord wall or ice front	$m\,s^{-1}$
V_i	Volume of basal ice in iceberg, i	
$\mathbf{v}_{p_1}$	Relative iceberg velocity before collision including angular velocity	$m\,s^{-1}$
$\mathbf{v}_{p_2}$	Relative iceberg velocity after collision including angular velocity	$m\,s^{-1}$
$\mathbf{v}_T$	Tidal water velocity	$m\,s^{-1}$
$\mathbf{v}_w$	Water velocity	$m\,s^{-1}$
W_o	Observed particle settling velocity (with flocculation)	$m\,s^{-1}$
w_g	Width of the tidewater glacier front	m
W_{out}	Downward velocity of a sediment grain in plume	
W_s	Particle fall velocity	
W_t	Theoretical particle settling velocity	$m\,s^{-1}$
x	Horizontal coordinate (along fjord)	
X	Normally distributed random variable	
y	Horizontal coordinate (across fjord)	
Y	Log-normally distributed random variable	
z	Vertical coordinate	

Greek Symbols

α	Entrainment coefficient	
β_S	Salinity expansion coefficient	
β_c	Critical angle in plume where sediment falls out (Figure 3.3)	
β_T	Thermal expansion coefficient	
$\Delta\rho$	Density difference between the sediment and the fluid	
ΔS	Salinity difference	PSU
Δt_c	Calving time step	$days$
Δt_m	Melting and moving time step	$hours$
ΔT	Temperature difference	$^\circ C$
η	Viscoplastic viscosity	$kg\,m^{-1}\,s^{-1}$
ε	Coefficient of restitution	
κ	Thermal diffusivity	$m^2\,s^{-1}$
λ	Dispersion ratio	
μ	Mean of normally distributed random variable X	
μ	Mean of random variable in Laplace distribution	
ν	Kinematic viscosity	$m^2\,s^{-1}$
ω	Angular velocity	
ϕ	Sediment concentration	$\frac{M}{L^3}$

φ	Volume fraction of particles	
ϕ_0	Initial sediment concentration in meltwater plume	$kg\,m^{-3}$
ρ_f	Density of interstitial fluid in plume/gravity current	$kg\,m^{-3}$
ρ_{gc}	Density of gravity current	$kg\,m^{-3}$
ρ_a	Ambient fluid density	$kg\,m^{-3}$
ρ_a	Air density	$kg\,m^{-3}$
ρ_{dep}	Density of deposited sediment	$kg\,m^{-3}$
ρ_m	Mean density	$kg\,m^{-3}$
ρ_p	Plume fluid density	$kg\,m^{-3}$
ρ_{ref}	Reference density	$kg\,m^{-3}$
ρ_s	Sediment density	$kg\,m^{-3}$
ρ_w	Density of seawater	$kg\,m^{-3}$
σ	Standard deviation of normally distributed random variable X	
$\hat{\sigma}$	Estimate of the standard deviation σ of a population	
θ	Angle ice block makes with the vertical	$radians$
θ	Local angle between the plume trajectory and the horizontal	$radians$
$\overline{\tau}_s$	Surface wind stress	$kg\,(m\,s)^{-1}$
ξ	$= \frac{\pi W_o}{Q_s}$	

Subscripts

∞	farfield
a	Air
c	Value of the plume property at the centreline
f	Interstitial fluid in plume/gravity current
i	Iceberg
s	Value where the plume meets the surface
w	Water
$wall$	ice wall
x	Component in x-direction
y	Component in y-direction
z	Component in z-direction

List of Figures

Chapter 1

Introduction

This thesis presents two numerical models, which have been developed to simulate sediment delivery from tidewater glaciers to fjord environments. The *SedBerg* Model concerns sedimentation from iceberg-rafting, from the point of iceberg calving until the icebergs have either melted away or drifted out of the modelled area. The *SedPlume* Model considers deposition from meltwater plumes emerging from the base of tidewater glaciers. The motivation for studying glacial sedimentation in fjords is because they are enclosed systems with high sedimentation rates and therefore provide high-resolution records of deglaciation. High-latitude environments are particularly sensitive to climatic change and often demonstrate pronounced responses to such change (ACIA, 2004; IPCC, 2007). The interpretation of fjord sediments can yield useful insights into the role of glaciers and ice sheets in the Earth system and the consequences of past, as well as the implications of future, climatic fluctuations.

This chapter provides a general overview of glacimarine sedimentation processes. More detailed descriptions, relevant to the *SedBerg* and *SedPlume* Models, are found in later chapters of the thesis.

1.1 Fjords

The definition of a fjord in Syvitski *et al.* (1987) is "a deep, high-latitude estuary which has been (or is presently) being excavated or modified by land based ice". Fjords are characteristically high- and mid-latitude geological features of mountainous coastlines where there has been past glacial activity. Fjords occur in a northern hemisphere belt, for example Greenland, Svalbard, Alaska, Norway and the British Isles above $56°N$, and a southern hemisphere belt, for example New Zealand's South Island, the Kerguelen Islands, Patagonia and Antarctica. In general most of the sediment accumulation within these glacially excavated overdeepened basins pertains to glacial and

proglacial processes during and since the last major ice advance, although in some fjords the record of several episodes of proglacial deposition may be preserved. The basement rock of fjords is usually parabolic in shape (Gilbert, 1985), with sediment infill generating the distinctive U-shape. The typical U-shaped cross section is clearly demonstrated in Figure 1.1, which shows the bathymetry of Kangerdlugssuaq Fjord in East Greenland. The trough is extremely deep, with water depths up to approxi-

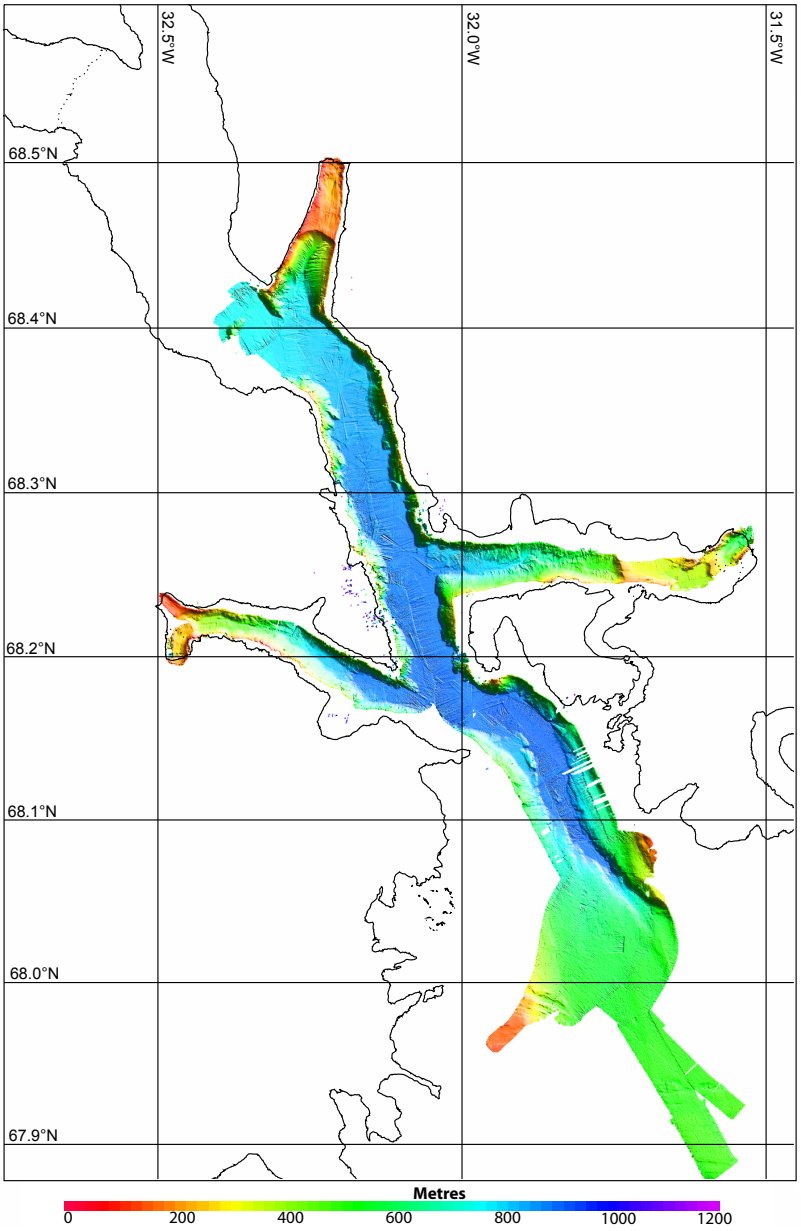

Figure 1.1: *Swath bathymetry of Kangerdlugssuaq Fjord in East Greenland collected aboard* R.R.S James Clark Ross *in 2004.*

mately 900 m. The base of the trough is remarkably flat in cross section with steep, almost sheer, side walls.

1.2 Tidewater Glaciers

Tidewater glaciers are defined as glaciers terminating in the ocean with a grounded margin. They occur in both open coast and fjord environments (Benn and Evans, 1998). Their dynamics are influenced by oceanic as well as atmospheric forcing, although the magnitude of glacier response and the relative importance of the two forcing mechanisms is a topic of debate (Luckman *et al.*, 2006; Rignot and Kanagaratnam, 2006; Thomas *et al.*, 2000).

Mass is lost from tidewater glaciers by iceberg calving and by meltwater at the ocean margin. The iceberg calving rate is influenced by changes in the glacier velocity and the advance or retreat of the ice front. Early calving relations were derived from measurement, with calving rate proportional to water depth (Brown *et al.*, 1982; Pelto and Warren, 1991). Another approach was developed by Van der Veen (2002) where the calving rate was determined by the glacier velocity and thickness change at the glacier front. Benn *et al.* (2007a) proposed a different model where the terminus position and calving rate depend on the ice velocity, strain rate, ice thickness and water depth.

The majority of water in the meltwater system of a glacier originates from the surface, which is melted by incoming solar radiation, convection and condensation. Precipitation falling on or near the glacier, including rain and snowfall that subsequently melts, also contributes to the meltwater budget. Meltwater is generated at the glacier bed from pressure melting due to the weight of the overlying ice. The meltwater travels on the surface as supraglacial streams, through the glacier in englacial conduits and at the glacier bed. The fluxes of meltwater from various sources are determined by factors such as the climatic conditions at the glacier (temperature, radiation flux and precipitation), ice thickness and geothermal heat flux (Benn and Evans, 1998). Gravity dictates that most of the meltwater, regardless of its origin, eventually reaches the glacier bed. There are several possible configurations of the subglacial drainage system. When there is a low flux, the meltwater tends to flow in a distributed thin film between the bed and the glacier (Weertman, 1972). With increasing meltwater supply, channelised transport paths develop. These take various forms: Rothlisberger channels (R-channels) incised into the ice (Röthlisberger, 1972), Nye channels (N-channels) cut into the underlying till (Nye, 1973) and linked cavities or a network of braided canals (Kamb, 1987). The morphology of the subglacial drainage system is controlled by the distribution of englacial conduits reaching the bed, ice thickness, glacier sliding speed, bed lithology, bed roughness and the seasonal glacier melt cycle (Fountain and Walder, 1998).

Glaciers erode and transport large volumes of sediment, both frozen into the ice

and by subglacial streams. The highest rate of sediment entrainment occurs at the bed and sides of the glacier. Regelation of ice into the pore spaces of subglacial sediment occurs when the pore-water pressure in the ice is higher than in the sediment (Iverson, 1993, 2000). Glaciohydraulic supercooling, when subglacial water ascends a sufficiently steep slope, causes basal-ice accretion (Alley *et al.*, 1998). Multiple freezing events by conductive cooling as ice slides over rigid bedrock may allow freeze-on to the glacier sole (Hubbard and Sharp, 1993, 1995). Another mechanism of basal sediment entrainment is the deformation (folding and thrusting) of the basal layer transporting sediment upward from the bed (Knight, 1997). Horizontal advection of cold ice to lower altitudes, where temperatures are warmer, can lead to steep temperature gradients forming at the base of the glacier and therefore high rates of sediment entrainment (Christoffersen *et al.*, 2006). This effect is particularly important at fast flowing outlet glaciers draining ice sheets. Since the entrainment of sediment occurs predominantly at the bed, this leads to high concentrations of sediment in a layer of ice at the bed, which is referred to as basal ice (Alley *et al.*, 1997).

In valley glaciers with steep sidewalls, various mass movements, e.g. rockfalls or avalanches, result in debris falling onto the glacier surface. Wind can also deliver fine-grained debris to the glacier surface. The debris either remains there as supraglacial ice or is incorporated into the interior of the glacier ice by falling into crevasses or burial by snow accumulation. Another mechanism of introducing sediment into the glacier is where two glaciers converge or at the confluence of ice around an obstacle. The interior of the glacier, which is referred to as englacial ice and makes up the bulk of the glacier, contains a relatively low concentration of sediment. Further details on the characterisation of glacier ice in terms of its location and sediment concentration are described in Section 2.7.

1.3 Glacimarine Sedimentation in Fjords

1.3.1 Processes

A flow diagram of the main processes contributing to glacimarine sedimentation is shown in Figure 1.2. This demonstrates the flow of sediment from sources to deposition in the marine environment. There are three main sources of marine sedimentation from tidewater glaciers in fjords: iceberg-rafting, subglacial meltwater plumes and glacier frontal melt. Sedimentation from glacier frontal melt was assessed to be negligible compared with the other two processes (Syvitski, 1989) and has been addressed elsewhere (Dowdeswell, 1987; Eijpen *et al.*, 2003; Motyka *et al.*, 2003), so it is not considered in this work. This thesis addresses the development and application

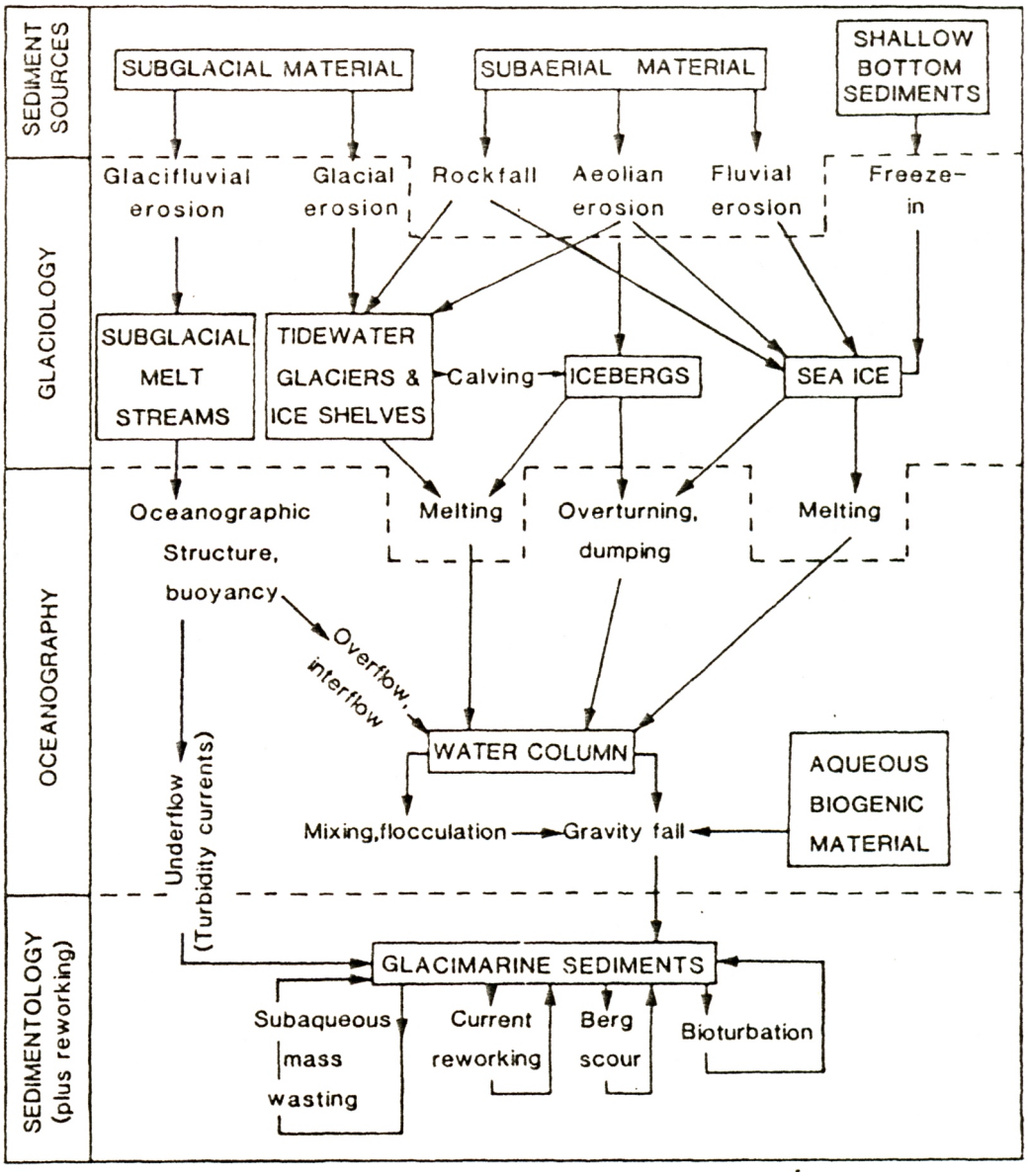

Figure 1.2: *The network of processes contributing to glacimarine sedimentation. The boxes refer to sediment stores and the other labels are glaciological, oceanographic and sedimentological processes (from Dowdeswell, 1987).*

of two numerical models, *SedBerg* and *SedPlume*, which simulate sedimentation by iceberg-rafting and glacial meltwater plumes, respectively. A schematic diagram of these sedimentation processes at a tidewater glacier front and the resulting lithofacies are shown in Figure 1.3. Also shown in the diagram is the reworking of sediment where a grounded glacier has advanced over pre-existing glacimarine sediments, forming deformation till and glaciotectonite. Deformation till is defined by Benn and Evans (1996) as:

> homogenized, usually diamictic material formed by glacially-induced shear

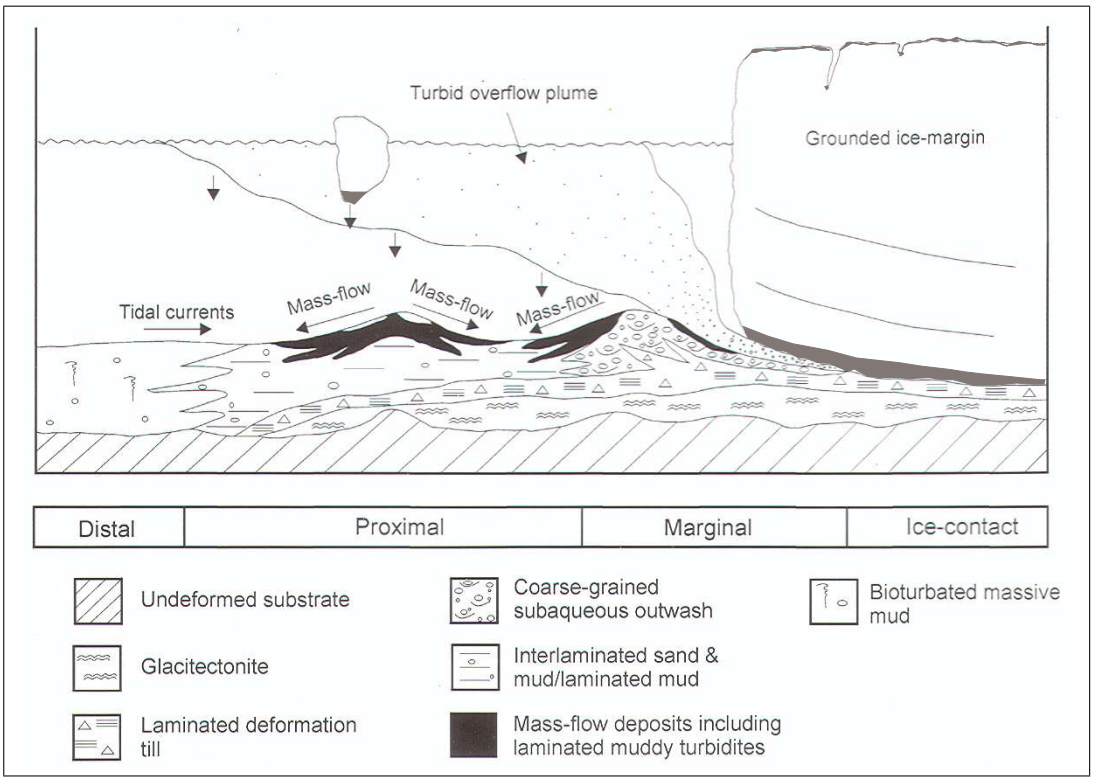

Figure 1.3: *Glacimarine sedimentation processes and lithofacies associations occurring at a the margin of a tidewater glacier, with vertical arrows representing sediment fall-out from icebergs and turbid meltwater plumes (modified from Ó Cofaigh and Dowdeswell, 2001).*

> of subsole materials. Three types are recognized: Type A, formed by pervasive, ductile deformation; Type B, formed by brittle shear; and comminution till, produced by the reduction of void space by in situ crushing and abrasion.

Glaciotectonite is characterised by Benn and Evans (1996) as:

> materials that have undergone subglacial shear but retain some of the structural characteristics of the parent material. Original structures may be truncated by glacitectonic fabric elements (Type A) or distorted but not truncated (Type B).

However, the glacial reworking of sediment is not considered in this thesis.

The primary sediment transport processes of iceberg-rafting and meltwater plumes and their importance to sedimentation in different climatic settings are described in the following sections.

1.3.1.1 Iceberg-rafting

Icebergs transport sediment large distances from the glacier, in some cases up to thousands of kilometres, releasing it gradually as they melt (Ruddiman and Wright, 1987). Occasionally they overturn and dump any sediment stored on their surface. Icebergs are of particular interest as they are one of the major mass loss mechanisms from glaciers and ice sheets, as well as supplying freshwater to the polar oceans (Death *et al.*, 2006). Layers of angular quartz sand (grain diameter $180\,\mu m$ to $3\,mm$) observed over wide areas of the North Atlantic have been attributed to extensive iceberg-rafting of sediment and are referred to as Heinrich Events (Heinrich, 1988). It is unclear whether Heinrich Events were triggered by global climate forcing or localised internal glaciological instabilities (Alley and Macayeal, 1994; Andrews, 1998). Regardless of the initiating mechanism, the presence of Heinrich layers demonstrates the significance of icebergs as vehicles for transporting sediment to the marine environment.

Much of the research on iceberg drift trajectories has been carried out to assess the hazards to the shipping and petroleum industries (Bigg *et al.*, 1996; Mountain, 1980). Another motivation for research has been to investigate the feasibility of towing icebergs as a source of fresh water for regions with water shortages (Weeks and Mellor, 1978b). Research by Bigg *et al.* (1997); Death *et al.* (2006); Gladstone *et al.* (2001); Matsumoto (1996) and Silva *et al.* (2006) focussed on the geophysical application of iceberg drift and melt models, for various geographic locations and time intervals, with calculations of large scale sedimentation rates and the spatial distribution of freshwater input to the ocean due to iceberg melting. More details of previous iceberg modelling work and the adaptations that have been made in the *SedBerg* Model to simulate iceberg-rafted sedimentation in fjords are discussed in Section 2.1.

Iceberg motion is determined by ocean and wind forcing, as well as the Coriolis force (Chirivella and Miller, 1978; Smith, 1993), see Section 2.5.1 for a full description of the equations utilised to model iceberg trajectories. The stability and potential for iceberg overturning was studied by Bailey (1994); Bass (1980) and Weeks and Mellor (1978a), see Section 2.6. In a fjord, it is necessary to model collisions of icebergs with the fjord walls and the glacier front. The approach employed in the *SedBerg* Model is described in Section 2.5.2.

The mechanisms of iceberg melt can be divided into subaerial processes on the face exposed to the atmosphere and subaqueous processes on the submerged faces. The main subaqueous processes are buoyant vertical convection, forced convection and wave erosion (El-Tahan *et al.*, 1987; Huppert and Josberger, 1980; Weeks and Campbell, 1973), which are described in Section 2.4.1. The predominant subaerial melt processes are sensible heat exchange (or forced convection) and radiative transfer of heat (El-

Tahan *et al.*, 1987; Løset, 1992), which are detailed in Section 2.4.2. Subaerial melt is also influenced by the layer of sediment that accumulates on the surface of the iceberg as melting occurs and suppresses further melting (Nicholson and Benn, 2006; Östrem, 1959).

The sediment contained within glacier ice is acquired by icebergs when they calve. The sediment concentration and the distribution of debris through the glacier, for example the thickness of the basal layer, have a significant effect on the sediment transported by icebergs (see Section 2.7).

1.3.1.2 Meltwater Plumes

In general, glacial meltwater plumes emerge from the base of glaciers, as most of the meltwater is transported in subglacial conduits. It is also feasible for meltwater flowing on the surface of the glacier to form a waterfall into the fjord and for englacial conduits to carry water into the fjord above and below the waterline. Meltwater entering the fjord at depth will rise as a plume due to the buoyancy difference between the fresh meltwater and the salty fjord water. It will either rise to the surface or until the plume achieves the same density as the ambient. Upon reaching the surface or becoming neutrally buoyant, the meltwater spreads laterally as a gravity current.

Glacial meltwater contains high sediment concentrations, although usually the concentration is not so high that an underflow develops (Mulder and Syvitski, 1995). In fact, sediment loads of over $40\,kg\,m^{-3}$ are needed to produce an underflow in polar waters at normal ocean salinity. The plume deposits some of its sediment load as it rises if the settling velocity of the grain is fast enough to escape the confines of the plume. The remainder is carried to the surface or to a level where the plume becomes neutrally buoyant. The sediment is then dispersed laterally as it rains out of the spreading horizontal gravity current. The grain size distribution plays an important role in the pattern and rate of sedimentation, as larger grain sizes have higher settling velocities and so will fall out of the plume and gravity current more rapidly. It is necessary to account for flocculation of silts and clays transported by glacial plumes (Curran *et al.*, 2004; Gilbert, 1983; Hill *et al.*, 1998), as this leads to particle aggregates sinking at velocities several orders of magnitude faster then their constituent grains (see Section 3.2.9.2).

Models of jets and plumes have been developed for various applications. Natural sources of buoyant jets include volcanic gas eruptions (Veitch and Woods, 2002), hydrothermal vents in the deep ocean (German and Sparks, 1993) and fresh groundwater plumes at the coast. Plumes also originate from man-made influences, such as mining and oil extraction operations, waste and sewage treatment and exhaust from cooling

towers. The diversity and range of jets and plumes is reflected in the extensive literature on the subject. Previous models of jets and plumes, some of which include the deposition of sediment, are discussed in Chapter 3.

1.3.1.3 Relative Importance of Iceberg-Rafted and Meltwater Sedimentation

Different climatic regimes result in a varying relative importance of sedimentation due to iceberg-rafting compared with glacial meltwater plumes. A schematic of this effect, with reference to various fjord locations, is shown in Figure 1.4. It can be seen that

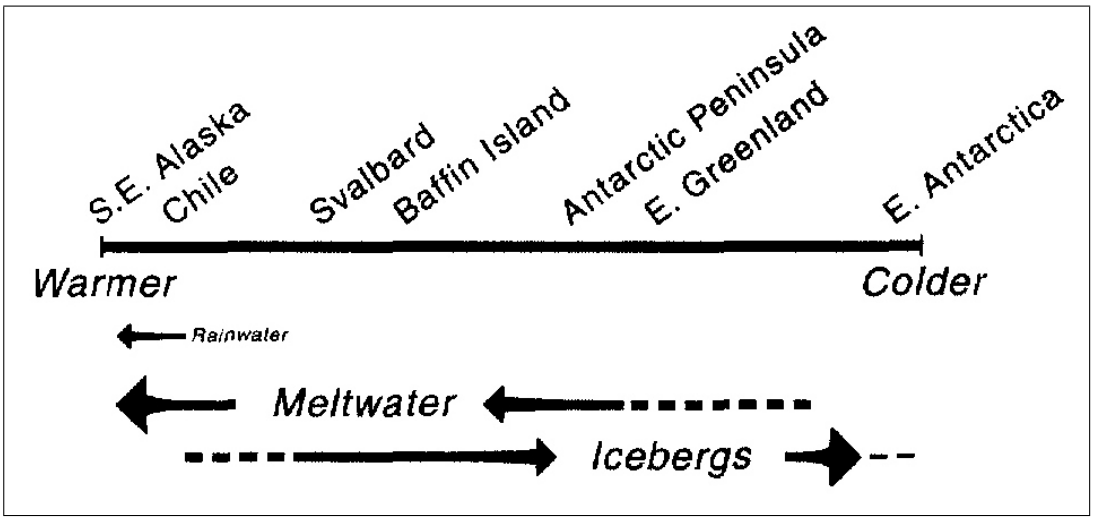

Figure 1.4: *Relative importance of meltwater and iceberg-rafted sedimentation in different climatic settings (Dowdeswell et al., 1998).*

relatively warm, moist environments are conducive to deposition mainly from meltwater plumes, for example South East Alaska and Svalbard, whereas sedimentation is dominated by iceberg-rafting in colder settings with lower precipitation rates, for example East Antarctica and East Greenland. This distinction between different fjord regions is employed when applying each of the *SedBerg* and *SedPlume* Models to a case study in Chapters 4 and 5.

1.3.2 Glacimarine Lithofacies

The major lithofacies deposited as a result of glacimarine sedimentation were described by Powell (1981):

- Diamicton
- Iceberg-zone mud
- Marine-outwash mud

- Morainal banks
- Piles of gravel and mud
- Laminated sand and mud
- Sediment gravity flows and Turbidity current channels
- Deltaic Wedges
- Tidal flat mud.

Diamicton lithofacies, or very poorly sorted sediments, are produced by a number of processes. The mixing of silt and clay from meltwater streams with coarse debris from numerous icebergs containing basal ice deposit a coarse diamicton (Dowdeswell *et al.*, 1994b). When icebergs are less numerous and contain mainly englacial ice, there is a higher proportion of silt and clay and lower proportion of coarse-grains, which leads to iceberg-zone mud (Powell, 1981). Diamicton lithofacies can also be generated by till deposition at the base of active glaciers (Eyles *et al.*, 1983), basal melting near the grounding line beneath floating ice shelves (Dowdeswell *et al.*, 1994b) and sediment gravity flows (Powell, 1981). It is difficult to distinguish between these diamicton facies without additional information about the environment in which the deposition occurred.

When the glacier front retreats so that it terminates on land, large deltaic wedges, comprised of coarse-grained fluvial deposits on the delta surface with sand on the foreslope, build up and prograde into the fjord (Powell, 1981). Further away from the ice front, marine-outwash mud consisting of glacial flour silt and clay with a minor coarse-grained component is deposited (Powell, 1981). In shallow water environments, if the glacier retreats even further, tidal flats made up of tidal-flat mud and braided stream and beach sands will form (Powell, 1981).

Morainal banks are formed during slow glacier front retreat or standstills during retreat. A large bank is deposited, which is composed of a mixture of diamicton, gravel, rubble and sand with contributions from calving icebergs, glacier front melt and subglacial streams (Powell, 1984). Smaller push moraines, consisting of gravel, rubble and diamicton, are formed during minor winter advances of an ice front and are preserved if the ice front undergoes rapid retreat the following summer (Ottesen and Dowdeswell, 2006). Piles of gravel and rubble are deposited by icebergs calving from a rapidly retreating ice front and overturning in the distal zone (Dowdeswell and Murray, 1990).

Laminated sand and mud lithofacies are formed by a number of different processes. Cowan *et al.* (1998) identified semi-monthly, monthly, bimonthly and annual cycles caused by tidal influences in meltwater-dominated Alaskan fjords. Near the glacier, two couplets were produced each day from the turbid layers resulting from the semidiurnal tides (Cowan and Powell, 1990). Spring-neap packages have also been

observed by Cowan *et al.* (1999) who recorded 15 couplets per fortnight. Variations in stream discharge on daily and seasonal time scales produce laminated mud deposits or cyclopel (Mackiewicz *et al.*, 1984). Sand laminae intercalated with mud are commonly deposited by turbidity currents or sediment gravity flows. Cowan *et al.* (1999) observed turbidity current deposits with a frequency of approximately once a month during the melt season and attributed their occurrence to the tidal drawdown mechanism described by Smith *et al.* (1990) and Phillips *et al.* (1991). During the spring low tide, the delta lip and plain is uncovered so channels are eroded. This releases a pulse of sediment into the basin, leading to instabilities, slope failures and turbidity currents.

In polar glacimarine fjords there is a decreased contribution of meltwater processes to sediment deposition. In the ice-distal parts of these fjords, the presence of shorefast sea ice intermittently prevents icebergs from transporting and depositing sediment. During periods of suppressed iceberg-rafting, suspension settling deposits from meltwater sources build up and when the sea ice breaks up, iceberg-rafting of sediment resumes. This results in layers of laminated fine silt and clay bounded by massive diamict (Dowdeswell *et al.*, 2000; Ó Cofaigh and Dowdeswell, 2001).

Different climatic conditions can result in the deposition of visually identical sediment lithofacies (Ó Cofaigh and Dowdeswell, 2001; Smith and Andrews, 2000). To identify the process responsible for a particular lithofacies, it is necessary to apply knowledge of the environmental conditions at the time of deposition to reveal a distinct sedimentological signature for each fjord environment.

1.4 Structure of Thesis

This thesis alternately describes aspects of the two numerical models, *SedBerg* and *SedPlume*, which simulate sediment deposition by iceberg-rafting and glacial meltwater plumes, respectively. Chapter 2 discusses the theory, design and implementation of the numerical routines underlying the *SedBerg* Model, which utilises Monte Carlo based techniques to simulate the formation, drift and melt of a population of icebergs, and the subsequent deposition of sediment from those icebergs. The subject matter of Chapter 3 is the theoretical foundation and the development of the *SedPlume* Model, which implements an integral model formulation for the conservation of volume, momentum, buoyancy and sediment mass along the path of a turbulent, entraining plume injected into stably stratified ambient fluid.

Two further chapters then examine a case study for each model, one with an iceberg-dominated and the other with a meltwater-dominated glacimarine sedimentary environment. Chapter 4 explores the application of the *SedBerg* Model to Kangerd-

lugssuaq Fjord in East Greenland, where field measurements were collected in 1991 and 1993, as well as during a scientific cruise in 2004 that I participated in. The *SedBerg* Model inputs are derived from these observations where possible and supplemented with other data from the East Greenland region. The output of the *SedBerg* Model is compared to a $17\,m$ sediment core, with a basal date of 1430±60 yrs B.P., collected in 1993. In Chapter 5 the *SedPlume* Model is applied to McBride Inlet in Glacier Bay, Alaska. The *SedPlume* Model results are compared to the extensive data set of sedimentation rates and the spatial variability of deposition collected by Powell and Cowan from 1984 to 1987. In addition, there have been many expeditions to the surrounding fjords of Glacier Bay, which provide values for the initial conditions.

Chapter 6 addresses the influence of various parameters on the rate and pattern of sediment deposition for both the *SedBerg* and the *SedPlume* Model. For the *SedBerg* Model, the parameters considered are: iceberg size; temperature and depth of thermocline and seeds of the random number generator for water and wind velocities. For the *SedPlume* Model, the parameters studied are: subglacial conduit radius and initial meltwater velocity; initial sand fraction and ambient density gradient.

Chapter 7 concludes the thesis and presents some ideas for future investigation.

Chapter 2

Iceberg-rafted Sedimentation: Theory and Development of *SedBerg* Model

2.1 Introduction

Icebergs play an important role as freshwater inputs to the polar oceans and transport significant volumes of sediment within fjords and to continental margins, where glaciers terminate in a lake or ocean. In this chapter a model of iceberg-rafted sedimentation, *SedBerg*, is described, which utilises Monte Carlo based techniques to simulate deposition of sediment from icebergs. The model simulates the formation, drift and melt of a population of icebergs, with a number of underlying parametric probability distributions to describe the stochastic behaviour of iceberg formation and dynamics.

The process of iceberg formation, where ice breaks off a glacier along lines of weakness and is released into the water, is called iceberg calving (Section 2.2). The newly formed iceberg inherits the sediment frozen within the glacier ice and transports it into the marine environment (Dowdeswell and Murray, 1990). An ice-facies classification scheme for glacier ice was first proposed by Lawson (1979), who distinguished ice-facies by style of debris suspension, concentration and zones of transport (basal, englacial and supraglacial). Basal ice is the layer at the bed of the glacier, which contains high concentrations of eroded debris. Supraglacial ice is found on the glacier surface, containing highly variable concentrations of debris. Englacial ice makes up the bulk of the ice in the interior of the glacier and usually contains very low sediment concentrations. The mechanisms by which debris is incorporated into subglacial, englacial and supraglacial ice are discussed in Section 2.7.

The position in the glacier where an iceberg originates from, dictates the concen-

tration of sediment frozen within the iceberg. Some icebergs inherit the sediment-rich basal layer from the glacier, whilst others are relatively 'clean' and contain low debris concentrations from the englacial layer. During the calving process, any supraglacial sediment is released if the iceberg overturns. This will be discussed in more detail in Section 2.2.

Mean iceberg sedimentation rates over a whole fjord or basin area can be estimated using (Dowdeswell and Dowdeswell, 1989):

$$\overline{r}_s = \frac{h_b \overline{c}_d}{100} \frac{(\overline{v}_g - \overline{m}_g)\, w_g}{a_s} \tag{2.1}$$

where $\overline{r}_s$ is the mean iceberg sedimentation rate over the basin area, h_b is the mean thickness of the debris-rich basal layer of the glacier (see Section 2.7), $\overline{c}_d$ is the mean percentage debris content by volume of the basal layer, $\overline{v}_g$ is the mean velocity at the tidewater glacier margin, $\overline{m}_g$ is the mean advance or retreat of the ice front over a given time period, w_g is the width of the tidewater glacier front and a_s is the area of the marine basin. However, this treatment does not provide information on the spatial distribution of sediment deposition within a fjord.

In addition to the parameters in equation 2.1, the rate and timing of sediment release from icebergs depends on the velocity of iceberg drift, the melt rate of the iceberg, the location of the glacial debris within the iceberg and the frequency of iceberg overturning (Syvitski *et al.*, 1987). The velocity at which an iceberg moves controls the deposition rate to a large extent. Obstructions, such as a shallow sill in a fjord mouth, may lead to larger icebergs blocking the exit for smaller icebergs, increasing the residence time in the fjord and therefore increasing the deposition rate behind the obstruction (Dowdeswell, 1987). Tides, winds and currents all affect an iceberg's progress within the fjord, resulting in the iceberg undergoing a 'random walk'. However, the time-averaged velocities of the icebergs are usually towards the open ocean. As the icebergs drift, the sediment frozen within is gradually released as they melt. The subaqueous and subaerial processes of iceberg melt will be discussed in detail in Section 2.4.

There has been interest in the study of icebergs for many years. In the 1970s and 1980s, icebergs were proposed as a potential source of fresh water for regions of the world where there is a shortage of water. This led to research on iceberg size distributions, spatial distributions, roll stability, the effect of forces on iceberg drift, such as wind and water drag (Morgan and Budd, 1978; Weeks and Mellor, 1978b), iceberg deterioration (Josberger, 1978) and iceberg melt rates (Russell-Head, 1980; Weeks and Campbell, 1973). Since icebergs present a hazard to ships and other man-made structures in the ocean, observational studies have been carried out (Mangor and

Zorn, 1983; Riggs *et al.*, 1980) and models developed to predict iceberg trajectories in areas where there are important shipping routes and petroleum drilling platforms (Løset, 1993b; Mountain, 1980; Smith, 1993; Smith and Banke, 1983).

With respect to modelling icebergs transporting sediment to the glacimarine environment, Dowdeswell and Murray (1990) formulated a simple two-dimensional model to calculate the flux of debris calved in icebergs from a tidewater glacier, iceberg melt rates and sedimentation with distance from the ice front. The icebergs are modelled to move along a transect away from the glacier with a constant velocity and the melt rates are calculated from the Weeks and Campbell and Russell-Head relationships. They incorporated overturning events through qualitative estimates of their frequency, and assumed that the iceberg would rotate through 180° on each overturn, so that the debris-rich basal ice would alternate between subaqueous and subaerial melting. They used an empirical relationship for subaerial melting under a debris layer derived by Östrem (1959). They used the model to assess sedimentation rates in a number of different polar environmental settings.

Matsumoto (1996, 1997) developed a three-dimensional iceberg drift and decay model in order to simulate the long-term ice-rafted debris and iceberg meltwater flux over an entire ocean basin. The drift model solved the equations of motion for an iceberg under forces of water drag, wind drag, Coriolis force and the gravitational force due to the surface slope of the ocean. The decay model utilised an empirical relation between the iceberg life expectancy and mass to incorporate all the melting and other deterioration mechanisms that reduce the iceberg's size over time. These parameters were tuned for each month of the year so that the modelled iceberg spatial distribution were close to contemporary observations.

Bigg *et al.* (1997) developed a model of iceberg drift and melt, which solved the equations of motion for an iceberg in a similar way to previous models (Matsumoto, 1996; Mountain, 1980; Smith, 1993; Smith and Banke, 1983). They implemented a more complex melting algorithm than Matsumoto (1996), as well as iceberg overturning if the stability criterion derived by Weeks and Mellor (1978b) was exceeded. The Bigg *et al.* (1997) Model has been applied to the Arctic Ocean and North Atlantic to model the large scale drift and melt of icebergs in this region, where it reproduced the observed southward limit of iceberg extent in the North Atlantic reasonably well (Bigg *et al.*, 1996). It has been utilised to model iceberg trajectories and meltwater injection in the Southern Ocean (Gladstone *et al.*, 2001; Silva *et al.*, 2006). It has also been employed to simulate iceberg meltwater production and sedimentation rates from the Eurasian Ice Sheet during the last glaciation (Death *et al.*, 2006).

A new model of iceberg-rafted sedimentation, *SedBerg*, is introduced in this chapter. Previous models are built upon to develop a new iceberg drift and sedimentation

model for fjord environments. A schematic of the *SedBerg* Model, where the axes and other symbols used in the model are defined, is shown in Figure 2.1. The main

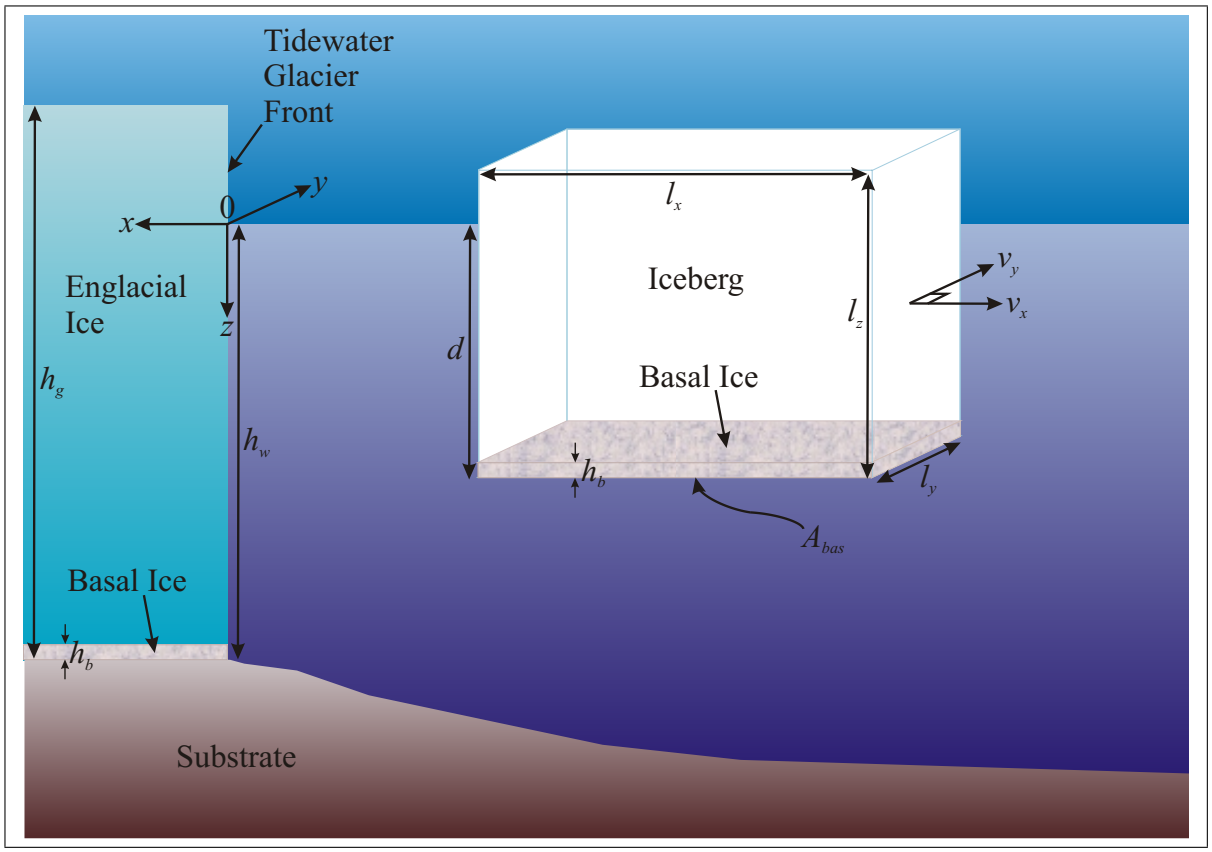

Figure 2.1: *Schematic of grounded tidewater glacier front showing the layer of sediment-rich basal ice at the bed and an example of an iceberg, which has inherited the basal layer from the glacier. The symbols and direction of axes used in iceberg sedimentation model are defined. N.B. the x-axis is positive towards the North.*

differences of the *SedBerg* Model compared to previous iceberg sedimentation models are as follows:

1. Water temperature variability with depth is included.
2. Icebergs are deflection by the fjord walls and ice front instead of becoming grounded.
3. A continuous iceberg size distribution is adopted.
4. A new treatment of iceberg stability is applied.

These modifications result in an iceberg-rafted deposition model tailored for fjord environments.

2.2 Iceberg Calving

Iceberg calving makes an important contribution to the mass loss from ice sheets and glaciers where they terminate in water, yet it is often poorly represented in ice flow models. This is not for lack of research effort. Calving rates have been studied in the field, which has resulted in the development of a variety of empirical calving relations derived from observations. More complex, semi-empirical models based on parameterisations of the underlying calving physics have also been constructed (Benn *et al.*, 2007b; Van der Veen, 2002). In addition, complex fracture mechanics models, which solve the equations from the forces acting on the ice at the front of a glacier, have been formulated (Hughes, 1992, 2002). The rate of iceberg production (or calving rate) from a glacier is usually expressed as a velocity. It is dependent upon many factors, including the glacier flow velocity and its spatial variation (which controls the strain rate and therefore the frequency and depth of crevassing on the glacier), whether the glacier is retreating or advancing, climatic/environmental conditions, the glacier geometry and the geometry of the underlying basin, which together determine whether the glacier is floating or grounded. The latter is an important control on the calving rate since the calving mechanisms for a grounded tidewater glacier are different from those at a floating glacier tongue.

The mechanism of calving will affect the calving rate, so the different calving mechanisms will be described next. Four styles of calving from a tidewater glacier have been defined by Syvitski (1989) and Van der Veen (2002), as shown in Figure 2.2. The calving mechanisms (a), (b) and (c) are dominant at grounded tidewater glaciers and mechanism (d) only occurs when the front of the glacier is floating. At grounded glacier margins, one of the most important factors is the steepening of the ice front due to the vertical velocity gradient, which causes an increase in the surface bending stresses, leading to crevasse deepening and eventual failure of the ice. In mechanism (a) submarine discharge has eroded an ice cave at the base of the glacier and along with a crevasse, this results in a line of weakness where subaerial jointing of ice blocks can take place. In mechanism (c) the ice cliff is eroded by tides and waves at the water surface, creating a tidewater indenture, which results in tidewater jointing. In both cases the supraglacial debris would be deposited during calving as the ice block falls from the glacier front. If the calving mechanism (c) occurs along with thermal erosion near the water-line, the glacier can form a protruding 'foot'. This results in calving mechanism (b), where buoyancy forces lead to the 'foot' breaking off and floating to the surface.

Mechanism (d) occurs where part of the glacier front reaches floatation and the bending of this section of the ice front by tides, and sometimes storm waves, leads

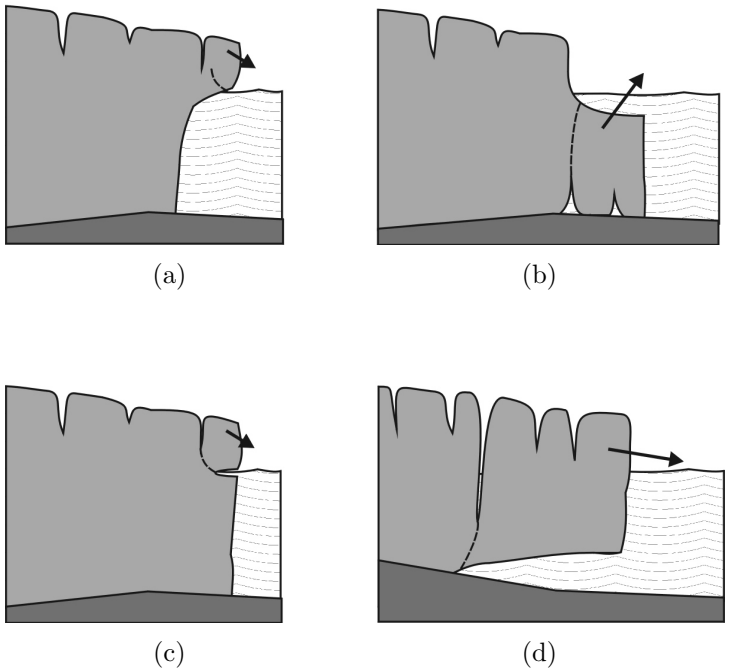

Figure 2.2: *Types of iceberg calving from a tidewater glacier terminus from Van der Veen (2002): (a) subaerial launch of a serac; (b) Subaqueous calving of submarine platform or ice 'foot'; (c) Separation of an iceberg along a joint intersecting a thermoerosional notch; (d) Separation along a deeply incised crevasse on a floating tongue.*

to crevasse deepening and weakens the ice at the point where it is grounded, until eventually a large mega-iceberg detaches from the glacier. This commonly occurs at basin constrictions, where large transverse crevasse systems exist. The velocity of the glacier is greatest on the centre line, which causes the glacier front to be convex in shape, and the central protruding region generally calves by the detachment of mega-icebergs. Little supraglacial debris is released by this method, as the iceberg does not tend to overturn during calving. It should be noted that this calving mechanism is important at the margins of fast flowing Greenland outlet glaciers, which commonly have a floating tongue. The mechanism of iceberg calving will affect the size distribution of icebergs produced and the calving rate. However, in the *SedBerg* Model the size distribution is defined empirically from observations, see Section 2.3.

There are a diverse range of calving models of differing complexity, some of which will be discussed here. In the literature calving models range from fracture mechanics models (Hughes, 1992, 2002) to empirical calving relations derived from field observations (Brown *et al.*, 1982; Pelto and Warren, 1991). A good review paper on the subject was written by Benn *et al.* (2007b).

Recently Benn *et al.* (2007a) introduced a new calving rate criterion, which depends on ice velocity, strain rate, ice thickness and water depth, and predicts calving when the depth of surface crevasses (calculated from strain rates and terminus position) equals

the height of the ice front above sea level. They coupled it with three different 'sliding laws' to model glacier flow. This iceberg sedimentation model has been developed separately from a glacier flow model, although it could be coupled to one in the future, along with a calving law such as the one developed by Benn *et al.* (2007a) or Van der Veen (2002).

More elaborate fracture mechanics calving models have been developed for grounded ice fronts by Hughes (1992) and for floating tongues by Hughes (2002). Hughes (1992) considered the forces and couples acting on the snout of the glacier for the calving of tabular icebergs from grounded ice walls. He found a calving rate v_c:

$$v_c = \frac{3\, g\, h_g^3\, \theta}{\eta\, d_{cc}^2} \left[(\rho_{ice} - \rho_w)\, h_g + \rho_w h_w \right] \tag{2.2}$$

where h_g is the glacier ice thickness, h_w is the water depth, g is the gravitational acceleration, d_{cc} is the distance from the glacier front where the critical crevasse forms, ρ_i is the density of ice, ρ_w is the density of seawater, θ is the angle that the ice block in front of the critical crevasse makes with the vertical and η is the viscoplastic viscosity. However, this bending-shear mechanism requires a substantial ice height above the floatation thickness, which limits its applicability to glaciers whose terminus approaches flotation (Van der Veen, 1996). Hughes (2002) went on to develop a more complex fracture mechanics model for subaerial calving of ice slabs and subaqueous calving of ice ledges from ice walls and ice shelves terminating in water. Applying such computationally intensive treatments for modelling calving rates over long time periods is not practical for this iceberg sedimentation model.

Van der Veen (1996) developed a different concept, which was adopted and modified slightly by Vieli *et al.* (2001). The calving model assumes that the glacier will retreat to the point where the effective basal pressure approaches zero, so that the terminus retreats if the thickness in excess of floatation becomes less then some critical value. This means that the retreat rate is a function of the thinning rate of the ice and by the basal geometry. The calving rate is then calculated from the difference between the ice velocity and the retreat rate. This model is applicable to glaciers where the climate is too warm, therefore the ice is too weak, for a floating tongue to form.

Alternatively, simple calving relations have been formulated empirically from observed calving rates. Brown *et al.* (1982) calculated the calving speed for 12 glaciers in Alaska by taking the calving speed to be the difference between the glacier speed and the rate of terminus advance. They found that the rate of iceberg calving, v_c, was directly proportional to the water depth at the terminus of the glacier, h_w:

$$v_c = b\, h_w \tag{2.3}$$

They found the value of the calving coefficient, $b = 27 \pm 2\,yr^{-1}$ with a goodness of fit, R^2, of 0.91. It should be noted that the calving rate of 9 of the 13 glaciers in their study was measured during a single ablation season, giving summer, not annual calving rates.

Pelto and Warren (1991) analysed mean annual calving rates and water depth data from 22 glaciers. In the same way as Brown *et al.* (1982), they took the calving rate as the difference between the ice velocity and the rate of advance. They took data from 11 grounded temperate glaciers, 7 grounded polar glaciers and 4 floating polar glaciers in Alaska, West Greenland and Svalbard. They found the following fit to the data:

$$v_c = 70 + 8.33 h_w \tag{2.4}$$

The correlation coefficient, ρ, between calving velocity and water depth was found to be 0.85 (or $R^2 = 0.72$). It was observed that the annual and summer calving speeds of Greenland glaciers do not vary as much as temperate glaciers.

Where data is available, it is also possible to use directly measured annual calving rates for the glacier to be modelled. The method of calculating the calving rate can be altered depending on the glacier being modelled. This chapter gives an idea of the available options. Since the iceberg sedimentation model is in the development phase, it will be run independently of a glacier flow model, therefore the calving laws which require information about glacier dynamics are not applied.

In the *SedBerg* Model the size of the calving time step, Δt_c in days, is calculated using the calving rate, v_c in $m\,yr^{-1}$, and the probability of calving in each time step, P_c is set to be 0.25, substituted into the following equation:

$$\Delta t_c = P_c \frac{365\ E\left(V_i\right)}{V_a} \tag{2.5}$$

where $E\left(V_i\right)$ is the expected, or mean, volume of an iceberg and V_a is the annual volume of ice calved from the glacier:

$$V_a = v_c h_g w_g \tag{2.6}$$

where h_g is the height of the glacier front and w_g is the width of the glacier front.

The condition for an iceberg to be produced is satisfied if a uniform random deviate (drawn each calving time step) is less than 0.25. In the *SedBerg* Model, testing for an iceberg calving event happens at intervals as close as possible to the calving time step, Δt_c, but in multiples of the moving and melting time step, Δt_m, as described in Section 2.5.1.

2.3 Iceberg Size Distribution

As mentioned in Section 2.2, the iceberg size distribution produced from a glacier depends on the calving mechanisms by which they formed (Dowdeswell and Bamber, 2007). Grounded tidewater glaciers, for example in Svalbard, which are heavily crevassed, produce large numbers of small, irregular icebergs because the dominant calving mechanisms are (a), (b) and (c) from Figure 2.2. Where the glacier tongue is floating, for example at some Greenland outlet glaciers, larger, tabular icebergs are commonly calved by mechanism (d) from Figure 2.2. Clearly, the maximum iceberg thickness will be limited by the thickness of the ice at the glacier front for both floating and grounded margins. The maximum horizontal iceberg dimension cannot be greater then the height of the ice front for grounded tidewater glaciers, unlike floating margins, which can produce large tabular icebergs (Dowdeswell *et al.*, 1992).

Iceberg size distributions have been measured in different locations around the globe, using a variety of methods. For the reasons stated above, the observed iceberg size distributions display high variability depending on the glacial environment from which the icebergs originated.

In the Barents Sea to the South-East of Svalbard, an area of grounded tidewater glaciers, Vinje (1989) used SPOT panchromatic satellite images to measure iceberg length, width and freeboard. The resolution of the SPOT satellite was $10\,m$, so they were able to measure 54 icebergs to the nearest $10\,m$ and found that iceberg width ranged from 20–$200\,m$ and the freeboard from 3–$17\,m$. Over 50% of the sample had widths greater than $50\,m$. The icebergs originated from a large number of source glaciers. It is not possible to tell how much time had passed, and thus how much weathering had occurred, since they were calved. Therefore these measurements may not be representative of the size distribution for freshly calved icebergs.

At a grounded tidewater margin in Kongsfjorden, North-West Spitsbergen, Dowdeswell and Forsberg (1992) measured 275 icebergs and bergy bits directly from a launch along four transects. For three of the transects collected in different parts of the fjord during the same year, similar size-frequency distributions were found for the maximum iceberg width. 35–40% of the icebergs were less than $0.5\,m$ and less than 10% exceeded $5\,m$ in width. The maximum observed iceberg width was $30\,m$, but this was an outlier.

In the Scoresby Sund fjord system in East Greenland, a region with large outlet glaciers, some of which have floating tongues, Dowdeswell *et al.* (1992) measured 1900 icebergs using shipboard radar and a sextant. They found that 69% of icebergs were less than $200\,m$ in width, 5 were greater than $1\,km$ and the largest was $2.7\,km$. The modal iceberg keel depths decreased from the head to the mouth of the fjord system: 400–$500\,m$ for Nordvestfjord, 300–$400\,m$ for Hall Bredning and 100–$200\,m$ for Scoresby

Sund.

In the South Atlantic Ocean, where large tabular icebergs have calved from Antarctic ice shelves, Wadhams (1988) measured the diameters of 174 icebergs using shipboard radar during the southern winter. He argued that a log-normal distribution was a reasonable fit to the data, because there is a preferred diameter resulting from wave-induced flexural failure and a threshold below which the iceberg disintegrates into bergy bits. These icebergs were exposed to severe weathering and therefore the character of their size distribution would have changed significantly since they were calved.

As mentioned above, a number of authors have likened the observed size distribution of icebergs to a log-normal (Dowdeswell and Forsberg, 1992; Dowdeswell *et al.*, 1992; Wadhams, 1988; Weeks and Mellor, 1978a). Freshly calved icebergs will display a central tendency about a preferred diameter, due to the crevasse spacing in the glacier from which they calved rather than wave-induced flexural failure, which produces a different log-normal size distribution for weathered icebergs, as observed by Wadhams (1988). Bigg *et al.* (1997) used a discretisation of the log-normal distribution for the iceberg sizes in their model. Therefore, it seems reasonable to assume that the iceberg size distribution is log-normal in the *SedBerg* Model.

The log-normal is an asymmetric, unimodal distribution. The probability density function of a log-normally distributed random variable, Y, is:

$$f(Y) = \frac{1}{Y\sqrt{2\pi\sigma^2}} \exp\left[-\frac{1}{2}\frac{(\ln(Y)-\mu)^2}{\sigma^2}\right] \tag{2.7}$$

where μ is the mean and σ is the standard deviation of a normally distributed random variable, X, and $Y = e^X$. The mean, or expectation, of Y is:

$$E(Y) = e^{\mu+\frac{\sigma^2}{2}} \tag{2.8}$$

and the standard deviation is:

$$SD(Y) = e^{\mu+\frac{\sigma^2}{2}}\sqrt{e^{\sigma^2}-1} \tag{2.9}$$

The observed iceberg size (width) distribution as measured by Dowdeswell *et al.* (1992) in Scoresby Sund, is shown in Figure 2.3. A log-normal distribution is fitted using maximum likelihood estimators calculated from the observed data. The expected value of the fitted log-normal distribution is $173.3\,m$. It can be seen that there is a reasonably close fit, and the fact that the log-normal distribution is equal to zero

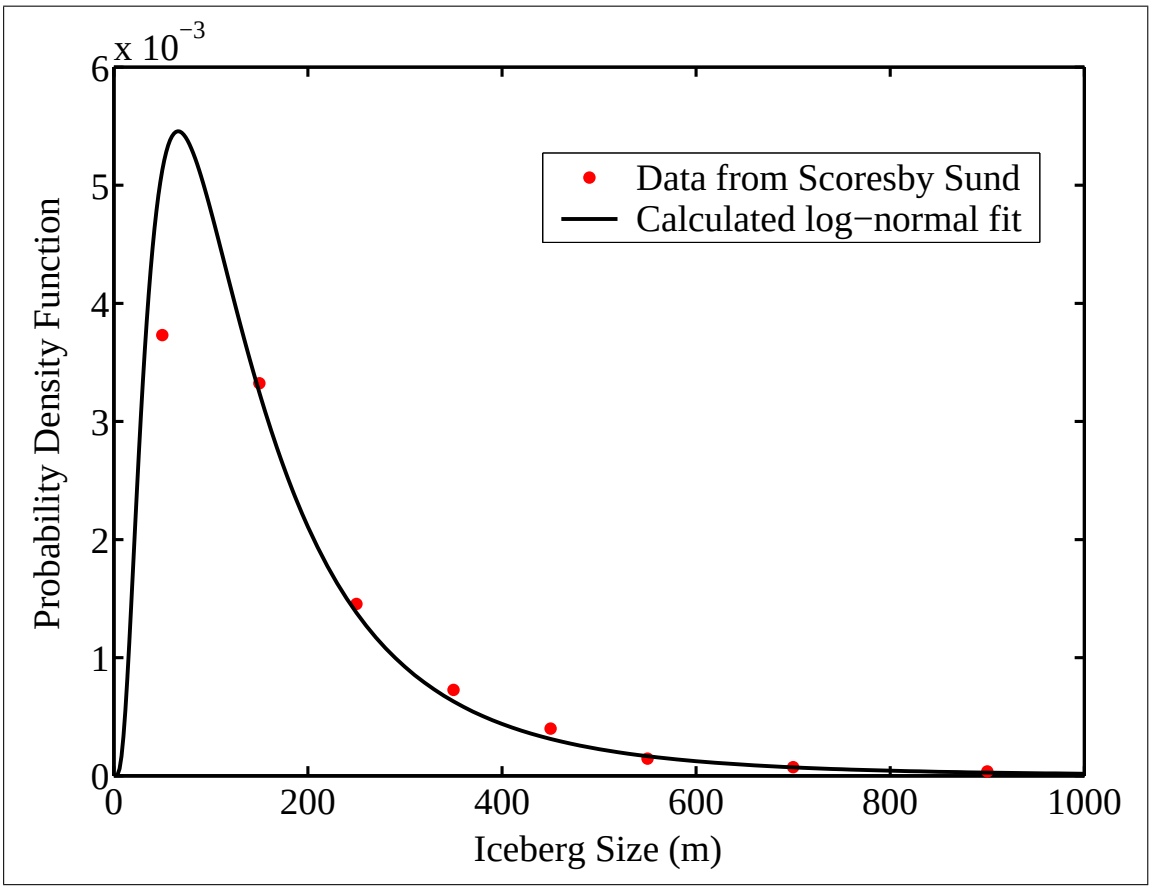

Figure 2.3: *Iceberg size distribution for Scoresby Sund (Dowdeswell et al., 1992), with a log-normal curve fitted*

at the origin is useful for avoiding producing icebergs that have zero size. Even so, it is necessary to limit the minimum iceberg size to the size of the model grid cells. Observations of iceberg size distribution are truncated at the lower end by not including icebergs below a threshold size, either due to satellite sensor resolution (Vinje, 1989), or data selection (Dowdeswell *et al.*, 1992). The iceberg thickness is censored so that is does not exceed the glacier thickness. The log-normal distribution does not fall to zero, even for very large Y (iceberg size), therefore it is necessary to censor the distribution so that the iceberg width and length do not exceed a maximum value.

The icebergs observed in the fjords of Scoresby Sund in East Greenland and Kongsfjorden in North-West Spitsbergen will have undergone some melt before they were measured by Dowdeswell *et al.* (1992) and Dowdeswell and Forsberg (1992), respectively. However, since fjord environments are fairly sheltered the icebergs would not have undergone severe weathering and breakup, so the observed iceberg size distribution can be assumed to be a good approximation to the size distribution of freshly calved icebergs.

Following Dowdeswell *et al.* (1992), the width:length ratio used is 1:1.62 as was

observed in Scoresby Sund in East Greenland. If L_i is the iceberg size calculated from the log-normal distribution, the iceberg volume is taken to be L_i^3, and in order to satisfy both this and the width:length ratio, the lengths of the respective iceberg sides are calculated to be:

$$L_x = 1.3793 L_i \tag{2.10}$$

$$L_y = 0.8514 L_i \tag{2.11}$$

$$L_z = 0.8514 L_i \tag{2.12}$$

where L_i is the iceberg size calculated from the log-normal distribution, L_x is the iceberg length, L_y is the iceberg width and L_z is the iceberg height, as defined in Figure 2.1.

The thickness is assumed to be equal to the width up to a maximum thickness, which is the height of the glacier from which it calved (Bigg *et al.*, 1997). If the thickness of an iceberg exceeds this when it is produced by the model, then it is 'censored', which means it is set to the specified maximum thickness. Maximum values are also specified for the iceberg width and length, and if an iceberg exceeds these, the value is also 'censored' and set to be equal to the maximum value instead.

Using the density of pure ice to calculate the iceberg mass, 13% of the iceberg should be above the water line. However, observations of tabular icebergs in the Southern Ocean by Weeks and Mellor (1978a) report that up to 18% of the iceberg length is above the water due to wave terracing. A compromise is to calculate the draught to freeboard ratio to be 5:1, which means that 16.7% of the iceberg is above the water (Bigg *et al.*, 1997).

2.4 Iceberg Deterioration

Icebergs deteriorate at large scales by fragmentation, and at smaller scales by melting. Both processes will be discussed here. As melting is the mechanism which releases sediment frozen within the iceberg into the water, this is important for the *SedBerg* Model. Melting also evolves the mass and shape of the iceberg over time, which affects the stability of the iceberg (see Section 2.6).

Models of iceberg melt vary from complex models utilising finite-differencing techniques to solve the heat diffusion equation for an iceberg, to more simple, empirical relationships based on observational and experimental data. An example of a complex two-dimensional numerical model of the temperature distribution and ablation of icebergs was developed by Løset (1993a) to investigate the rate of deterioration and therefore the expected life time of icebergs. He discretised the heat diffusion equation

and solved it in two-dimensions using finite-difference techniques. Løset (1993b) coupled the iceberg heat transfer model of Løset (1993a) with a drift model in order to simulate the drift and decay of nine icebergs in the Barents Sea, for which temperature profiles were obtained. For modelling the melt rate of large numbers of icebergs, solving the heat diffusion equation using finite differences in two-dimensions for each iceberg is too computationally expensive and requires detailed input parameters, which are not available.

Instead, a more empirical approach will be taken in the *SedBerg* Model, with the melt rate due to each process averaged over the appropriate side so that the iceberg remains a rectangular parallelepiped (Bigg *et al.*, 1997). This means that only three melt rates need to be calculated for each iceberg: corresponding to the sides, base and top. The water temperature is calculated as the average over the iceberg keel depth for the melt rate of the iceberg sides and taken as the temperature at the keel depth for the melt rate of the iceberg base. This attribute of the *SedBerg* Model differs from the Bigg *et al.* (1997) Model of iceberg drift and melt, which used the sea surface temperature to calculate iceberg melt rates.

The mechanisms of iceberg melt described in the following sections are: subaqueous forced convection, subaqueous buoyant convection, wave erosion, subaerial forced convection and solar radiation.

2.4.1 Subaqueous Melt Processes

2.4.1.1 Forced Convection

Turbulence from the relative motion of water past an iceberg results in the transfer of heat. This turbulent heat transfer occurs at the base and sides of an iceberg as water flows past. Weeks and Campbell (1973) first applied this process of melt to icebergs and derived the melt rate, R_{fc}, from the theory of Eckart and Drake (1959) for turbulent heat transfer past a flat plate. They began with the following relationship for the Nusselt number, Nu, which is used to measure the enhancement of heat transfer that occurs by convection as opposed to solely by conduction:

$$Nu = 0.037 Re^{0.8} Pr^{1/3} \tag{2.13}$$

The Nusselt number is the ratio of convective to conductive heat transfer, which is given by:

$$Nu = \overline{h} L_x / k_w \tag{2.14}$$

where $\overline{h}$ is the average heat transfer coefficient, L_x is the horizontal long-axis of the

iceberg and k_w is the thermal conductivity of sea water.

The Reynolds number, Re, is the ratio of inertial to viscous forces, calculated by:

$$Re = \frac{|\mathbf{v}_w - \mathbf{v}_i| \; L_x}{\nu_w} \tag{2.15}$$

where $|\mathbf{v}_w - \mathbf{v}_i|$ is the relative free stream velocity and ν_w is the kinematic viscosity of water.

The Prandtl number, Pr, is the ratio of momentum diffusivity (viscosity) and thermal diffusivity, given by:

$$Pr = \frac{c_p \mu_w}{k_w} \tag{2.16}$$

where c_p is the specific heat and μ_w is the dynamic viscosity of water.

If equation 2.13 is evaluated with the values: $k_w = 0.563\, W(m\,^\circ C)^{-1}$; $\nu_w = 1.826 \times 10^{-6}\, m^2\, s^{-1}$ and $Pr = 13.1$, this results in:

$$\overline{h} = 1914 \frac{|\mathbf{v}_w - \mathbf{v}_i|^{0.8}}{L_x^{0.2}} \tag{2.17}$$

where $\overline{h}$, $|\mathbf{v}_w - \mathbf{v}_i|$ and L_x are given in $W\,(m^2\,^\circ C)^{-1}$, $m\,s^{-1}$ and m, respectively. The heat flow rate, q, for a given face of the submerged portion of the iceberg is then given by:

$$q = \overline{h} A_m \Delta T \tag{2.18}$$

where A_m is the area of the face and ΔT is the temperature difference between the ice and the water. The rate of melting of the iceberg face due to forced convection is:

$$R_{fc} = \frac{q}{A_m \rho_i \Gamma_i} \tag{2.19}$$

where the average density of an iceberg, $\rho_i = 850\, kg\, m^{-3}$ and the latent heat of fusion of ice, $\Gamma_i = 3.34 \times 10^5\, J\, kg^{-1}$.

By substituting equations 2.17 and 2.18 into equation 2.19, R_{fc} can be expressed, in $m\, day^{-1}$ as:

$$R_{fc} = 0.582\, |\mathbf{v}_w - \mathbf{v}_i|^{0.8}\, \frac{T_w - T_i}{L_x^{0.2}} \tag{2.20}$$

where $\mathbf{v}_w$ is the water velocity, $\mathbf{v}_i$ is the iceberg velocity, T_w is the sea water temperature and T_i is the ice temperature. T_i is taken to be $-4^\circ C$ as this is the equilibrium ice skin temperature in the high resolution melting study of Løset (1993b).

Forced convection is the dominant melt process and occurs on all submerged sides of the iceberg as well as the base. When calculating the forced convection melting on the iceberg sides, T_w is taken to be the average temperature over the iceberg keel

depth. When calculating the forced convection melting on the iceberg base, T_w is taken to be the water temperature at the maximum keel depth.

2.4.1.2 Buoyant Vertical Convection

Ice melting in sea water results in cooling, which generates denser water, and dilution, which generates less dense water. Thus thermal buoyancy will be directed downwards and saline buoyancy will be directed upwards. Such phenomena, where there are gradients of two or more properties with different molecular diffusivities, are termed double-diffusive convection.

For a vertical ice wall melting in stably stratified warmer salty water, consider a small fluid parcel which has just melted from the bottom of the ice wall. Initially it is colder and fresher then the surrounding sea water with the salinity difference as the dominant buoyancy force, therefore the parcel rises in a thin, turbulent boundary layer, entraining ambient sea water as it rises. Since the ambient fluid is stratified, eventually the fluid parcel reaches a level where it has the same density as the surrounding fluid and so it travels laterally along this density contour. Since heat diffuses more quickly than salt, the parcel acquires heat more quickly than salt across the diffusive interface with the ambient water at the top of the layer below, so it travels at a small angle above the horizontal. Along the top of the layers, there is a return flow of ambient water to replace the outflowing meltwater, which mixes with the melt water near to the ice face. In this way a series of convection cells are set up, driven by the melting of the ice wall in an ambient salinity gradient.

This convection cell phenomenon has been observed on small scales in the laboratory (Huppert and Josberger, 1980). The resulting temperature and salinity profile has a characteristic 'stepped' structure, since the mixing in the convection cells leads to constant temperature and salinity in the cells with distinct boundaries between the cells. This 'stepped' structure has been observed in the Weddell Sea by Foster and Carmack (1976) and these observations were linked to melting icebergs by Huppert and Turner (1978).

Huppert and Josberger (1980) and Huppert and Turner (1980) related the vertical scale of the layers to the thermal Grashof number:

$$h_{cc} = 0.65 \left[\rho\left(T_{wall}, S_{\infty}\right) - \rho\left(T_{\infty}, S_{\infty}\right)\right] \left(\frac{d\rho}{dz}\right)^{-1} \tag{2.21}$$

where h_{cc} is the layer thickness of the convection cells.

The overall Grashof number, Gr, represents the approximate ratio of the buoyancy

to viscous forces acting on a fluid:

$$Gr = \frac{g\left[\rho\left(T_\infty, S_\infty\right) - \rho\left(T_{wall}, S_{wall}\right)\right]}{\nu^2} d^3 \tag{2.22}$$

where d is the length of the boundary layer, ν is the kinematic viscosity, $\rho\left(T, S\right)$ is the density as a function of temperature and salinity and the subscripts $wall$ and ∞ refer to the values at the wall and in the farfield, respectively. It is related to the Rayleigh number and Prandtl number by:

$$Gr = \frac{Ra}{Pr} \tag{2.23}$$

The Rayleigh number, Ra, is used when studying convective processes as a parameter which "expresses the balance between the driving buoyancy forces and the two diffusive processes which retard the motion and tend to stabilise it" (Turner, 1979):

$$Ra = \frac{g\beta_T \Delta T d^3}{\nu\kappa} \tag{2.24}$$

where β_T is the thermal expansion coefficient, $\beta_T = -\frac{1}{\rho_m}\frac{\partial\rho}{\partial T}$, ρ_m is the mean density, κ is the thermal diffusivity, ΔT is the temperature difference and d is the characteristic length.

There is an equivalent "saline Rayleigh number" which is defined as:

$$Rs = \frac{g\beta_S \Delta S d^3}{\nu\kappa} = \frac{\beta_S \Delta S}{\beta_T \Delta T} Ra \tag{2.25}$$

where β_S is the salinity expansion coefficient, $\beta_S = -\frac{1}{\rho_m}\frac{\partial\rho}{\partial S}$ and ΔS is the salinity difference.

The Prandtl number approximates the ratio of momentum diffusivity (viscosity) and thermal diffusivity and can be calculated with equation 2.16, or alternatively:

$$Pr = \frac{\nu}{\kappa} \tag{2.26}$$

The density gradients are shown for three CTD stations from Kangerdlugssuaq Fjord in South East Greenland in Figure 2.4. There is an extremely high density gradient in the upper $100\,m$, which is approximately $0.04\,kg\,m^{-3}\,m^{-1}$. Below about $400\,m$ the density gradient is almost linear with a value of $5.105 \times 10^{-3}\,kg\,m^{-3}\,m^{-1}$. Huppert and Josberger (1980) report that salinity gradients in the Weddell Sea vary between $10^{-3}‰\,m^{-1}$ in the upper $100\,m$ and $10^{-5}‰\,m^{-1}$ in a relatively unstratified region down to $400\,m$. Therefore the Greenland fjord environment is highly stratified compared to the Antarctic. This is to be expected since there is much melting on the surface of the Greenland Ice Sheet but little on most of the Antarctic Ice Sheet.

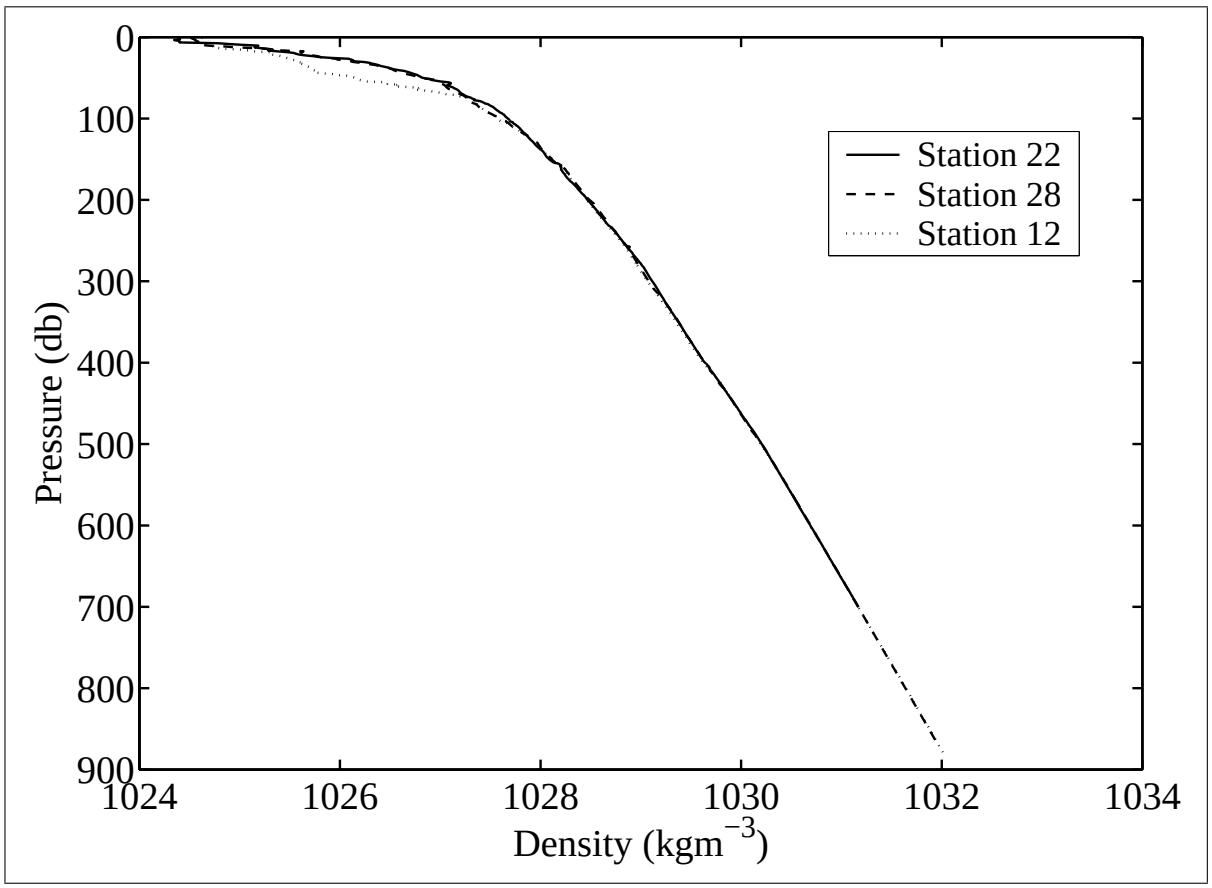

Figure 2.4: *Density gradients from three CTD stations from Kangerdlugssuaq Fjord, South East Greenland (Locations of CTD stations are shown in Figure 4.9)*

To calculate the length scale of the width of the convection cells in a typical Greenland fjord, equation 2.21 can be used. For a temperature difference of $1\,^{\circ}C$ between the ice and the ocean, the typical width of convection cells caused by icebergs melting in density gradient of the upper $100\,m$ is found to be of order $1\,m$. The overall Grashof number for layers of order $1\,m$ is calculated using equation 2.22 to be of order 10^{14}, which is much larger than the value calculated by Huppert and Josberger (1980) of order 10^{8} at which the flow induced by ice melting in a stratified fluid becomes turbulent.

Estimates of the net effect of melting due to buoyant convection have been made from experimental measurements and field observations. Neshyba and Josberger (1980) estimated the melting due to buoyant vertical convection by performing a parabolic least squares fit to data collected by Morgan and Budd. The effect of iceberg mass wastage by factors other then melting (such as wave erosion), was removed by using a datum iceberg, which was frozen in pack ice in a fjord, so the only cause of melting was buoyant vertical convection. El-Tahan *et al.* (1987) used this relationship in their work on the deterioration of Arctic icebergs to calculate the melt rate due to buoyant

vertical convection, R_{bc}, in $m\,day^{-1}$:

$$R_{bc} = 7.62 \times 10^{-3} T_d + 1.29 \times 10^{-3} T_d^2 \tag{2.27}$$

where $T_d = T_w - T_{fp}$ is the thermal driving temperature (elevation of seawater temperature above freezing point). The freezing point of seawater, T_{fp} is calculated by the following equation (Fofonoff and Millard, 1983):

$$T_{fp} = \frac{1}{1.00024} \left(a_0 S + a_1 S \sqrt{S} + a_2 S^2 + b\, P \right) \tag{2.28}$$

where S is the salinity, P is the pressure (taken to be approximately equal to depth, and the coefficients are: $a_0 = -0.0575$, $a_1 = 1.710523 \times 10^{-3}$, $a_2 = -2.154996 \times 10^{-4}$, $b = -7.53 \times 10^{-4}$.

Buoyant vertical convection occurs only on the iceberg sides, where convection cells can develop. Where there are high salinity gradients, such as in the Arctic, the convection cells that develop are small and will be disturbed by turbulence created by the movement of the iceberg. Where the salinity gradients are lower, larger convection cells form, which are more robust and are even visible in the ocean density structure at some distance from an iceberg, such as observed by Foster and Carmack (1976) in the Weddell Sea, Antarctica. Where there are large tidal velocities the dominant process of iceberg melt is forced convection, although in areas where the icebergs do not undergo such rapid acceleration, buoyant vertical convection can play an important role. The relationship in equation 2.27 was utilised by El-Tahan *et al.* (1987) to study the deterioration of Arctic icebergs. They included buoyant vertical convection, as well as surface melt due to insolation, melting due to forced convection (air and water), wave erosion and calving of overhanging ice slabs. They showed that their model provided a reasonable approximation to the icebergs that were tracked. In their quantitative assessment of iceberg deterioration in the Grand Banks and the Labrador Sea, they found that 2% of the total melt rate was attributed to buoyant vertical convection, compared with 80% due to wave effects (erosion and calving of overhanging slabs), 16% due to forced convection and less than 0.5% each for wind convection and solar radiation. If the effects of wave action are removed, as icebergs are protected from waves in fjords, buoyant convection is responsible for 10.5% of the melt rate, forced convection for 84% and wind convection and solar radiation 2.5% each. Therefore, it is important to include the effect of buoyant convection in this iceberg melt model and equation 2.27 is the best available approximation for the melt rate due to this process.

2.4.1.3 Wave Erosion

Wave erosion is an important iceberg deterioration mechanism in the open ocean and is the dominant process when water temperatures rise above $0°C$ (El-Tahan *et al.*, 1987; Venkatesh *et al.*, 1994). However, in fjords the fetch distance is not vary far so large waves are not able to build up, even in strong winds. Wave-cut notches will be eroded at the waterline of icebergs, with vertical extent dependent an water temperature above freezing, amplitude and period of waves (Martin *et al.*, 1978), therefore these will have a small vertical extent in a fjord environment. In the *SedBerg* Model the melt rate is calculated as a single, average value for each side, and it is assumed that the small vertical extent of the thermoerosional notch cut by wave action will not have a great effect on the overall melt rate of the iceberg while it is present in the fjord.

The theory of iceberg wave erosion is described here for completeness, as this mechanism can be included in the model once the icebergs have left the sheltered environment of the fjord, if desired.

El-Tahan *et al.* (1987), following the theoretical estimates of White *et al.* (1980), gave the melt per degree Celsius of water temperature above freezing due to wave erosion at the water-line in $m\,s^{-1}\,{}^{\circ}C^{-1}$ as:

$$R_{we_1} = 1.46 \times 10^{-4} \left(\frac{h_r}{h_{wv}}\right)^{0.2} \left(\frac{H}{P}\right) \tag{2.29}$$

where h_r is the roughness height of the iceberg surface, assumed to be $0.01\,m$ by El-Tahan *et al.* (1987), h_{wv} is the mean height of the waves and P_w is the mean period of the waves.

Erosion of the iceberg at the waterline due to waves was found to be the most important erosional loss by Bigg *et al.* (1997), who were investigating large scale iceberg drift in the open ocean. They formulated a relation between sea state, S_s, and melt rate due to wave erosion, R_{we_2} in $m\,day^{-1}$, by extrapolating the observations of Løset (1993b):

$$R_{we_2} = 0.5 S_s \tag{2.30}$$

Gladstone *et al.* (2001) modified equation 2.30 to include the dependence of the wave erosion rate on water temperature and sea-ice concentration:

$$R_{we_2} = \frac{1}{12} S_s \left[1 - \cos\left(\pi C_{si}\right)\right] \left(T_w + 2\right) \tag{2.31}$$

where C_{si} is the sea ice concentration.

The relationship between sea state, S_s, and the magnitude of the wind velocity,

$|\mathbf{v}_a|$, according to the 1946 Beaufort scale, is defined by the empirical formula:

$$S_s = \left(\frac{|\mathbf{v}_a|}{0.836}\right)^{\frac{2}{3}} \tag{2.32}$$

However, in fjords as the fetch distance is limited, equation 2.32 is not appropriate.

Wave erosion at the water-line contributes to ice blocks calving off the iceberg. Fragmentation of icebergs will be discussed in Section 2.4.3.

2.4.2 Subaerial Melt Processes

It has been shown by Mattson *et al.* (1993); Östrem (1959) and Nicholson and Benn (2006) that a layer of sediment over ice has a non-linear effect on subaerial ice ablation. The results of measurements on various glaciers around the world are shown in Figure 2.5 from Mattson *et al.* (1993). A thin layer of debris ($\sim 2\,cm$) increases the melt

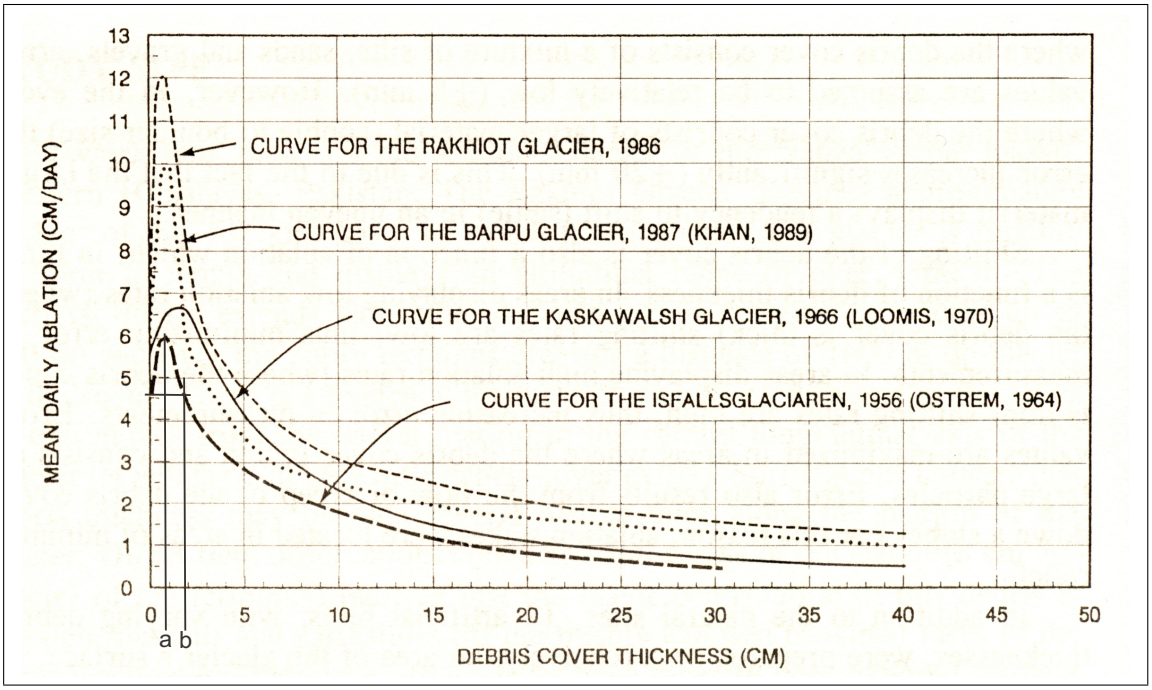

Figure 2.5: *Empirical measurements of the relationship between debris thickness and ice ablation rate on Rakhiot Glacier, Punjab Himalaya; Barpu Glacier, Karakoram Himalaya, Pakistan; Kaskawalsh Glacier, Yukon, Canada; and Isfjallsglaciären, Sweden. There is variation between glaciers in the debris thickness that gives rise to the maximum melt rate and the debris thickness above which melt becomes inhibited compared to clean ice, as indicated by* a *and* b *for Isfjallsglaciären. Reproduced from Mattson et al. (1993) with modifications as in Nicholson and Benn (2006).*

rate and the melt rate rapidly decreases for thicknesses above this. Since in the model the icebergs are assumed to be tabular, when sediment is melted out of the ice on the

iceberg surface it remains there until the iceberg overturns. Therefore, the melt rate will be enhanced compared to clean ice initially and, when the debris layer exceeds a certain thickness, the melt rate decreases. The relationship between debris thickness and melt rate, when the debris thickness exceeds the threshold b in Figure 2.5, is approximately exponential. Nicholson and Benn (2006) measured and modelled melt rates of ice with a debris layer at Larsbreen in Svalbard, which showed a comparable melt rate versus debris thickness curve as Isfjallsglaciären in Sweden. As Larsbreen is at a similar latitude to the Greenland fjord that the *SedBerg* Model is applied to in Chapter 4, the measurements from Larsbreen/Isfjallsglaciären are used to adjust the subaerial melt rate underneath a debris layer. When there is a debris layer less than $2\,cm$ over ice, the melt rate is a factor of 1.33 greater than the melt rate of clean ice. When the debris layer exceeds $2\,cm$, the relationship between melt rate and debris thickness can be approximated by an exponential curve, which is fitted to the data in Figure 2.6. The melt rate of ice under a debris layer is normalised as a fraction of the

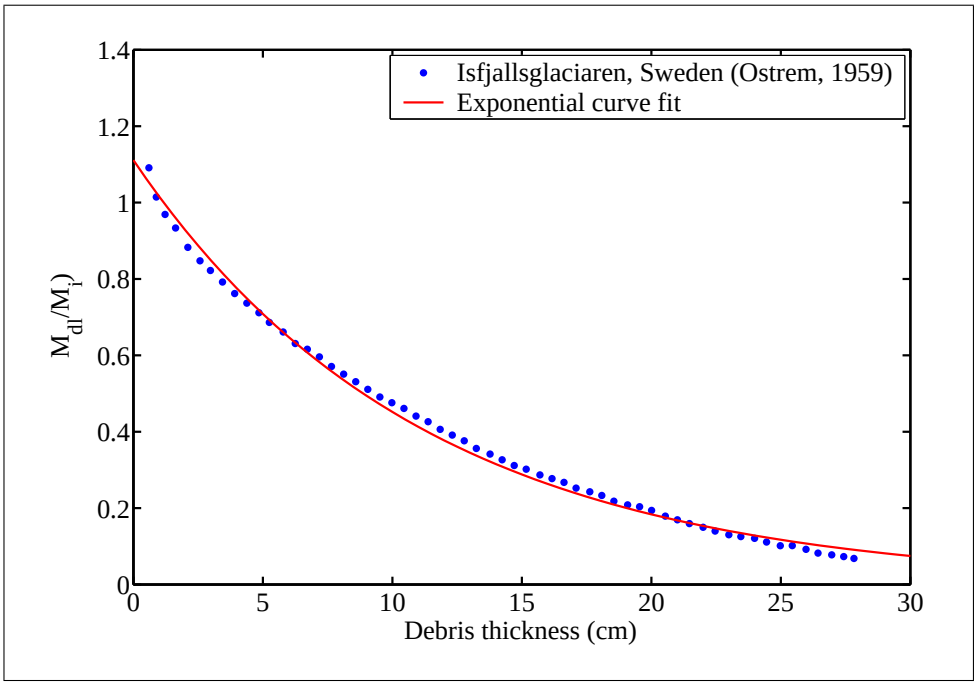

Figure 2.6: *Exponential curve fit to data from Isfjallsglaciären, Sweden (Östrem, 1959). The melt rate of ice under a debris layer is normalised as a fraction of the melt rate of clean ice.* $\frac{R_{dl}}{R_a} = A \exp[-B\,t]$, *where* R_{dl} *is melt rate of ice with debris layer,* R_a *is melt rate of clean ice and* t_d *is the thickness of the debris layer. The coefficients are* $A = 1.11$ *and* $B = 0.09$

melt rate of clean ice, with the following equation:

$$\frac{R_{dl}}{R_a} = A \exp[-B\,t_d] \tag{2.33}$$

where M_{dl} is melt rate of ice with debris layer, M_a is the total subaerial melt rate of ice without debris layer and t_d is the thickness of the debris layer. The coefficients are $A = 1.11$ and $B = 0.09$.

In the *SedBerg* Model, the subaerial melt rate for clean ice, as calculated in Sections 2.4.2.1–2.4.2.2, is multiplied by the appropriate factor from equation 2.33 as the debris accumulates on top of the iceberg. Once the debris layer on the iceberg surface increases to a thickness greater than $30\,cm$, the melt rate decreases to a negligible level, as shown in Figure 2.6, so the melt rate of the underlying ice is then set to zero in the *SedBerg* Model.

2.4.2.1 Forced Convection or Sensible Heat Exchange

Surface melting due to forced convection or sensible heat exchange with the air occurs in cases where the temperature of the ice, T_i, is higher than the ambient air temperature, T_a, as described by Løset (1993a) and El-Tahan *et al.* (1987). The mechanism is the same as forced convection in water, c.f. Section 2.4.1.1. The surface melt rate due to sensible heat transfer, R_{sh}, used in the *SedBerg* Model is:

$$R_{sh} = \frac{q_a}{\rho_i \Gamma_i} \tag{2.34}$$

where Γ_i is the latent heat of fusion of ice and q_a is defined as:

$$q_a = \frac{Nu\, k_a\, (T_a - T_i)}{L_x} \tag{2.35}$$

where Nu is the Nusselt number and k_a is the thermal conductivity of air.

If the surface of the iceberg is treated as a horizontal and smooth plate orientated parallel to the flow field, c.f. section 2.4.1.1, which forms a turbulent boundary layer, the Nusselt number for tabular icebergs can be written as:

$$Nu = 0.0296\, Re_l^{0.8}\, Pr^{1/3} \tag{2.36}$$

Re_l is the local Reynolds number - ratio of inertial to viscous forces:

$$Re_l = \frac{|\mathbf{v}_a - \mathbf{v}_i|\; L_x}{\nu_a} \tag{2.37}$$

where $|\mathbf{v}_a - \mathbf{v}_i|$ is the relative free stream velocity between the iceberg and the air and ν_a is the kinematic viscosity of air. Pr is the Prandtl number - ratio of momentum

diffusivity (viscosity) and thermal diffusivity (c.f. equations 2.16 and 2.26):

$$Pr = \frac{\nu_a}{\kappa_a} \tag{2.38}$$

where κ_a is the thermal diffusivity of air.

2.4.2.2 Solar Radiation

The melt rate due to radiative transfer of heat by short-wave and long-wave radiation has a relatively small role to play (Løset, 1992), but it is included for completeness. The net long-wave radiation depends on the air temperature and the cloudiness. The solar radiation heat transfer (or short-wave radiation) varies with solar altitude, the transmittance of the atmosphere, cloudiness and the short-wave radiation absorbing properties of the iceberg surface. Rather than calculate solar radiation flux variation over time scales of less than a day, a mean monthly solar radiation flux (both long-wave and short-wave) is used in the *SedBerg* Model. This captures annual variation, which is sufficient complexity since the variation in the sedimentation rate over the fjord basin is not resolvable over shorter time scales than this.

The melt rate due to solar radiation, R_{sr}, is calculated in the *SedBerg* Model using:

$$R_{sr} = \frac{F_{sol}}{\rho_i \Gamma_i} \tag{2.39}$$

where F_{sol} is the solar radiation flux.

It is possible to download the long-term monthly mean solar radiation flux gridded for the region north of 65° in the Arctic Global Radiation (AGR) data set (Box *et al.*, 1998). The AGR data set is the most complete Arctic radiation climatology available and combines previous Russian studies to produce a time series of monthly fluxes calculated from land stations, ocean drifting stations and empirically-derived long-term climatological estimates. For the region north of $60°N$, the radiation time series at some of the stations are quite short, whereas others span over 40 years. From the data, a long-term monthly mean gridded climatology for the region north of $65°N$ has been interpolated and these mean monthly values are used as inputs for the model.

2.4.3 Fragmentation

The disintegration of icebergs into fragments can play an important role in the destruction of icebergs in the open ocean where the icebergs are subject to wave erosion and flexure, which exacerbates any weakness in the ice and leads to break up. Orheim (1980) collected a suite of measurements on large tabular Antarctic icebergs. He pro-

posed that internal weakness in icebergs contribute to their rapid disintegration in open water. He suggested that in Antarctica there is a mixture of short-lived (< 2 months) icebergs containing flaws and long-lived (> 1 year) icebergs which are fairly free of faults. Kristensen *et al.* (1982) and Orheim *et al.* (1982) presented evidence that the principal agent in the break up of tabular icebergs is ocean waves. Kristensen (1983) postulates that enhanced melting at the water-line probably does not make a significant contribution to the fragmentation of icebergs, but rather it is the subsequent calving of overhanging cliffs that has an important influence. Since large waves do not develop in fjords, as discussed in Section 2.4.1.3, icebergs are not exposed to large bending stresses resulting in fragmentation. As a result, fragmentation of icebergs can be neglected in the model of fjord sedimentation. Once icebergs leave the shelter of the fjord they become susceptible to breaking up in the open ocean. Icebergs become increasingly unstable with age because weathering leaves them prone to rolling (Section 2.6) and fragmentation.

2.5 Iceberg Dynamics

Icebergs drift around a fjord in response to ocean currents, wind forcing and the influence of the Coriolis effect. This section describes their dynamics and the forces acting on them as they meander along a fjord, as well as the mechanics of occasional collisions with the fjord walls or the ice front.

2.5.1 Motion

Each iceberg's drift trajectory is modelled individually by applying the equation of motion for an iceberg, which has been used by Bigg *et al.* (1997); Clarke and La Prairie (2001); Løset (1993b); Matsumoto (1996) and Smith (1993):

$$M_i \frac{d\mathbf{v}_i}{dt} = -M_i f \hat{\mathbf{k}} \times \mathbf{v}_i + \mathbf{F}_a + \mathbf{F}_w + \mathbf{F}_r + \mathbf{F}_p \tag{2.40}$$

where M_i is the iceberg mass, $\hat{\mathbf{k}}$ is the unit vector in the z-direction, $\mathbf{v}_i$ is the iceberg drift velocity, f is the Coriolis parameter ($f = 2\Omega_0 \sin\theta$), Ω_0 is the angular velocity of the Earth, $\mathbf{F}_a$ is the wind drag, $\mathbf{F}_w$ is the water drag, $\mathbf{F}_r$ is the wave radiation force and $\mathbf{F}_p$ is the horizontal pressure gradient force. The first term on the right hand side of equation 2.40 is referred to as the Coriolis force and is the influence of the Earth's rotation on a moving object.

The relationship for the drag forces is (Bigg *et al.*, 1997; Smith, 1993):

$$\mathbf{F}_x = \frac{1}{2}\rho_x C_x A_\perp \left|\mathbf{v}_x - \mathbf{v}_i\right| (\mathbf{v}_x - \mathbf{v}_i) \tag{2.41}$$

where the subscript x refers to a=air and w=water, $A_\perp$ is the cross sectional area of the side of the iceberg normal to the stressing force and C_x is the form drag coefficient. The form drag coefficients for air and water are taken to be $C_a = 1.3$ and $C_w = 0.9$, respectively. These were the values used by Bigg *et al.* (1997), from work by Chirivella and Miller (1978) and Smith (1993). There are a multitude of other papers documenting field and laboratory measurements of iceberg drag coefficients, for example, Banke and Smith (1974); Mauviel (1980); Russell *et al.* (1977); Shirasawa *et al.* (1984).

The wave radiation force, $\mathbf{F_r}$, is (Bigg *et al.*, 1997; Smith, 1993):

$$\mathbf{F}_r = \frac{1}{4}\rho_w g\, a_{wv}^2 L_\perp \frac{\mathbf{v}_a}{|\mathbf{v}_a|} \tag{2.42}$$

where $L_\perp$ is the length of the berg normal to incident waves and a is the wave amplitude.

The incident waves are assumed to have the same direction as the air velocity (Bigg *et al.*, 1997; Smith, 1993). Each iceberg is assumed to be rectangular, with a width to length ratio of 1:1.62, as observed by Dowdeswell *et al.* (1992). The berg is assumed to travel with its long axis parallel to the surrounding water flow. The wave amplitude was estimated by Bigg *et al.* (1997) from data in the marine Beaufort scale to depend on the wind speed as:

$$h_{wv} = 2a_{wv} = 0.02025|\mathbf{v}_a|^2 \tag{2.43}$$

where h_{wv} is the wave height.

The pressure gradient force, $\mathbf{F}_p$, is the force the sea surface slope exerts on the water volume displaced by the iceberg (Bigg *et al.*, 1997):

$$\mathbf{F}_p = -M_i \frac{\nabla P_h}{\rho_w} \tag{2.44}$$

where P_h is the horizontal pressure field. The pressure gradient force can be found by re-arranging the equation of motion for $\mathbf{v}_w$:

$$\frac{d\mathbf{v}_w}{dt} + f\hat{\mathbf{k}} \times \mathbf{v}_w = -\frac{\nabla P_h}{\rho_w} + \frac{1}{\rho_w}\frac{\partial \overline{\tau}_s}{\partial z} \tag{2.45}$$

where $\overline{\tau}_s$ is the surface wind stress.

The surface wind stress term can be approximated by the following (Bigg *et al.*,

1997; Gill, 1982):

$$\frac{\partial \overline{\tau}_s}{\partial z} = \frac{1.5 \times 10^{-3} \rho_a |\mathbf{v}_a| \mathbf{v}_a}{E_k} \tag{2.46}$$

where E_k is the Ekman depth, which is taken to be iceberg draught or $90\,m$, whichever is shallower.

The four equations of motion for an iceberg are, therefore:

$$\frac{dx}{dt} = v_{i_x} \tag{2.47}$$

$$\frac{dy}{dt} = v_{i_y} \tag{2.48}$$

$$\frac{dv_{i_x}}{dt} = +f\left(v_{i_y} - v_{w_y}\right) + \frac{1}{M_i}F_{a_x} + \frac{1}{M_i}F_{w_x} + \frac{1}{M_i}F_{r_x} + \frac{1}{M_i}F_{p_x} \tag{2.49}$$

$$\frac{dv_{i_y}}{dt} = -f\left(v_{i_x} - v_{w_x}\right) + \frac{1}{M_i}F_{a_y} + \frac{1}{M_i}F_{w_y} + \frac{1}{M_i}F_{r_y} + \frac{1}{M_i}F_{p_y} \tag{2.50}$$

where the subscripts x and y denote the component of that vector in the x and y-direction, which are equivalent to north and east coordinates, respectively, and equations 2.47-2.48 are found by expanding equation 2.40 in terms of the x and y velocity components.

Equations 2.47–2.50 are solved for each iceberg in the system at each time step, utilising the fourth order Runge-Kutta method as described by Press *et al.* (2002). A time step size, Δt_m, of 1.8 minutes is used for the iceberg dynamics and melt, slightly less than the time step of 2.25 minutes used by Bigg *et al.* (1997). Testing for an iceberg calving event occurs at intervals as close as possible to the calving time step, Δt_c (equation 2.5), but in multiples of the moving and melting time step, Δt_m.

2.5.2 Collision With Fjord Walls Or Ice Front

The icebergs are constrained to the boundaries of the fjord. It is assumed that due to the extremely steep slopes of the fjord walls, commonly approaching the vertical, icebergs are deflected when they collide with the fjord sides instead of becoming grounded. If an iceberg 'hits' a wall or the glacier front, it undergoes an inelastic collision resulting in the loss of kinetic energy. In the *SedBerg* Model, the velocity of the iceberg after a collision needs to be calculated.

Much of the research on iceberg collisions has focussed on the forces resulting from iceberg collisions on man-made structures in the ocean. Duthinh and Marsden (1986) modelled the mechanics of eccentric collisions of spherical and cuboid icebergs on a vertical cylindrical structure in the ocean by solving the equations of the forces acting on each element of an iceberg over the time of the collision. Static and kinetic friction are parameterised in the model and the ice strength is required as an input

parameter (assumed constant). The geometry of the iceberg is updated at each time step to remove ice that has been crushed. For a spherical berg impacting on a vertical cylindrical structure, they found the final kinetic energy of the iceberg to be zero for a head-on collision, rising non-linearly to 75% of the initial kinetic energy for a glancing blow. Duthinh and Marsden (1986) also made the approximation that friction is infinite at the point where the iceberg impacts the rigid structure and effectively 'sticks' to it at the point of contact, which acts as a hinge. An exact solution of the momentum-impulse equations could then be found for the kinetic energy after the collision.

Duthinh and Fuglem (1988) developed a computational model of iceberg collisions for assessing the potential damage of iceberg impacts on fixed structures in the ocean such as oil rigs. They assumed the worst case scenario in terms of damage to the structure — a head-on iceberg impact with the final kinetic energy in the iceberg reduced to zero because its energy is dissipated by ice crushing. Duthinh *et al.* (1990) carried out experimental work in Antarctica where a 5000 tonne iceberg was towed so that it collided with a rock face while iceberg velocity, impact force and pressure were monitored. The iceberg came to rest after the collision, as its kinetic energy was completely dissipated.

Matskevitch (1997) developed a linearised model for eccentric collisions of icebergs with offshore structures and ships. He assumed that the impacted structure is rigid and does not move due to the impact, and that the surface of the structure is vertical and flat, which are also appropriate assumptions for an iceberg colliding with a fjord wall. The iceberg was approximated by a cylindrical surface of elliptical cross-section. The other assumptions were:

- A single point of contact, i.e the contact area is small compared with the iceberg size.
- The impact occurs over a short period of time.
- There is no friction between the iceberg and the rigid wall.
- The normal load varies in direct proportion to the indentation depth.

Using these assumptions, the equations of motion of the iceberg simplify to two linear differential equations which were solved over the duration of the impact.

The other body of literature, which is relevant to iceberg collisions, concerns sea ice dynamics and floe-floe collisions of pancake-ice. Frankenstein and Shen (1997) performed laboratory experiments on the collision of ice floes. It was observed that floes with rough edges would adhere together during collisions, but some floes underwent a 'clean' collision and bounced apart after colliding. They measured the ratio of velocities before and after 'clean' collisions. This is referred to as the coefficient

of restitution, a fractional value between 0 and 1, which equals the amount of energy lost during a collision. They measured the average coefficient of restitution to be 0.14. Hopkins and Shen (2001) used a computer model to simulate pancake-ice dynamics with a coefficient of restitution of 0.25 for floe-floe collisions.

The models developed by Duthinh and Marsden (1986) and Matskevitch (1997) are more complex than is necessary for the *SedBerg* Model, where such numerical routines would substantially increase the run time of the sedimentation model. A more simplified method can be applied, which encapsulates the important physics of the collision and is also computationally quick.

In the *SedBerg* Model, the icebergs are assumed to be cuboids, which occasionally collide with a vertical plane (the fjord walls). The aim is to calculate the effect of a collision on the iceberg velocity. The symbols used in the collision model are defined in Figure 2.7, which illustrates two different orientations for an iceberg with the same velocity before the collision, $\mathbf{v}_{i_1}$, resulting in opposite directions of rotation after the collision, ω_2, where the subscripts 1 and 2 refer to values before and after the collision, respectively. The centre of mass of each iceberg is labelled c and the point of contact is labelled p.

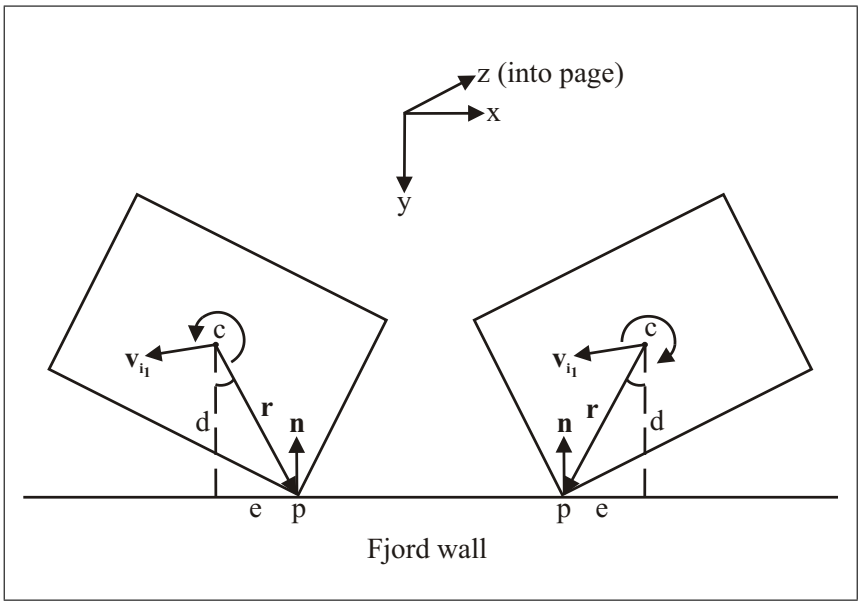

Figure 2.7: *Schematic of two icebergs colliding with one of the fjord walls with different orientations.*

The iceberg is modelled as a rigid body colliding with a plane, using the concept of collision impulse, which is the change in momentum during the collision (Rao, 2006). This requires the assumption that the collision occurs instantaneously, i.e. a large force is applied over a very short period of time, while the position and orientation of the iceberg remains the same. This is an additional simplification compared to the

model by Matskevitch (1997). The only variable that changes during the collision is the velocity, and therefore the momentum ($\mathbf{p} = m\mathbf{v}$) also changes, which is the impulse of the collision. Without this assumption, all the forces acting on the iceberg and fjord wall during the collision would have to be calculated for the duration of the collision, and information about the iceberg material strength and how it deforms and bends under stress would need to be defined, which would be extremely computer intensive.

It is assumed that there is no friction during the collision, which would produce a force in the direction parallel to the fjord wall. Therefore the only force during the collision acts in the direction perpendicular to the fjord wall, $\hat{\mathbf{n}}$. The net impulse of the collision is defined as $i\,\hat{\mathbf{n}}$, where i needs to be determined. The change in velocity during the collision is therefore $i\,\hat{\mathbf{n}}/M_i$.

The iceberg is assumed to have zero initial angular velocity, since its long axis is aligned with the direction of the water velocity (see Section 2.5.1). Any angular velocity produced by a collision with the fjord walls is assumed to dissipate rapidly afterwards and the long axis returns to its previous orientation parallel to the water flow.

Two velocities are defined for the iceberg: the velocity of the centre of mass, $\mathbf{v}_i$, and the velocity of the point p relative to the fjord wall, $\mathbf{v}_p$, which includes the effect of the angular velocity. They are related in the following way:

$$\mathbf{v}_p = \mathbf{v}_i + \omega\hat{\mathbf{k}} \times \mathbf{r} \tag{2.51}$$

where ω is the angular velocity, $\hat{\mathbf{k}}$ is the unit normal in the x-direction and $\mathbf{r}$ is the vector from the centre of iceberg to the corner in contact with the fjord wall or ice front, as shown in Figure 2.7.

The collision is elastic with a coefficient of restitution, ε, therefore the velocity at p before the collision, $\mathbf{v}_{p_1}$, is related to the velocity at p after the collision, $\mathbf{v}_{p_2}$, by:

$$\mathbf{v}_{p_2} \cdot \hat{\mathbf{n}} = -\varepsilon \mathbf{v}_{p_1} \cdot \hat{\mathbf{n}} \tag{2.52}$$

where $\mathbf{n}$ is the normal vector to the fjord wall or ice front, as shown in Figure 2.7, and $\hat{\mathbf{n}}$ is the normalised, or unit, vector.

The value of the coefficient of restitution, ε, used in the *SedBerg* Model is based on the experimental results of Frankenstein and Shen (1997) and the theoretical work of Hopkins and Shen (2001). On one hand, an iceberg would be expected to be stiffer than a sea ice floe with a corresponding larger coefficient of restitution; however, on the other hand, since the iceberg impacts a solid surface of the ice front or the fjord walls, the coefficient of restitution may be smaller than that for the collision of two

sea ice floes. The value chosen is 0.2, because this is approximately midway between the value of 0.14 found by Frankenstein and Shen (1997) and that used by Hopkins and Shen (2001) of 0.25. Thus, in the *SedBerg* Model the velocity of an iceberg after a collision is reduced to 20% of its value before the collision.

As stated above, the change in velocity caused by a collision is equal to the change in momentum, or impulse, $i\mathbf{n}$, divided by the iceberg mass. Thus, the velocity of the centre of mass after the collision can be calculated using the following equation:

$$\mathbf{v}_{i_2} = \mathbf{v}_{i_1} + \frac{i\hat{\mathbf{n}}}{M_i} \tag{2.53}$$

The change in angular momentum of the iceberg with the impulse $i\mathbf{n}$ is given by $\mathbf{r} \times i\hat{\mathbf{n}}$. The impulse acts on the point p and produces an instantaneous torque there. The change in angular momentum needs to be divided by the moment of inertia of the iceberg, I, which has units of mass×length^2, to convert it into the change in angular velocity. The angular velocity of the iceberg after the collision can be calculated using:

$$\omega_2 \hat{k} = \omega_1 \hat{k} + \frac{(\mathbf{r} \times i\hat{\mathbf{n}})}{I} \tag{2.54}$$

For a solid cuboid such as an iceberg of width, l_y, and length, l_x, the moment of inertia is:

$$I = \frac{1}{12} M_i \left(l_y^2 + l_x^2\right) \tag{2.55}$$

To find the velocity of the centre of mass, equation 2.53 needs to be solved, and in order to do so, an expression for i is required. To find i, first take equation 2.52 and substitute equation 2.51 for the relative velocity after the collision, $\mathbf{v}_{p_2}$:

$$\left(\mathbf{v}_{i_2} + \omega_2 \hat{k} \times \mathbf{r}\right) \cdot \hat{\mathbf{n}} = -\varepsilon \mathbf{v}_{p_1} \cdot \hat{\mathbf{n}} \tag{2.56}$$

Then substitute equations 2.53–2.54 into the above equation:

$$\left(\mathbf{v}_{i_1} + \frac{i\mathbf{n}}{M_i} + \left(\omega_1 \hat{k} + (\mathbf{r} \times i\hat{\mathbf{n}})\right) \times \mathbf{r}\right) \cdot \hat{\mathbf{n}} = -\varepsilon \mathbf{v}_{p_1} \cdot \hat{\mathbf{n}} \tag{2.57}$$

Taking $\mathbf{v}_{p_1} \cdot \hat{\mathbf{n}}$ from the left to the right of equation 2.58, as defined by equation 2.51 gives:

$$\left(\frac{i\mathbf{n}}{M_i} + (\mathbf{r} \times i\hat{\mathbf{n}}) \times \mathbf{r}\right) \cdot \hat{\mathbf{n}} = -\left(1 + \varepsilon\right) \mathbf{v}_{p_1} \cdot \hat{\mathbf{n}} \tag{2.58}$$

To rearrange 2.58, the *scalar triple product* rule is used:

$$(\mathbf{A} \times \mathbf{B}) \cdot \mathbf{C} = (\mathbf{B} \times \mathbf{C}) \cdot \mathbf{A} \tag{2.59}$$

to show that the following is true:

$$\begin{aligned}(\mathbf{A}\times\mathbf{B})\times\mathbf{A}\cdot\mathbf{B} &= (\mathbf{A}\times\mathbf{B})\cdot(\mathbf{A}\times\mathbf{B}) \\ &= (\mathbf{A}\times\mathbf{B})^2 \end{aligned} \tag{2.60}$$

where the square of the vector is taken to be equivalent to taking the dot product with itself.

Substituting the identity calculated in equation 2.60 into equation 2.58, and rearranging in terms of i, results in:

$$i = \frac{-(1+\varepsilon)\,\mathbf{v}_{p_1}\cdot\hat{\mathbf{n}}}{\frac{1}{M_i}+\frac{(\mathbf{r}\times\hat{\mathbf{n}})^2}{I}} \tag{2.61}$$

There are three possible faces within the fjord that an iceberg can impact: the ice front and either of the two walls at the side of the fjord. If the axes directions are defined as in Figure 2.1, then the normal vectors are as follows:

$$\text{East fjord wall:} \qquad \hat{\mathbf{n}} = (0,-1) \tag{2.62}$$

$$\text{West fjord wall:} \qquad \hat{\mathbf{n}} = (0,1) \tag{2.63}$$

$$\text{Ice front:} \qquad \hat{\mathbf{n}} = (-1,0) \tag{2.64}$$

If the along-fjord direction is aligned north to south with the fjord mouth south of the ice front, then the final velocity of the centre of mass will be:

East fjord wall:

$$v_{xi_2} = v_{xi_1} \tag{2.65}$$

$$v_{yi_2} = v_{yi_1} - \frac{i}{M_i} \tag{2.66}$$

$$i = \frac{v_{yi_1}(1+\varepsilon)}{\frac{1}{M_i}+\frac{r_x^2}{I}} \tag{2.67}$$

West fjord wall:

$$v_{xi_2} = v_{xi_1} \tag{2.68}$$

$$v_{yi_2} = v_{yi_1} + \frac{i}{M_i} \tag{2.69}$$

$$i = -\frac{v_{yi_1}(1+\varepsilon)}{\frac{1}{M_i}+\frac{r_x^2}{I}} \tag{2.70}$$

Ice front:

$$v_{xi_2} = v_{xi_1} - \frac{i}{M_i} \tag{2.71}$$

$$v_{yi_2} = v_{yi_1} \tag{2.72}$$

$$i = \frac{v_{xi_1}\,(1+\varepsilon)}{\frac{1}{M_i} + \frac{r_y^2}{I}} \tag{2.73}$$

In this way, the velocity of the iceberg after a collision is calculated in the *SedBerg* Model. Since this is a much simplified model of reality, the angle between the iceberg and the fjord wall or ice front is given an uniform random variation of $\pm 5°$, and the magnitude of the velocity after the collision is given an uniform random variation of $\pm 10\%$.

2.6 Iceberg Stability

Iceberg stability affects the probability of an iceberg overturning and, therefore, controls the orientation of the basal debris layer in the iceberg (if there is such a layer). Since the icebergs will preferentially erode laterally rather than vertically, a berg will roll onto its side if it exceeds a critical measure of instability. There have been a number of studies of iceberg stability, with the emphasis on determining the stability of an iceberg to be towed. Weeks and Mellor (1978a,b) first used buoyancy considerations to calculate the roll stability of cuboid icebergs. Bass (1980) extended this treatment to consider different shaped iceberg cross-sections. Bailey (1994) utilised the frequency of the rolling mode as a measure of iceberg stability and re-stated the Weeks-Mellor stability criterion in terms of the roll frequency and the iceberg width, which is a useful method for assessing an iceberg's stability in the field.

The Weeks-Mellor stability criterion was derived in the following way. If the total thickness of an iceberg is L_z, the draft is approximated by $0.81\,L_z$ and the depth from the waterline to the centre of buoyancy, G, as $0.405\,L_z$. The density of the iceberg is assumed to increase with depth, and therefore the depth from the top of the iceberg to the centre of gravity, G, is approximated by $\left(\frac{L_z}{2} + 6\right)\,m$. The vertical distance between the centre of buoyancy and the centre of gravity is then calculated as $(0.095\,L_z + 6)\,m$ and the volume of water displaced by the iceberg per unit length as $0.81\,L\,L_z$, where L is the horizontal length of the iceberg perpendicular to the axis of rotation. The moment of inertia of a rectangular iceberg cross section (per unit length) is $L^3/12$. The metacentre, M, is defined as the point where the lines of the centre of buoyancy and the centre of gravity intersect, as shown in Figure 2.8. The distance between the centre of gravity and the metacentre (GM) is called the metacentric height, H_m, which

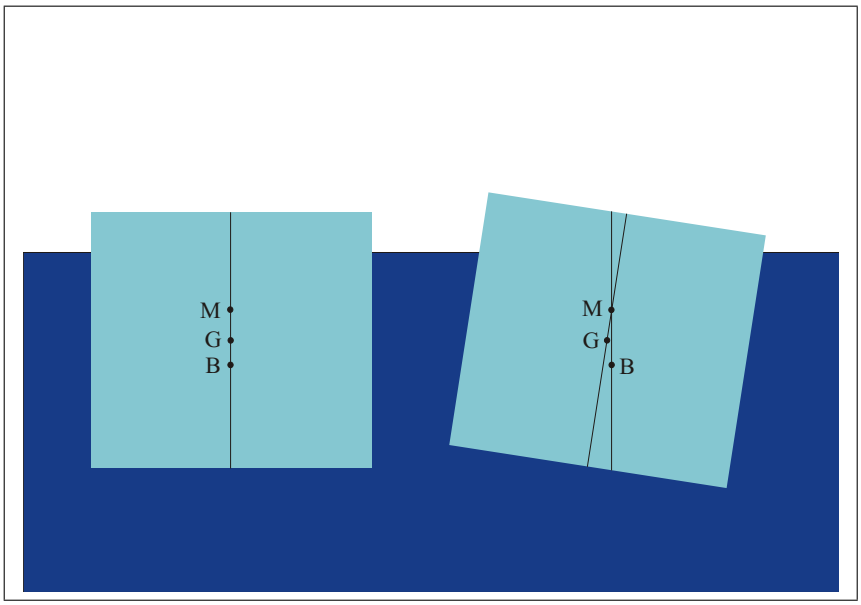

Figure 2.8: *Schematic diagram (not to scale) showing position of centre of buoyancy, B, the centre of gravity, G, and the metacentre, M both when an iceberg is upright and tilted over to one side. The centre of gravity is fixed, but the position of the centre of buoyancy and the metacentre change as the iceberg tilts*

can be calculated using:

$$H_m = \frac{L^3}{12 \times 0.81\, L\, L_z} - (0.095\, L_z + 6)\ \ m$$
$$H_m = \frac{L^2}{9.72\, L_z} - 0.095\, L_z - 6\ m \tag{2.74}$$

If the minimum requirement for stability is $H_m > 0$, equation 2.74 can be rearranged, to form the Weeks-Mellor stability criterion (Weeks and Mellor, 1978a), which indicates that an iceberg is stable if it satisfies the following:

$$\frac{L}{L_z} > \sqrt{0.9234 + \frac{58.32}{L_z}} \tag{2.75}$$

Equation 2.75 was used by Bigg *et al.* (1997). It requires that the horizontal length (x or y-direction), is greater than the iceberg thickness, for example if the thickness is $200\,m$, the length and width need to be greater than $220\,m$ to satisfy the Weeks-Mellor stability criterion. This equation was constructed to estimate if a particular iceberg would be stable enough to tow to arid areas as a potential source of freshwater. In the *SedBerg* Model, the thickness and width are assumed to be equal when the icebergs are calved (as was assumed by Bigg *et al.* (1997)), but, if this is the case, an iceberg will

be perpetually unstable along its long axis and will overturn repeatedly; therefore, the Weeks-Mellor stability criterion is not suitable for use in a dynamic model of icebergs moving and melting. Instead, the icebergs are assumed to be stable when the length (or width) to thickness ratio is greater than a fraction, α:

$$\frac{L}{L_z} > \alpha \tag{2.76}$$

A value of $\alpha = 0.7$ is chosen, as the approximate upper boundary of the spread of width to thickness ratios observed by Dowdeswell *et al.* (1992). The icebergs are checked for stability to rotate about the x-axis and the y-axis, with L equal to L_y and L_x respectively. If an iceberg overturns along either axis, it is assumed to rotate by 90° about that axis, with the direction determined from a random draw and the longest horizontal dimension is assumed to orientate itself parallel to the direction of the water velocity.

2.7 Sedimentation

Glacier ice varies in its debris content according to where it is located within an ice mass (Lawson, 1979). Basal ice is the layer of ice close to the bed of the glacier, which is in contact with the bedrock or subglacial sediments (till). It usually contains high concentrations of sediment — greater than 50% by volume in some cases (Dowdeswell, 1986) — that has been eroded at the glacier bed and sides by abrasion and quarrying and entrained into the ice at the base of the glacier.

The surface layer of the glacier is referred to as supraglacial ice. In valley glaciers which are bounded by steep walls, mass movements from adjacent mountain slopes such as rockfall, rock slide, snow and ice avalanching, debris flow and creep as well as stream flow, result in material being deposited onto the surface of the glacier (Benn and Evans, 1998). Other processes, which transport sediment to the surface of the glacier, are wind blown dust, volcanic eruptions, sea spray transporting salts and micro-organisms, meteorites, and pollutants from human sources. The sediment contained in supraglacial ice shows high spatial variability in concentration, thickness, lithology and grain size, which reflects the distribution of debris sources and transport paths. There are usually lateral bands and sometimes medial bands of higher concentrations.

Between the subglacial and supraglacial ice is englacial ice, which makes up the bulk of the ice in the interior of the glacier. The sediment concentration is variable, but in general it contains very low debris concentrations less than 0.001% by volume (Dowdeswell and Murray, 1990). Debris can be incorporated into the body of the

glacier through burial by snowfall or snow and ice avalanches and by falling down crevasses, which are opened when the glacier experiences tensile stresses, or other holes in the glacier surface, such as moulins (holes created by meltwater). Another mechanism which introduces sediment into englacial ice is at the confluence of ice around an obstacle or where two glaciers converge. A medial debris septum is formed down-glacier of the confluence. If the confluence occurs in the accumulation zone, the medial septum will be buried by snow, and exposed at the surface by melting in the ablation zone. If the confluence occurs in the ablation zone, the medial debris septum will extend from the bed to the surface, as shown in Figure 2.9.

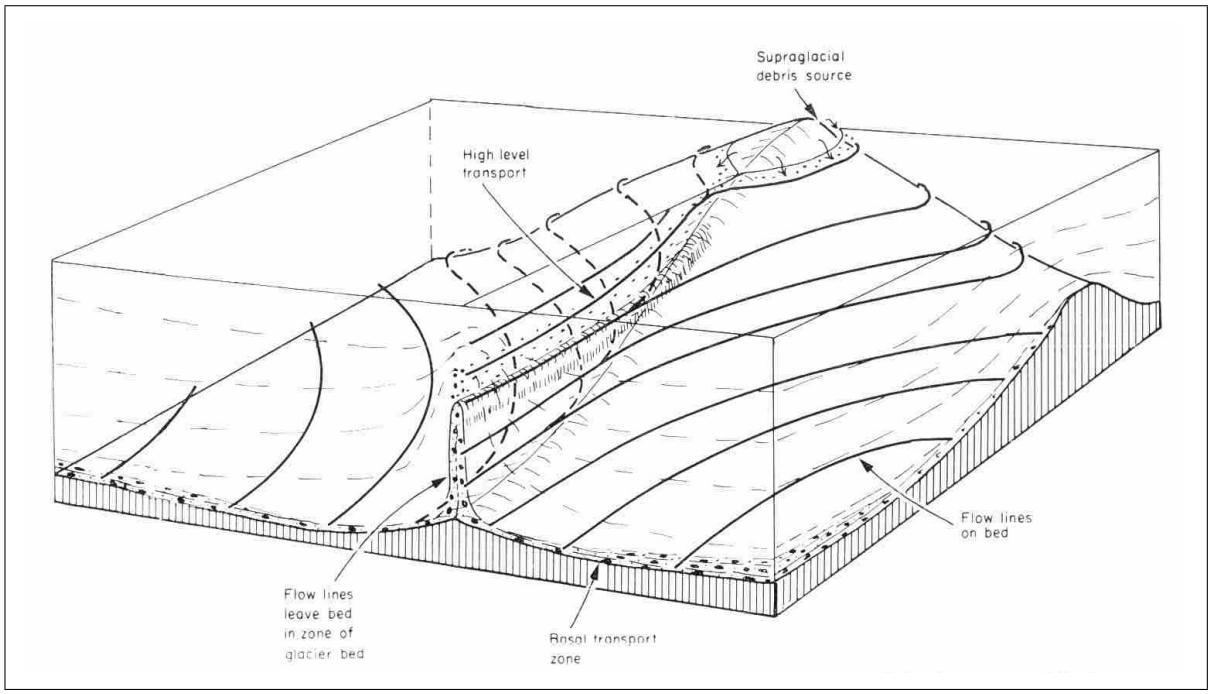

Figure 2.9: *Schematic diagram showing possible movement of debris from the basal transport zone to high level transport path in the compressive zone at a glacier confluence (Boulton, 1978).*

In the *SedBerg* Model the supraglacial ice is not accounted for due to the variability in its sediment concentration. Therefore, the glacier ice is assumed to consist of just two layers: sediment-rich basal ice, and englacial ice containing low sediment concentrations. Estimates of the thickness of the basal layer and the sediment concentrations in the two layers can be made from observations. Table 2.1 summarises the variation in basal ice thickness for different environmental settings - the data are from Dowdeswell and Murray (1990), except the Greenland value which is from Syvitski *et al.* (1996).

Location of tidewater glacier	Basal ice thickness (m)
S.E. Alaska⋆	10
Svalbard⋆	3
High Arctic⋆	3
Greenland†	3
Antarctic pen⋆	2

⋆ Dowdeswell and Murray (1990)
† Syvitski *et al.* (1996)

Table 2.1: *Thickness of basal debris-rich glacier ice in different environmental settings*

Syvitski *et al.* (1996) observed two overturned icebergs in Kangerdlugssuaq fjord, South East Greenland, where the basal layer was visible, from which they estimated the basal layer thickness to be $3\,m$. At a glacier in Spitsbergen, Dowdeswell and Dowdeswell (1989) found the layer of debris-rich basal ice to be between 0.6 and $1.3\,m$, with a sediment content of 3–12% by weight. Dowdeswell and Dowdeswell (1989) also took measurements from icebergs originating from three different glaciers in Spitsbergen and found that the sediment concentration of debris rich layers varied between 0.02% to nearly 28% by weight, with most debris-rich layers containing greater than 3% by weight of sediment. Measurements of a tidewater glacier on Southern Baffin Island in Canada by Dowdeswell (1986) reported that the basal layer was 0.8 to 2.9m thick, with sediment concentrations of 32–80% by weight (mean of 62% by weight) and by comparison the concentration of sediment in the englacial layer was much lower - less than 0.01% by weight.

When a calving event occurs in the *SedBerg* Model, it is assumed that the equivalent volume of the iceberg is lost from the front of the glacier. A slice with thickness $t_g = \frac{V_i}{h_g\, w_g}$ is removed from the glacier front, where V_i is the volume of the iceberg, h_g is the height of the glacier and w_g is the width of the glacier. When the icebergs are calved, they have a probability of inheriting the sediment-rich basal layer from the glacier. As the smallest iceberg is much larger than the height of the basal sediment layer, it is assumed that the iceberg either carries all of the basal layer or none of it. To conserve the ratio of basal to englacial sediment which is calved from the iceberg, it is assumed that the volume of sediment in the icebergs is equal to the volume of basal sediment lost from the glacier.

The volume of sediment carried in the population icebergs calved from the glacier is:

$$V_{sed\ bergs} = n_b\, h_b \frac{1}{n_b} \sum_{i=1}^{n_b} A_{bas_i} \tag{2.77}$$

where n_b is the number of icebergs calved containing basal sediment, A_{bas_i} is the area

of the face of iceberg, i, containing basal sediment, as defined in Figure 2.1. The summation is over all icebergs containing basal sediment.

The volume of sediment lost from the glacier is:

$$V_{sed\ glacier} = n_{tot} \frac{h_b}{h_g} \frac{1}{n_{tot}} \sum_{i=1}^{n_{tot}} V_i \tag{2.78}$$

where n_{tot} is the total number of icebergs calved, V_i is the volume of iceberg, i, which are summed over the whole population of icebergs.

Using the *law of large numbers*, which states that an infinite sum of independent random variables will have a sample average which converges to the expectation, equation 2.77 can be written as:

$$V_{sed\ bergs} \approx n_b\, h_b E\left(A_{bas_i}\right) \tag{2.79}$$

where $E\left(A_i\right)$ is the expected or mean iceberg cross-sectional area of the population of icebergs.

In the same way, equation 2.78 can be written as:

$$V_{sed\ glacier} \approx n_{tot} \frac{h_b}{h_g} E\left(V_i\right) \tag{2.80}$$

where $E\left(V_i\right)$ is the expected or mean iceberg volume of the population of icebergs.

Equations 2.77 and 2.78 must be equal to one another and therefore equations 2.79 and 2.80 will be approximately equal for large numbers of random draws:

$$n_b\, h_b\, E\left(A_{bas_i}\right) \approx n_{tot} \frac{h_b}{h_g} E\left(V_i\right) \tag{2.81}$$

Equation 2.81 can be rearranged to:

$$\frac{n_b}{n_{tot}} \approx \frac{E\left(V_i\right)}{h_g\, E\left(A_{bas_i}\right)} \tag{2.82}$$

For a log-normal distribution of iceberg size, L_i, the iceberg volume is calculated to be L_i^3, although the respective lengths of the iceberg sides are calculated using equations 2.10–2.12, so that $L_y = L_z$ and $L_x = 1.62 L_y$.

The expectation of the iceberg size, L_i is:

$$E\left(L_i\right) = e^{\mu + \frac{\sigma^2}{2}} \tag{2.83}$$

The expectation of the iceberg area, A_i is:

$$E\left(A_i\right) = e^{2\mu+2\sigma^2} \tag{2.84}$$

The expectation of the iceberg volume, V_i is:

$$E\left(V_i\right) = e^{3\mu+4.5\sigma^2} \tag{2.85}$$

In the model, when an iceberg is calved, a random number, $U \in [0, 1]$, is generated and if $U < \frac{E(V_i)}{h_g\, E(A_i)}$, the iceberg contains the basal layer, otherwise the iceberg only contains englacial ice.

The orientation of the iceberg always places the long axis parallel with the flow of water. However, if the iceberg contains a basal layer, the initial orientation of the basal layer can be rotated around the long axis of the iceberg with an equal probability of being on any of the possible four faces. If the basal layer lies on the top (or aerial) face then it is melted by solar radiation and convective heating and when the iceberg overturns all the melted out sediment is deposited in a sudden 'dumping' event.

When ice is melted from the iceberg, as discussed in Section 2.4, the volume of sediment contained in that ice is released into the water column. The sediment is assumed to have an individual grain density, ρ_s, of $2700\,kg\,m^{-3}$. The accumulation rate is calculated by assuming the deposited sediment, ρ_{dep}, has a density of $1700\,kg\,m^{-3}$. The thickness of sediment deposited, T_{face}, for each face of an iceberg, in each melting and moving time step, Δt_m, is calculated with the following equation:

$$T_{face} = R_{tot}\,\Delta t_m\,\left(A_{bas}\,f_{bas} + A_{eng}\,f_{eng}\right)\,\rho_s\,A_{dep}\,\rho_{dep} \tag{2.86}$$

where R_{tot} is the total melt rate of the iceberg face, A_{bas} is the area of the iceberg face containing basal sediment, f_{bas} is the volume fraction of sediment in basal ice, A_{eng} is the area of the iceberg face containing englacial sediment, f_{eng} is the volume fraction of sediment in englacial ice and A_{dep} is the area of the fjord floor over which the sediment is deposited (depositional area). The depositional area is calculated from the distance the sediment is spread over in the x and y directions. These distances are calculated as the sum of the distance moved by the iceberg in the time step, plus the size of the iceberg, plus an additional distance over which the sediment is dispersed. This 'dispersion distance' reflects the time taken for sediment to settle to the fjord floor, the tidal velocity and residual outflow velocity, as well as mixing due to eddies within the fjord. For each iceberg, the thickness deposited from each face is summated. Then, in a two-dimensional array of sediment thickness, representing the x and y dimensions of the fjord, the total thickness deposited by that iceberg is added to the existing

sediment thickness in cells which lie within the depositional area of the iceberg.

2.8 Summary

This chapter has described the theory and development of the *SedBerg* Model, which has been developed with the aim of modelling iceberg-rafted sedimentation in fjord environments. In each calving time step there is a probability of an iceberg calving event occurring, depending on the calving rate and iceberg size distribution, as defined in equation 2.5. If a calving event occurs, the size of the iceberg is drawn at random from a log-normal distribution. At each moving and melting time step, for the population of icebergs in the fjord, the model simulates the motion due to wind action and water currents (equations 2.47-2.50), melting by subaqueous (equations 2.27 and 2.20) and subaerial processes (equations 2.39 and 2.34). If an iceberg becomes unstable (equation 2.76), it overturns and any sediment accumulated on the iceberg surface is deposited. In each moving and melting time step, the thickness of sediment melted from each iceberg and deposited on the fjord floor is calculated using equation 2.86. If an iceberg collides with a fjord wall or the ice front, its new velocity is determined by equations 2.65-2.73. The *SedBerg* Model is applied to a case study of Kangerdlugssuaq Fjord in East Greenland in Chapter 4. Chapter 6 describes some model experiments testing the response of the sedimentation rate to various initial conditions.

Chapter 3

Meltwater Plume Sedimentation: Theory and Development of *SedPlume* Model

3.1 Introduction

Glacial meltwater flows to the glacier bed through conduits, which are formed and maintained by flowing water melting the walls with the necessary heat produced by viscous dissipation and friction (Röthlisberger and Lang, 1987). Once at the bed, the meltwater flows through the subglacial drainage system. There are several possible types of subglacial drainage system, which can be categorised as either discrete systems, where water is confined to a small number of channels or conduits, or distributed systems, where the water is transported through a large proportion of the bed. For mid- and high-latitude glaciers, discharges are very low during winter when surface melting is minimal and increase rapidly in spring at the start of the ablation season. The first flood event of the melt season has been termed the "spring event" by Röthlisberger and Lang (1987), and this is associated with a channelised drainage system being re-established through and underneath the glacier. Thus, during the ablation season, meltwater emerges from one or more conduits at the glacier front. As the meltwater flows along the base of the glacier, it entrains and transports glacially eroded basal sediment, which is often present in high concentrations.

Tidewater glaciers are grounded ice masses, which terminate in fjords with their margins partially submerged in the ocean. The meltwater emerges from a circular conduit at the submerged glacier base and forms a radially symmetric plume. The fresh but usually turbid meltwater is almost always less dense than the ambient seawater. Gilbert (1983) asserted that a sediment load of $30\,kg\,m^{-3}$ would be required for an

underflow to develop based on some simplifying assumptions and Mulder and Syvitski (1995) performed a more detailed calculation of sea water density in various climates to find that sediment concentrations would have to exceed $40\,kg\,m^{-3}$ in polar waters. Thus in general glacial meltwater rises as a positively buoyant forced plume as it enters the saline water of a fjord. When the plume reaches the surface it spreads as a radial surface gravity current. A Landsat ETM+ false colour composite satellite image of Glacier Bay National Park, with the turbid plume from Lamplugh Glacier visible in a cyan colour due to the large volume of sediment contained within it, is shown in Figure 3.1.

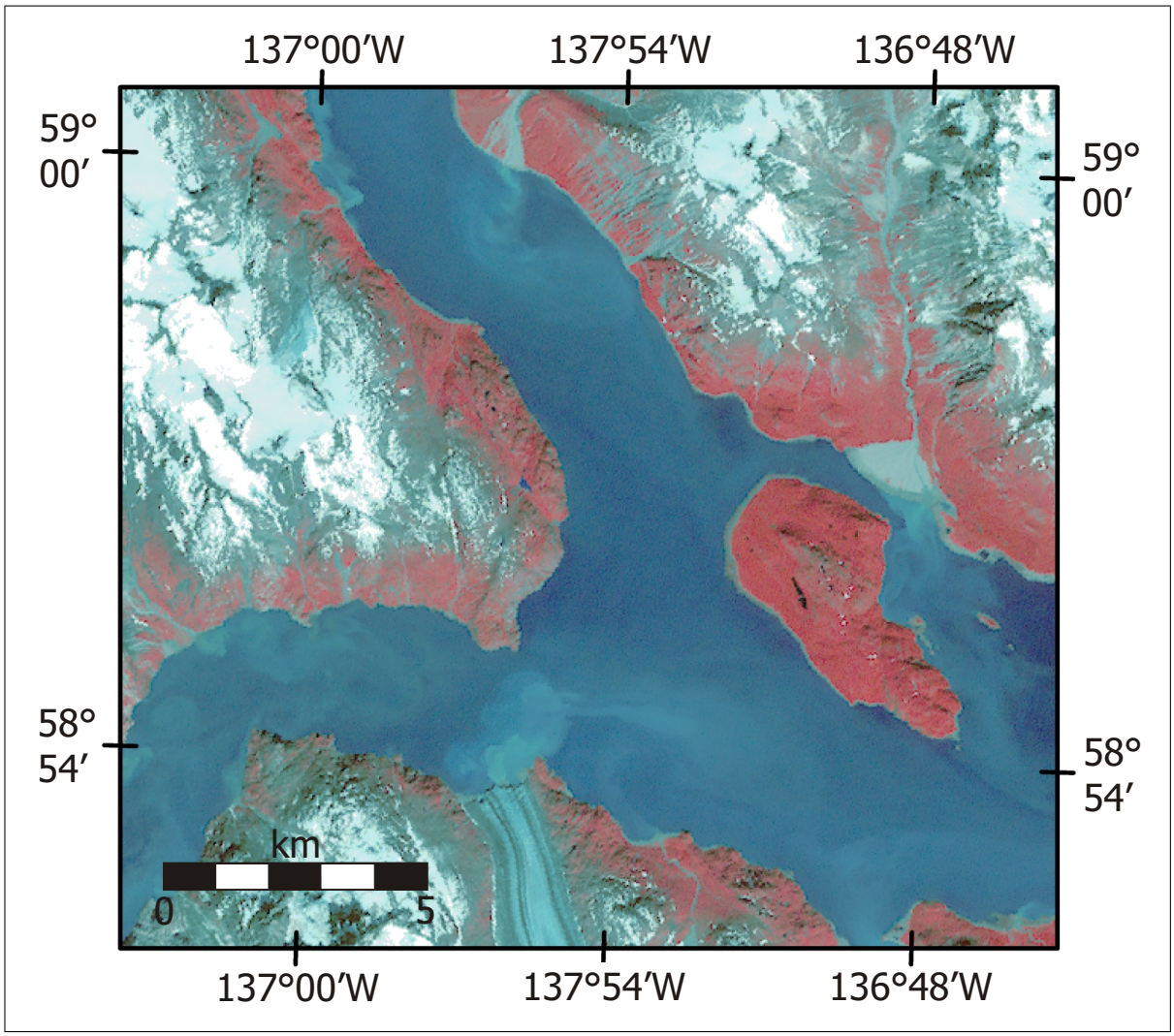

Figure 3.1: *Landsat ETM+ false colour composite satellite image (Bands 4–3–1, Resolution = 30 m) of Glacier Bay National Park. Turbid water is evident as a cyan colour and sediment-free water is visible as dark blue. A plume can be distinguished flowing from Lamplugh Glacier near the bottom of the image and near the top and the middle of the image, two plumes can be observed from glacial rivers, which have formed deltas as they enter the fjord.*

This chapter introduces a model, *SedPlume*, developed to simulate sediment depo-

sition from a glacial plume that enters a fjord at depth, rises to the surface and then flows as a laterally spreading gravity current.

3.2 Forced Plumes

Fluid motion that results from a buoyancy difference between two fluid bodies is defined as a pure plume; fluid motion that results from a pressure drop through an orifice is defined as a pure jet. In the case of fresh water emerging from a subglacial orifice the source of kinetic energy and momentum flux is a combination of the buoyancy difference and the pressure drop between the fluid emerging from the orifice and the ambient fluid. In the literature this is referred to as either a forced plume or a buoyant jet and these terms can be thought of as interchangeable. For fresh water emerging from a subglacial orifice, the term forced plume is perhaps more suitable as the motion is mainly due to the buoyancy difference and the pressure drop has a less important role. For the sake of brevity, when referring to glacial meltwater flowing into a fjord the term plume will sometimes be used in place of the term forced plume.

3.2.1 Historical Perspective

There has been a large volume of papers published about jets and plumes, with a view to understanding natural phenomena such as volcanic eruptions and hydrothermal vents, and engineering applications such as gaseous emissions into the atmosphere (e.g. smokestacks or cooling towers), and liquid releases into water bodies (e.g. sewage or industrial waste). The first detailed experimental measurements were carried out by Prandtl and co-workers in the 1920s. The results were interpreted using boundary layer theory and the assumption that fluid momentum, buoyancy and scalars are spread by turbulent diffusion. In the 1940s, German scientists such as Schmidt, Reichardt, Tollmein and Görtler found similarity solutions for the development of the axial and cross-sectional velocity and radius of jets, by using different forms of Prandtl's turbulent mixing length hypothesis to relate the shear stresses to the mean flow. It was established during this time by experimental measurements that the Gaussian profile is a satisfactory first-order approximation for the cross-sectional properties of jets.

The models of jet and plume flow were based on the laws of conservation of mass, momentum and buoyancy. These laws can be expressed by partial differential equations. Integral methods involve making assumptions about the properties across the cross-section of the plume so that the partial differential equations can be integrated to form ordinary differential equations describing the axial variation of plume properties.

Finally, to close the system of equations, an assumption has to be made about the entrainment of ambient fluid into the turbulent buoyant jet. Early work developing such models was carried out by Rouse *et al.* (1952), who included an equation for turbulent diffusion to account for entrainment, but assumed that the vertical heat flux is constant with height above the source. The contribution of Priestley and Ball (1955) was to obtain solutions for cases when the ambient fluid is thermally stratified.

The seminal paper by Morton *et al.* (1956), which was written as Priestley and Ball (1955) was in press, also addressed the issue of a density gradient in the ambient fluid, as well as introducing the concept that the mean entrainment velocity is proportional to the mean centreline velocity of the plume. This is still used as the basis of jet and plume models today. Morton (1959) formulated the treatment of jets as special cases of forced plumes. In this paper, it becomes clear that stratification of the ambient fluid has an important effect on a plume. Taking the example of a vertical plume with a given buoyancy flux: in a uniform environment the plume will rise to the surface; in a stably stratified environment, the plume will reach a maximum height before spreading horizontally where it becomes neutrally buoyant. If the initial mass and momentum flux is increased in the stratified environment, the maximum height will decrease. A very large momentum flux is required to increase the maximum height reached by the plume.

3.2.2 Governing Equations for Vertical Forced Plumes

Morton *et al.* (1956) considered axisymmetric vertical forced plumes in an incompressible environment where gravity acts in the negative z-direction. They assumed 'top hat' cross-sectional profiles of mean vertical velocity and mean buoyancy (the use of cross-sectional profiles are discussed further in Section 3.2.3). This means that the velocity and buoyancy force are taken to be constant across the plume and zero outside it. Their three main assumptions were:

1. The rate of entrainment at the edge of the plume is proportional to the velocity at that height.
2. The horizontal profiles of mean vertical velocity and mean buoyancy take a similar form at all heights.
3. The local variations of density in the plume are small compared to the ambient density at the level of the source.

Under these assumptions, they constructed the following governing equations for the flow:

The equation for mass conservation (Continuity equation):

$$\frac{d}{dz}\left(R^2\,U\right) = 2\,\alpha\,R\,U \tag{3.1}$$

where U is the vertical velocity, R is the radius of the plume and α is the proportionality constant relating the rate of entrainment at the edge of the plume to the vertical velocity within the plume.

The equation for momentum conservation:

$$\frac{d}{dz}\left(R^2\,U^2\right) = R^2\,g' \tag{3.2}$$

where g' is the reduced buoyancy $g' = g\left(\rho_a\left(z\right) - \rho_p\right)/\rho_{ref}$, ρ_p is the local plume density, ρ_a is the ambient fluid density and ρ_{ref} is a reference density.

The equation for buoyancy conservation:

$$\frac{d}{dz}\left(R^2\,U\,g'\right) = R^2\,U\frac{g}{\rho_{ref}}\frac{d\rho_a}{dz} \tag{3.3}$$

These equations for vertical plumes proposed by Morton *et al.* (1956) provide a useful foundation for the *SedPlume* Model, where both horizontal and vertical motion of plumes are considered.

3.2.3 Cross-sectional Plume Properties

In the literature, either Gaussian or 'top-hat' profiles for the properties across the plume cross-section are assumed, which are integrable functions, $h(x)$, where $\int_{-\infty}^{\infty} h(x)\,dx < \infty$. This property enables the partial differential equations in polar coordinates z (along plume axis) and r (radial coordinate) to be reduced to ordinary differential equations (ODEs) in the z-direction. As discussed in Section 3.2.2, this was the approach used by Morton *et al.* (1956) using 'top-hat' cross-sectional profiles of plume properties.

Top-hat profiles are also assumed for the plume properties (velocity and density) by Lane-Serff and Moran (2005). In cases where there are strong currents in the ambient fluid, the top-hat profile is useful, as pointed out by Chu and Lee (1996). The path-averaged (or top-hat) profile solves the problem when the direction of the excess velocity (the relative velocity between the jet and the ambient fluid) relative to the path of the plume is not parallel. The resulting transverse shear leads to vortex-pair

flow, which has an effect on the entrainment mechanism.

In the *SedPlume* Model, there is no attempt to simulate jets in a cross-flow, therefore Gaussian distributions of the local axial velocity V, reduced gravity g' and the sediment concentration Q_ϕ are used as adopted by Crapper (1977); Jirka (2004); Morton (1959, 1971); Priestley and Ball (1955), to name but a few. The experimental evidence that Gaussian profiles are suitable representations for jets and plumes comes from a wealth of papers, such as Rouse *et al.* (1952) and Chu *et al.* (1999). The velocity, reduced gravity (equivalent to density) and sediment concentration profiles can be written as:

$$\begin{aligned} V &= V_c\, e^{-r^2/b_v^2} \\ g' &= g'_c\, e^{-r^2/b_{scalar}^2} \\ \phi &= \phi_c\, e^{-r^2/b_{scalar}^2} \end{aligned} \tag{3.4}$$

where r is the radial coordinate from the plume centreline and the subscript c refers to the plume property at the centreline. b_v and b_{scalar} are the radial dimensions at which the velocity and scalar quantities (density and sediment concentration), respectively, are reduced to e^{-1} of the centreline value. A dispersion ratio is defined, λ, which is proportional to the turbulent Schmidt number and is a measure of a plume's ability to disperse density relative to momentum, (Morton, 1959):

$$\lambda = \frac{b_{scalar}}{b_v} \tag{3.5}$$

Equation 3.4 can be rewritten in terms of the radial dimension at which the velocity is reduced to e^{-1}, b_v (which from now on will simply be referred to as b) and λ:

$$\begin{aligned} V &= V_c\, e^{-r^2/b^2} \\ g' &= g'_c\, e^{-r^2/(\lambda b)^2} \\ \phi &= \phi_c\, e^{-r^2/(\lambda b)^2} \end{aligned} \tag{3.6}$$

From experimental measurements, List (1982) found a value of λ to be 1.18, Rodi (1982) found λ to be 1.19, and Chu *et al.* (1999) found λ to be 1.2. For practical purposes, the visible edge of the plume, $R \approx \lambda b$.

The supposition that the properties across the plume cross-section can be written as a function of the distance from the source and the radial distance from the jet centreline, so that integration in the radial direction is possible and partial differential equations can be simplified to ordinary differential equations, is referred to as the similarity assumption. This formulation of the equations is called the integral method.

3.2.4 Integral Model Formulation

A schematic diagram of a glacial meltwater plume is shown in Figure 3.2 with definitions of the nomenclature used in the text.

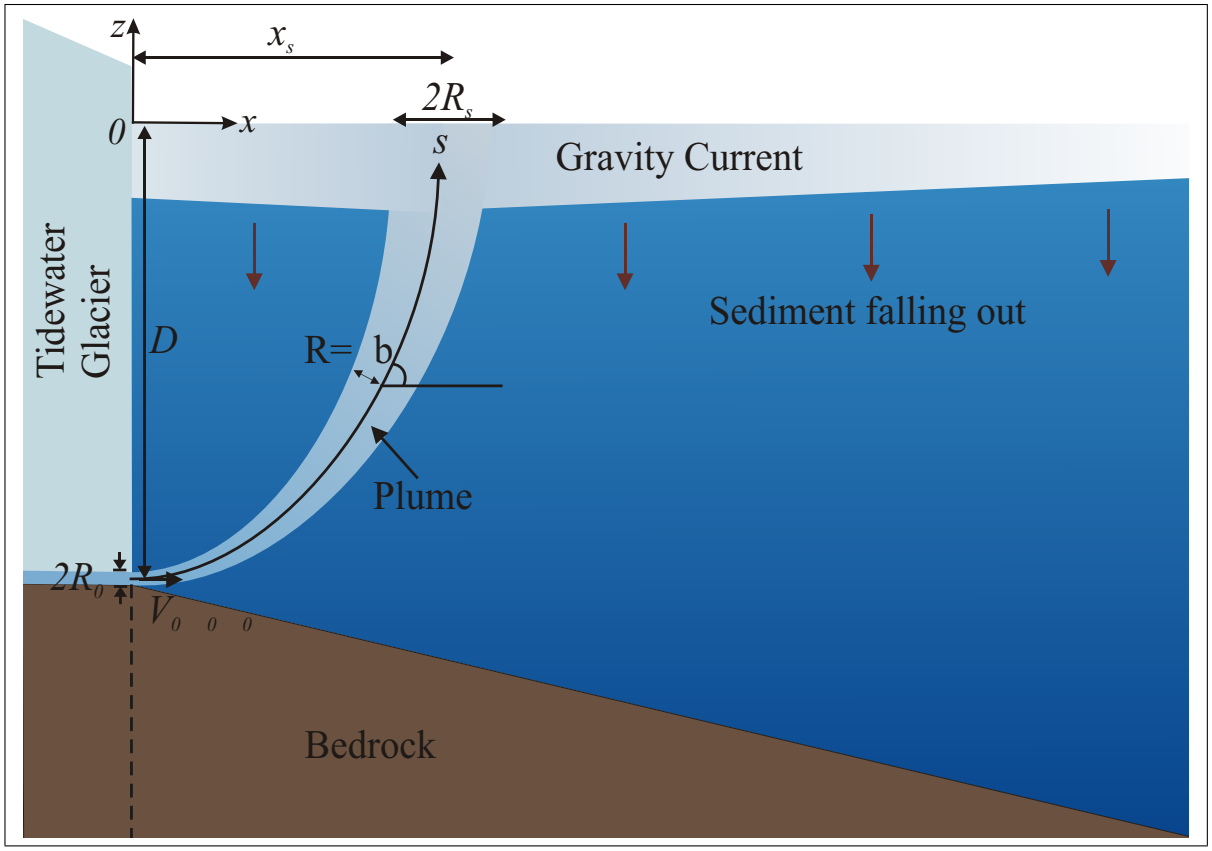

Figure 3.2: *The meltwater rises as a plume from a horizontal subglacial conduit. Its momentum causes the meltwater to flow away from the glacier front, with buoyancy forces dominating more and more, which results in a curved trajectory deflecting upwards towards the surface. Once at the surface the meltwater spreads radially as a surface gravity current*

The Boussinesq approximation can be applied, since density differences are small enough to be neglected as the fluid is incompressible, except where they appear in the buoyancy terms, which are those multiplied by g (Turner, 1979). The integral method makes use of the boundary layer nature of the flow, and this assumption requires that the pressure within the plume is equal to that in the ambient fluid. This condition is not met if there is excessive entrainment or the plume undergoes strong curvature.

The plume flow is assumed to be steady and it is of interest to find a solution for the plume properties as a function of distance from the source; therefore an Eulerian reference frame is most appropriate. This representation means that changes at a fixed point in the fluid are considered and the fluid properties such as velocity and density are assigned to each fixed point in space. The alternative is a Lagrangian reference frame where the observer follows an individual fluid particle, i.e. along a trajectory,

as it moves through space and time (Chu *et al.*, 1999; Chu and Lee, 1996; Middleton, 1979).

The *SedPlume* Model is formulated as an integral model, similar to that described by Jirka (2004), but for two dimensions, as the plume is assumed to be initiated at an angle in the x–z plane with no ambient flow in the y-direction (or cross flow). It therefore remains in this plane throughout its trajectory. Equations are added to account for sediment deposition, in a similar way to Lane-Serff and Moran (2005). In order to solve the equations for a turbulent, entraining plume injected at an angle into stationary, stably stratified ambient fluid, the equations are formulated so that the ODEs are solved along the path of the plume (in the s direction) and the integrals are solved across the Gaussian cross-section of the plume (in the r direction) as shown in Figure 3.2.

3.2.5 Conserved Variables

The integral equations are formulated in terms of flux quantities, such as mass and momentum, rather than local variables, such as b and V_c, since the flux quantities are mostly conservative (constant or gradually changing), whereas local variables can undergo strong changes or contain singularities, which affects the accuracy of solutions. The following conserved variables are defined, as in Jirka (2004), through cross-sectional integration, as described in Section 3.2.3.

Volume Flux:

$$Q = 2\pi \int_0^\infty V r \, dr = \pi b^2 V_c \tag{3.7}$$

Momentum Flux (along the plume trajectory):

$$M = 2\pi \int_0^\infty V^2 r \, dr = \frac{1}{2} \pi b^2 V_c^2 \tag{3.8}$$

Buoyancy Flux:

$$B = 2\pi \int_0^\infty V g' r \, dr = \pi b^2 \left(\frac{\lambda^2}{1+\lambda^2} \right) V_c \, g'_c \tag{3.9}$$

Sediment Mass Flux:

$$Q_\phi = 2\pi \int_0^\infty V \phi r \, dr = \pi b^2 \left(\frac{\lambda^2}{1+\lambda^2} \right) V_c \, \phi \tag{3.10}$$

The local jet variables can be written in terms of the integral variables (equa-

tions 3.7–3.10) as follows:

$$V_c = \frac{2M}{Q} \tag{3.11}$$

$$b = \frac{Q}{\sqrt{2\pi M}} \tag{3.12}$$

$$g'_c = \frac{B}{Q_{scalar}} \tag{3.13}$$

$$\phi = \frac{Q_\phi}{Q_{scalar}} \tag{3.14}$$

where

$$\begin{aligned} Q_{scalar} &= \left(\frac{\lambda^2}{1+\lambda^2}\right)\pi b^2 V_c \\ &= \left(\frac{\lambda^2}{1+\lambda^2}\right) Q \end{aligned} \tag{3.15}$$

3.2.6 Entrainment

The theoretical treatment of the mechanism by which a plume entrains ambient fluid has been the focus of much research—useful review papers have been written by Ellison and Turner (1959) and Turner (1986). In early work, such as Rouse *et al.* (1952), a term for turbulent diffusion was included to account for entrainment. Priestley and Ball (1955) used a conservation of energy equation to derive the entrainment function. The seminal paper by Morton *et al.* (1956) first introduced an entrainment hypothesis, where the mean entrainment velocity, E, is proportional to the mean centreline velocity, $E = \alpha V_c$, where α is a constant determined by experimental measurements. Morton (1959) adopted a value of $\alpha = 0.116$ for top-hat profiles, from measurements of non-buoyant jets, and this translates to a value for Gaussian profiles of $\alpha_G = \alpha/\sqrt{2}$ (Turner, 1979). This treatment of entrainment has proved to be sufficiently accurate for many applications.

The value of α is different for pure jets and pure plumes, therefore, a forced plume (or buoyant jet), which has jet-like properties initially and develops more plume-like properties as it rises, will have an entrainment parameter that changes along its trajectory. List and Imberger (1973, 1975) attempted to determine an entrainment coefficient which is appropriate for forced plumes/buoyant jets and depends on the local densimetric Froude number. By substituting the appropriate constants found from experimental data, Crapper (1977) expressed the List and Imberger (1973) entrainment

coefficient as:

$$\alpha = 0.051 + \frac{0.650}{Fr^2} \tag{3.16}$$

where the local densimetric Froude number is defined as:

$$Fr = \frac{V_c}{\sqrt{g'_c b}} \tag{3.17}$$

Equation 3.16 is slightly modified by Jirka (2004) for a non-vertical jet or plume:

$$\alpha = 0.051 + \frac{0.650 \sin\theta}{Fr^2} \tag{3.18}$$

It is widely accepted that a good approximation is $\alpha \approx 0.1$ and this value is taken in this model, as in Lane-Serff and Moran (2005).

3.2.7 Conservation Equations

The equation for the conservation of volume (the continuity equation) is:

$$\frac{dQ}{ds} = 2\pi b \left(\alpha V_c\right) \tag{3.19}$$

The entrainment velocity is αV_c and the length over which entrainment occurs is the circumference of the plume, $2\pi b$.

The equations for the conservation of momentum in the x and z-directions are, respectively:

$$\frac{d}{ds}\left(M\cos\theta\right) = 0 \tag{3.20}$$

$$\frac{d}{ds}\left(M\sin\theta\right) = \pi\lambda^2 b^2 g'_c \tag{3.21}$$

While the plume remains narrow, it is justifiable to neglect a pressure term in equation 3.21. Applying the product rule to equation 3.20 yields:

$$\begin{aligned}
M\frac{d}{ds}\left(\cos\theta\right) + \cos\theta\frac{dM}{ds} &= 0 \\
\cos\theta\frac{dM}{ds} &= -M\left[\frac{d\theta}{ds}\frac{d}{d\theta}\left(\cos\theta\right)\right] \\
\frac{dM}{ds} &= \frac{1}{\cos\theta}\left[M\sin\theta\frac{d\theta}{ds}\right] \\
\frac{dM}{ds} &= M\tan\theta\frac{d\theta}{ds}
\end{aligned} \tag{3.22}$$

In the same way, equation 3.21 can be expanded and rearranged as:

$$\begin{aligned} M\frac{d}{ds}(\sin\theta) + \sin\theta\frac{dM}{ds} &= \pi\lambda^2 b^2 g' \\ M\left[\frac{d\theta}{ds}\frac{d}{d\theta}(\sin\theta)\right] &= \pi\lambda^2 b^2 g' - \sin\theta\frac{dM}{ds} \\ \frac{d\theta}{ds} &= \frac{1}{M\cos\theta}\left[\pi\lambda^2 b^2 g' - \sin\theta\frac{dM}{ds}\right] \end{aligned} \tag{3.23}$$

Substituting equation 3.23 into equation 3.22:

$$\begin{aligned} \frac{dM}{ds} &= \frac{M\tan\theta}{M\cos\theta}\left[\pi\lambda^2 b^2 g' - \sin\theta\frac{dM}{ds}\right] \\ \frac{dM}{ds}\left(1+\tan^2\theta\right) &= \frac{\tan\theta}{\cos\theta}\pi\lambda^2 b^2 g' \\ \frac{dM}{ds} &= \frac{\tan\theta}{\cos\theta\left(1+\tan^2\theta\right)}\pi\lambda^2 b^2 g' \\ \frac{dM}{ds} &= \frac{\sin\theta}{\cos\theta}\frac{\cos^2\theta}{\cos\theta}\pi\lambda^2 b^2 g' \\ \frac{dM}{ds} &= \pi\lambda^2 b^2 g'\sin\theta \end{aligned} \tag{3.24}$$

And substituting equation 3.22 into equation 3.23:

$$\begin{aligned} \frac{d\theta}{ds} &= \frac{1}{M\cos\theta}\left[\pi\lambda^2 b^2 g' - M\sin\theta\tan\theta\frac{d\theta}{ds}\right] \\ \frac{d\theta}{ds}\left(1+\tan^2\theta\right) &= \frac{1}{M\cos\theta}\pi\lambda^2 b^2 g' \\ \frac{d\theta}{ds} &= \frac{1}{M\cos\theta\left(1+\tan^2\theta\right)}\pi\lambda^2 b^2 g' \\ \frac{d\theta}{ds} &= \frac{\cos^2\theta}{M\cos\theta}\pi\lambda^2 b^2 g' \\ \frac{d\theta}{ds} &= \pi\lambda^2 b^2 g'\frac{\cos\theta}{M} \end{aligned} \tag{3.25}$$

The equation for the conservation of buoyancy is:

$$\frac{dB}{ds} = Q\frac{g}{\rho_{ref}}\frac{d\rho_a}{dz}\sin\theta \tag{3.26}$$

The density gradient in the ambient fluid, $\frac{d\rho_a}{dz}$, is assumed to be constant, so let the constant G be defined as:

$$G = \frac{g}{\rho_{ref}}\frac{d\rho_a}{dz} \tag{3.27}$$

Then equation 3.26 becomes:

$$\frac{dB}{ds} = QG\sin\theta \tag{3.28}$$

Suspended sediment is assumed to have a negligible impact on the buoyancy and the change in buoyancy of glacial plumes. This is a reasonable assumption for most glacial plumes, since sediment concentrations are low compared to the density difference between the plume and the ambient. For very high sediment concentrations or for a low salinity ambient, an additional term would be required in equation 3.28.

The equations which define the trajectory of the plume are:

$$\frac{dx}{ds} = \cos\theta \tag{3.29}$$

$$\frac{dz}{ds} = \sin\theta \tag{3.30}$$

3.2.8 Plume Sedimentation

Much of the experimental and theoretical work on plume sedimentation originates from the volcanology literature, to understand the behaviour of volcanic eruption columns and hydrothermal plumes at mid-ocean ridges (black smokers). For example, Sparks *et al.* (1991) developed a theoretical model for sedimentation from radially spreading gravity currents resulting from vertically rising sediment-laden plumes and compared it with experimental data, with environmental applications such as volcanic ejecta and black smokers in mind. Veitch and Woods (2000, 2002) used a plume sedimentation model in addition to experimental observations to simulate particle recycling and oscillations in the particle-laden, buoyant plumes resulting from volcanic eruptions.

In this model, the formula which is derived by Lane-Serff and Moran (2005) is used. Sediment particles fall out of the plume when the radial component of the sediment fall velocity is greater than the entrainment velocity, as shown in Figure 3.3:

$$W_{out} = W_s\cos\theta\sin\beta - \alpha V_c > 0 \tag{3.31}$$

where W_{out} is the downward velocity of a sediment grain, W_s is the particle fall velocity, β is defined in Figure 3.3 and θ in Figure 3.2. The inequality in equation 3.31 can be rearranged to:

$$\sin\beta > \frac{\alpha V}{W_s\cos\theta} \tag{3.32}$$

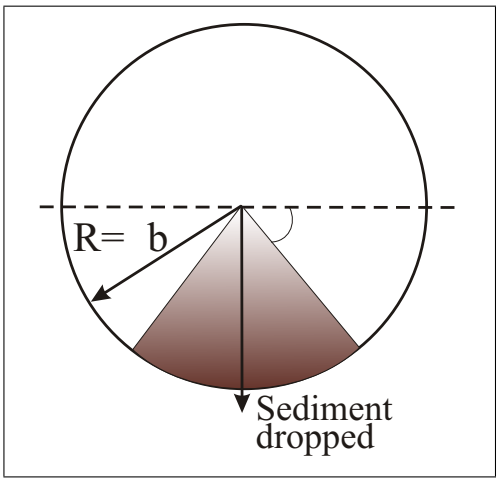

Figure 3.3: *Cross section of a plume showing segment where sediment is dropped at angles greater than* β.

This will be satisfied for $\beta > \beta_c$, as long as $\sin\beta_c < 1$, where:

$$\sin\beta_c = \frac{\alpha V}{W_s \cos\theta} \tag{3.33}$$

When these conditions are satisfied, the sediment flux derivative with respect to s is:

$$\frac{dQ_\phi}{ds} = -2\int_{\beta_c}^{\pi/2} W_{out}\,\phi\lambda b\,d\beta \tag{3.34}$$

The integral can be solved to give:

$$\frac{dQ_\phi}{ds} = -2\phi\lambda b\left[W_s\cos\theta\cos\beta_c - \alpha V\left(\pi/2 - \beta_c\right)\right] \tag{3.35}$$

Equation 3.35 gives the rate of sediment falling from the plume in units of mass per time per unit distance in the s-direction. To convert this to units of mass per time per unit horizontal distance (in the x-direction), equation 3.35 should be divided by $\cos\theta$. This deposition rate needs to be converted into a thickness deposited per unit time, so that it can be added to the sediment array at the bottom of the fjord. First, the deposition rate should be divided by the width of the plume, to give the units of mass per area per time. Then this should be divided by the density of the deposited sediment to give the thickness deposited per unit time.

3.2.9 Particle Settling Velocity

Sedimentation occurs from the plume when the component of the particle fall velocity normal to the plume boundary exceeds the entrainment velocity. The relative settling velocity of different grain sizes has a significant effect on the resultant ratio of different grain sizes in the deposited sediment.

3.2.9.1 Stokes' Law

Stokes' Law is commonly used to calculate the particle settling velocity for fine sands, silts and clays, but the relation is not valid for coarser sand. For larger grain sizes, there are alternative experimentally derived relations.

Hallermeier (1981) performed a series of experiments and collated a large number of other results for settling velocities of sands. The data were collected using non-spherical sediment grains, which were significantly different compared with the settling velocities of spherical grains of similar diameter. Hallermeier found expressions for the settling velocity by fitting curves to experimental data for various values of A, the Archimedes buoyancy index, which is defined as:

$$A = \frac{\rho_w \, \Delta\rho \, g \, d_s^3}{\mu_w^2} \tag{3.36}$$

where d_s is the sediment grain diameter in m, $\Delta\rho = \rho_s - \rho_p$ is the density difference between the sediment and the fluid in the plume, which can be assumed to be a constant as the plume density is approximately equal to the ambient fluid density. μ_w is the dynamic viscosity of water, which depends on temperature, T. Between 0 and $20°C$, μ_w can be calculated (in units of $kg\,m^{-1}s^{-1}$) using the following equation (Lide, 2000):

$$\mu_w = 0.1 \times 10^{\left(\frac{1301}{998.333+8.1855(T-20)+0.00585(T-20)^2} - 3.30233\right)} \tag{3.37}$$

The dynamic viscosity of water at different temperatures, calculated using equation 3.37, is shown in Figure 3.4.

Taking the values:

$$\mu_w = 1.567 \times 10^{-3} \; kg\,m^{-1}s^{-1} \,(\text{at } 4°C)$$
$$\Delta\rho = 1470 \; kg\,m^{-3}$$
$$\rho_w = 1000 \; kg\,m^{-3}$$

For sediment sizes up to fine sand ($A < 39$ or $d_s < 188\,\mu m$), Stokes' equation was

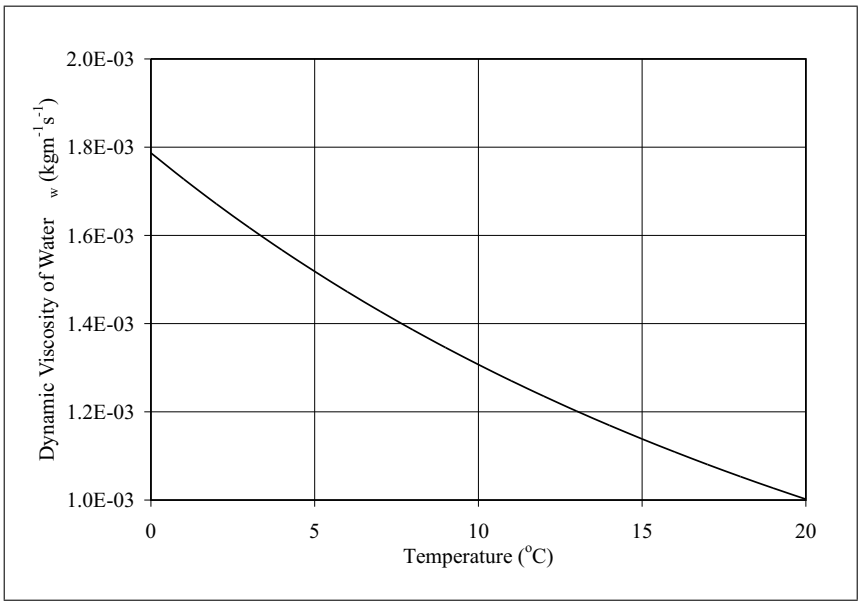

Figure 3.4: *Dynamic Viscosity of Water*

found to fit the data well:

$$W_t = \frac{g\, d_s^2\, \Delta\rho}{18\mu_w} \tag{3.38}$$

where W_t is the theoretical particle settling velocity.

However, for larger grain sizes from fine to coarse sand ($39 < A < 10^4$ or $188\,\mu m < d_s < 1.19\,mm$), a different relationship for the settling velocity was found based on the data:

$$W_t = \frac{(g\,\Delta\rho)^{0.7}\; d_s^{1.1}}{6\,\mu_w^{0.4}\,\rho_w^{0.3}} \tag{3.39}$$

These two equations are used in the *SedPlume* Model to calculate the particle settling velocity, with appropriate adjustments made for flocculation, as will be discussed in Section 3.2.9.2.

3.2.9.2 Flocculation

Flocculation is the process by which silt and clay particles aggregate to form larger assemblages. Very fine particles are negatively charged. However, their charge is neutralised by the ions in salt water and Van der Waals forces cause the particles to bind together. Once there is sufficient entrainment of marine water in the fresh meltwater plume to induce flocculation, it has an important influence on the rate of particle setting in fjord environments (Dowdeswell, 1987; Gilbert, 1983; Ó Cofaigh and Dowdeswell, 2001; Syvitski, 1989). Flocculation occurs when there are sufficient

particle collisions and adhesion of particles during collision. Much work was carried out by Kranck (1975, 1980, 1981), who found that inorganic suspended sediments in coastal environments have stable size distributions with a modal size which depends on the modal size of the deflocculated single grain distributions. For salinities greater than $3\,PSU$, most fine inorganic sediment flocculates readily (Kranck, 1973).

Syvitski *et al.* (1985) collected water and sediment samples, measured salinity, temperature and current velocity profiles, and deployed sediment trap moorings to investigate the dynamics of suspended particles in a fjord. The field measurements were collected in Bute Inlet in the Pacific Range of the Coast Mountains, British Columbia, which is a $78\,km$ long fjord with an average width of $4.2\,km$. The maximum water depth is $650\,m$ with a $280\,m$ deep sill. The mean tidal range is $3.6\,m$ with spring tides up to $5.5\,m$ above sea level. The fjord is fed by two rivers at its head, the Homathko and the Southgate. The average annual discharge of the Homathko is $250\,m^3s^{-1}$ with a summer maximum of $800\,m^3s^{-1}$. The fjord is stably stratified throughout the year. They found that as the salinity increased with depth, the floc size increased, and therefore the settling velocity also increased - from $30\,m\,day^{-1}$ at $5\,m$ to $100\,m\,day^{-1}$ at $30\,m$. The particles discharged from the Homathko are mostly inorganic minerals with less then 3% organic detritus. An array of sediment traps at different depths was located near the outlet of the Homathko River at the head of the fjord. The traps were used to measure the vertical flux of particles and the concentration of a given particle size at a particular depth, from which the average *in situ* settling velocity was calculated.

Figure 16 in Syvitski *et al.* (1985) shows their observations of settling velocity and velocity enhancement factor, $EH = \frac{W_o}{W_t}$ against grain diameter at different water depths, where W_o is the observed settling velocity and W_t is the theoretical settling velocity. They also published equations for the relationship between W_o and W_t at $5\,m$ water depth, but not for the deeper depths. Since it would be more instructive to use the deepest measurement available (this is $30\,m$), the relationship between W_o and W_t at $30\,m$ water depth was measured and calculated from the published graph. The relationships found, where d_s is measured in μm, are:

$$W_o = 1610.39\,W_t\,d_s^{-1.755} \qquad \text{if } d_s \leq 14\,\mu m \tag{3.40}$$

$$W_o = 282.51\,W_t\,d_s^{-1.115} \qquad \text{if } 14\,\mu m < d_s \leq 169\,\mu m \tag{3.41}$$

$$W_o = W_t \qquad \text{if } d_s > 169\,\mu m \tag{3.42}$$

As appropriate, equations 3.40–3.42 are used to adjust the theoretical particle settling velocity from equation 3.38 for particles with $d_s \leq 188\,\mu m$ and equation 3.39 for particles with $d_s > 188\,\mu m$.

The difference between settling velocities for different particle sizes, with and without flocculation taken into account, is shown in Figure 3.5. The scale is log-log, and it

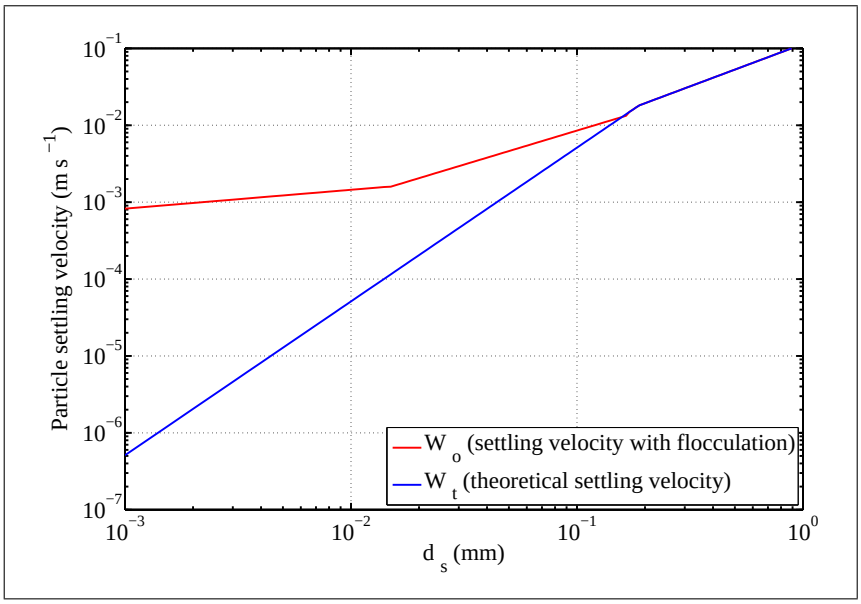

Figure 3.5: *Particle settling velocity against grain size with and without the effects of flocculation. Equations 3.40–3.42 are used to calculate the settling velocity with flocculation, which are derived from measurements by Syvitski et al. (1985).*

can be seen that flocculation has a very important effect for particles with $d_s \leq 169\,\mu m$, i.e. particles classified using the Wentworth scale from fine sand to clay. For individual particle sizes less than $0.01\,mm$, the aggregating effect of flocculation increases the rate of particle settling by between one and three orders of magnitude.

Curran *et al.* (2004) carried out a study of fine-grained sediment flocculation beneath a glacial meltwater plume in Disenchantment Bay, Alaska. They found that floc sizes and the fraction of mass bound within flocs exhibit a pronounced increase with depth, but there was no change down fjord. They also found there was no change in the disaggregated inorganic grain size (DIGS) down fjord, which implied that flocculation has an important influence on the settling velocity of sediment through the water column. The DIGS at $160\,m$ were similar to those at $10\,m$, which supports the idea that flocculation is very important in removing sediment from the plume. The bottom DIGS were slightly enriched in larger grains compared to the surface layer, which suggests that there is some single grain settling for larger particle sizes. Median floc sizes observed at the surface were of the order of $1\,mm$, increasing to approximately $1.5\,mm$ at $160\,m$ depth.

Syvitski *et al.* (1995) used a Floc Camera Assembly (FCA) to obtain the in-situ size, shape, concentration and settling velocity of particles in Halifax Inlet, a deep-water estuary, in 22, 35 and 70 m of water. They found mean floc diameters of 0.6 to 1.9 mm, with the largest solitary flocs having a long axis of 7.6 mm and a diameter of $\sim$ 3.7 mm. The constituent grain size was mostly in the 38 μm range. The shape of flocs observed was most commonly oval, becoming more elongated with floc size, although some were highly irregular. Hill *et al.* (1998) took measurements with an FCA at 325 m water depth in Tarr Inlet, Glacier Bay, Alaska. They found that the settling velocities of flocs measured were similar to those for like-sized flocs in diverse marine environments. They found settling velocities of order 1 $mm\,s^{-1}$ for flocs with diameters of approximately 1 mm, which implies that gravity (sinking force) usually exceeds turbulent forces in these environments.

3.2.10 Solving the Ordinary Differential Equations

The seven ordinary differential equations derived above solved by the *SedPlume* Model are:

$$\frac{dQ}{ds} = 2\pi b\,(\alpha V_c) \tag{3.43}$$

$$\frac{dM}{ds} = \pi\lambda^2 b^2 g' \sin\theta \tag{3.44}$$

$$\frac{d\theta}{ds} = \pi\lambda^2 b^2 g' \frac{\cos\theta}{M} \tag{3.45}$$

$$\frac{dB}{ds} = QG\sin\theta \tag{3.46}$$

$$\frac{dX}{ds} = \cos\theta \tag{3.47}$$

$$\frac{dZ}{ds} = \sin\theta \tag{3.48}$$

$$\frac{Q_\phi}{ds} = -2\phi\lambda b\left[W_o\cos\theta\cos\beta_c - \alpha V\left(\pi/2 - \beta_c\right)\right] \tag{3.49}$$

In the *SedPlume* Model, equations 3.43-3.49 are solved using the adaptive stepsize fourth order Runge-Kutta method as described by Press *et al.* (2002). This method utilises step-doubling and the Cash-Karp parameters to adjust the size of each step and achieve the specified accuracy, depending on how quickly the parameters are changing. This is an efficient way of finding an accurate solution whilst minimising computation time, an important consideration when the equations are solved repeatedly to find the plume sedimentation in fjords over time periods of up to thousands of years.

The integration is stopped at the point where the plume reaches the surface. This is taken to be when the centreline passes through the horizontal plane of the water

surface. The final step size is adjusted so that the final point of the integration is at the surface.

Figure 3.6 shows the proportion of sediment dropped in the plume against grain

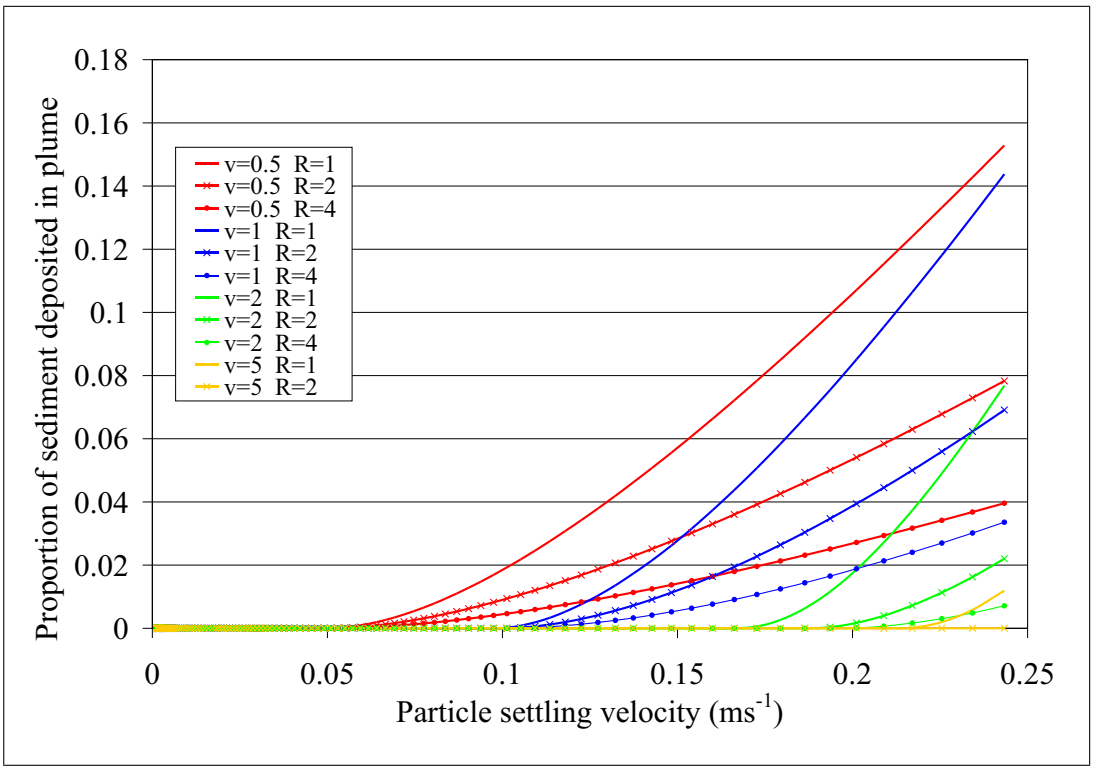

Figure 3.6: *Proportion of sediment deposited in the plume for different particle settling velocities*

size when equations 3.43–3.49 are solved for a range of different initial conditions. The smallest particle settling velocity where sediment falls out in the rising plume is $0.05\,m\,s^{-1}$ for the range of initial conditions shown. This means that for grain sizes below $0.5\,mm$, or from clay up to and including medium sand (see figure 3.5), no sediment is deposited in the plume and all the sediment is carried to the surface. Here it is deposited in the radially spreading gravity current, which is described in the next section. If the initial plume velocity falls to lower values, smaller grain sizes are deposited in the plume.

3.3 Gravity Currents

When the turbid plume reaches the surface in the *SedPlume* Model, it is treated as a constant flux gravity current. A gravity current is a wedge of fluid intruding laterally into an ambient body of fluid of a different density, in the case of glacial plumes the buoyant particle-laden plume reaches the surface and flows above the ambient seawater which has a greater density. Therefore the concentration of particles in the gravity

current is not sufficiently high that the density of the gravity current is greater than that of seawater.

3.3.1 Dynamics

Gravity currents are always driven by a density difference between two fluids. There is a substantial literature on gravity currents: a good review on the subject was written by Kneller and Buckee (2000). Authoritative papers have been published on gravity currents containing sediment: for two-dimensional gravity currents which are more dense than the ambient see Bonnecaze *et al.* (1993); for axisymmetrical gravity currents which are more dense than the ambient see Bonnecaze *et al.* (1995); and for two-dimensional gravity currents which are less dense than the ambient see Maxworthy (1999); Sparks *et al.* (1993). Gravity currents can be described by the one-layer shallow-water equations if the ambient fluid is much deeper than the thickness of the gravity current. Bonnecaze *et al.* (1995) consider an axisymmetric particle-driven gravity current with bulk density ρ_{gc}, composed of particles of density ρ_s suspended in an interstitial fluid of density ρ_f, with volume fraction of particles φ. The density of the current is given by:

$$\rho_{gc}(\varphi) = (\rho_s - \rho_f)\,\varphi + \rho_i$$

The radial shallow-water equations for the case of an axisymmetrical gravity current in dimensionless form are:

$$\frac{\partial h}{\partial t} + \frac{1}{r}\frac{\partial}{\partial r}(ruh) = 0 \tag{3.50}$$

$$\frac{\partial}{\partial t}(uh) + \frac{1}{r}\frac{\partial}{\partial r}\left(ru^2h\right) + \frac{\partial}{\partial r}\left(\frac{1}{2}(\varphi - \gamma)\,h^2\right) = 0 \tag{3.51}$$

$$\frac{\partial \varphi}{\partial t} + u\frac{\partial \varphi}{\partial r} = -\beta\frac{\varphi}{h} \tag{3.52}$$

where u is the velocity, r is the radial distance from the point where the plume reaches the surface, h is the height of the gravity current, the contribution of the interstitial fluid to the reduced gravity is:

$$\gamma = (\rho_a - \rho_f) / [(\rho_s - \rho_f)\,\varphi_0] \tag{3.53}$$

and the dimensionless settling velocity is:

$$\beta = W_s / (g'_0 h_0)^{1/2}\,. \tag{3.54}$$

For certain boundary conditions there are analytical solutions to equations 3.50–3.52, which are discussed in the next section.

3.3.2 Sediment deposition

Bonnecaze *et al.* (1995) found the solution for the volume fraction distribution in a gravity current resulting from constant flux axisymmetric release of suspended sediment, at long time periods, to be:

$$\begin{aligned}\varphi(r_h) &= \varphi_s \exp\left[-\frac{\pi W_o}{Q_s}\left(r_h^2 - R_s^2\right)\right] \\ &= \varphi_s \exp\left[-\xi\left(r_h^2 - R_s^2\right)\right]\end{aligned} \tag{3.55}$$

where φ_s is the volume fraction of particles at the surface of the plume, r_h is the radial horizontal distance from the point where the plume reaches the surface ($r_h = x - x_s$) and R_s is the plume radius at the surface. Therefore, the sediment concentration distribution can be written as:

$$\phi(r_h) = \phi_s \exp\left[-\xi\left(r_h^2 - R_s^2\right)\right] \tag{3.56}$$

where ϕ_s is the sediment concentration at the surface of the plume.

In the literature, there have been a number of experimental investigations of the sedimentation from a radially spreading surface gravity current formed when a vertical buoyant plume reaches the surface, which have been compared to the theoretical equation 3.56. Sparks *et al.* (1991) took the above closed form solution to derive the deposition rate. Firstly, the proportion of particles released from a gravity current between the edge of the plume and distance r is the difference between the initial sediment concentration and the concentration of sediment in the gravity current (equation 3.56 multiplied by the mass flux at the surface):

$$Q_s\,\phi(r_h) = Q_s\,\phi_s\left(1 - \exp\left[-\xi\left(r_h^2 - R_s^2\right)\right]\right) \tag{3.57}$$

The derivative of equation 3.57 gives the mass flux of particles falling out of the gravity current per unit distance:

$$\begin{aligned}S_{gc}(r_h) &= Q_s \frac{d\phi(r_h)}{dr_h} \\ &= 2\pi W_o \phi_s r_h \exp\left[-\frac{\pi W_o}{Q_s}\left(r_h^2 - R_s^2\right)\right] \\ &= 2Q_s \xi \phi_s r_h \exp\left[-\xi\left(r_h^2 - R_s^2\right)\right]\end{aligned} \tag{3.58}$$

The mass flux of sediment from the gravity current per unit area, D_{gc}, is:

$$\begin{aligned} D_{gc}(r_h) &= Q_s \frac{d\phi(r_h)}{dr} \frac{1}{2\pi r} \\ &= W_o \phi_s \exp\left[-\frac{\pi W_o}{Q_s}\left(r_h^2 - R_s^2\right)\right] \\ &= W_o \phi_s \exp\left[-\xi\left(r_h^2 - R_s^2\right)\right] \end{aligned} \tag{3.59}$$

The series of experiments described in Carey *et al.* (1988), Sparks *et al.* (1991) and Ernst *et al.* (1996) involved releasing fresh water containing silicon carbide particles into a tank of salty water and observing the resulting vertical plume. Sparks *et al.* (1991) compared equation 3.58 to the data and concluded that it was a good fit to the laboratory plumes. The theory is applicable on larger scales, as shown by Bursik *et al.* (1992), who measured sedimentation from a 24 km high volcanic eruption column.

Zarrebini and Cardoso (2000), Cardoso and Zarrebini (2001) and Cardoso and Zarrebini (2002) performed experiments investigating the deposition from buoyant vertical plumes carrying a suspension of Ballotini glass beads with root mean square particle diameter between 50 and 80 μm. They fitted equation 3.58, as derived by Sparks *et al.* (1991), to their results for the sediment deposition rate.

Lane-Serff and Moran (2005) carried out experiments for buoyant plumes which were initially travelling horizontally, or at some small angle above or below the horizontal. The plumes were positively buoyant, but contained a suspension of sand particles. They presented results using two size fractions: $75 - 150$ μm and $150 - 300$ μm. They modelled both deposition in the plume and the gravity current. The sediment deposition rate from a gravity current is treated as a Gaussian distribution, where the maximum deposition rate is centred on the middle of the plume at the point where it surfaces. The probability density function for the Gaussian distribution is:

$$P(x) = \frac{1}{\sigma\sqrt{2\pi}} \exp\left[-\frac{1}{2}\left(\frac{x-\mu}{\sigma}\right)^2\right] \tag{3.60}$$

where μ is the mean of the distribution and σ is the standard deviation.

The (dimensional) spreading radius in Lane-Serff and Moran (2005) is:

$$R_{spread} = \sqrt{\frac{Q_s}{\pi W_o}} \tag{3.61}$$

As the radius of the plume at the surface is of the same order as the predicted

spreading radius R_{spread}, Lane-Serff and Moran (2005) approximated the total spread, or standard deviation, as the sum of the predicted spreading radius, R_{spread}, and the plume radius at the surface, R_s.

Lane-Serff and Moran (2005) proposed the following equation for sedimentation along the centreline of a radial surface gravity current:

$$S_{gc}(x) = \frac{Q_{\phi_s}}{\sqrt{\pi}\left(R_{spread}+R_s\right)} \exp\left[-\left(\frac{(x-x_s)}{\left(R_{spread}+R_s\right)}\right)^2\right] \tag{3.62}$$

$$= \frac{Q_{\phi_s}}{\sqrt{\pi}\left(R_{spread}+R_s\right)} \exp\left[-\left(\frac{(r_h)}{\left(R_{spread}+R_s\right)}\right)^2\right] \tag{3.63}$$

This implies that $\mu = x_s$ and $\sigma = (R_{spread} + R_s)/\sqrt{2}$. $Q_{\phi_s} = Q_s\phi_s$ is the total amount of sediment remaining in the plume at the surface (units of mass/time).

The equation 3.58 (Sparks *et al.*, 1991; Zarrebini and Cardoso, 2000) and equation 3.62 (Lane-Serff and Moran, 2005) are compared in Figure 3.7 and Figure 3.8,

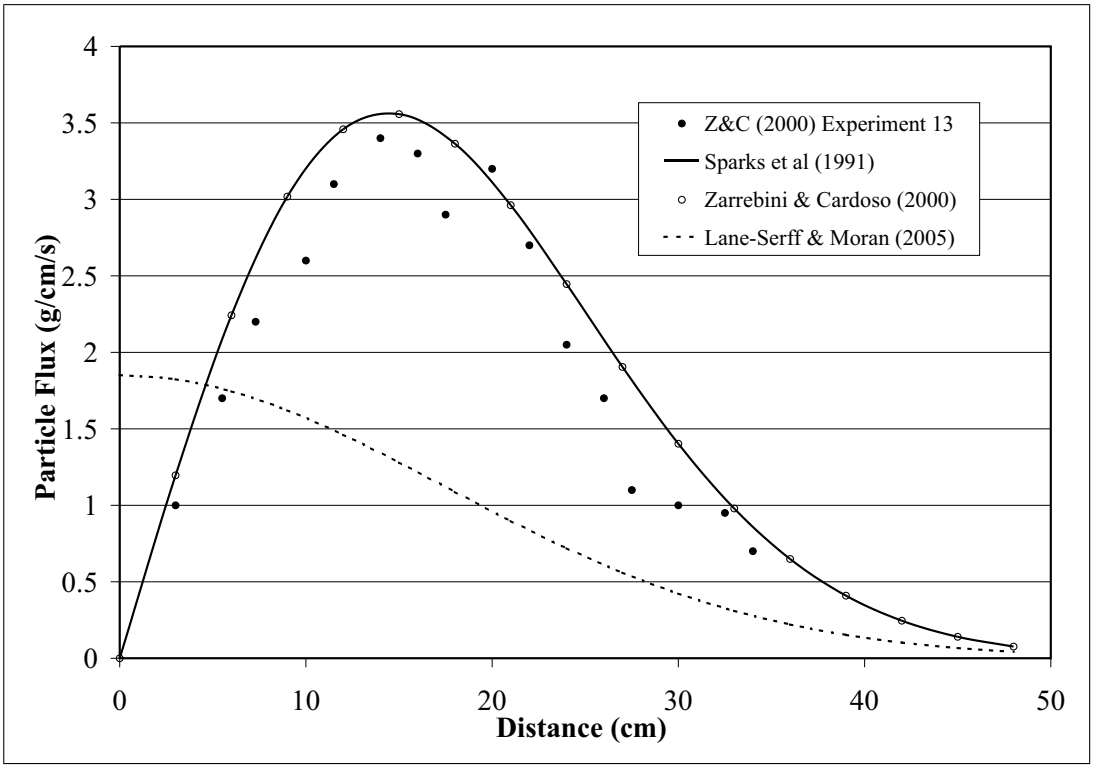

Figure 3.7: *Comparison of theoretical equations of gravity current deposition for experiment 13 (Zarrebini and Cardoso, 2000)*

experiment 13 from Zarrebini and Cardoso (2000) and experiment 1 from Lane-Serff and Moran (2005), respectively. The input parameters for these two experiments are shown in Table 3.1, and the constants used were $\mu_w = 0.01567\ g/(cm\,s)$ and $\alpha = 0.1$.

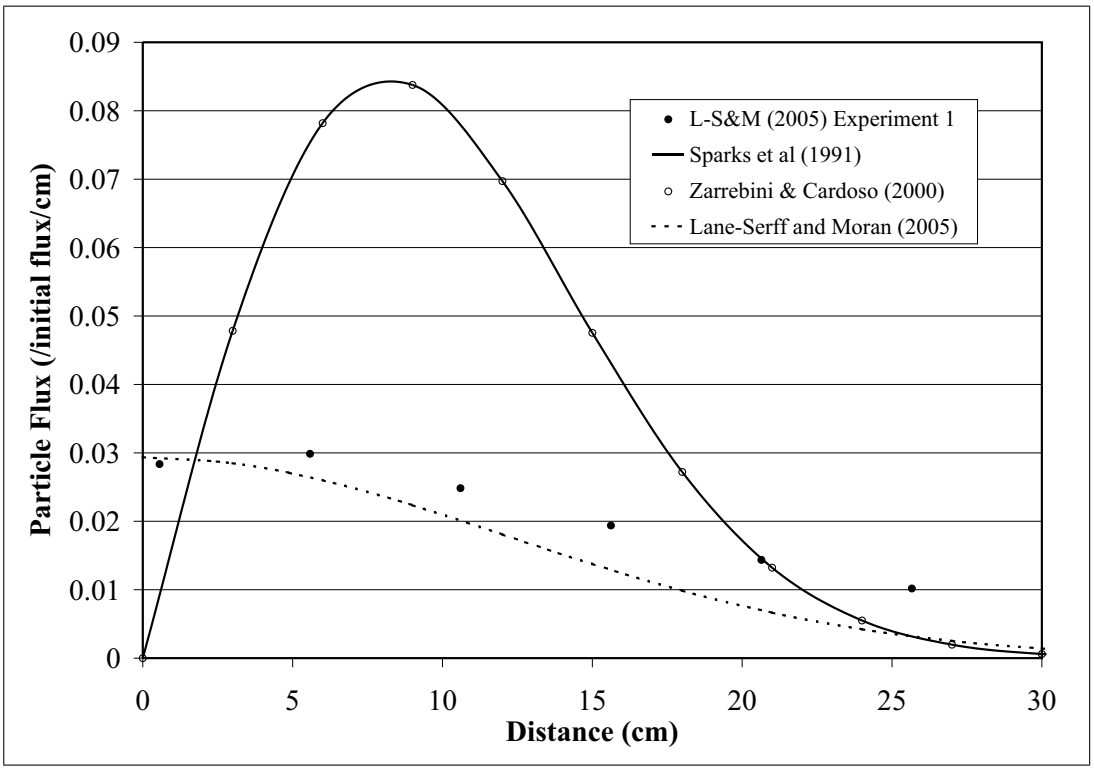

Figure 3.8: *Comparison of theoretical equations of gravity current deposition for experiment 1 (Lane-Serff and Moran, 2005)*

Experiment	Flow Rate Q_0 (cm^3/s)	Buoyancy Flux B_0 (cm^4/s^2)	Particle Diam. d_s (μm)	Particle Dens. ρ_s (g/cm^3)	Ambient Dens. ρ_a (g/cm^3)	Initial Particle Conc. ϕ_0 (g/cm^3)
13	13.52	236.1	65.03	2.47	1.02	0.006
1	13.35	512.7	131.46	2.47	1.04	< 0.01

Table 3.1: *Input Parameters for Experiments in Figure 3.7 and Figure 3.8*

In Figure 3.7, it can be seen that equation 3.58 gives the best fit, whereas equation 3.62 provides the best fit in Figure 3.8. The main difference between the two experiments is the size of particles in suspension, suggesting that equation 3.58 is a better fit for the deposition of smaller particle sizes and equation 3.62 is a better fit for the deposition of larger particle sizes.

Equation 3.62 results in the maximum sedimentation rate from the gravity current occurring at the point where the plume reaches the surface. Lane-Serff and Moran's equation was designed to fit sedimentation rate data for plumes which were not initially vertical and where the plume radius at the surface was larger than or a similar order of magnitude to the spreading radius. In reality, because the tank was shallow, the plume was not rising vertically by the time it reached the surface (Mugford and Lane-Serff, 2007). In Cardoso and Zarrebini's experiments, the plume is vertical and the

particle sizes are smaller, therefore re-entrainment is important and the sedimentation maximum occurs at some distance from the centre of the plume.

For the application to glacial meltwater plumes in the *SedBerg* Model, equation 3.59 from Sparks *et al.* (1991) and Zarrebini and Cardoso (2000) is used. Glacial plumes are dominated by buoyancy forces and as they rise over large depths, they travel approximately vertically by the time they reach the surface, so it is reasonable to assume that the resulting gravity current will behave in the same way as one formed from a vertical plume with the same volume and particle flux at the surface. It should be noted that if the horizontal plume velocity is very large, the plume may reach the surface at an angle from the vertical. In this case, the full equations for a gravity current would need to be solved, instead of simply using equation 3.59.

It is the small particle fractions (silts $< 60\ \mu m$) that spread great distances and contribute to deposition far from the glacier margin: from the comparison between Figure 3.7 and 3.8, equation 3.58 is a better fit for smaller particles. The equations of Sparks *et al.* (1991) have been applied successfully at scales from laboratory experiments to fall-out from volcanic eruption columns, therefore the theory has been shown to be independent of the scale of flow.

Equation 3.59 can be converted from units of mass per area per time to thickness per time, T_{gc}, by dividing by the density of deposited sediment, ρ_{sed}:

$$T_{gc}(r_h) = \frac{W_o \phi_s}{\rho_{sed}} \exp\left[-\xi\left(r_h^2 - R_s^2\right)\right] \tag{3.64}$$

Glacial plumes surface near to the glacier front from which they originated. The glacier front forms a barrier to the Gaussian pattern of sedimentation from the gravity current described by equation 3.64. Since the gravity current spreads radially, the volume of sediment affected will not be very large compared with the total volume deposited. Therefore in the model, the sediment carried beyond the glacier front is neglected. In reality, sediment that reaches the glacier front will either be deposited there or upwelling currents due to frontal melt and tidal currents will cause the sediment to be redistributed over the fjord.

3.4 Summary

The glacial meltwater plume model, *SedPlume*, described in this chapter, utilises an integral model formulation for the conservation of volume (equation 3.19), momentum (equation 3.22), buoyancy (equation 3.26) and sediment mass (equation 3.35) along the path of the plume, which results in a set of coupled first-order differential equations

(Section 3.2.10). An adaptive stepsize fourth-order Runge-Kutta method is applied to find numerical solutions to the system of non-linear first-order ODEs. When the plume reaches the surface, it is treated as a radially spreading surface gravity current, for which exact solutions exist for the mass flux of sediment deposited.

Entrainment is assumed to be proportional to the centreline velocity of the plume along the trajectory. The initial density difference between the plume and the ambient is high in glacial fjords and the sediment load is assumed to be low enough that it has a negligible affect on the buoyancy of the plume. The *SedPlume* Model provides a first order calculation of plume sedimentation from glaciers at the head of fjords, which are not greatly affected by ambient currents. Ambient flow has an important effect on plumes from side-entry glaciers in fjords and glaciers bordering on the open ocean, see Figure 3.1. In environmental settings where ocean circulation plays an important role in the transport of suspended sediment, ambient flow could be included by adjusting V_c in the plume equations with an ocean circulation model providing the initial conditions.

In Chapter 5, the application of the *SedPlume* Model to an Alaskan tidewater glacier is described, as a case study of an environment with abundant glacial meltwater plume deposition. The effects of changing various initial conditions in the *SedPlume* Model on the pattern and rate of sediment deposition are investigated in Chapter 6.

Chapter 4

Case Study for *SedBerg* Model: Kangerdlugssuaq Fjord, East Greenland

4.1 Introduction

Kangerdlugssuaq Fjord is at $68° 00'N$ $31° 45'W$ in East Greenland. The location of the fjord, together with other areas of interest, is shown in Figure 4.1. Kangerdlugssuaq Fjord is chosen as a case study for the *SedBerg* Model discussed in Chapter 2, as it is a good example of an iceberg-dominated sedimentary environment (Dowdeswell *et al.*, 1998; Dowdeswell and Ó Cofaigh, 2002). As with most fjords, there is a mixture of iceberg-rafting and meltwater dispersal of sediment, but the relative effect of iceberg-rafted debris has a much greater impact on sedimentation than the input of sediment from meltwater sources in Greenland fjords (Dowdeswell *et al.*, 2000, 1994b; Syvitski *et al.*, 1996), as illustrated in Figure 1.4.

Kangerdlugssuaq Gletscher drains an area of $51\,027\,km^2$ (Rignot and Kanagaratnam, 2006). Reeh (1984) estimated that the fjord receives $15\,km^3\,yr^{-1}$ of icebergs from Kangerdlugssuaq Gletscher. Rignot and Kanagaratnam (2006) used satellite radar interferometry to measure ice velocity and airborne radio echo sounding to measure ice thickness for the major outlet glaciers around the coast of Greenland. They calculated that the discharge rate of Kangerdlugssuaq Gletscher was almost double Reeh's earlier estimate at $27.8\,km^3\,yr^{-1}$ in 1996. The overall mass balance was a net loss of $5\,km^3\,yr^{-1}$ in 1996, increasing to a loss of $36\,km^3\,yr^{-1}$ in 2005. The ice discharge is much greater than the estimated combined flux of subglacial and supraglacially derived meltwaters, which is approximately $4\,km^3\,a^{-1}$ (Andrews *et al.*, 1994). The total discharge from the Greenland Ice Sheet was found to be $310\,km^3\,yr^{-1}$ by Reeh (1984)

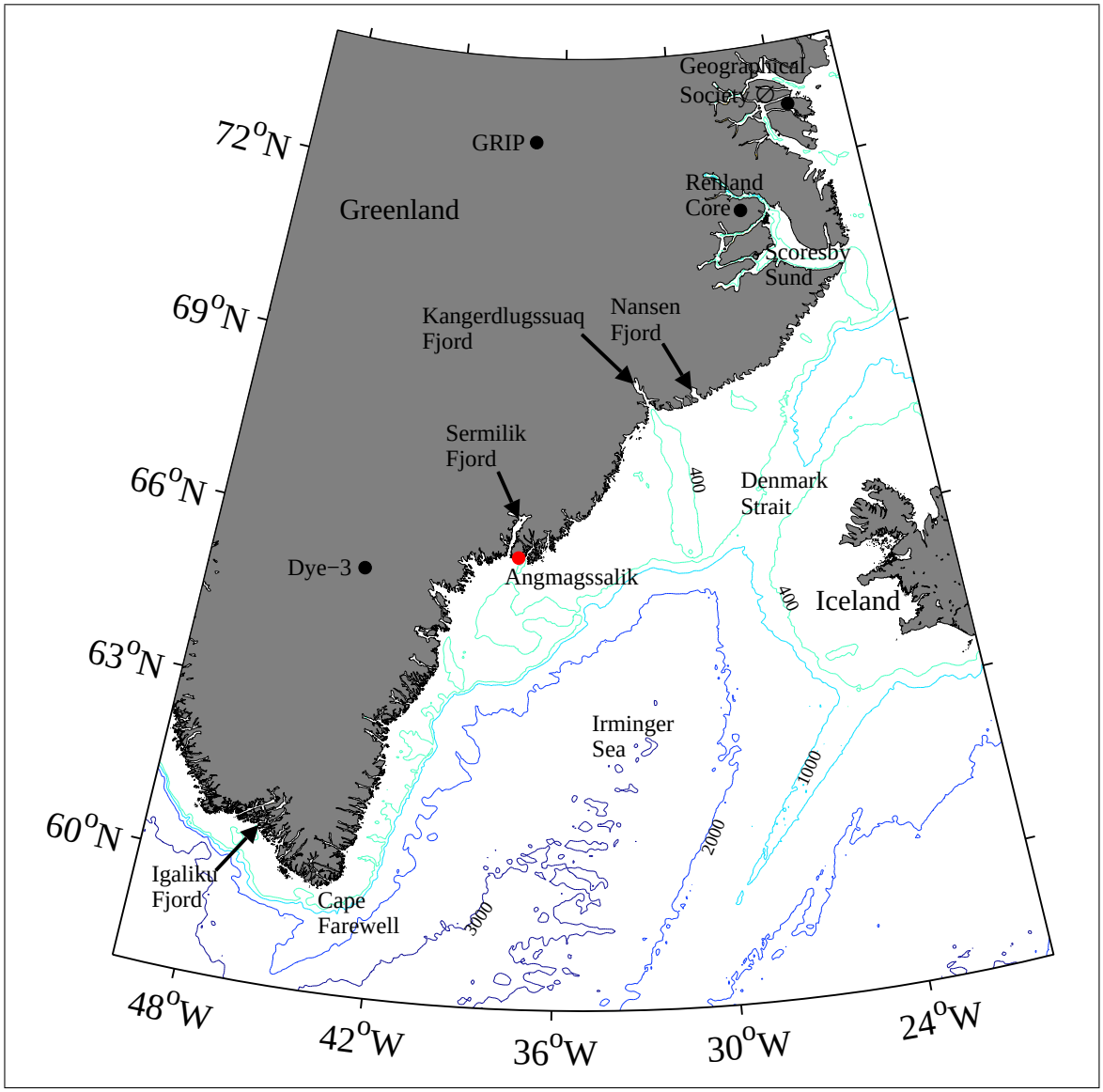

Figure 4.1: *Map of South-East Greenland with labels for the fjord systems mentioned in text, ocean basins, the weather recording station at Angmagssalik and ice core sites (bathymetry in metres).*

in 1984 and 357 $km^3\,yr^{-1}$ by Rignot and Kanagaratnam (2006) in 1996. Therefore, Kangerdlugssuaq Gletscher is one of the major outlet glaciers draining the Greenland Ice Sheet, with a discharge of ∼5–8% of the estimated total iceberg calving flux of Greenland.

There is a reasonably extensive data set for Kangerdlugssuaq Fjord, both from satellite observations and a number of field campaigns to the area. Two satellite images of the fjord in May and August 2002, which highlight the variation in sea ice conditions through an annual cycle, are shown in Figure 4.2.

Ship-based measurements were collected in 1991 aboard the M/V Bjarni Saed-

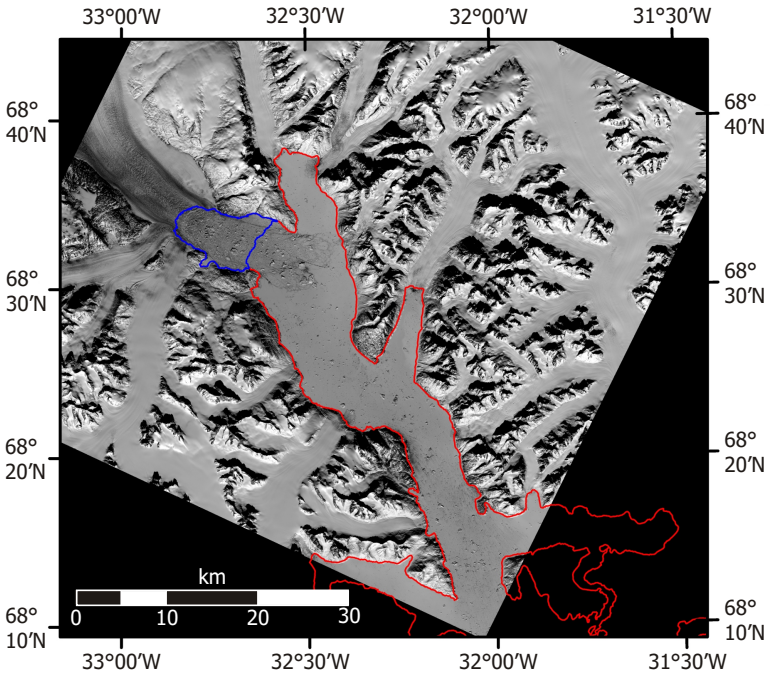

(a)

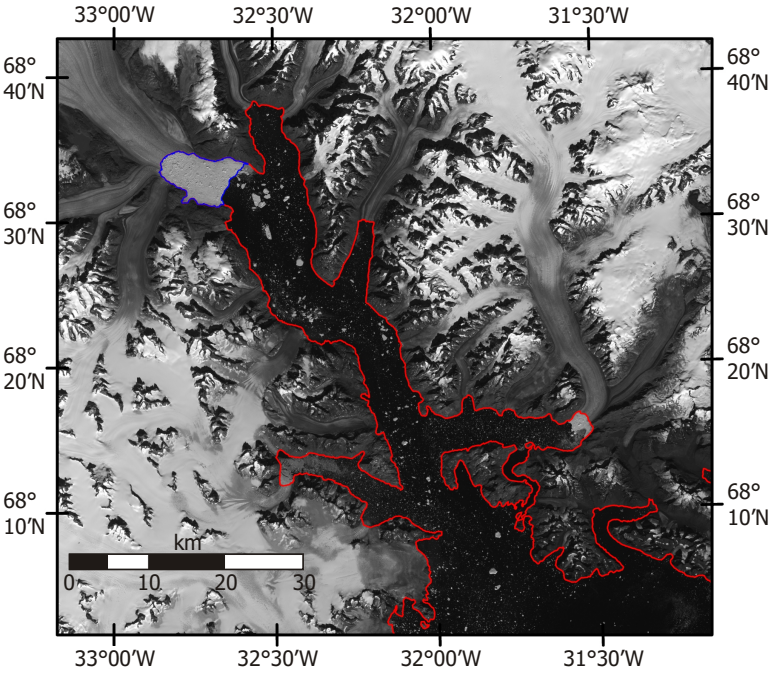

(b)

Figure 4.2: *Satellite images of Kangerdlugssuaq Fjord, with the coastline highlighted in red and the sikussak outline (as of 16th August 2002) in blue (a) 1st May 2002: ASTER (Advanced Spaceborne Thermal Emission and Reflection Radiometer) Nadir-looking, Near Infrared Band 3N, Resolution 15 m (b) 16th August 2002: Landsat Enhanced Thematic Mapper (ETM) Band 8 (Panchromatic, Resolution 15 m). Coastline and sikussak outline vectors courtesy of Toby Benham, SPRI.*

mundsson and in 1993 aboard the C.S.S. Hudson. A map of the fjord, with the tributary fjords and glaciers marked, and the sediment core and water stations from the 1993 cruise labelled, is shown in Figure 4.3(a).

From 30th August to 10th September 2004, I took part in cruise JR106b aboard the R.R.S. James Clark Ross, where a suite of oceanographic and sedimentological data was collected in the fjord and trough system. The cruise tracks from JR106b are shown in Figure 4.3(b). The maps show that there are three tributary fjords leading

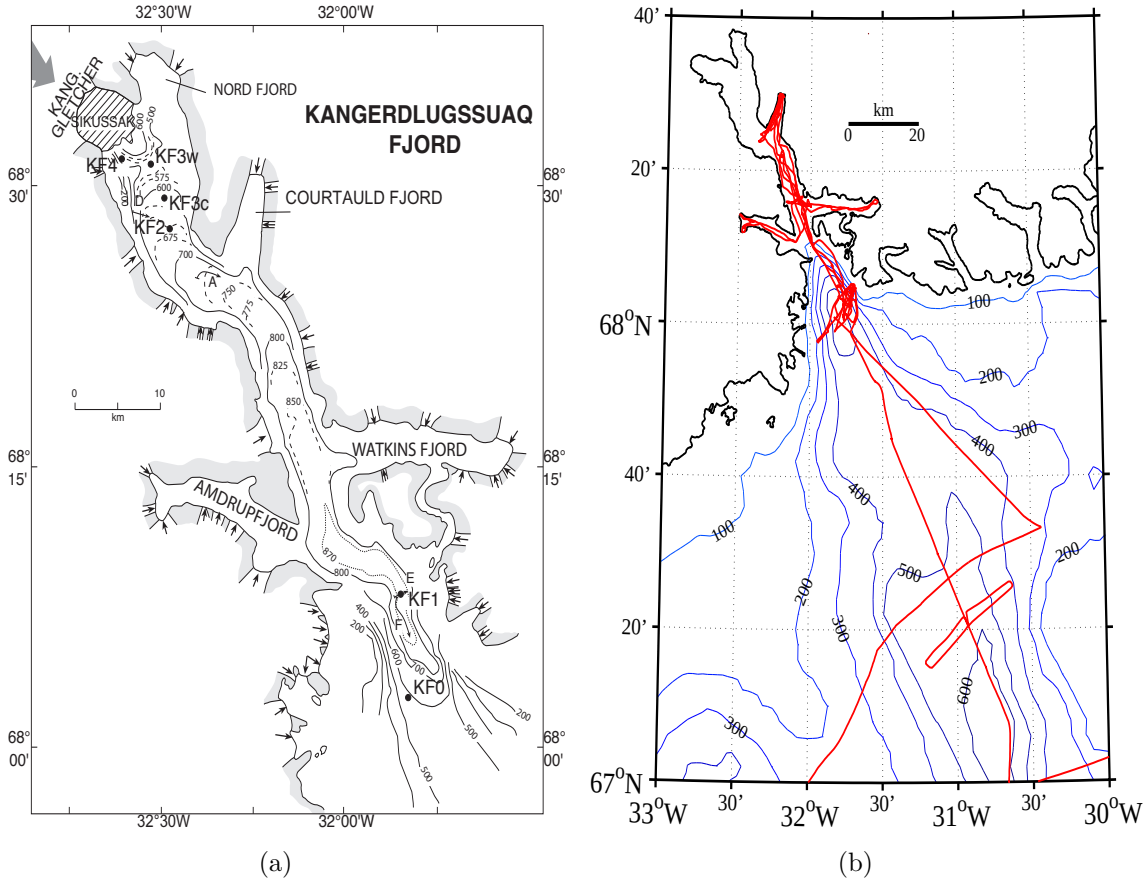

Figure 4.3: *Map of Kangerdlugssuaq Fjord (a) For the study aboard C.S.S. Hudson in September 1993 (Syvitski et al., 1996). Calving tidewater glaciers are indicated by arrows, bathymetry is in metres and the positions of core and CTD stations are labelled and marked with black dots (KF3c is a core-only station and KF3w is a CTD-only station); (b) For cruise JR106b aboard R.R.S. James Clark Ross in September 2004 with the ship tracks marked in red, bathymetry is in metres.*

into the main fjord, which is $\sim 70\,km$ long with an effective width of $5\,km$ (Syvitski *et al.*, 1996). The fjord is orientated in a North-South direction with Kangerdlugssuaq Gletscher, a major outlet glacier, at its northern edge, and to a rough approximation is rectangular in plan view.

4.2 Climatic Conditions During the Past 1500 Years

In this chapter, the sedimentation rate due to iceberg rafting is simulated with the *SedBerg* Model for Kangerdlugssuaq Fjord over the last 1500 years, with climatic, oceanographic and glacial conditions estimated from a mixture of present day measurements and inferences from the sedimentary record. This time span encompasses the Medieval Warm Period (MWP), when the climate was warmer and more stable than today, and the Little Ice Age (LIA), an interval with variable climate interrupted by several cold intervals.

The output of the *SedBerg* Model is compared to the accumulation rate measured from core KF1 collected by Syvitski *et al.* (1996) in 1993 (Figure 4.3(a)). Four cores were collated to form a $17\,m$ long composite section, including a box core, Lehigh core, piston trigger weight core and wide-diameter piston core. The organic carbon and magnetic susceptibility measured in the core, Figure 13 from Syvitski *et al.* (1996), are shown in Figure 4.4. The base of the core was dated at 1430±60 yrs B.P. using

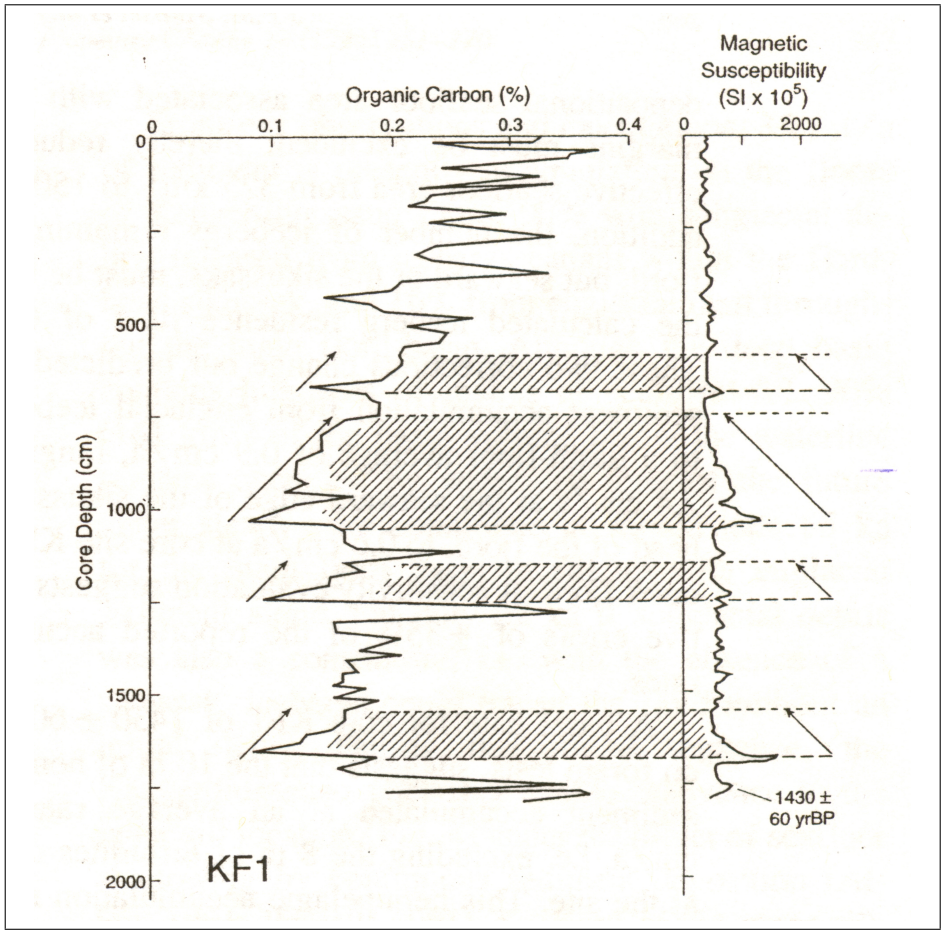

Figure 4.4: *Core KF1 collected in Kangerdlugssuaq Fjord from* C.S.S Hudson *in 1993 (Syvitski et al., 1996, Figure 13). Note the radiocarbon date of 1430*±60 *yr B.P. at the base of the core.*

bulk radiocarbon dating. The shaded areas were attributed to turbidite deposits due to the upward fining of the layers from sand to clay, with the basal sands having a high magnetic susceptibility and low carbon content. Excluding the deposits associated with turbidites, Syvitski *et al.* (1996) found a hemipelagic accumulation rate due to the release of iceberg-rafted debris of $0.7\,cm\,yr^{-1}$. This is comparatively higher than Holocene sedimentation rates of 0.01–$0.03\,cm\,yr^{-1}$ found from ^{14}C measurements of cores collected in Scoresby Sund by Dowdeswell *et al.* (1994a). The magnetic susceptibility at a depth of 1250–1550 cm has an average value slightly higher than the more recent record at a depth of 0–580 cm, suggesting that the average grain size is larger in the older deposits. The organic carbon content is also depleted in the older deposits, suggesting a potentially higher sedimentation rate at this time, given the same supply rate of organic carbon. This is supported by the presence of turbidites in the middle and bottom of the core record, which implies sediment instability caused by higher deposition rates.

The palaeoclimatic record for East Greenland includes sediment cores from two lakes in the outer coastal region of Geographical Society Ø (Wagner *et al.*, 2000), an ice core from the Renland peninsula in Scoresby Sund (Johnsen *et al.*, 1992) and foraminiferal and lithofacies analyses of sediment cores from Nansen Fjord (Jennings and Weiner, 1996). A 50 000 year-long temperature history has been acquired at the Greenland Ice Core Project (GRIP) borehole at the summit of the Greenland Ice Sheet, and a 7000 year history has been collected at the Dye-3 borehole, 865 km farther south (Dahl-Jensen *et al.*, 1998). Past temperatures were inferred from direct measurements of temperature down boreholes at both GRIP and Dye-3. A coupled heat- and ice-flow model along with a Monte Carlo method was used to extract the climatic information from the measured temperature profiles (Dahl-Jensen *et al.*, 1998). The temperature record from the Dye-3 borehole shows the same trend as at the GRIP borehole, but the amplitudes are 50% higher. The climate at GRIP is influenced by maritime air from the North Atlantic as well as air masses from northeastern Canada, whereas the climate at Dye-3 is influenced to a greater degree by the North Atlantic maritime air masses. Further sediment cores have been collected in Igaliku Fjord, South Greenland (Jensen *et al.*, 2004). The locations of these palaeoclimatic records are shown in Figure 4.1.

During the time period from 500 A.D. to the beginning of the MWP at *c.* 770 A.D. a cold and moist climate prevailed. This is referred to as the pre-MWP in this text. The diatom record of the inner Igaliku Fjord indicates cold surface water with extensive fjord-ice formation, which was assumed to be due to increased precipitation rates in South Greenland (Jensen *et al.*, 2004). This corresponds to a period of low borehole temperatures ($0.5°C$ colder then the present) in the GRIP and Dye-3 records (Dahl-Jensen *et al.*, 1998).

Jennings and Weiner (1996) estimated that the MWP in East Greenland occurred between *c.* 730 and 1100 A.D. since the foraminiferal assemblage indicates that Atlantic Intermediate Water (AIW) occupied the Nansen Fjord floor over this period. The data suggest that climatic conditions were stable and warmer than today, with less sea ice in the fjord and reduced offshore pack ice compared to present conditions. Two lithofacies core logs from the inner and outer Nansen Fjord (K13B and K14, respectively), which were published by Jennings and Weiner (1996), are shown in Figure 4.5. The time period that Jennings and Weiner (1996) associated with the

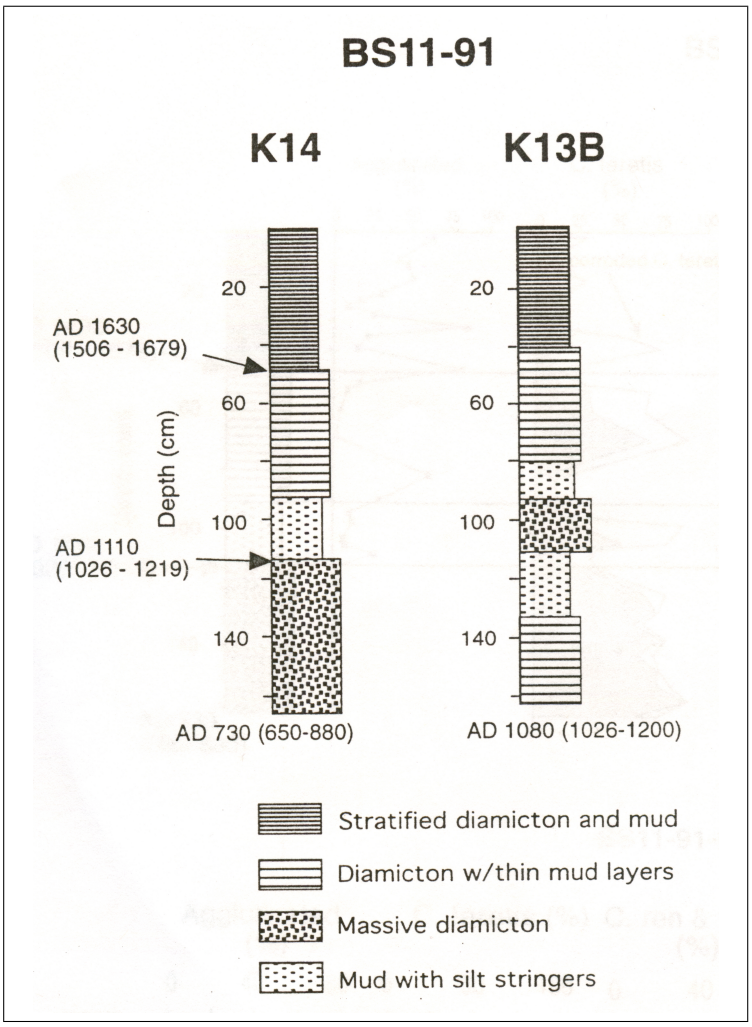

Figure 4.5: *Lithofacies core logs of K13B (inner fjord) and K14 (outer fjord) from Nansen Fjord, with calibrated radiocarbon dates (one sigma errors in parentheses) (Jennings and Weiner, 1996, Figure 3).*

MWP corresponds to a layer of massive diamicton in the core from the outer part of Nansen Fjord (K14). They attributed this to sediment accumulation by continuous iceberg-rafting in a moderate sea-ice environment, which led to higher deposition rates than that during the subsequent intervals.

The MWP was recognised to extend for a longer period from *c.* A.D. 800 to 1250 by Jensen *et al.* (2004) in Igaliku Fjord, South Greenland, with cooling events between *c.* A.D. 960 to 1140. The MWP was only vaguely recorded in the Renland ice core isotopic record (Johnsen *et al.*, 1992), but well expressed in the palaeotemperature record from the GRIP borehole, indicating temperatures *c.* 1000 A.D. were $1°C$ warmer than the present (Dahl-Jensen *et al.*, 1998). In the pollen record from the lake sediments in Geographical Society Ø, a period of warming is indicated from *c.* A.D. 1100 to 1500, slightly delayed from the MWP (Wagner *et al.*, 2000).

The transition between the MWP and LIA is referred to as the Transition Period (TP) in this work. This time period in Igaliku Fjord was characterised by fluctuating climatic conditions from *c.* A.D. 1245 to 1580 (Jensen *et al.*, 2004). Jennings and Weiner (1996) found the interval between *c.*A.D. 1270 to 1400 recorded cold intervals in Nansen Fjord, with the coldest part of the record at *c.* A.D. 1370. This is followed by a warm interval beginning between *c.* A.D. 1370 and 1470, culminating at *c.* A.D. 1470 and declining towards the onset of the LIA in *c.* A.D. 1630. Low values for biogeochemical parameters starting at *c.*A.D. 1200 in the lake sediment core record at Geographical Society Ø signify a cooling period, coinciding with the end of the MWP (Wagner *et al.*, 2000).

The LIA was a period of extremely variable and rapidly changing climate with similar conditions to those of the present day at times, which were punctuated by short spells of severely cold conditions. Jennings and Weiner (1996) interpreted the LIA to extend from *c.* A.D. 1630 to 1900 in Nansen Fjord. In inner Igaliku Fjord, the most extensive sea ice cover occurred in the period *c.*A.D. 1700 to 1830 (Jensen *et al.*, 2004). The sediment core record at Geographical Society Ø shows evidence of cool conditions between *c.*A.D. 1700 to 1900 (Wagner *et al.*, 2000), which are mirrored in the Renland ice core record (Johnsen *et al.*, 1992). A simultaneous temperature decrease is indicated in central Greenland by the GRIP borehole record, which suggests two temperature minima, with temperatures $0.5°C$ and $0.7°C$ colder than present, at 1550 and 1850 A.D. (Dahl-Jensen *et al.*, 1998). This cooling has been traced back to reduced summer insolation (Overpeck *et al.*, 1997).

Following the LIA, the GRIP borehole record shows temperatures reached a maximum around A.D. 1930, then decreased over the last decades, although these measurements are subject to high uncertainties (Dahl-Jensen *et al.*, 1998). Wagner *et al.* (2000) observed an increase in the dwarf shrub pollen percentage and a weak rise in most biogeochemical parameters at the sediment surface of both lakes at Geographical Society Ø, which indicate a recent warming.

Comparing the cores collected in Nansen Fjord by Jennings and Weiner (1996) (Figure 4.5) to KF1 core from Kangerdlugssuaq Fjord (Figure 4.4), suggests that the

larger mean grain size (from magnetic susceptibility) and the higher sedimentation rate (lower organic carbon content and presence of turbidity currents) corresponds to the MWP interval, from a depth of approximately 1550 cm to a point between 1250 cm and 580 cm where the three turbidite layers interrupt the record. This signifies that the deposition from the base of the core to a depth of 1680 cm corresponds to the interval 570–730 A.D., the pre-MWP, with a sedimentation rate of 0.69 $cm\,yr^{-1}$. Assuming that the first turbidite layer occurs at the beginning and the final one indicates the end of the MWP, the accumulation rate during this interval is calculated as 1.2 $cm\,yr^{-1}$, so double the pre-MWP rate. The upper section of the core would then encompass the TP and LIA to the present day. If a constant sedimentation rate is assumed during this time, a deposition rate of 0.65 $cm\,yr^{-1}$ is found.

4.3 Model Input Parameters

4.3.1 Position of Calving Front

In terms of the timescale of the model (the last 1500 years), the glacier front is assumed to have been at approximately the same position as in 1993 when the cores were collected (Syvitski *et al.*, 1996). Csathó *et al.* (1999) compared the position of the calving front of Kangerdlugssuaq Gletscher in 1933 (from a map based on aerial photographs), with that on 23rd June 1966 and 24th September 1966 (from satellite data). They reported a retreat of 1–2 km from 1933 to 1966. However, they did not quantify the distance of retreat since the glacier front also retreated slightly in September 1966 compared to June 1966, demonstrating a seasonal effect, and in addition the original aerial photographs on which the 1933 map was based were not available to confirm that the retreat was real. Thomas *et al.* (2000) found that the calving front, observed from satellite images in 1966, 1988, 1992 and 1995/6, and laser surveys in 1993 and 1998, has remained in approximately the same position, probably pinned at the edge of a bathymetric slope into deeper water seaward of this location. During the winter of 2004-5, Howat *et al.* (2007) observed a 5 km retreat, much greater than the previously observed seasonal fluctuations of 1–2 km. The recent retreat of Kangerdlugssuaq Gletscher may be a response to late 20th century climate warming (Howat *et al.*, 2007).

4.3.2 Calving Rate

The rate of calving of icebergs from Kangerdlugssuaq Gletscher will have an important effect on the sedimentation rate. More detail on the mechanics and theories of iceberg

calving is found in Section 2.2. There have been a number of studies of the dynamics of Kangerdlugssuaq Gletscher and calving rates have been measured directly. These observations are used to estimate the calving rate for the last 1500 years, which is input into the *SedBerg* Model. This section will describe the observations, which demonstrate that in recent times Kangerdlugssuaq Gletscher has undergone extreme dynamic changes.

Kangerdlugssuaq Gletscher has been observed to have had a stable speed from 1962 until 1996, when it underwent rapid thinning of 50 metres over the front $5\,km$ of the glacier (Rignot *et al.*, 2004; Thomas *et al.*, 2000). Since then it has undergone dramatic and rapid changes, accelerating by 210% between 2000 and 2005, to a flow velocity of 13 to $14\,km\,yr^{-1}$ at the calving front (Rignot and Kanagaratnam, 2006). The acceleration increased the magnitude of the negative mass balance (or difference between mass gained and mass lost from the glacier) from -5 $km^3\,yr^{-1}$ in 1996 (Rignot *et al.*, 2004) to -36 $km^3\,yr^{-1}$ in 2005 (Rignot and Kanagaratnam, 2006).

There have been a number of estimates of ice discharge, utilising surface elevation and velocity data to infer the calving rate. Reeh (1984) estimated the calving flux to be $15\,km^3\,yr^{-1}$ by assuming that the ice sheet was in balance with the measured accumulation rate distribution. The accumulation rate (or precipitation) distribution was obtained from firn stratigraphic methods (pit studies, ice cores) and precipitation records from coastal stations. Melting or ablation rates were estimated from scattered measurements in the ablation zone and from computed relationships between ablation and altitude at different latitudes, as derived by Braithwaite (1980).

Dwyer (1995) used Landsat data to measure surface velocities and retreat rates of East Greenland glaciers from 1978-1991. He found that Kangerdlugssuaq Gletscher retreated by $620\,m$ during this time with a velocity of $5\,km\,yr^{-1}$ in 1988.

Csathó *et al.* (1999) used Declassified Intelligence Satellite Photographs (DISP) from 1966 to find the velocity of Kangerdlugssuaq Gletscher at that time. They found a centreline velocity of $6 \pm 0.33\,km\,yr^{-1}$ and concluded that this was not significantly faster than the velocity found by Dwyer (1995) for 1988, due to inclusion of points in the slower moving glacier margins in the latter.

Thomas *et al.* (2000) reported a substantial thinning ($50\,m$ in the front $5\,km$) of Kangerdlugssuaq Glacier between 1993 and 1998 from airborne laser altimetry. From the measured ice velocities in 1966, 1988, 1996 and 1999, they estimated the ice flux to be 13–14 $km^3\,a^{-1}$ (no measurement was reported in 1998 after the thinning, which was assumed to occur between 1996 and 1998). By balancing total net upstream snow accumulation with ice discharge (excluding the point in 1998 after the substantial thinning) they estimated a flux of $17\,km^3\,a^{-1}$ in 1966, 1988, 1995-1996 and 1999, and a flux of $23\,km^3\,yr^{-1}$ from 1996-1998.

A more recent study was performed by Rignot and Kanagaratnam (2006), who used satellite synthetic aperture radar interferometry to measure ice velocity and airborne radio echo sounding to measure ice thickness. They calculated that the discharge rate was $27.8\,km^3\,yr^{-1}$ in 1996. Howat *et al.* (2007) reported that between 2004-2005 the glacier underwent substantial thinning of at least $40\,m$ extending $40\,km$ inland and acceleration of $\sim 80\,\%$ from observations of surface elevation and velocity derived from satellite data. From July 2005 to July 2006 there was a slight deceleration from $12\,km\,yr^{-1}$ to $10.6\,km\,yr^{-1}$ at a distance of $10\,km$ from the glacier front, with the acceleration propagating inland, or upstream. These satellite data demonstrate that Kangerdlugssuaq Gletscher is very dynamic and is capable of extremely rapid acceleration, deceleration and thickness changes, with associated variation in calving rate. However, it is not clear from the data whether the recent changes have been due to external atmospheric/oceanic forcing or to internal glacier dynamics.

The measured calving rates can be compared to empirical calving relations. The calving relation in equation 2.4, which was developed by Pelto and Warren (1991), is dependent on water depth, and was estimated from observations of 22 glaciers in Alaska, West Greenland and Svalbard. At the front of Kangerdlugssuaq Gletscher, the water depth has been estimated to be between 450–650 m, with an ice front height of $\sim 650\,m$ (Syvitski *et al.*, 1996). Substituting a water depth of $550\,m$ into equation 2.4, results in a calving velocity of $4650\,m\,yr^{-1}$. If the width of the glacier is taken to be $4.6\,km$ and the height of the ice front is $650\,m$, this gives a calving flux of $13.9\,km^3\,yr^{-1}$, which agrees well with the observed fluxes. It should be noted that Kangerdlugssuaq Gletscher is thought to have a floating tongue (Howat *et al.*, 2007), but the Pelto and Warren (1991) calving relation was constructed for grounded tidewater glaciers and does not take into account the further increase in calving rate that is likely to occur if the ice front thins and becomes fully buoyant.

At glaciers with floating tongues, seasonal oscillations in the calving rate have been observed; for example at Jakobshaven Glacier in West Greenland, where the summer calving rates were six times those in winter for the time period 1962-1996 (Sohn *et al.*, 1998). In Ellesmere Island, summer calving rates have been observed to be 2-8 times higher then winter rates (Williamson *et al.*, 2007). The controlling factors on the calving rate are thought to be the presence of shorefast sea ice in winter, which exerts a back pressure on the calving front and hence slows down the iceberg production rate, and meltwater production in summer, which lubricates the glacier bed causing higher velocities and calving rates. In Kangerdlugssuaq Fjord, shorefast sea ice occupies the fjord during the winter months from October to May (Syvitski *et al.*, 1996), as seen in the satellite image in Figure 4.2(a). To investigate the effect of this seasonal variation in the calving rate, the two extreme cases, where calving occurs only in the summer

months and where the calving rate is constant all year round are examined with the model. In addition, the Jakobshaven-type scenario is also explored where the summer calving rate is six times the winter rate.

There is a sikussak present in front of Kangerdlugssuaq Gletscher, which is a nearly solid mass of icebergs, bergy bits and shorefast multi-year sea ice, highlighted with a blue outline in the satellite images of the fjord in Figure 4.2. The presence of a sikussak traps icebergs for a period of time and subglacial debris frozen within the iceberg is released before they drift through the fjord (Smith and Andrews, 2000; Syvitski *et al.*, 1996) suppressing sedimentation by iceberg-rafting. Dowdeswell *et al.* (2000) proposed that extensive sikussak formation during colder climatic intervals led to the deposition of fine-grained laminated glacimarine sediment in Scoresby Sund and Nansen Fjord in East Greenland (see Figure 4.1). The presence of a sikussak trapped icebergs, suppressing sedimentation by iceberg-rafting. Therefore, during these intervals the dominant source of sediment was from turbid meltwater plumes, and the variation of the meltwater flux over time resulted in the laminated units observed in cores.

The sikussak in Kangerdlugssuaq Fjord has been observed to disintegrate very rapidly, and it is thought that this occurs periodically on a decadal timescale (Syvitski *et al.*, 1996), releasing a large number of icebergs at one time. The consequent release of back pressure when the sikussak breaks up may also cause an increase in the calving rate. A sikussak has also been observed to form for short periods of time at other glaciers in the Kangerdlugssuaq Fjord system, for example there was a sikussak in front of Watkins Gletscher in 2002, as seen in the Landsat image Figure 4.2(b), but it was not present during the *R.R.S. James Clark Ross* cruise in 2004.

In 2004, a series of MODIS images recorded a rapid break up of the sikussak in front of Kangerdlugssuaq Gletscher, which occurred over a period of a few weeks, as shown in Figure 4.6.

Therefore, four different scenarios for seasonal variation of calving rate are investigated with the *SedBerg* Model:

a. Calving only occurs during the summer months.
b. The calving rate is constant all year round.
c. Summer calving rates are six times those in winter.
d. Icebergs are trapped until the sikussak breaks up, so 10 years' worth of icebergs are released over 28 days from 17$^{\text{th}}$ August to 13$^{\text{th}}$ September.

The aim is to model sedimentation from iceberg-rafting over the last 1500 years. Kangerdlugssuaq Glacier may have undergone cycles of thinning and increased calving flux during this time, as occurred in 1996-1998 and 2000-2005. These observed dynamic changes may be only a recent phenomenon, since the calving rate was observed to be

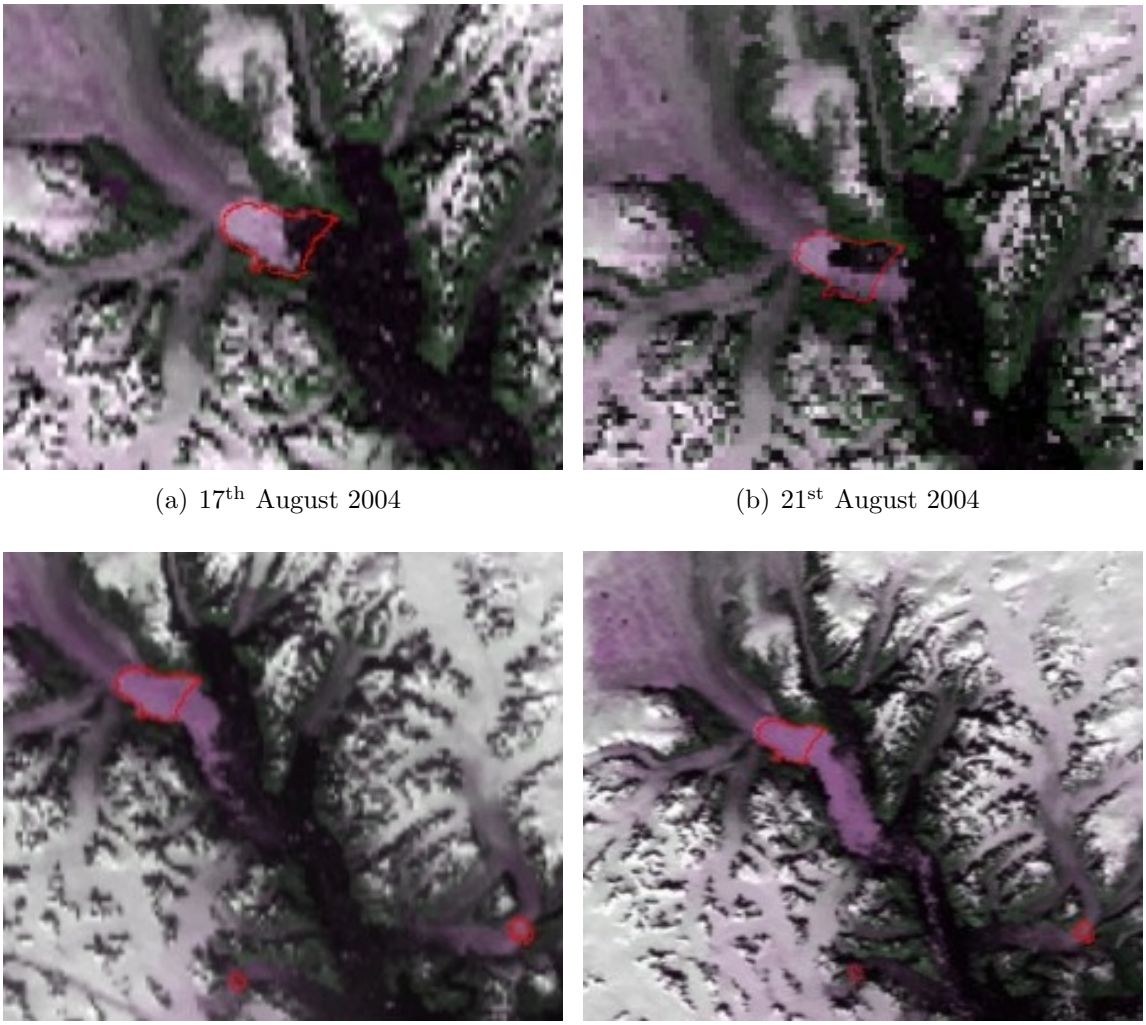

(a) 17th August 2004

(b) 21st August 2004

(c) 29th August 2004

(d) 6th September 2004

Figure 4.6: *Sequence of false colour composite MODIS (Moderate Resolution Imaging Spectroradiometer) satellite images during a break up of the sikussak, with 2002 extent shown in red.*

reasonably stable, at about 13–15 $km^3\,yr^{-1}$, for over 40 years previous to this (Reeh, 1984; Thomas *et al.*, 2000). Therefore, the calving rate chosen as representative of an average value over the last 1500 years is 15 $km^3\,yr^{-1}$.

In practice, the actual volume of model icebergs calved is less than the volume flux specified. This is because the iceberg size distribution is restricted or "censored" so that the iceberg length, width and height do not exceed a certain threshold - this will be discussed in Section 4.3.3. Therefore, the specified volume flux must be greater than the volume flux produced. Since a random number generator is used to calculate the iceberg size, there is no way of calculating how much greater the specified volume flux needs to be than the volume flux produced. So, for each iceberg size distribution, the iceberg calving part of the model is run without the moving and melting routines,

in order to find the value of the specified volume flux which produces the volume flux required.

There are also differences in the ratio of specified volume flux to the actual volume flux produced by the model for each of the seasonal calving rate variation scenarios. The seed for the random number generator, from which the calving probability is calculated in each calving time step, is the same for each seasonal calving rate variation scenario, so this is not the source of the difference. Variation in the actual volume flux produced is caused by different values of the calving step size (in winter and summer) in the different scenarios. Since testing for an iceberg calving event occurs at intervals as close as possible to the calving time step, Δt_c, but in multiples of the moving and melting time step, Δt_m, (Section 2.5.1) this leads to variation in the number of calving time steps per year, and therefore the number and volume of icebergs produced.

4.3.3 Iceberg Size Distribution

As discussed in Section 2.3, the iceberg size, L_i, is calculated from the log-normal distribution, where the iceberg volume is taken to be L_i^3, the width:length ratio is 1:1.62 and the width:thickness ratio is 1:1 (equations 2.10–2.12).

The measurements of iceberg size distribution collected by Dowdeswell *et al.* (1992) in Scoresby Sund, 400 km north of Kangerdlugssuaq Fjord in East Greenland, are the geographically closest available. In addition, the glaciological setting is very similar, with the fast-flowing outlet glacier Daugaard Jensen Gletscher being the dynamic equivalent of Kangerdlugssuaq Gletscher. The iceberg 'size' in this case was the width measured using radar, so depending on the side of the iceberg facing the ship, both length and width would have been measured. Figure 2.3 shows all the iceberg width data collected from the Scoresby Sund fjord system with a log-normal probability density function fitted to it. The log-normal distribution is described in Section 2.3, with the probability density function calculated using equation 2.7. A log-normal distribution is fitted using the maximum likelihood estimators calculated from the iceberg width (L_i) data measured in Scoresby Sund. The following parameters are found: $\mu = 4.835$ and $\sigma = 0.80$ with $E(L_i) = 173.3\,m$ and $SD(L_i) = 164.2\,m$.

The mean, or expected value of the iceberg keel depth in Kangerdlugssuaq Fjord was estimated by Syvitski *et al.* (1996) to be around 250 m, but the iceberg size distribution was not measured. Therefore, a second iceberg size distribution is used, which has the same standard deviation as the log-normal fit to the Dowdeswell *et al.* (1992) data, but with an expectation, or mean, of 294 m, which corresponds to a mean width/thickness of 250 m. In the absence of more observations, both of these size distributions are used as potential representations of the actual iceberg size distribution

in Kangerdlugssuaq Fjord over the last 1500 years and are shown in Figure 4.7.

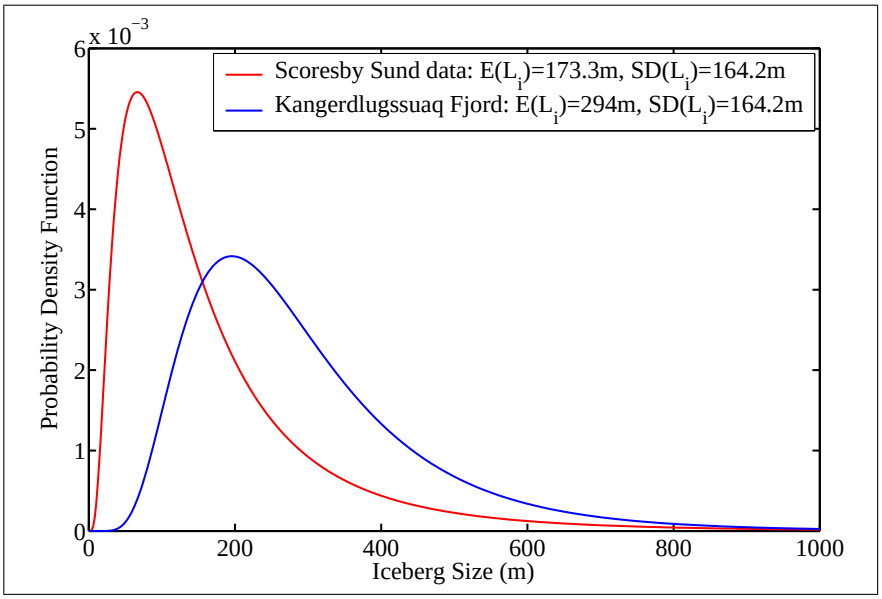

Figure 4.7: *Iceberg size distributions, L_i, used for modelling Kangerdlugssuaq Fjord: red line is calculated from log-normal fit to Scoresby Sund observations ($\mu = 4.835$ and $\sigma = 0.80$) and blue line is assumed size distribution for Kangerdlugssuaq Fjord with mean of $294\,m$ and standard deviation equal to Scoresby Sund log-normal fit ($\mu = 5.548$ and $\sigma = 0.521$).*

The iceberg thickness is 'censored', so that if it exceeds the glacier thickness ($650\,m$), it is set to equal this value instead. The iceberg length and width are also 'censored' so that they do not exceed $2000\,m$, and if a larger iceberg is produced by the model, its length and width are adjusted to equal this maximum value instead.

4.3.4 Iceberg Sediment Concentration

There are few observations of the debris content of icebergs. However, Dowdeswell (1986) measured the sediment concentration of the 2–3 m thick debris-rich basal layer from a Baffin Island tidewater glacier to be on average 53 % by mass. This value was applied to icebergs in Kangerdlugssuaq Fjord by Syvitski *et al.* (1996). If the density of sediment grains $\rho_s = 2700\,kg\,m^3$ and the density of ice $\rho_i = 917\,kg\,m^3$, this is equivalent to 28 % by volume. For the same Baffin Island glacier, Dowdeswell (1986) measured the debris content of englacial ice, which forms the bulk of the glacier thickness, to be on average 0.25 % by mass, or 0.085 % by volume. This value was also applied to icebergs in Kangerdlugssuaq Fjord by Syvitski *et al.* (1996). Syvitski *et al.* (1996) observed two overturned icebergs in Kangerdlugssuaq Fjord with visible basal layers, from which they estimated the basal layer thickness to be $3\,m$.

Certain circumstances lead to the removal of basal debris from the glacier or icebergs, preventing the long-distance rafting of sediment. At floating glacier tongues, the

base of the glacier is exposed to sea water, which melts away the layer of basal ice prior to icebergs calving. Therefore, under cold climatic conditions when glacier tongues reach floatation, icebergs would contain only englacial ice with low sediment concentration, hence reducing the distal deposition rate Reeh (2004); Reeh *et al.* (1999).

The sikussak in front of Kangerdlugssuaq Gletscher, shown in Figure 4.2, has an important effect on the release of debris from icebergs. Icebergs reside in the sikussak for some time after they have been calved and basal sediment frozen within the icebergs has usually completely melted away by the time they escape to transit out of the fjord (Dowdeswell *et al.*, 1998). Dwyer (1993) found from satellite observations that the largest icebergs are trapped in the sikussak for upwards of two years. He also found that there had not been significant fluctuations in the dimensions of the sikussak in the 20 years of remote sensing that was available from 1973-1993. Syvitski *et al.* (1996) concluded, from a comparison of observations and rough estimates of iceberg-rafted sedimentation rates, that the majority of subglacial debris frozen within icebergs had indeed melted out in the sikussak zone during the last 1500 years. However, since they observed icebergs containing a basal layer in the fjord, clearly some icebergs transit across the sikussak in a short enough time to still contain basal debris.

Therefore when simulating intervals with a sikussak in front of Kangerdlugssuaq Gletscher, the model is run for two scenarios. A 'no-basal' run is performed assuming that icebergs on the seaward side of the sikussak contain only englacial sediment with a concentration of 0.085 % by volume. A 'basal' run is also carried out for the case when some icebergs do contain the basal ice layer, with the proportion calculated using equation 2.82. To calculate the sedimentation rate over a time period, the proportion of time that icebergs pass through the sikussak before all their basal ice has melted is estimated, and the appropriate fractions of the two modelled sedimentation rates are summated.

Syvitski *et al.* (1996) found that the suspended particulate matter in the iceberg melt zone consisted of 30–50% coarse silt and fine sand mineral grains with diameters 40–200 μm. Floc camera measurements were collected and these suggested that finer particles flocculated to sizes in excess of 1 mm. They calculated a population settling velocity of the order of 200 m/day. Therefore, the time taken for sediment grains melted out of icebergs to reach the fjord floor will be 1–4 days, depending on the water depth and the depth of the iceberg. The measured sediment concentration in the water column was well mixed and reasonably uniform across-fjord, decreasing along-fjord. The dispersion distance, described in Section 2.7, is set at 2 km either side of the maximum and minimum in the y direction and 4 km either side of the maximum and minimum in the x direction. Once the sediment is deposited, it is assumed to have a density of 1700 $kg\,m^{-3}$ (Syvitski *et al.*, 1996). This results in thicker sediment

deposits than if the density of the deposit was the same as the individual grain density ($\rho_s = 2700\,kg\,m^3$).

4.3.5 Seawater Temperature

The East Greenland Current (EGC) is a southward flowing current which follows the shelf break off the coast of Greenland. The Irminger Current (IC) flows northwards from the Atlantic and meets the shelf break near the Kangerdlugssuaq Trough, where it bifurcates so that one branch travels anticlockwise to join the EGC, while the other carries Atlantic water to the north of Iceland. These ocean currents in the area south-east of Greenland and west of Iceland are shown in Figure 4.8. Water temperatures in

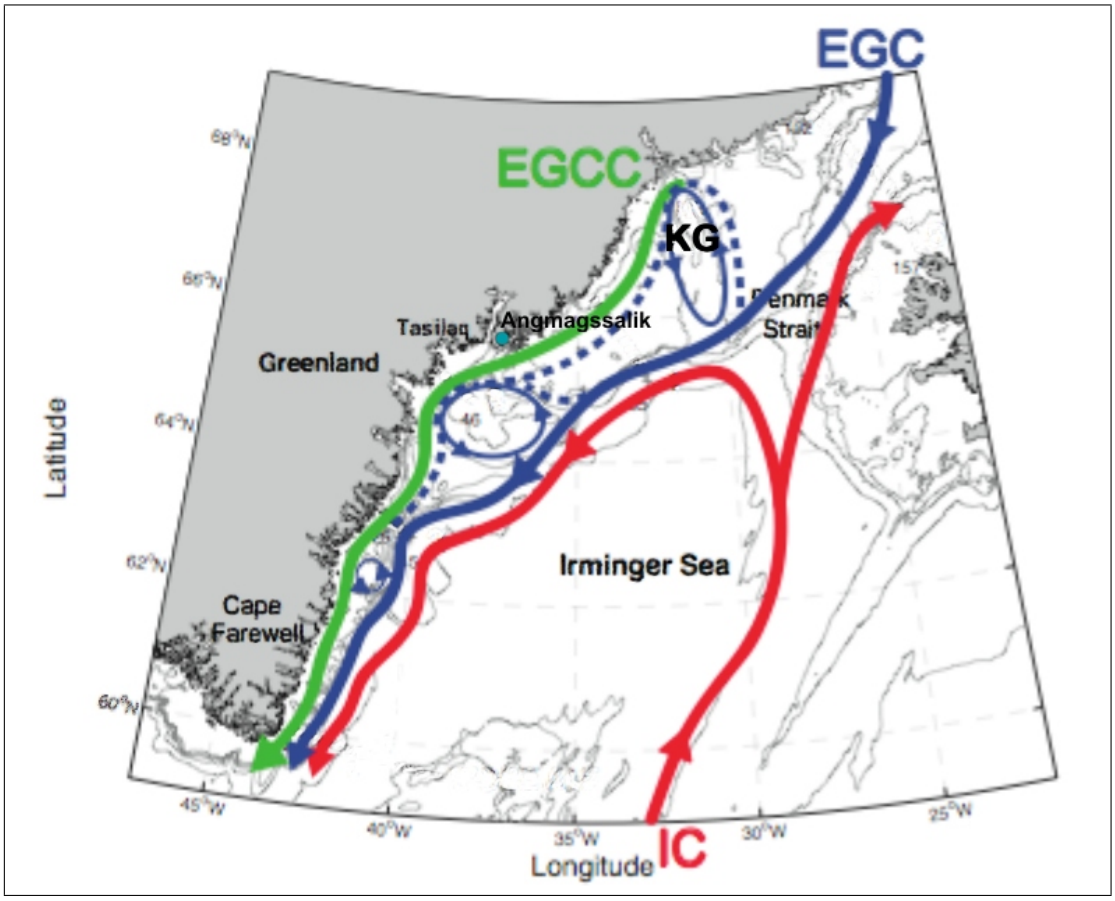

Figure 4.8: *Surface circulation schematic for the summertime boundary current system in the Irminger Sea, with the Kangerdlugssuaq Trough labelled KG. Solid lines show observed paths of the East Greenland Current (EGC), East Greenland Coastal Current (EGCC) and the Irminger Current (IC), while dotted lines refer to intermittent flow paths induced by variation in the strength of the stratification of the EGC and the intensity of the wind forcing (Sutherland and Pickart, 2007, modified from Figure 16).*

Kangerdlugssuaq Fjord are strongly dependent on the relative strength of flow of water masses in the EGC, since the deep trough provides a bathymetric pathway from the

shelf break to the fjord, as shown in Figure 4.8, where the trough is labelled KG. The EGC flows southward along the shelf break carrying with it both Polar Water (PW) and Atlantic Intermediate Water (AIW). Glaciers and icebergs contribute meltwater to the EGC as it progresses along the East Greenland coast. The Irminger Current (IC) is a relatively warm current ($8°C$) and since it meets the EGC where Kangerdlugssuaq Trough meets the shelf break, this is another source of temporal variation in the water masses present in Kangerdlugssuaq Fjord.

It has been theorised that, at times, the East Greenland Current (ECG) diverges at the shelf break of Kangerdlugssuaq Trough and follows the isobaths of the trough into the fjord (Sutherland and Pickart, 2007). Part of the EGC then follows the coast of Greenland to the south of the fjord, forming the East Greenland Coastal Current (EGCC), as shown in Figure 4.8. As mentioned previously, there is high temporal and spatial variability in the constituent water masses carried by the EGC and the strength of the water flux into the fjord. The main influences on this temporal and spatial variability are likely to be the strength of the stratification of the EGC and the intensity of the wind forcing, together with the subsequent interaction with the complex bathymetry in the region (Sutherland and Pickart, 2007).

Conductivity-Temperature-Depth (CTD) profiles were collected during scientific cruises to Kangerdlugssuaq Fjord in 1993 and 2004. The positions of the CTD stations occupied in 1993 are shown in Figure 4.3(a) and the positions of the CTD stations collected in 2004 are shown in Figure 4.9.

A selection of potential temperature profiles collected in 1993 and 2004 are shown in Figure 4.10. Potential temperature is the temperature that a parcel of water at pressure P would acquire if it were to be adiabatically brought to a standard reference pressure P_0, which in this case is $1\,bar$. It is more important that potential temperature is used when comparing deep ocean temperatures (at depths greater than $1000\,m$), although it is used here for correctness.

The temperature profiles shown with the same colour in Figure 4.10 were collected from approximately the same position in the fjord in both 1993 and 2004, where data from 1993 are shown with dotted lines, and data from 2004 are shown with solid lines. Furthest away from the glacier front are Station 3 in 2004 and KF0 in 1993. It can be seen that the surface water was up to $4°C$ warmer in 2004 compared to 1993 at this point. Moving towards the glacier front, Station 12 in 2004 and station KF1 in 1993 also show pronounced warming of the surface water in 2004. The two pairs of measurements nearest the glacier show a smaller difference but there is still a warming from 1993 to 2004 of approximately 1–$2°C$. The mean potential temperature profiles from the data collected in the fjord in 1993 and 2004, along with $\pm$ the standard error of the mean, are shown in Figure 4.11. The standard error, S_E, of the mean of a

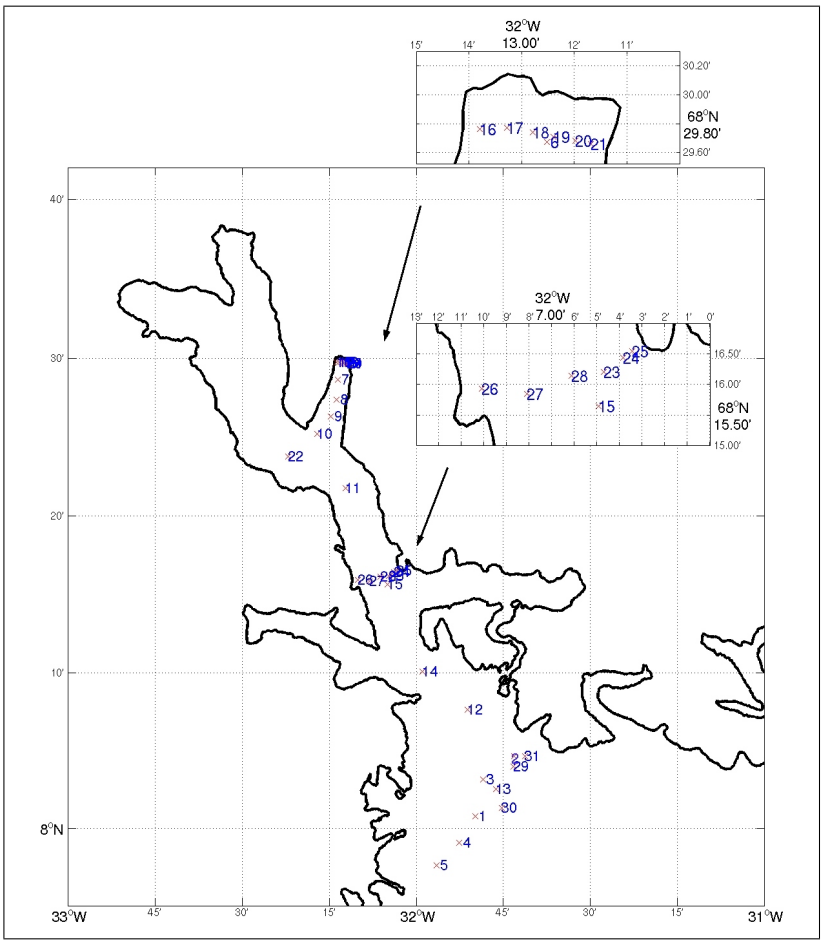

Figure 4.9: *Positions of CTD stations in Kangerdlugssuaq Fjord, where data were collected in September 2004 aboard the RRS James Clark Ross.*

sample from a population is estimated by:

$$S_E = \frac{\hat{\sigma}}{\sqrt{N}} \tag{4.1}$$

where $\hat{\sigma}$ is the standard deviation of the sample (or the standard deviation of the potential temperature measured at the different CTD stations for each depth), which is an estimate of the standard deviation σ of the population (potential temperature profile for the whole fjord), and N is the number of samples (number of CTD stations).

For the 1993 data, profiles KF0, KF1, KF2, KF3 and KF4 were used to calculate the mean potential temperature against depth shown in Figure 4.11. The standard error of the potential temperature profile is seen to decrease with depth. This is despite the number of samples decreasing with depth because some CTD stations were shallower than others, which would act to increase S_E according to equation 4.1. Below $\sim 300\,m$ the potential temperature is approximately constant with depth, with

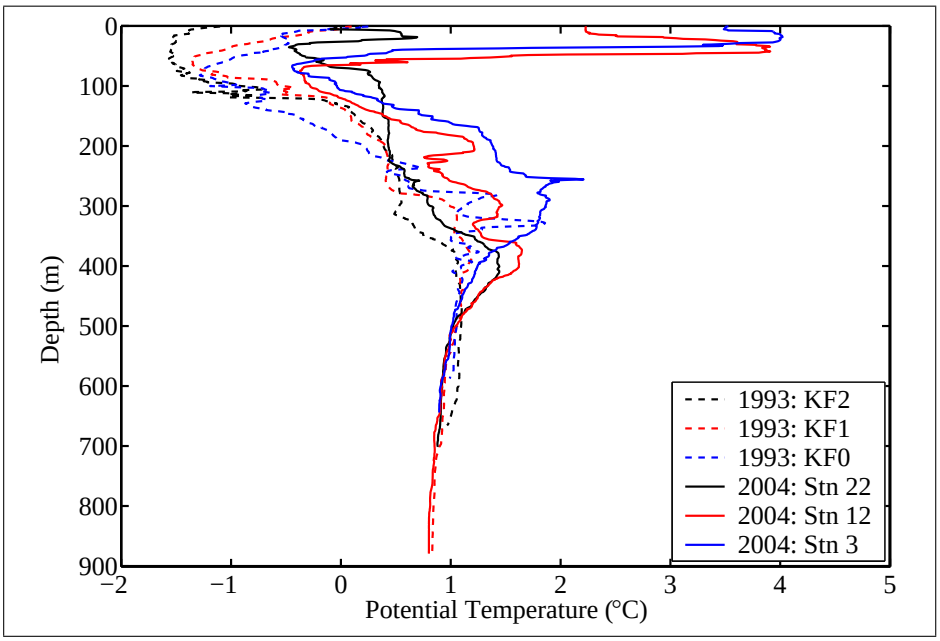

Figure 4.10: *Temperature profiles in Kangerdlugssuaq Fjord collected in 1993 and 2004, where lines of the same colour were collected at approximately the same position.*

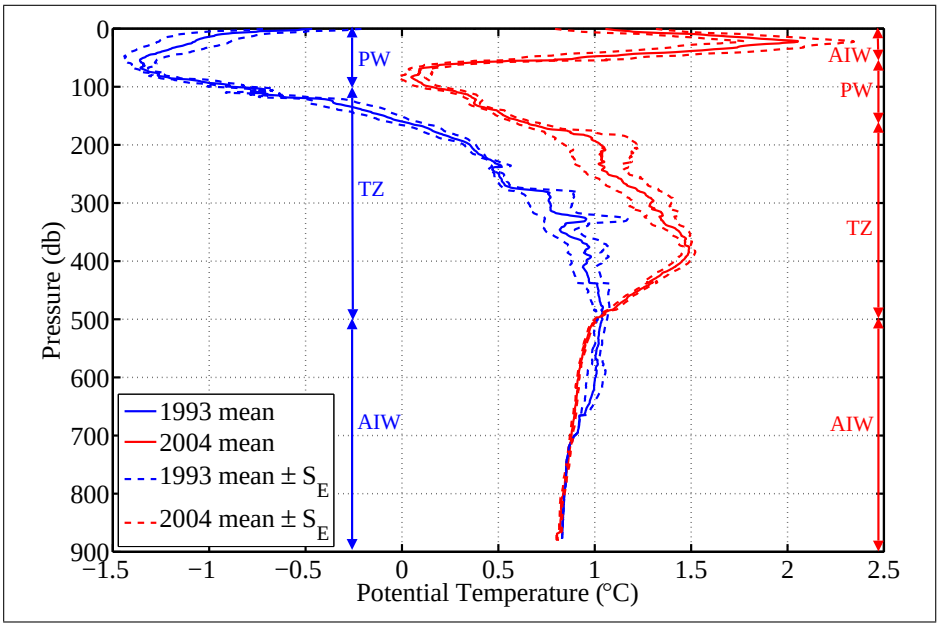

Figure 4.11: *Average temperature profiles over Kangerdlugssuaq Fjord from 1993 and 2004. Arrows show approximate locations of layers of Polar Water (PW), Atlantic Intermediate Water (AIW) and the Transition Zone (TZ) - blue for 1993 data and red for 2004 data.*

a small deviation from the mean. In 1993, the water mass in the fjord can be roughly split into a layer of PW on the surface and a deep layer of AIW, with a Transition Zone (TZ) in between, as labelled by the blue arrows in Figure 4.11.

For the 2004 data, all the CTD stations in the fjord (1, 2, 3, 4, 5, 11, 12, 13, 14,

15, 22, 23, 24, 25, 26, 27, 28, 29, 30 and 31) were used to calculate the mean potential temperature against depth shown in Figure 4.11. The total number of samples is much larger in 2004, but again not all profiles extend to the deepest depth shown, so the number of samples decreases with depth. Despite this, the standard error in the potential temperature profile decreases with depth. Below $\sim 500\,m$ the potential temperature is almost constant, with a small deviation from the mean throughout the fjord. In 2004, there is an additional surface layer of warm AIW between 0–$50\,m$, which is shown along with the approximate locations of the PW, TZ and deep AIW layers by red arrows in Figure 4.11.

Comparing the 1993 and 2004 average potential temperature profiles, it can be seen that there is a warming in 2004 over the whole of the surface $500\,m$. The warming is most pronounced at $\sim 50\,m$, where the difference is up to $\sim 3°C$. From 100–$400\,m$ the difference decreases to $\sim 0.5°C$. Between 400–$500\,m$ the potential temperatures in the two years converge to similar values, until below $\sim 500\,m$ the fjord potential temperatures are approximately the same in both 1993 and 2004.

It is clear that there is a high degree of variability in fjord water temperatures from year to year and this will have an impact on the iceberg melt rate, as discussed in Section 2.4.1. To understand the mechanisms causing this variability, it is necessary to look at the ocean currents that transport water into the fjord, which are shown in Figure 4.8. Cross-sections of potential temperature along the fjord and out into the trough, where the distance is measured from the glacier front, are plotted in Figure 4.12(a) and 4.12(b) for 1993 and 2004, respectively. The difference between the potential temperature in 2004 and 1993, with positive values showing warming in 2004, is shown in Figure 4.12(c). The station locations, which are used to plot the cross-sections in Figure 4.12 and marked by *s at the top of the cross-sections (1993 in red and 2004 in purple), are shown in Figure 4.13, where 1993 stations are shown in red and 2004 stations in yellow. The X in Figure 4.13 is the point where the 'distance from the glacier front' is measured from for the cross-sections in Figure 4.12.

In 2004, a warm near-surface plume of Atlantic Intermediate Water was observed to advance up Kangerdlugssuaq Trough (Figure 4.12(c)). It appears to have displaced the Polar Water, which is shifted to deeper depths and extends further away from the fjord than in 1993. This is demonstrated by the $2°C$ contour, which is closer to the glacier front in 2004 compared to 1993 at the surface. However, at a depth of $400\,m$, it extends further away from the glacier in 2004 than in 1993. Therefore, the temperature gradients are higher both horizontally and vertically in 2004 compared to 1993. This variability is probably due to changes in the strength of the flux of the EGC into the trough at the shelf break and also related to changes in the constituent water masses carried by the EGC, as discussed earlier in this section.

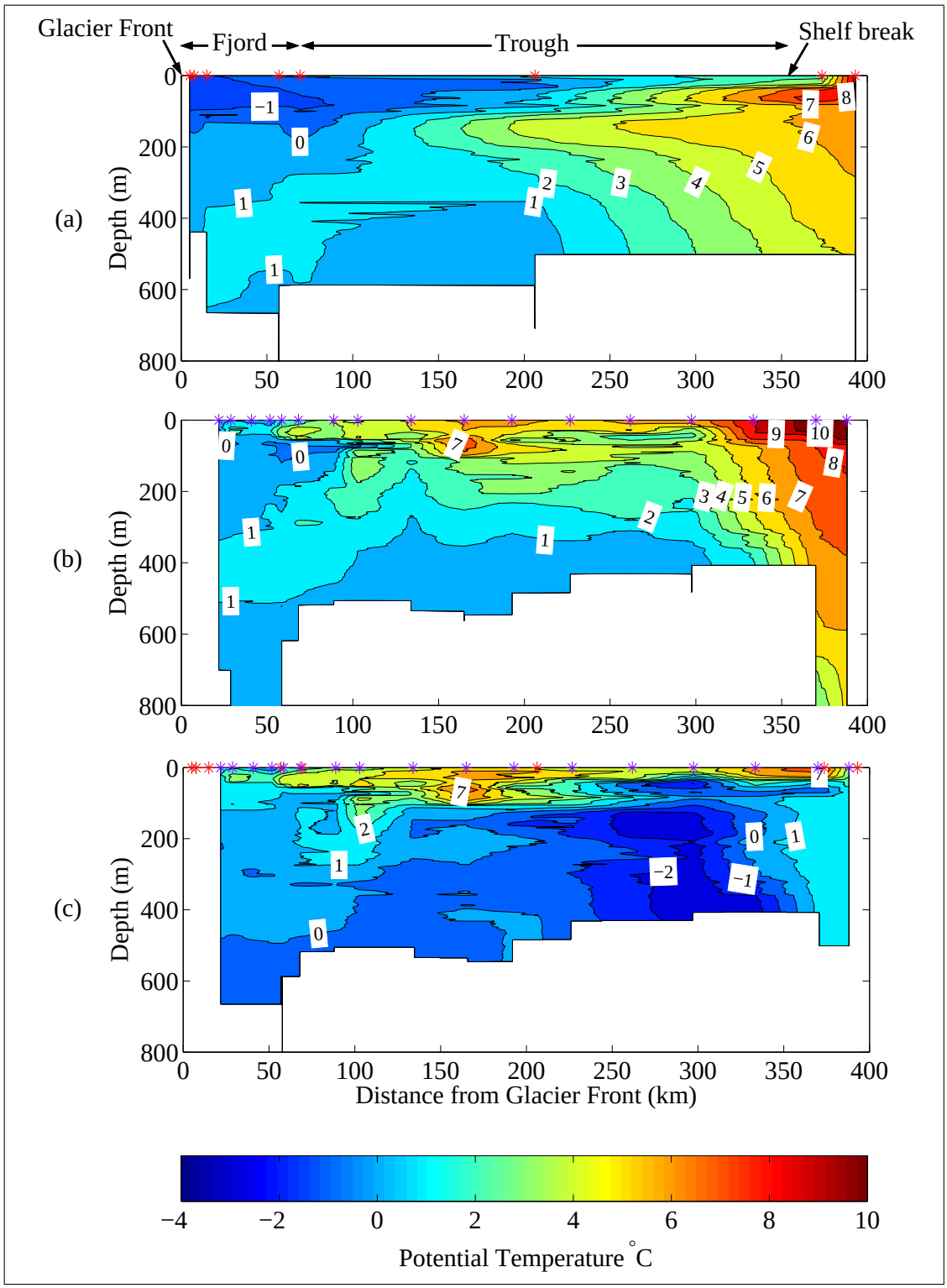

Figure 4.12: *Potential temperature cross-section along Kangerdlugssuaq Fjord and Trough, with distance measured from the glacier front (X in Figure 4.13), from CTD stations marked in Figure 4.13 (a) 1993, with CTD stations marked with *; (b) 2004, with CTD stations marked with *; (c) Difference between 2004 and 1993—positive values show warming in 2004.*

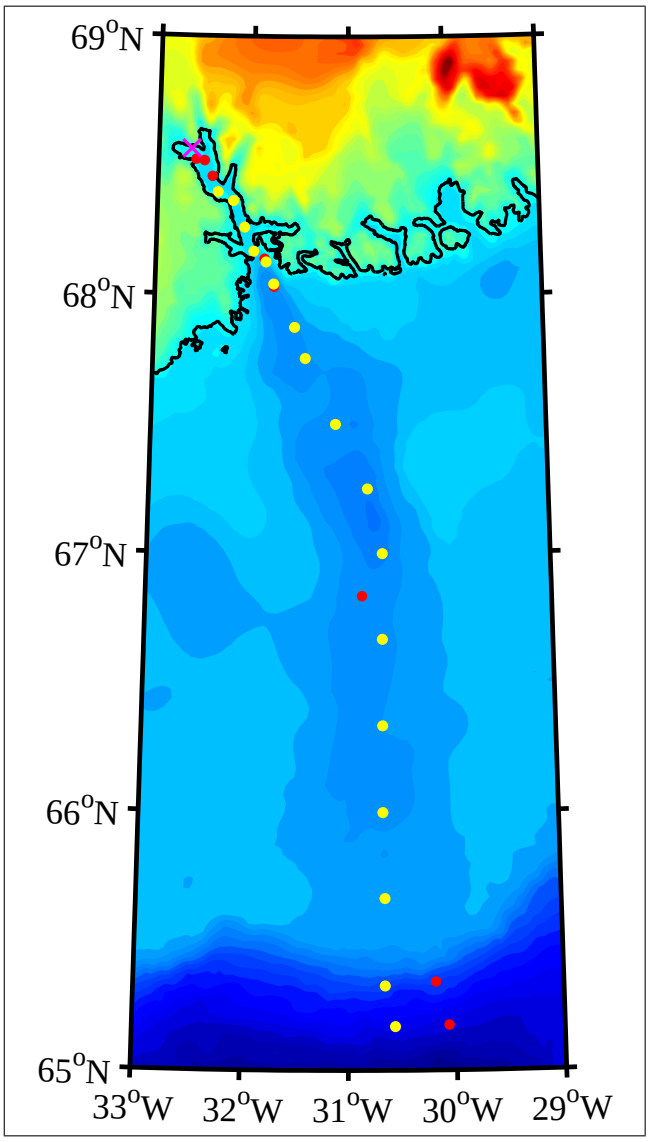

Figure 4.13: *Positions of CTD stations from 1993 (red) and 2004 (yellow) in Kangerdlugssuaq fjord and trough.*

Even though there is a high degree of variability in the absolute value of the potential temperature at different depths from year to year, the water mass in the fjord observed in 1993 can be roughly split into three layers: Polar Water at the surface, a Transition Zone below that, followed by a deep layer of Atlantic Intermediate Water, as indicated in blue in Figure 4.11. In 2004 all the water masses above $500\,m$ are warmer by between 0.5–3°C compared to 1993. There is an additional warm surface layer of Atlantic Intermediate Water of $\sim 1.75°C$ in 2004, then below that is a layer of Polar Water, followed by a Transition Zone and finally a deep layer of Atlantic Intermediate Water, which are labelled in red in Figure 4.11.

For the model input, a single profile of water temperature with depth is required,

and this profile is linearly interpolated between the input values to the specified vertical resolution. The simplified water temperature profiles used as inputs to the model for winter (October to May) and summer (June to September), based on the 1993 and 2004 observations, are shown in Figure 4.14. The two summer profiles for the fjord

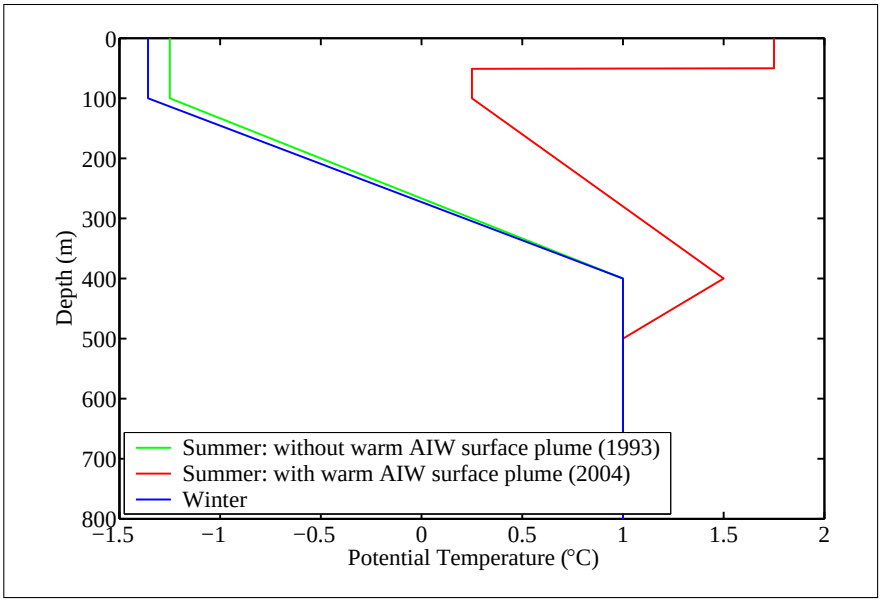

Figure 4.14: *Water temperature profiles used as model inputs. Winter: October to May. Summer: June to September.*

represent periods either when a warm AIW surface plume is present or when there is no warm AIW surface plume, corresponding to the 2004 and 1993 data, respectively. The winter profile has a cold upper layer, which is assumed to have a temperature of $-1.358°C$, the freezing point of seawater at the surface with a salinity of $25\,PSU$. The winter deep layer is assumed to be at the same temperature as the summer deep layer (Karen Heywood, personal communication 2007).

4.3.6 Seawater Salinity

The average salinity profiles for 1993 (stations KF0, KF1, KF2, KF3 and KF4) and 2004 (stations 1, 2, 3, 4, 5, 11, 12, 13, 14, 15, 22, 23, 24, 25, 26, 27, 28, 29, 30 and 31), with the standard error calculated using equation 4.1, are shown in Figure 4.15. The salinity profiles in both 1993 and 2004 show a fresher surface layer and the salinity increases with depth to a constant value below a depth of 300–400 m. In 1993 the surface water had a lower salinity than in 2004. This supports the notion that warm AIW entered the fjord in 2004, displacing the PW at the surface.

In the *SedBerg* Model, the salinity is required to calculate the freezing point of water, using equation 2.28, for input into equation 2.27. Two salinity profiles are used,

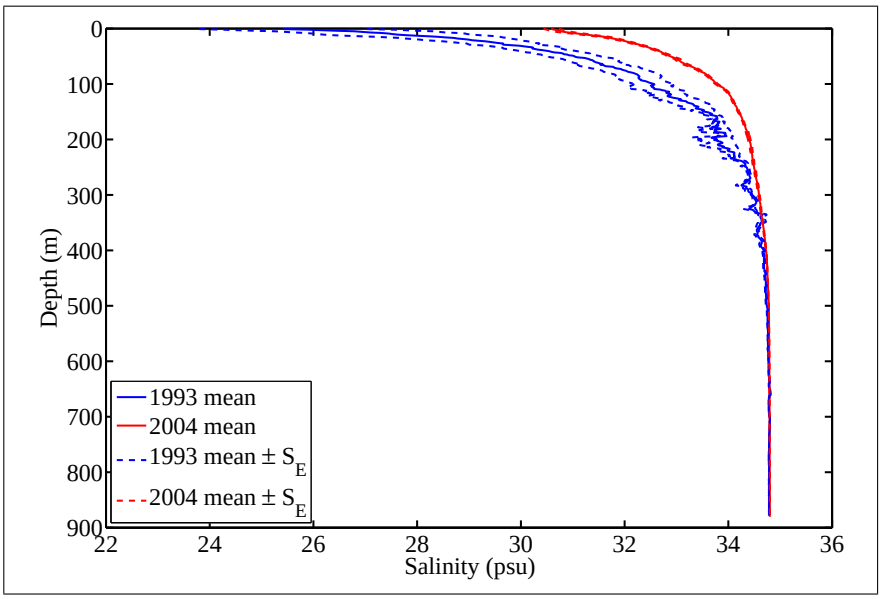

Figure 4.15: *Average salinity profiles with errors, as measured in 1993 and 2004.*

corresponding to the present day situation with and without a warm AIW surface plume - 2004 and 1993 in Figure 4.15, respectively. The depth averaged salinity for each modelled iceberg is calculated from one of these profiles, depending on the hydrographic conditions being simulated.

4.3.7 Air Temperature

Air temperature data are obtained for Angmagssalik from the Global Historical Climatology Network (GHCN-Monthly) data base, accessed through the U.S. Department of Commerce National Climatic Data Centre (Peterson and Vose, 1997; Peterson *et al.*, 1998). Angmagssalik is a weather station at $65°36'N$ $037°38'W$ and $50\,m\,a.s.l$, (see Figure 4.1 for location map), where weather observations have been made from 1895–present. Angmagssalik is the closest weather station to Kangerdlugssuaq Fjord, at a distance of $370\,km$ to the south-west, with the next closest being Scoresby Sund, which is $470\,km$ away to the north-east. The weather station at Angmagssalik is located on the coast. It is therefore assumed that Kangerdlugssuaq Fjord experiences a relatively similar climate to Angmagssalik, and the air temperature data from Angmagssalik can be used as inputs for modelling Kangerdlugssuaq Fjord.

The mean annual temperatures are shown as departures from the long-term average for the period 1895–2006 in Figure 4.16. Over this time period, it is apparent that there were intervals of warmer and cooler climate. The temperature record at Angmagssalik encompasses the end of the *Little Ice Age*, which was a period of cooling, up to the present day, including late 20^{th} Century warming. From 1895 to 1925, there was a

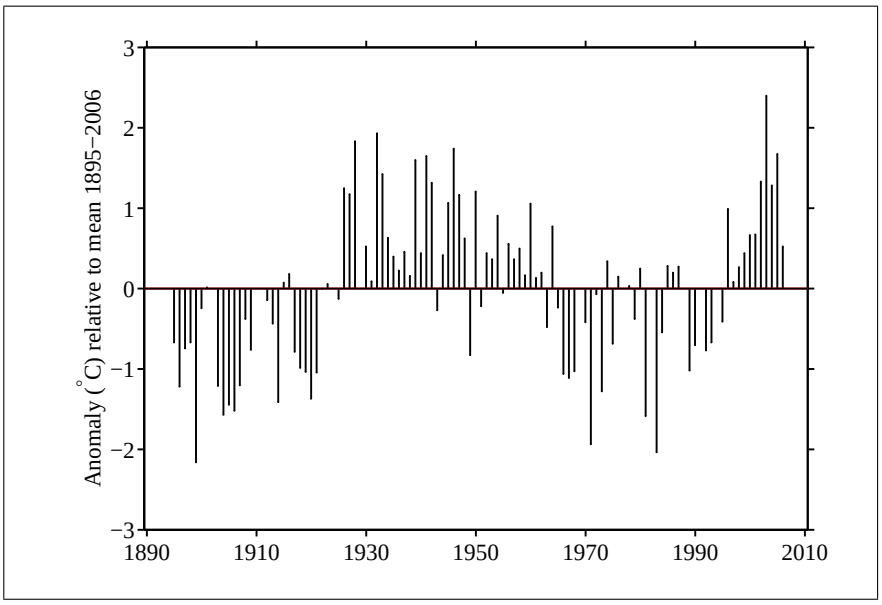

Figure 4.16: *Air temperature records at Angmagssalik from 1895–2006. The mean annual temperatures are calculated and shown as departures from the long-term average (1895–2006).*

'Cold' era at the end of the *Little Ice Age*, followed by a relatively 'Warm' era from 1926 to 1964. This was succeeded by another cooler period from 1965, and finally a warming trend from the early 90s to the present day has resulted in higher than average temperatures. Monthly mean temperatures calculated for the 'Cold' era, 1895–1925, and the 'Warm' era, 1926–1964, with standard errors calculated using equation 4.1 (dotted lines) are shown in Figure 4.17. The monthly mean air temperatures during the 'Cold' era are used as representative of *Little Ice Age* air temperatures and the monthly mean air temperatures during the 'Warm' era are used as approximations for air temperatures during the *Medieval Warm Period*. Since the end of the *Little Ice Age* 80 years ago, there have been both 'Cold' and 'Warm' periods, with approximately 63% 'Warm' years and the remaining 37% 'Cold' years. The model uses these ratios of 'Cold' to 'Warm' years to simulate sedimentation over the past 80 years.

4.3.8 Fjord Currents

The water currents flowing in fjords can be considered to be composed of two components: a tidal velocity, with a time-averaged mean of zero, and a residual outflow velocity, due to freshwater entering the fjord system from the glacier at its head. There is usually considerable spatial variation of currents in a fjord system due to the bathymetric configuration, as well as temporal variations caused by tidal oscillation and changes in the freshwater flux (Syvitski *et al.*, 1987).

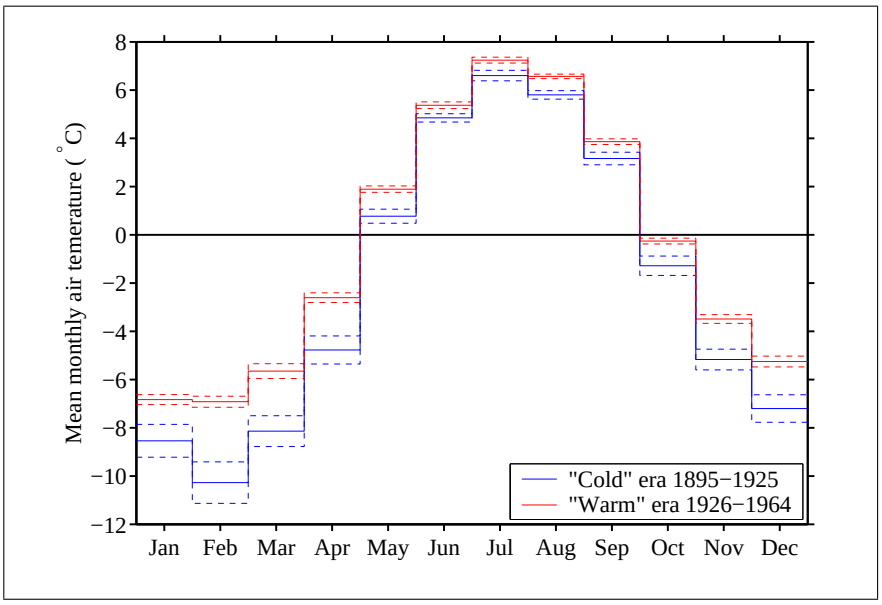

Figure 4.17: *Monthly mean air temperatures at Angmagssalik for a 'Cold' era from 1895–1925 and a 'Warm' era from 1926–1964, with dotted lines showing standard errors of the measurements.*

4.3.8.1 Tidal Forcing

Tidal velocities in fjords show high degrees of spatial and temporal variation, and to solve the full fluid equations to simulate the currents in a fjord would be computationally expensive. The main role of tides in the model developed in Chapter 2 is to move the icebergs around in an oscillatory fashion with approximately the correct amplitude, in order to simulate iceberg acceleration/deceleration and drift pattern. The range of iceberg velocity affects the melt rate and therefore the sedimentation rate. Spatial variations in the tidal velocity are not important, as the observed sediment deposition does not show spatial variability over long time periods. Therefore, a simplified tidal forcing can be simulated with the following equations for the tidal velocity components (Clarke and La Prairie, 2001):

$$v_{T_x} = A_T \sin\left(\frac{2\pi t}{T_T}\right) \tag{4.2}$$

$$v_{T_y} = A_T \cos\left(\frac{2\pi t}{T_T}\right) \tag{4.3}$$

where $\mathbf{v}_T$ is the tidal water velocity vector with x and y indicating the North and East components, respectively, A_T is the amplitude of the tidal water velocity, T_T is the period of the tidal oscillation (12 hours) and t is time.

An estimate of the amplitude of the tidal water velocity is required for equations 4.2–4.3. This can be obtained from the data collected in 2004. The R.R.S

James Clark Ross had a RD Instruments 153.6 kHz Acoustic Doppler Current Profiler (ADCP) mounted within the hull in a recessed sea chest to provide protection from sea ice. There is a 'blank before transmit' distance of 4 m and a pulse distance of 8 m; therefore the centre of the first bin is at a depth of 18 m, the second bin is at 26 m and so on. The water velocity data collected during the 10 days that were spent in the fjord, at four different depths are shown in Figure 4.18. The water velocity data

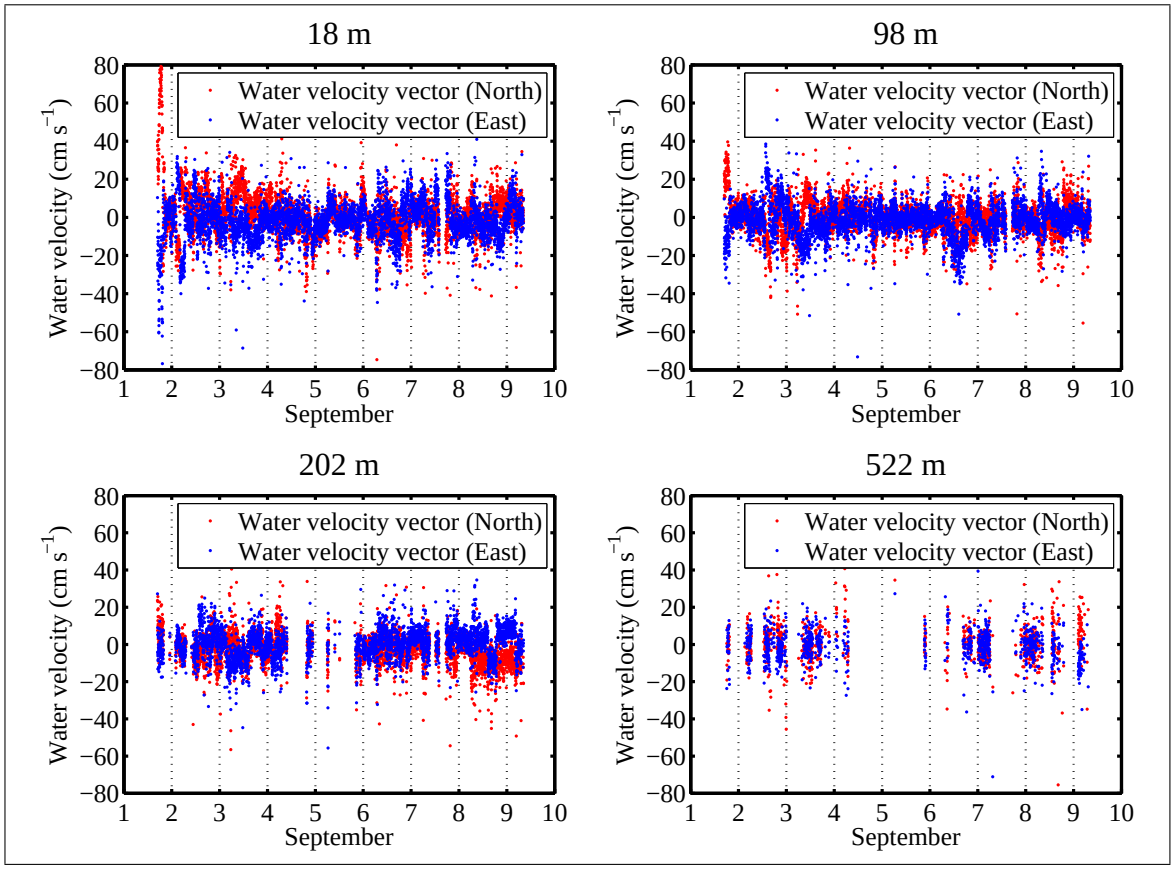

Figure 4.18: *Time series of the 18 m, 98 m, 202 m and 522 m water velocity vectors, corresponding to the North-South direction, where North is positive, and the East-West direction, where East is positive, collected with the vessel mounted ADCP during the 2004 cruise aboard the R.R.S James Clark Ross.*

are shown as two vectors, corresponding to the North-South direction, where North is positive, and the East-West direction, where East is positive. The position of the ship during the cruise, coloured by day to show where the measurements in Figure 4.18 were taken, is shown in Figure 4.19. For example, it can be seen that the ship spent the second half of 5th September in Courtauld Fjord and the components of the velocity vector show slightly less variation during this time than when the ship was in the main fjord.

There is no obvious tidal oscillation visible because there is a high spatial variability in the tidal velocity and the ship was usually moving. However, Figure 4.18 does show

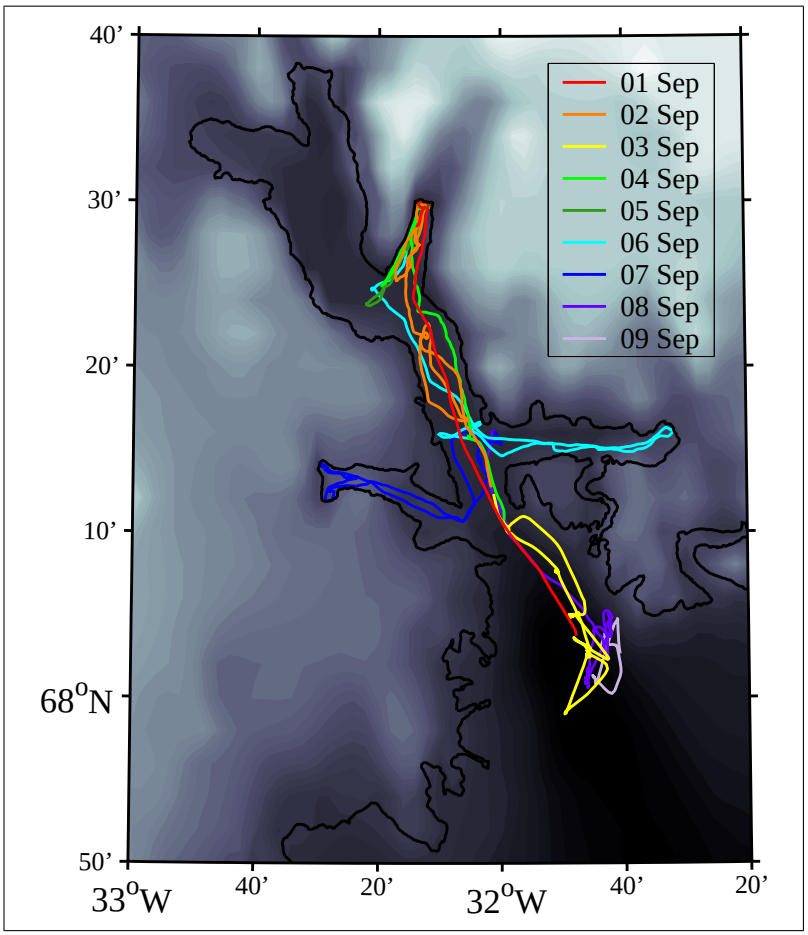

Figure 4.19: *Map of the position of R.R.S James Clark Ross during the field work in 2004. The days are colour-coded to show where the ship was during each day of the cruise*

the maximum and minimum tidal velocities, which are approximately $\pm 15\,cm\,s^{-1}$, if the outliers are ignored. This does decrease slightly with depth, but not significantly; therefore, in the model, the water velocity is assumed to be independent of depth and $A_T = 15\,cm\,s^{-1}$ in equations 4.2–4.3.

4.3.8.2 Residual Outflow Velocity

The outflow velocity (water flowing through the fjord to the ocean) was derived by Syvitski *et al.* (1996) by calculating the hydraulic head set up by the addition of freshwater to the fjord system, which is assumed to flow through the fjord as a surface layer. They calculated the residual velocity from the total freshwater discharge divided by the product of the effective width of the fjord ($5\,km$) and the surface layer depth ($10\,m$). The melt-season discharge (for the four months of the year when icebergs are free to move around the fjord) is based on subglacial discharge from Kangerdlugssuaq Gletscher ($60\,m^3 s^{-1}$ from Andrews *et al.* (1994)), which flows all year, plus supraglacial

melt ($195\,m^3s^{-1}$ from Andrews *et al.* (1994)), plus iceberg melt ($270\,m^3s^{-1}$ from Syvitski *et al.* (1996)), plus sea-ice melt ($60\,m^3s^{-1}$ based on $2\,m \times 6500\,m \times 50000\,m$ per year from Syvitski *et al.* (1996)). Contributions from rainfall on the glacier surface and basal melt of the glacier, if some portion of the terminus is afloat, are neglected. This provides a melt-season discharge of $585\,m^3s^{-1}$. The residual surface layer velocity (not including tidal oscillation), v_r, is then calculated to be $1.2\,cm\,s^{-1}$ or $0.0432\,km\,hr^{-1}$ and this results in an iceberg residence time of 68 days in summer. If the glacier tongue becomes ungrounded, as occurred during the recent retreat of Kangerdlugssuaq Glacier (Luckman *et al.*, 2006), there will be additional freshwater inputs from basal melting of the floating tongue. Melt rates have been observed underneath floating tongues, which can be used to calculate the contribution to the total freshwater discharge. Rignot (1996) measured basal melt rates averaging $10 \pm 2\,m\,a^{-1}$ at Peterman Gletscher, North Greenland. If the length of the floating tongue is estimated to be $2\,km$ and the width of the calving front is $4.6\,km$, the melt area would be $9.2\,km^2$, producing a freshwater contribution of $3\,m^3s^{-1}$. This is small compared to the other sources of freshwater and therefore does not have a large impact on the overall freshwater discharge.

In winter, there is shorefast sea ice in the fjord, but there is still a residual outflow velocity. The subglacial discharge is $60\,m^3s^{-1}$ all year round and if it is assumed that 20% of icebergs remain in the fjord over the winter months, this results in a contribution of $54\,m^3s^{-1}$ due to iceberg melt in winter, giving a total of approximately $114\,m^3s^{-1}$. The residual sub-surface water velocity in winter underneath sea ice is therefore $0.23\,cm\,s^{-1}$ or $0.008\,km\,hr^{-1}$.

The along-fjord outflow velocity, v_o, is given a uniform random variation of up to $\pm 10\%$ every 5 minutes (since this is the timescale that the wind velocity is assumed to vary over, which will be described in Section 4.3.10) by drawing a uniform random variate, $U \in [-0.1, 0.1]$, and calculating v_o using $v_o = v_r + U\,v_r$. The across-fjord velocity, v_a is assumed to be zero, with a uniform random variation of up to $\pm 10\%$ of the along-fjord outflow velocity, which is also calculated every 9 minutes by drawing a uniform random variate $U \in [-0.1, 0.1]$, where $v_a = U\,v_r$.

4.3.9 Sea Ice

Syvitski *et al.* (1996) reported that Landsat images from 1983-1993 show that during the 8 winter months (October to May) Kangerdlugssuaq Fjord is covered with shorefast sea ice, which freezes any icebergs present in one place for the winter. Therefore, in the model, the icebergs only move between June and September. There is a sikussak in front of the Kangerdlugssuaq Gletscher, as described in Section 4.3.2, which is a mass of icebergs, bergy bits and shorefast multi-year sea ice present all year round.

This traps icebergs for a period of approximately 2 years (Dwyer, 1993), before they are freed to drift along the fjord. In the model the time when an iceberg is calved is taken to be the time when it leaves the sikussak. The presence of the sea ice in winter prevents icebergs from escaping the sikussak (or 'calving'). When the sea ice melts around the beginning of June, the icebergs trapped in that winter's sea ice are released, but those in the sikussak remain. In the model the sea ice melts at the beginning of June. At this time, any icebergs that were 'calved' during the winter along with those further down the fjord, which have all been trapped in the sea ice, are released.

4.3.10 Wind Velocity

The wind velocity is required as an input for equation 2.40, the equation of motion for the icebergs, in order to calculate the wave radiation force (equation 2.42) and the air drag force (equation 2.41). The wind forcing provides a random variation in the forces acting on the icebergs, which is superimposed on the regular oscillatory tidal forcing.

The wind data collected from Kangerdlugssuaq Fjord in 2004 are shown in Figure 4.20. The R.R.S James Clark Ross is equipped with an anemometer, which col-

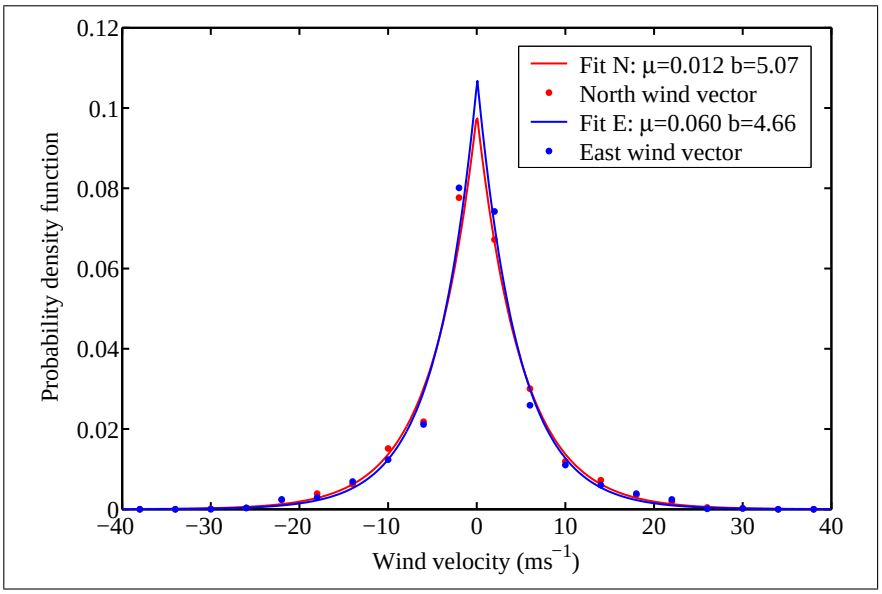

Figure 4.20: *Observed wind data (vectors in North and East directions) over 10 days in Kangerdlugssuaq Fjord with fitted Laplace distributions*

lected readings of wind speed and direction every second. The data were converted into 5 minute means. The data included in Figure 4.20 were collected while the ship was in the fjord, from 12:00 on 1st September until 08:00 on 9th September (see Figure 4.19). These are the only wind speed and direction data available for Kangerdlugssuaq Fjord. The 5 minute means for wind speed and direction were converted into north and east

vector components and then sorted into 20 bins, which are plotted as dots in Figure 4.20 and a Laplace, or double exponential, distribution is fitted to the 5 minute means of the north and east wind vectors.

The probability density function for the Laplace distribution of a random variable, x, is:

$$f(x) = \frac{1}{2b} \exp\left[-\frac{|x-\mu|}{b}\right] \tag{4.4}$$

where μ is the mean of the random variable and b is the scale parameter ($b = \sigma/\sqrt{2}$ where σ is the standard deviation of the random variable).

The parameters μ and b are found for each of the north and east wind vectors (5 minute mean data). The estimator of μ can be found from the sample mean:

$$\hat{\mu} = \frac{1}{N_{tot}} \sum_{n=1}^{N_{tot}} x_n \tag{4.5}$$

where N_{tot} is the total number in the sample.

The maximum likelihood estimator of b can be found using the following equation:

$$\hat{b} = \frac{1}{N_{tot}} \sum_{n=1}^{N_{tot}} |x_n - \hat{\mu}| \tag{4.6}$$

The distributions for both the north and east vectors of wind velocity are very similar and the means of both are approximately equal to zero, which implies that there is no preferred wind direction in the fjord. Therefore, it is assumed that the North and East components of the wind velocity are independent, so the modelled wind velocity vectors components are computed by taking two independent random draws from a Laplace distribution with $\mu = 0$ and $b = 4.87$. To accomplish this, a uniform random variate, $U \in (-1/2, 1/2)$, is drawn and the Laplace random variate, X, is calculated using:

$$X = \mu - b \operatorname{sgn}(U) \ln(1 - 2|U|) \tag{4.7}$$

where

$$\operatorname{sgn}(U) = \begin{cases} -1 & \text{if } U < 0 \\ 0 & \text{if } U = 0 \\ 1 & \text{if } U > 0 \end{cases}$$

The wind velocity was observed to vary fairly rapidly over time, so in the model a new velocity is calculated every 5 minutes.

4.3.11 Solar Radiation

The solar radiation flux is required as an input into equation 2.39. The long-term monthly mean solar radiation flux in the region of Kangerdlugssuaq Fjord is acquired from the Arctic Global Radiation (AGR) data set (Box *et al.*, 1998), and is shown in Figure 4.21. The AGR data set is the most complete Arctic radiation climatology

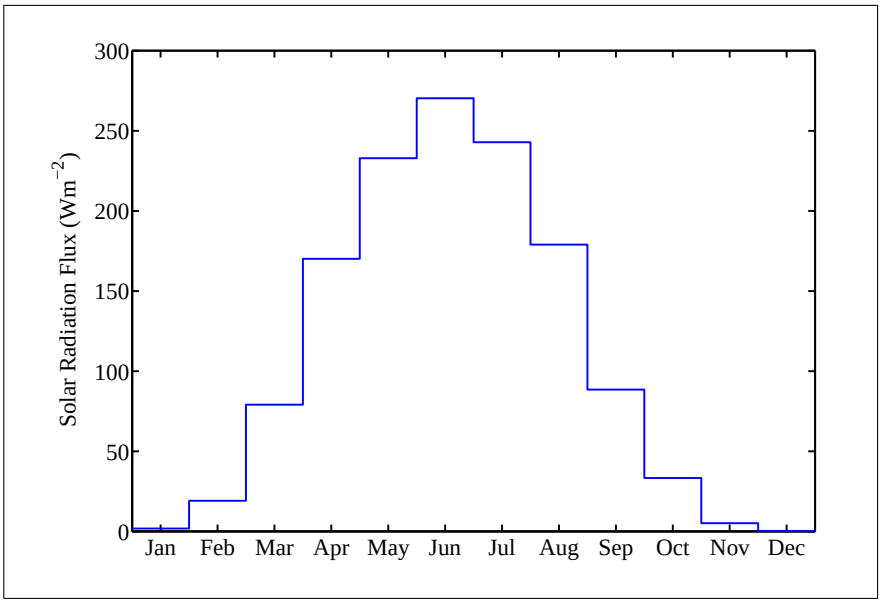

Figure 4.21: *Long-term monthly mean solar radiation flux in Kangerdlugssuaq Fjord from AGR data set*

available and combines previous Russian studies to produce a time series of monthly fluxes calculated from land stations, ocean drifting stations and empirically-derived long-term climatological estimates. Some of the station time series are quite short, whereas others span over 40 years. From the data, a long-term monthly mean gridded climatology for the region north of $65°N$ has been interpolated.

4.4 Model Output

The parameters described above are used as inputs for the *SedBerg* model, and where there is some uncertainty in the actual value of the parameter, different possible values are investigated. The results of the various model experiments simulating sediment deposition rates for Kangerdlugssuaq Fjord over the last 1500 years are discussed in detail in this section.

4.4.1 Iceberg Drift Tracks

The drift track of an iceberg is determined by equations 2.47–2.50. The dominant forces acting on the iceberg are those due to the changing tidal water velocity and the residual outflow velocity. Perturbations to the tidal motion are superimposed due to changing wind velocity and random fluctuations in the water velocity.

The drift track of an iceberg over a 12 hour period (one tidal oscillation), demonstrating the motion due to tidal forcing, is shown in Figure 4.22. This model output

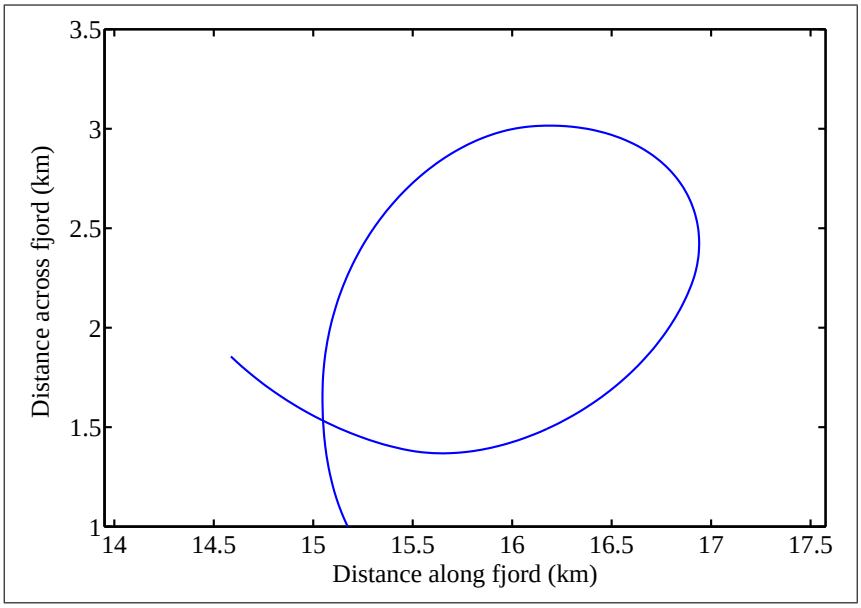

Figure 4.22: *Model output of iceberg trajectory during a 12 hour period (one tidal oscillation).*

compares well to a swath image of a sea-floor scour-track created by an iceberg offshore of Bråsvell Glacier, Svalbard, which travelled in a loop due to tidal forcing, shown in Figure 4.23. The modelled and observed loops are of comparable dimensions. The distance across the loop in Figure 4.22 is approximately $1.4\,km$, which is of a similar order of magnitude as the iceberg scour in Figure 4.23.

A map of drift tracks of three icebergs through the fjord is shown in Figure 4.24. The icebergs have different sizes but are subjected to the same forcing parameters and initial position. It can be seen that the smaller the iceberg, the more it is influenced by the forcing parameters, since a smaller iceberg has a smaller mass to surface area ratio and therefore a lower inertia. The effect of tidal forcing is apparent, superimposed by the additional random fluctuations in forcing by wind and water velocity. The way that the iceberg collides with and is deflected by the sides of the fjord can also be seen.

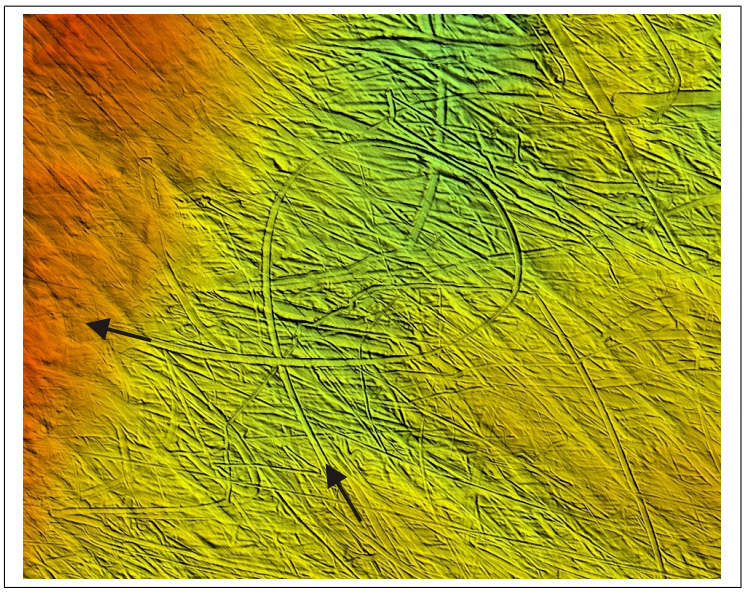

Figure 4.23: *Swath image of sea floor scours produced by iceberg keels offshore of Bråsvell Glacier, Svalbard. The 'looped' scour demonstrates the effect of tidal forcing on an iceberg's trajectory. The image is approximately* $3.5\,km$ *across and the diameter across the iceberg scour loop is approximately* $1.2\,km$*. Courtesy of Dag Ottensen* © *Norwegian Hydrographic Service.*

4.4.2 Iceberg Melt Rate

In this section, the melt rate of a test iceberg is investigated, under the influence of different climatic conditions. From the data available (Sections 4.3.5 and 4.3.6), two regimes of water temperature and salinity are taken to represent the extreme cases, and it is likely that conditions usually lie between these extremes. Extremes for air temperature are also found from data (Section 4.3.7). Therefore, two extreme cases are possible, and it is likely that climatic conditions in Kangerdlugssuaq Fjord fluctuate between the two extremes from year to year. These two extreme scenarios are summarised in Table 4.1. The melt rate of an iceberg of size $= 173.3\,m$ (length $= 239\,m$ and width/thickness $= 147.5\,m$) under 'Cold' and 'Warm' conditions, is shown in Figure 4.25.

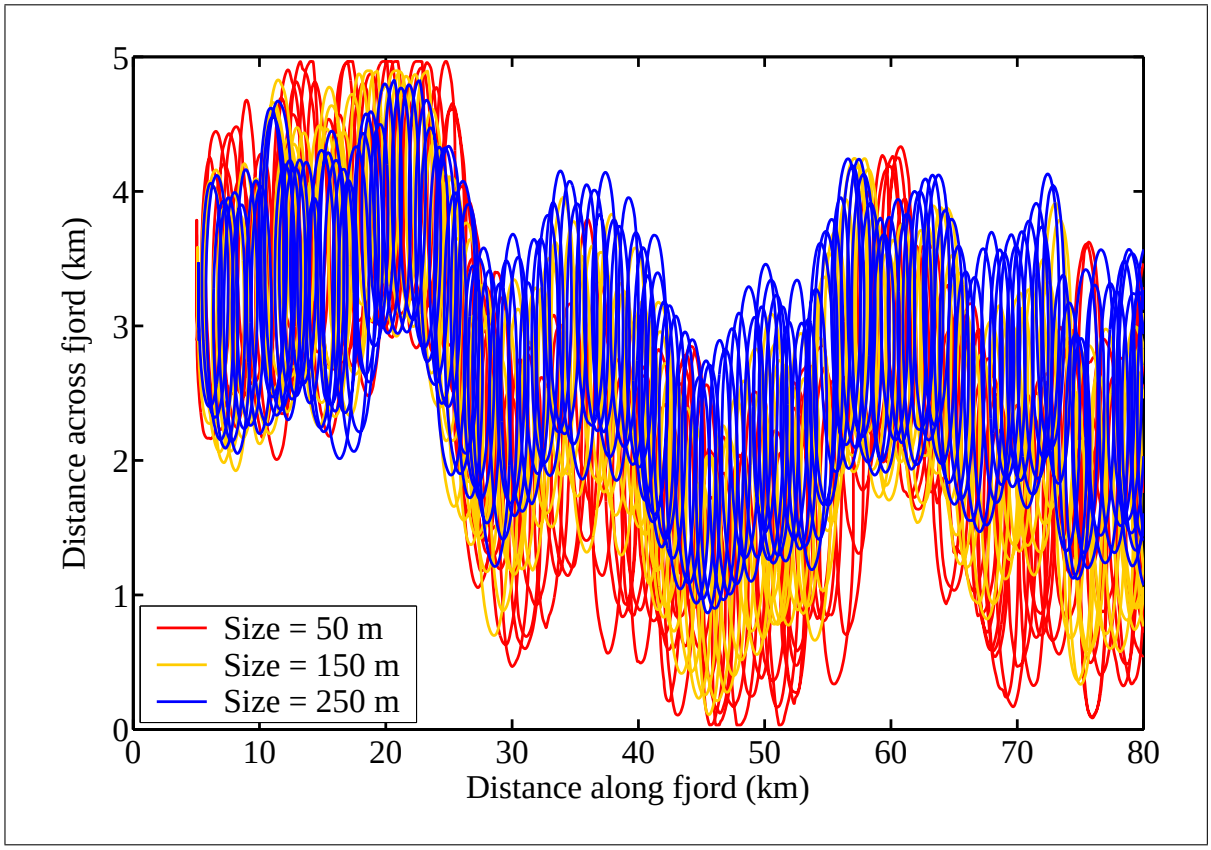

Figure 4.24: *Model output of the trajectories of three icebergs through the fjord, which are subjected to identical forcing parameters.*

	'Cold'	'Warm'
Summer Water Temperature	Cold (1993 data)	Warm (2004 data)
Summer Water Salinity	High Stratification (1993 data)	Low Stratification (2004 data)
Air Temperature	Cold (average 1895-1925)	Warm (average 1926-1964)

Table 4.1: *Model Parameters for 'Cold' and 'Warm' scenarios: summer water temperatures are those shown in Figure 4.14.*

In the summer months (May to August), the melt rate on top of the iceberg (subaerial) rises to values of $0.08\,m\,day^{-1}$. However, the subaerial melt rate shown in Figure 4.25 does not include the effect of a layer of sediment which accumulates on the surface as the ice melts, as discussed in Section 2.4.2. This results in the melt rate falling to zero once the surface layer of sediment is $> 30\,cm$. The subaqueous melt rates (sides and base) fluctuate rapidly, due to water (mainly tidal) and wind

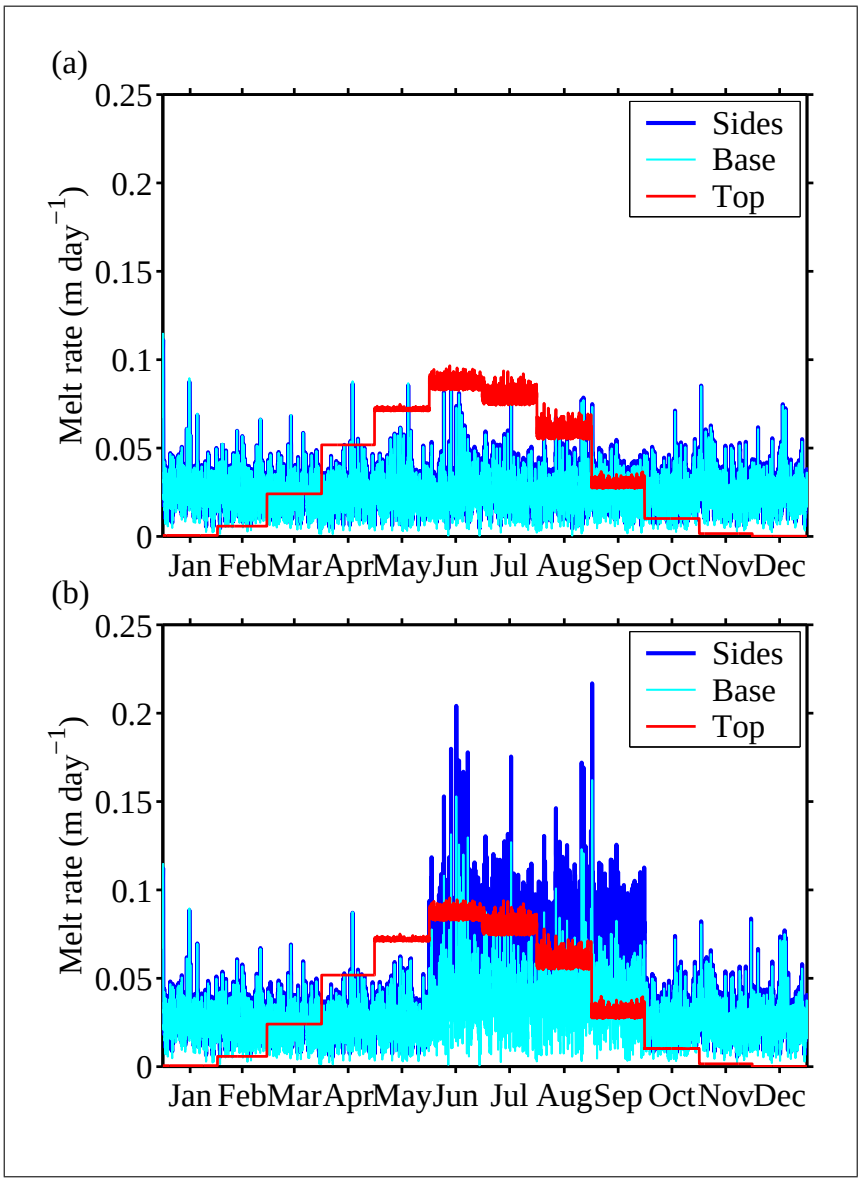

Figure 4.25: *Model output of melt rate over an annual cycle for an iceberg with length= 239 m and width/thickness= 147.5 m (size = 173.3 m) (a) 'Cold' conditions (b) 'Warm' conditions (defined in Table 4.1)*

forcing causing the velocity between the water and the iceberg (equation 2.20) to continually change over short time scales. In the 'Cold' scenario in Figure 4.25 (a) the mean values of the subaqueous melt rates do not show much variation over the annual cycle, because there is not much difference in the summer and winter water temperature (Figure 4.14). However, in the 'Warm' scenario in Figure 4.25 (b), there is a large increase in the mean melt rate of the iceberg sides in summer, due to the higher surface water temperatures (Figure 4.14) compared to in winter. The mean melt rate of the iceberg base is slightly higher in summer compared to winter. Since the temperature difference is not as large at the mean iceberg keel depth ($\sim$123 m) as

at shallower depths, the summer/winter difference is not as pronounced for the iceberg base as it is for the sides.

The change in length, width and height of a relatively small iceberg melting over the period of a year is shown in Figure 4.26. For the purpose of this plot, the iceberg

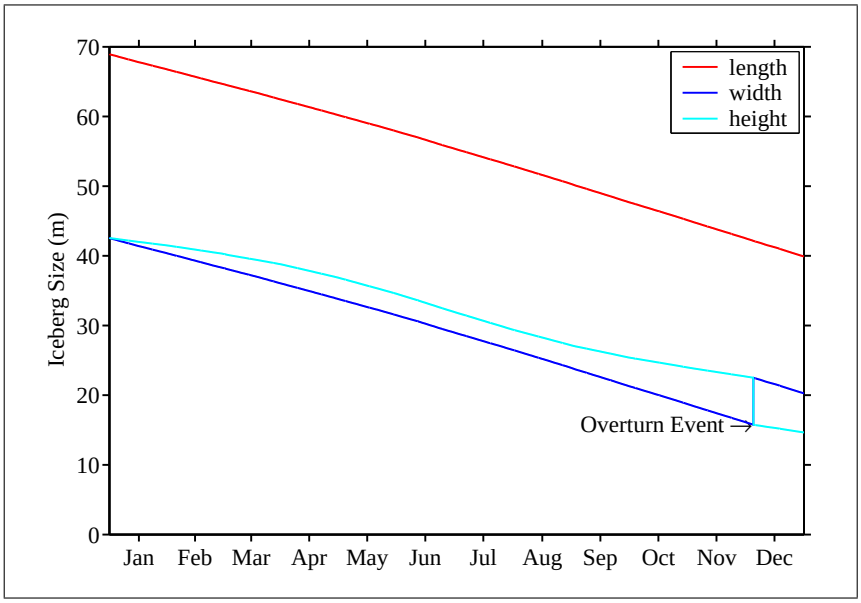

Figure 4.26: *Model output of iceberg melt rate over an annual cycle, with an overturn event in mid-November.*

is calved on the 1^{st} January, it is allowed to move all year round, and the temperature scenario is 'Cold' (Table 4.1). The iceberg sides melt more quickly then the base and the surface, therefore the iceberg width decreases more quickly than the height. However in summer, solar radiation increases the melt rate of the surface of the iceberg (until a layer of sediment greater than $30\,cm$ forms on its surface), so that its height decreases at approximately the same rate as its width. In mid-November the iceberg overturns since the stability criterion is exceeded (equation 2.76).

4.4.3 Sedimentation Rates

As discussed earlier in this chapter, the values of certain inputs for the *SedBerg* Model are not well defined; therefore, in this section, outcomes of the model under various initial conditions and assumptions are examined. One such parameter is the seasonal calving rate variation, as described in Section 4.3.2, another is climatic conditions, and a third is the mean iceberg size. The effects of changing these parameters on the results for sedimentation modelled over the fjord are presented and discussed in this section. Each model run simulates 10 years of sediment accumulation from icebergs and the icebergs are assumed to contain only englacial sediment, with a concentration

of 0.085 % by volume.

4.4.3.1 Variation of Calving Rate through Annual Cycle

Four different scenarios for the seasonal variation in calving rate are investigated:

a. Calving only occurs during the summer months.
b. The calving rate is constant all year round.
c. Summer calving rates are six times those in winter.
d. Icebergs are trapped until the sikussak breaks up, so 10 years' worth of icebergs are released over 28 days from 17$^{\text{th}}$ August to 13$^{\text{th}}$ September.

In each case, the equivalent calving rate over a year is $15\,km^3$. As discussed in Section 4.3.2, the volume of icebergs calved per year specified in the model needs to be higher than $15\,km^3\,yr^{-1}$ because an upper limit of $2\,km$ is applied to the iceberg width and length, and the maximum iceberg thickness is the thickness of the glacier ($650\,m$). The actual volume of icebergs calved per year is calculated during the program and for this to equal approximately $15\,km^3\,yr^{-1}$, given a mean iceberg size of $173.3\,m$, the specified iceberg volume flux needs to be equal to $21.7\,km^3\,yr^{-1}$ and given a mean iceberg size of $294\,m$ the specified iceberg volume flux needs to be equal to $16.66\,km^3\,yr^{-1}$. The theoretical number of icebergs produced per year, for a mean iceberg size of $173.3\,m$ is approximately 611 and for a mean iceberg size of $294\,m$ is approximately 290. The actual volume of icebergs produced for each of the combinations of seasonal calving rate scenario, environmental temperature regime and mean iceberg size are shown in Figure 4.27. The dotted black lines are at $\pm 10\%$ of the required volume flux, and all the actual volume fluxes lie well within this region, with a maximum variation of 3.75% from the required volume flux.

Maps of the sedimentation rate over the fjord for mean iceberg size of $= 294\,m$ and 'Warm' environmental conditions (Table 4.1) are shown in Figure 4.28 for the four seasonal calving rate variation scenarios. It can be seen that for 10 years of simulation, the sedimentation rates for the four scenarios show small spatial fluctuations due to the stochastic driving processes, but in general are reasonably smooth, and demonstrate the differences between scenarios. The patchiness of the deposition pattern is caused by random variations in the forcing parameters on the last day of summer, which determine the position of the icebergs at the time they are frozen in one place for the winter. Each of the icebergs is frozen at a randomly determined time during the last day of summer to ensure that tidal forces do not have a systematic effect on the mean position of the icebergs across the fjord when they stop moving for the winter, as would occur if they all stopped at the same time.

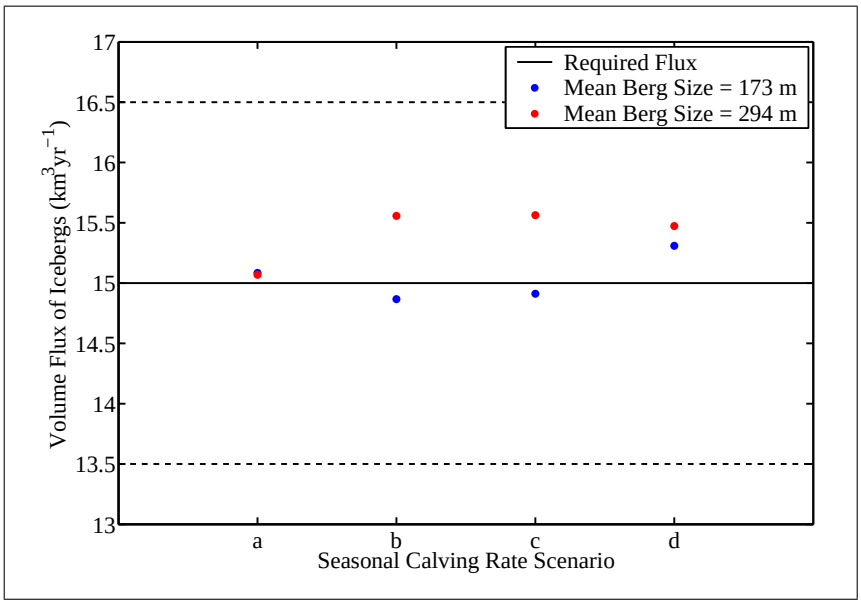

Figure 4.27: *Actual volume flux of icebergs produced by model with starting flux of* $21.7\,km^3\,yr^{-1}$ *for mean iceberg size of* $173.3\,m$ *and* $16.66\,km^3\,yr^{-1}$ *for mean iceberg size of* $294\,m$ *for the four seasonal calving rate variation scenarios (a) Summer calving only (b) Calving rate constant all year round (c) Summer calving rate 6 times winter rate (d) Sikussak break-up event.*

The glacier front is at an along-fjord distance of $5\,km$, shown as dark blue area at the top of each map (northern edge of fjord). The maximum rate is fixed at $2\,cm\,yr^{-1}$, so that differences in the sedimentation rates in Figure 4.28 (a), (b) and (c) can be distinguished.

The peak sedimentation rate is skewed slightly towards the west side of the fjord. This asymmetry is due to the Coriolis effect, which acts to deflect moving objects due to the rotation of the Earth, and is included in the model of iceberg drift, equation 2.40. In the Northern Hemisphere objects are deflected to the right of their direction of travel, so in the case of the modelled Kangerdlugssuaq Fjord, the icebergs are in general moving in a southerly direction towards the mouth of the fjord, so are deflected to the western size of the fjord (left of Figure 4.28). Gilbert (1982) observed turbid overflow plumes deflected toward the right bank due to the Coriolis effect in fjords on Baffin Island, N.W.T., Canada. As a consequence the sediment accumulation was higher on the right side of the fjord than on the left by 10 to 20%. Even though the sediment deposition in these fjords is predominantly by glacial plumes, some sedimentation is due to iceberg-rafting. The *SedBerg* Model demonstrates that icebergs, and therefore iceberg-rafted deposition, are also affected by the Coriolis effect.

The dark red areas in front of the glacier in Figure 4.28 (b) and (c) and in the centre of the fjord in Figure 4.28 (d) far exceed this threshold. The high sedimentation rates

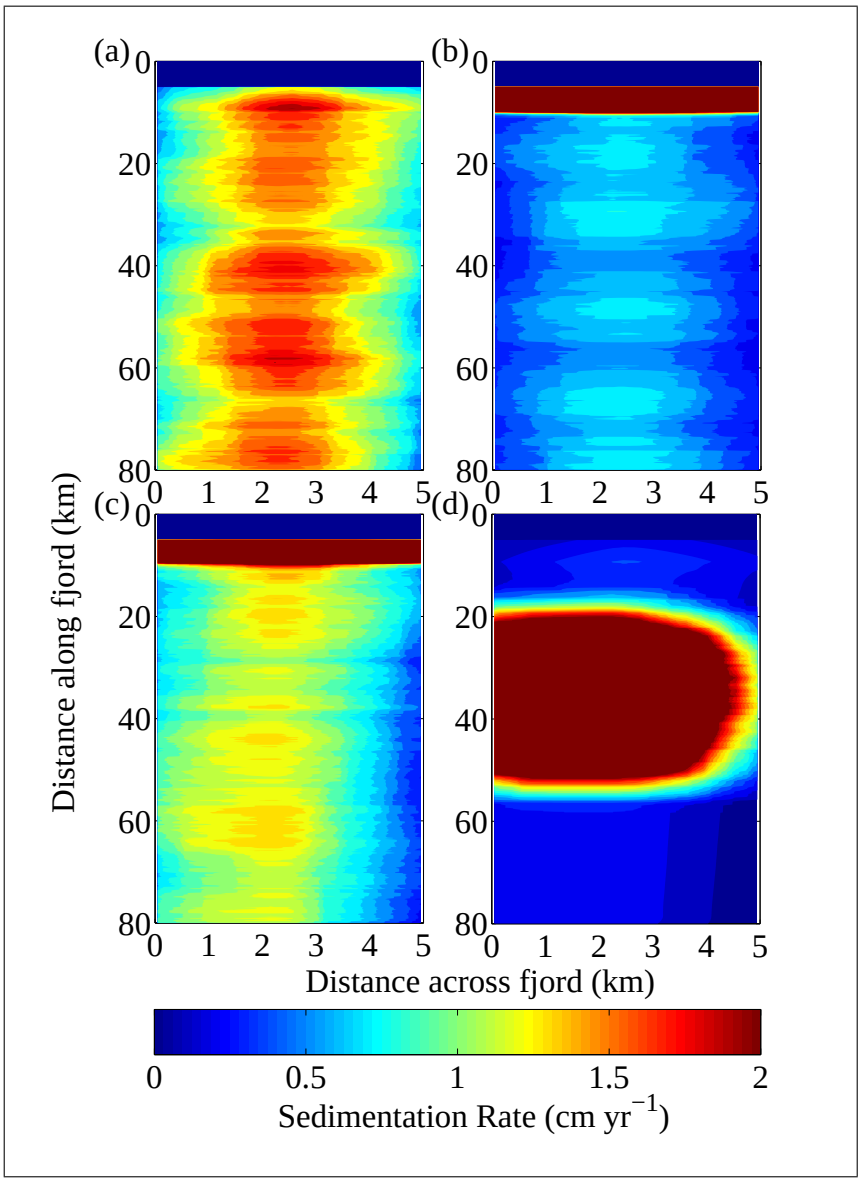

Figure 4.28: *Maps of sedimentation rate over Kangerdlugssuaq Fjord (North is at the top of the page) for mean iceberg size = 294 m and 'Warm' environmental conditions for the four seasonal calving rate variation scenarios (a) Summer calving only (b) Calving rate constant all year round (c) Summer calving rate 6 times winter rate (d) Sikussak break-up event.*

in front of the glacier in Figure 4.28 (b) and (c) are caused by the glacier continuing to calve during winter and subsequently freezing in front of the glacier by sea ice, unable to move but still melting subaqueously and depositing sediment. The maps of sedimentation rates over the fjord for each of the four scenarios in Figure 4.28 are not able to show high enough resolution to compare the scenarios at both low and high sedimentation rates. However, transects of sedimentation rates along and across the fjord enable the inclusion of high sedimentation rates, while differences between the scenarios at low sedimentation rates can also be distinguished.

The along-fjord transect is calculated from the average sedimentation rate across the central 1 km, and these are shown for the four scenarios in Figure 4.29. At scales

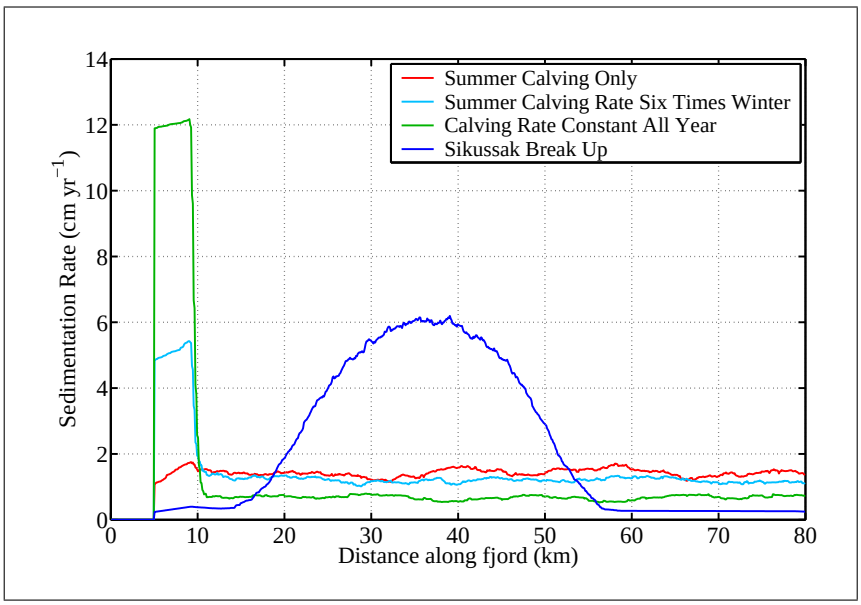

Figure 4.29: *Transect along the fjord (mean of central* 1 km *wide section) for mean iceberg size* = 294 m *and 'Warm' environmental conditions for the four seasonal calving rate variation scenarios.*

displaying the areas of high sedimentation, differences in areas of low sedimentation can now be determined. As in Figure 4.28, the glacier front is at a position of 5 km. It can be discerned that the build up of sediment in front of the glacier due to icebergs calved during the winter is higher when the calving rate is constant all year (b) that when the summer calving rate is six times the winter rate (c). This is intuitive since the calving rate will be higher in winter for the constant annual calving rate. Past a distance of approximately 6 km from the glacier front, the region of high sedimentation ends abruptly. The reason for such a sharp boundary between the high winter sedimentation and the lower 'all year' sedimentation is the additional 'dispersion distance', which is a constant 4 km up and down fjord of the edges of the iceberg. The slight spread of the falling edge, is due to the dispersion in iceberg lengths. The reason for the maximum sedimentation rate increasing slightly away from the glacier is because when the icebergs move, the overall effect is transit away from the glacier. Therefore over a period of time, the up-fjord limit of deposition will move away from the glacier front, depositing sediment 'ahead' of it, and 'behind' the down-fjord limit of deposition. Since the down-fjord limit of deposition is at some distance away from the glacier when an iceberg is produced, there is no 'cross-over' between up-fjord and down-fjord limits of deposition 'behind' the down-fjord limit. This leads to an increase with distance from the glacier front until the initial down-fjord limit of deposition.

In the region of lower 'all year' sedimentation (excluding the sikussak break up scenario), the order of highest to lowest sedimentation rate is: summer calving only, summer rate six times winter and finally calving constant all year round. This is because for the cases where no or fewer icebergs are produced in winter, the calving rate needs to be higher in summer to produce the same annual flux of icebergs. This leads to a higher iceberg density in the fjord and when the fjord freezes over and traps icebergs in one place over winter, results in higher sedimentation rates.

For the sikussak break up scenario, there is a strong peak in sedimentation rate at about 20–50 km along the fjord, due to the surge of icebergs produced over a short period of time. The position of this peak depends on when in the year the break up occurs relative to when the fjord freezes and traps the icebergs in one place over the winter. The spread in the peak is due to the time over which the icebergs are produced (in this case 28 days), as well as a dispersion due to the iceberg size distribution, as the smaller icebergs are affected more by wind and water forcing (Figure 4.24).

The across-fjord transects are calculated as the mean sedimentation rate along the whole length of the fjord, therefore they represent in integrated sedimentation rates over the whole fjord. Across-fjord transects are shown for the four calving rate seasonal variation scenarios in Figure 4.30. The distance across the fjord is measured

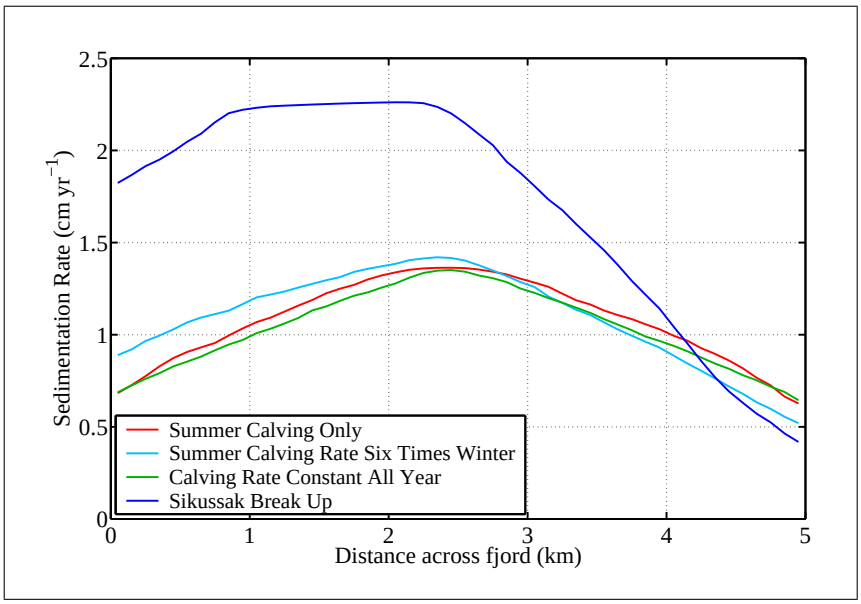

Figure 4.30: *Transect across the fjord (mean along whole length of fjord) for mean iceberg size*= 294 m *and 'Warm' environmental conditions for the four seasonal calving rate variation scenarios.*

from the western side. All four curves have a peak near the fjord centreline due to icebergs bouncing from one wall to the other and therefore spending more time in the middle than at either side (Figure 4.24). Out of all the seasonal calving rate variation

scenarios, the sikussak break up scenario leads to the highest total accumulation of sediment in the fjord. This is because the break up happens from 17$^{\text{th}}$ August to 13$^{\text{th}}$ September, so all the icebergs produced, i.e. 10 years' worth of icebergs, remain trapped in the fjord over winter.

The total volume of sediment is greatest where calving takes place in summer only, then where the summer calving rate is six times the winter rate, and the lowest accumulation rate in the whole fjord is where the calving rate is constant all year round. This is due to the density of icebergs in the fjord at the end of summer, when they are frozen in place for the winter: the higher the summer calving rate, the higher the annual deposition rate over the fjord. This will be counter balanced to a certain extent by the icebergs produced during winter, which melt next to the glacier front and are also included in the across-fjord mean, but the effect of higher summer calving rate is the dominant factor.

4.4.3.2 Variation of Climatic Conditions

To examine the effect of different climatic conditions, two extreme cases are investigated with the model: a 'Cold' and a 'Warm' scenario, as defined in Table 4.1. Along-fjord transects (mean of central 1 km wide section) comparing 'Cold' and 'Warm' environmental conditions, for a mean iceberg size of 173.3 m and the four seasonal calving rate variation scenarios are shown in Figure 4.31. Higher deposition rates oc-

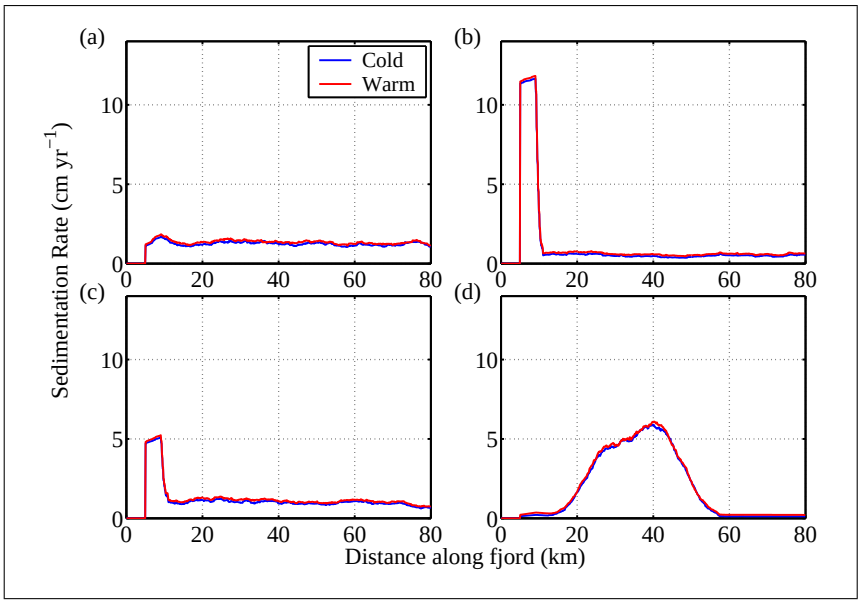

Figure 4.31: *Transect along the fjord (mean of central* 1 km *wide section) comparing 'Cold' and 'Warm' environmental conditions, for mean iceberg size of* 173.3 m *and the four seasonal calving rate variation scenarios (a) Summer calving only (b) Calving rate constant all year round (c) Summer calving rate 6 times winter rate (d) Sikussak break up event.*

cur for the 'Warm' scenario, and since the seeds for the random number generator used to calculate the forcing parameters are the same in both cases, the changes observed can be attributed to the different climatic conditions, rather than random variations between model runs. The difference is not easy to evaluate with the y-axis scale in Figure 4.31, so the same data is shown with a higher magnification in Figure 4.32. It

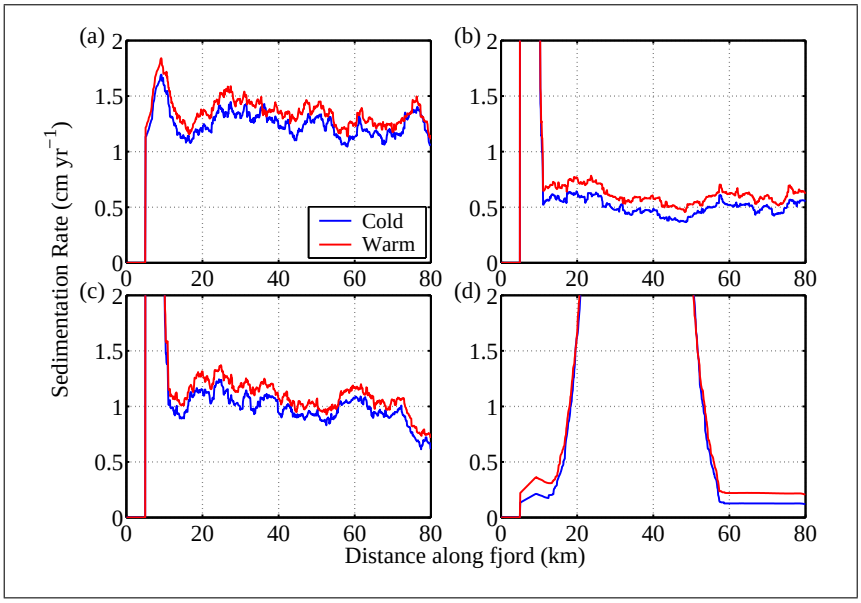

Figure 4.32: *Magnified transect along the fjord (mean of central 1 km wide section) comparing 'Cold' and 'Warm' environmental conditions, for mean iceberg size of 173.3 m and the four seasonal calving rate variation scenarios (a) Summer calving only (b) Calving rate constant all year round (c) Summer calving rate 6 times winter rate (d) Sikussak break up event.*

can clearly be seen that the deposition rate is approximately $0.1\,cm\,yr^{-1}$ higher for 'Warm' conditions than 'Cold' conditions. Slight fluctuations above and below this value are due to the iceberg sizes that deposited sediment at each point, since they determine whether the sedimentation rate is affected to a greater or lesser degree by the change in water temperature.

The across-fjord transects (mean along whole length of the fjord) comparing 'Cold' and 'Warm' environmental conditions, for a mean iceberg size of $173.3\,m$ and the four seasonal calving rates, are shown in Figure 4.33. Since the across-fjord transects are the mean sedimentation rate over the whole length of the fjord, Figure 4.33 provides an integrated view of the effect changing climatic conditions on the accumulation rate in the fjord. The maximum increase in sedimentation in the 'Warm' scenario is approximately $0.1\,cm\,yr^{-1}$ and this increase is approximately the same for the different seasonal calving rate variation scenarios. It may be expected that the scenarios with the highest iceberg density in summer, i.e. highest summer calving rate, would be the

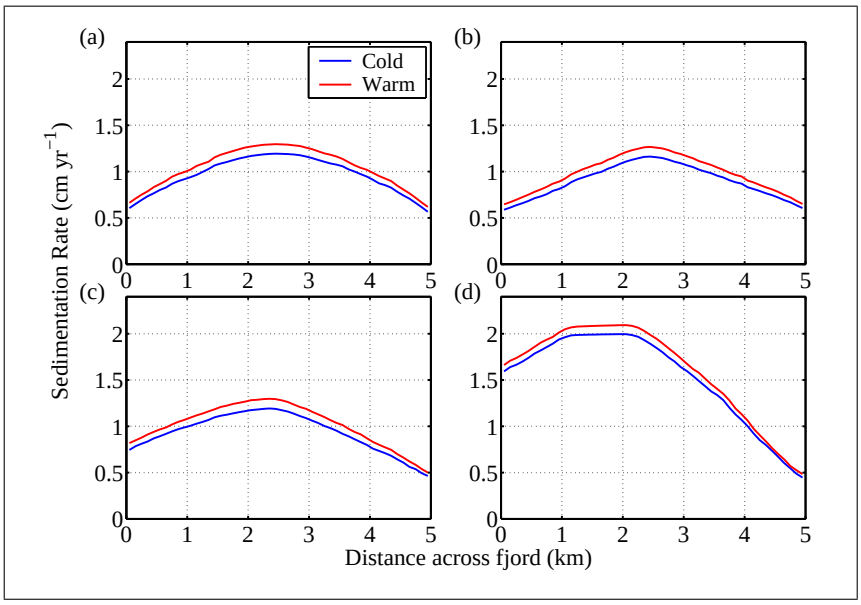

Figure 4.33: *Transect across the fjord (mean along whole length of fjord) comparing 'Cold' and 'Warm' environmental conditions, for mean iceberg size of* 173.3 m *and the four seasonal calving rate variation scenarios (a) Summer calving only (b) Calving rate constant all year round (c) Summer calving rate 6 times winter rate (d) Sikussak break up event.*

most affected by increased summer sea temperatures, however, this effect is imperceptible.

4.4.3.3 Variation of Mean Iceberg Size

The iceberg size distribution in Kangerdlugssuaq Fjord is likely to be similar to one of the two log-normal distributions discussed in Section 4.3.3: with a mean of either 173.3 m or 294 m. The effect of changing the iceberg size distribution is investigated, along with the influence of climatic conditions on different iceberg size distributions.

The along-fjord transect (mean of central 1 km wide section) comparing mean iceberg size of either 173.3 m and 294 m and 'Cold' and 'Warm' environmental conditions, for the four seasonal calving rate variation scenarios are shown in Figure 4.34. At this scale, differences in sedimentation rate for the sikussak break up event for the two mean iceberg sizes can be seen. The shapes of the peak sedimentation rate are different for the different iceberg size distributions, even though the forcing parameters are the same. The explanation for this is, for example, in the case of the iceberg size distribution with the larger mean (294 m), more deposition occurs because more of the icebergs are affected by the warmer water below 100 m (see Figure 4.14). At this scale it is difficult to see the differences for the other three seasonal calving rate variation scenarios, therefore magnified versions of the along-fjord transects are shown in Figure 4.35. The fluctuations in the sedimentation rate along the fjord for the two

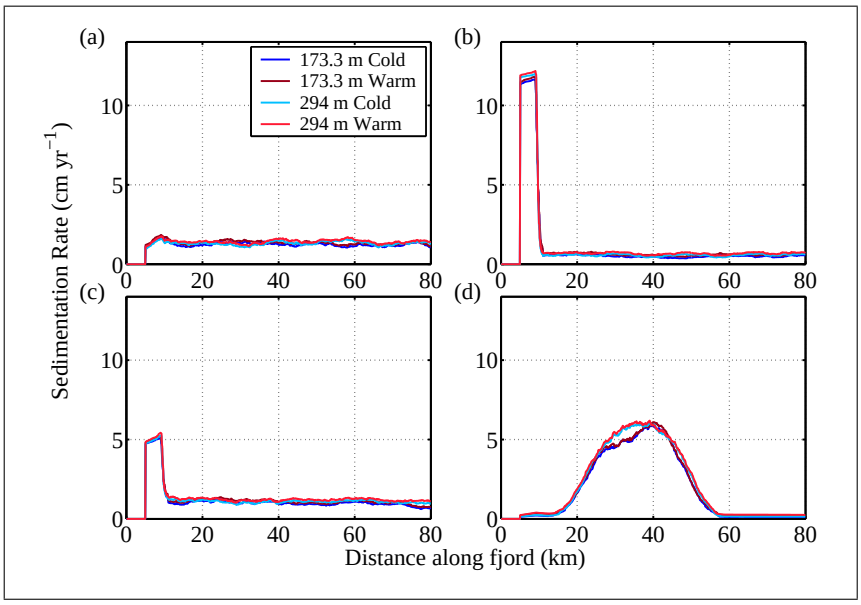

Figure 4.34: *Transect along the fjord (mean of central* 1 *km wide section) comparing mean iceberg size of* 173.3 *m and* 294 *m and 'Cold' and 'Warm' environmental conditions, for the four seasonal calving rate variation scenarios (a) Summer calving only (b) Calving rate constant all year round (c) Summer calving rate 6 times winter rate (d) Sikussak break up event.*

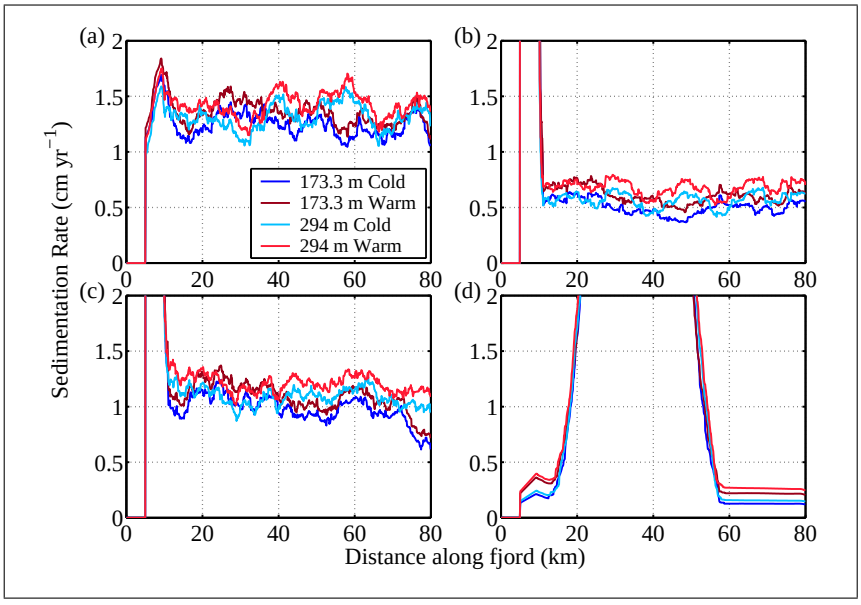

Figure 4.35: *Magnified transect along the fjord (mean of central* 1 *km wide section) comparing mean iceberg size of* 173.3 *m and* 294 *m and 'Cold' and 'Warm' environmental conditions, for the four seasonal calving rate variation scenarios (a) Summer calving only (b) Calving rate constant all year round (c) Summer calving rate 6 times winter rate (d) Sikussak break up event.*

size distributions make it difficult to tell which size distribution has the higher sedimentation rate. The fluctuations are due to different sizes of icebergs being present in the fjord, which are affected differently by the random forcing parameters (which are the same). However, the sedimentation rates for each size distribution under different climatic conditions show strong correlation, as discussed in Section 4.4.3.2, with small differences due to different sized icebergs being affected to a greater or lesser extent by the difference in temperature.

Transects across the fjord (mean along whole length of fjord) comparing a mean iceberg size of 173.3 m and 294 m and 'Cold' and 'Warm' environmental conditions, for the four seasonal calving rate variation scenarios are shown in Figure 4.36. In the

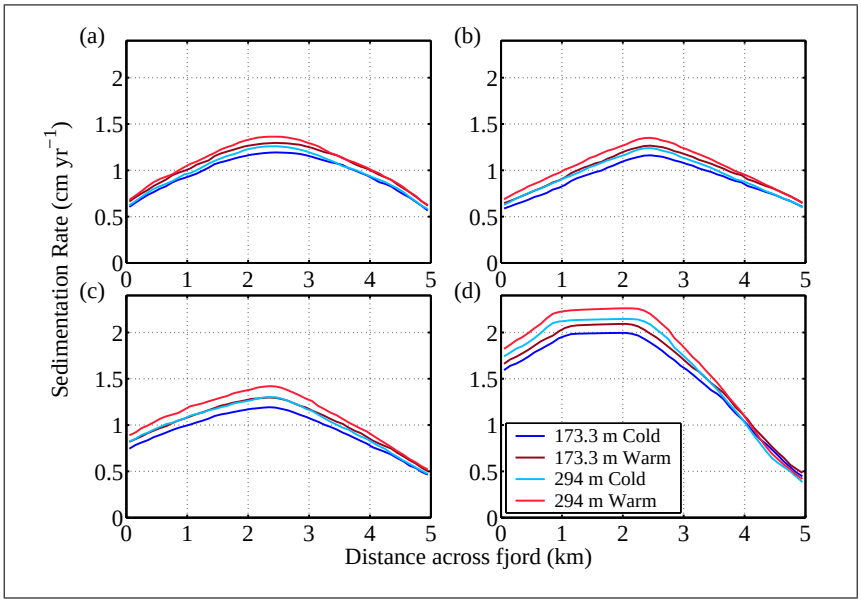

Figure 4.36: *Transects across the fjord (mean along whole length) comparing mean iceberg size of* 173.3 m *and* 294 m *and 'Cold' and 'Warm' environmental conditions, for the four seasonal calving rate variation scenarios (a) Summer calving only (b) Calving rate constant all year round (c) Summer calving rate 6 times winter rate (d) Sikussak break up event.*

across-fjord transects, the integrated effect of the different iceberg size distributions can be seen and the size distribution with the larger mean has a higher deposition rate for both climate conditions. The effect of the different size distributions on the sedimentation rate is shown in Table 4.2.

seasonal calving rate variation scenarios	% increased deposition rate (mean size from 173.3 m to 294 m)
Summer Calving Only	5.8
Calving constant all year	7.1
Summer 6 times winter rate	9.0
Sikussak release	7.7

Table 4.2: *Effect of iceberg size distribution on sedimentation rate for the four seasonal calving rate variation scenarios.*

It is important to note that the difference in all cases is greater than the difference in iceberg flux between the two distributions (Figure 4.27), although this may account for the seemingly larger effect on scenario (b) and (c) than (a). It may be expected that the greatest effect would be for the calving rate scenario where the iceberg density is greatest. Therefore in order of most to least affected would be: sikussak release, summer calving only, summer calving 6 times winter rate, constant calving all year round. However, this is not seen due to the small overall effect of changing the iceberg size distribution and the difference in the volume flux produced by the model for each of the different seasonal calving rate variation scenarios, for different iceberg size distributions.

4.4.4 Proportion of Icebergs Reaching Fjord Mouth

For iceberg drift models in the open ocean, the number of icebergs that exit the fjord (80 km long) compared to the number calved, or the proportion of icebergs that melt completely during transit through the fjord, are required. *SedBerg* Model results for the number of icebergs exiting the fjord as percentages of the total number of icebergs calved are shown in Figure 4.37. Two iceberg size distributions with means of 173.3 m and 294 m (Section 4.3.3), under both 'Cold' and 'Warm' environmental conditions (Table 4.1) for the four seasonal calving rate variation scenarios: (a) Summer calving only, (b) Calving rate constant all year round, (c) Summer calving rate 6 times winter rate and (d) Sikussak break-up event, are considered. The greatest influence on the percentage of icebergs exiting the fjord is the iceberg size distribution, with a much greater percentage melting away in the fjord for the size distribution with a smaller mean. Within the different calving rate senarios, the highest percentage of icebergs reach the mouth of the fjord when the calving rate is constant throughout the year. This is because the summer calving rate is lowest in this scenario, so the density of icebergs when they are frozen in place for the winter is the lowest of all the scenarios. The number of icebergs frozen in the fjord over winter has the biggest impact on the

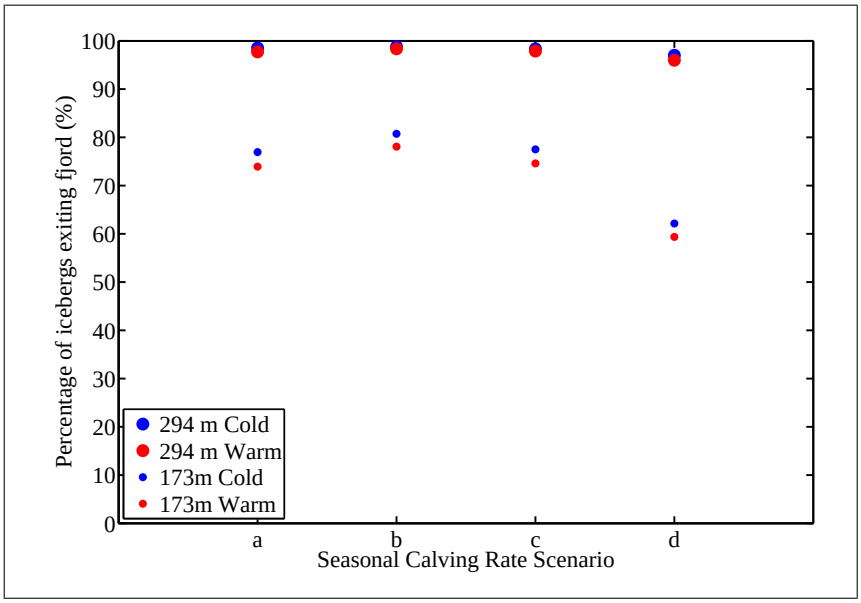

Figure 4.37: *Percentage of icebergs exiting the fjord (80 km long) compared to the total number calved for a mean iceberg size of* 173.3 *m and* 294 *m under both 'Cold' and 'Warm' environmental conditions for the four seasonal calving rate variation scenarios (a) Summer calving only (b) Calving rate constant all year round (c) Summer calving rate 6 times winter rate (d) Sikussak break-up event.*

percentage of icebergs melted completely during transit through the fjord. The sikussak break-up event scenario has the highest percentage of icebergs melted completely in the fjord. This is because 10 years' worth of icebergs are calved over a period of 28 days from 17$^{\text{th}}$ August to 13$^{\text{th}}$ September and the majority of these icebergs remain frozen in the fjord over the winter. More icebergs melt in the fjord under 'Warm' than 'Cold' environmental conditions, although this is a secondary effect compared with the influence of the mean iceberg size and the calving rate scenario.

4.5 Sediment Accumulation over the Past 1500 years

The sedimentation rates produced by the *SedBerg* Model for 10 simulated years under various environmental conditions can be summed to generate sediment accumulation rates over the past 1500 years in Kangerdlugssuaq Fjord. As discussed in Section 4.1, the past 1500 years encompasses several different climatic regimes. These are represented by varying fractions of the 'Cold' and 'Warm' climatic regimes. These two climate patterns were applied to the iceberg model in Section 4.4.3. They are representative of Polar Water filling the fjord and Atlantic Intermediate Water extending well into the fjord, respectively. From year to year, conditions in the fjord fluctuate, so the different climate intervals are simulated by different fractions of 'Cold' and 'Warm'

regimes, to reproduce the corresponding climate. The fractions used are as follows:

	Time Period A.D.	Fraction of 'Cold' climatic conditions	Fraction of 'Warm' climatic conditions
Pre-MWP	500–729	0.75	0.25
MWP	730–1100	0	1
TP	1101–1629	0.5	0.5
LIA	1630–1900	1	0
Modern	1901–1993	0.5	0.5

Table 4.3: *Fraction of 'Cold' and 'Warm' climatic conditions over the past 1500 years.*

The seasonal variation of the calving rate will have differed for these five intervals:

1. During the Pre-MWP, due to winter sea ice, the calving rate scenario is likely to have been similar to today, with the summer rate six times the winter rate and sea ice freezing the icebergs in place over the winter.
2. Sea ice was less extensive than today during the MWP (Jennings and Weiner, 1996), so a constant calving rate throughout the year is assumed and the icebergs are assumed to move throughout the year.
3. The Transition Period (TP) was an interval of varying climatic conditions with fluctuating sea ice cover from year to year. The seasonal calving rate variation scenario chosen is summer calving rate six times the winter rate, with sea ice in winter.
4. Due to abundant sea ice during the LIA, icebergs would have spent long periods of time trapped in the sikussak, so the most appropriate calving rate scenario is the sikussak release scenario.
5. The modern interval is likely to have a summer calving rate six times the winter rate, due to the presence of sea ice in winter, as is the case for Jakobshaven Glacier in West Greenland (Sohn *et al.*, 1998).

The iceberg size distribution adopted is lognormal with mean size (defined in Section 2.3) of $294\,m$ and standard deviation of $164.2\,m$.

During the TP, the pre-MWP and the modern interval, there was a sikussak in front of Kangerdlugssuaq Gletscher, but it was permeable enough (presumably because of limited thickness) to allow some icebergs to pass through and reach the fjord still containing basal ice (as observed by Syvitski *et al.* (1996)). Therefore, the ratio of 'basal' to 'no basal' model runs used (as defined in Section 4.3.4) is 1:10, or 10% 'basal' runs). During the LIA, it is assumed that the sikussak was thicker and therefore more

of an impedance to the icebergs. Its presence in front of Kangerdlugssuaq Gletscher, as well as sikussaks possibly forming at other outlet glaciers, is likely to have resulted in only a very small percentage of icebergs reaching the fjord containing basal sediment. Therefore 5% 'basal' runs are assumed, and this is due to icebergs containing basal ice being released during sikussak break-up events. During the MWP, the sikussak is likely to have broken up completely at times, therefore icebergs containing basal sediment would have been free to drift through the fjord. However, there were also colder periods, when the sikussak may have reformed. Therefore, the estimated percentages of 'basal' and 'no basal' model runs used are 50% each.

The TP and the modern interval have the same climatic conditions, percentage of 'basal' runs and seasonal calving rate variation scenario. Therefore, the sedimentation in Kangerdlugssuaq Fjord over the past 1500 years can be split into four different sedimentation regimes. Maps of the sedimentation rate, in $cm\,yr^{-1}$, for each of these regimes are shown in Figure 4.38. The glacier front is at $5\,km$ down the fjord, shown in blue at the top of each map. Note that the scale of the sedimentation rate is different for (b) and (c) compared to (a) and (d). The sedimentation rates for Pre-MWP (a) and TP/modern (d) are very similar (although (d) is slightly higher), because these intervals have the same seasonal calving rate variation scenario, and only a small difference between the ratio of 'Cold' to 'Warm' climatic conditions. The sedimentation map shown for the LIA (c) is the result of just one sikussak break up. Many such break ups occurring at slightly different times of year (determining the deposition peak) would lead to a smoother sedimentation pattern over the whole fjord, with a rate over the whole fjord lower than the peak rate for one release event. By calculating an across-fjord transect of mean sedimentation rate along the length of the fjord, the peak deposition rate (near the centre) is approximately $3.5\,cm\,yr^{-1}$. Peak sedimentation rates of approximately $7\,cm\,yr^{-1}$ occur during the MWP, so rates are approximately double those during the other time periods. This is in agreement with the relative sedimentation rates during the MWP and the other intervals estimated from the KF1 core record (discussed in Section 4.2).

However, the magnitudes of the modelled sedimentation rates are considerably higher— between 5 and 5.8 times the observed rates. An explanation for this discrepancy is due to the location of core KF1 at the mouth of Kangerdlugssuaq Fjord (Figure 4.3(a)). Here the fjord widens to $12\,km$ (the effective width not including the steep edges of the fjord), so 2.4 times the modelled width of $5\,km$. Syvitski *et al.* (1996) observed the spatial distribution of icebergs along the fjord and from this they estimated that sedimentation rates at the head of the fjord (KF4) would be 3.9 times higher than at the mouth (KF1). This takes into account the widening of the fjord at KF1, allowing the icebergs to spread over a larger width, as well as higher velocity

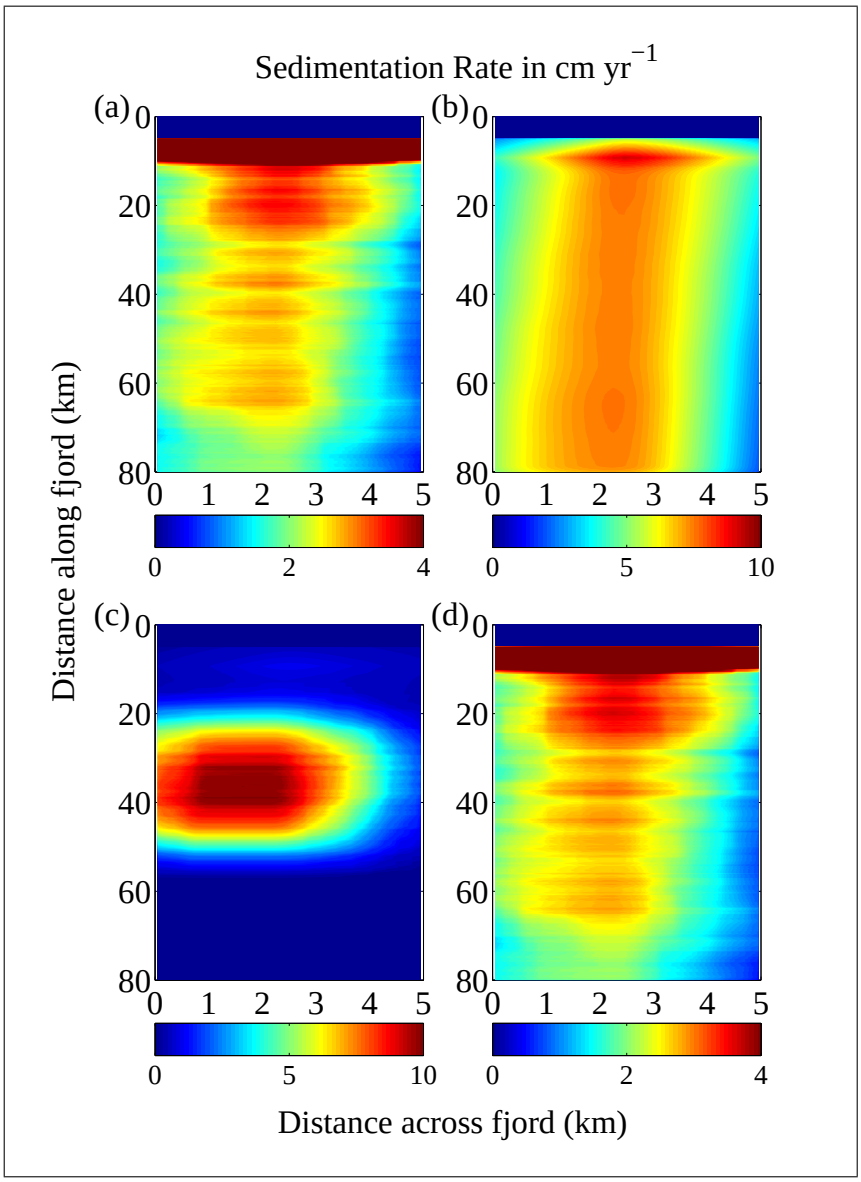

Figure 4.38: *Maps of sedimentation rate over Kangerdlugssuaq Fjord (North is at the top of the page) for mean iceberg size= 294 m, appropriate ratios of climatic conditions from Table 4.3, percentage of 'basal' runs and seasonal calving rate variation scenarios as described in the text for the time intervals (a) Pre-MWP (b) MWP (c) LIA (d) TP and Modern. Sedimentation rate is shown by the colour bar below each sediment map. Note that the scales differ between maps.*

water currents at the mouth of the fjord transporting icebergs out to sea more quickly. This effect is not simulated in the model, as the fjord width is assumed to be a constant of 5 *km* and the water velocity is assumed constant along the length of the fjord.

If the model results are adjusted by the Syvitski *et al.* (1996) factor, the magnitude of the modelled sedimentation rates become 1.5 times the observed rates, so in reasonable agreement with them. This is certainly within the errors of the estimation

of parameters such as the calving rate, which is assumed constant over the past 1500 years in these model runs. Even the estimation of the present day calving rate is subject to large uncertainties, given the small number of measurements over a relatively short period of time for a process which occurs as discrete calving events rather than a continuous mass loss. Therefore, it makes sense to refer to average calving rates over a relatively long period of time (a number of years) due to the discrete and sporadic nature of iceberg calving. It is highly probable that the long term average calving rate fluctuated over the past 1500 years, and that the value estimated for use in the model ($15\,km^3yr^{-1}$), is not entirely characteristic of the rate over the whole time period.

Across-fjord transects, calculated as the mean along the length of the fjord ($80\,km$), represent integrated accumulation rates assuming a constant sedimentation rate along the whole fjord. If these transects are divided by the Syvitski *et al.* (1996) factor (3.9), this provides an estimate of the accumulation rate at core KF1. To simulate the past 1500 years, the appropriate across-fjord transect of sedimentation rate for each of the five time intervals is converted into accumulation by multiplying by the time spanned by the respective time interval. The accumulation during each of the time intervals calculated in this way is shown as a cross section through the across-fjord transect in Figure 4.39. The sediment thickness deposited during the MWP by the model (at the

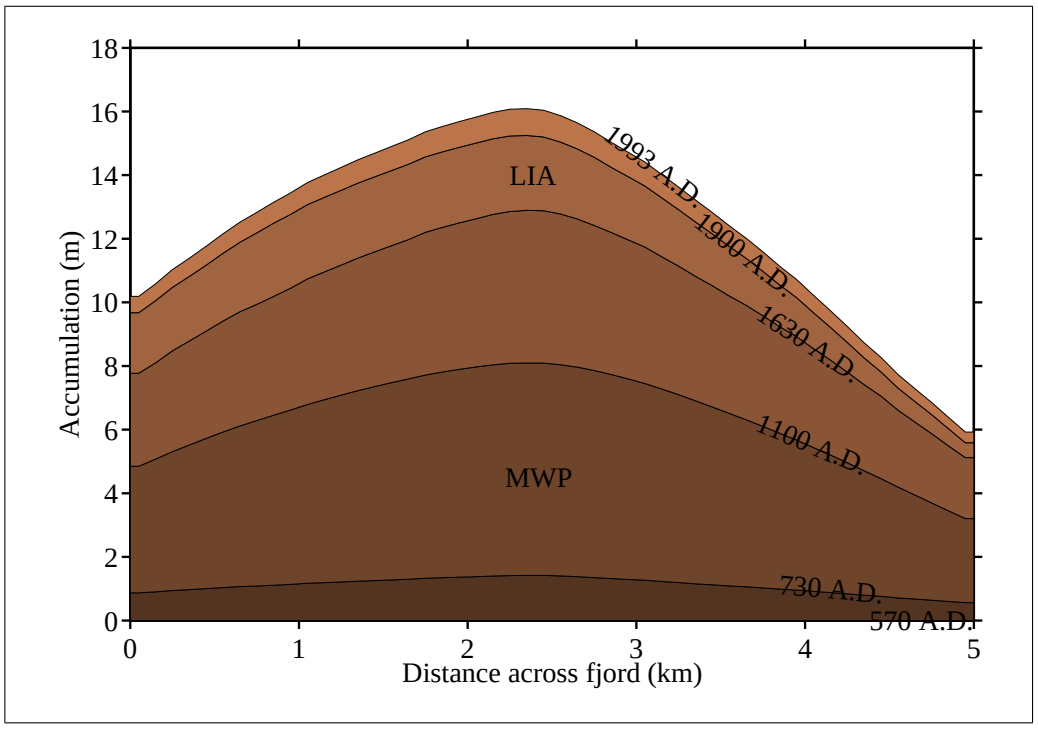

Figure 4.39: *Simulated cross section of sediment accumulation across the fjord at the location of core KF1 (Figure 4.3(a)). The layers deposited during the LIA and MWP are marked, as well as the dates of the layer boundaries.*

peak of the across-fjord transect) is 663 cm, compared to an estimated 444 cm in core KF1. From 1100 A.D. to present, the model deposited 796 cm and for the same period in core KF1 the sediment thickness is estimated to be 583 cm. Therefore, the model over-estimates the sediment accumulation by 37–49%. This indicates that the model performs well in comparison with the sedimentary record and reproduces accumulation rates with an acceptable level of agreement.

The *SedBerg* Model predicts a variation in the sedimentation rate over the last 1500 years, with the MWP a period of higher sedimentation rates. This is consistent with the sedimentary record observed by Jennings and Weiner (1996) in Nansen Fjord, and could be confirmed by dating additional samples through the KF1 core.

4.6 Summary

In this chapter, the *SedBerg* Model introduced in Chapter 2 has been applied to Kangerdlugssuaq Fjord in East Greenland, to simulate the sediment accumulation rate over the past 1500 years. Syvitski *et al.* (1996) measured the accumulation from core KF1, 50 km from the head of the fjord, to be 1139 cm over this time period. Using the assumption that the spatial variation of sedimentation rate could be based on the observed spatial distribution of icebergs, as proposed by Syvitski *et al.* (1996), the accumulation rate produced with the *SedBerg* Model at KF1 is 1674 cm. This demonstrates a reasonable concurrence with the sedimentary record.

During the MWP, the climate was stable and warmer than the present in East Greenland with less extensive sea ice. When these conditions are applied to the Model, higher sedimentation rates are predicted. Since there is only one dated sample from the base of the KF1 core, it is not possible to verify this. However, in future more samples could be dated along the core to confirm or reject this hypothesis. It is proposed here that, during the MWP, the intermittent absence of a sikussak would have allowed icebergs containing basal debris to drift through the fjord. The massive diamicton deposited would have had a larger mean grain size than sediment deposited during the subsequent period, when the sikussak was present more frequently, and this can be distinguished in core KF1 (Figure 4.4). If the upper turbidite layer is taken to be the end of the MWP, the ratio of accumulation observed in the core during the MWP compared to the subsequent period is 0.76, compared to a modelled ratio of 0.83. These two values show remarkable agreement, which provides confidence in the climatic conditions over the past 1500 years that were rationalised in Section 4.3.

Due to the lack of available input data, some model variables have to be inferred from the sedimentary record. This may lead to circular reasoning, as assumptions for model inputs are made based on the sedimentary record and then outputs are

compared back to the observations for verification. It is important to be aware of this, although to a certain extent it is an unavoidable problem.

The *SedBerg* Model is capable of producing sediment accumulation profiles with high resolution, which can be compared to the sedimentary record. At present insufficient samples have been dated from core KF1 to resolve the variation in sedimentation rate over the past 1500 years in Kangerdlugssuaq Fjord. However, the accumulation rates were high enough to enable the identification of climatic changes over shorter timescales if the data were available. The model has proved to be a useful tool for testing hypotheses of the effect of varying environmental conditions on the sedimentation rate from iceberg-rafting, and provides realistic estimates of accumulation rates for the case study explored in this chapter.

Chapter 5

Case Study for *SedPlume* Model: Alaskan Tidewater Glaciers

5.1 Introduction

Alaskan fjords accommodating a tidewater glacier at their head are good examples of meltwater-dominated glacimarine sedimentary environments (Dowdeswell *et al.*, 1998). A proportion of iceberg-rafted debris is also deposited in Alaskan fjords, but the volume can be up to several orders of magnitude less than meltwater dispersal of glacial sediment. For example, Hunter *et al.* (1996) studied three glaciers in Glacier Bay, Alaska (Grand Pacific, Margerie and Muir) and found iceberg-rafted sediment fluxes to be 10^5 to $10^6\,m^3a^{-1}$, compared to glaciofluvial sediment fluxes of 10^6 to $10^7\,m^3a^{-1}$. Therefore transportation of glacial debris by meltwater has a much greater influence on fjord sedimentation than the input of sediment from iceberg-rafting in Alaskan fjords (see Figure 1.4 in Section 1.3).

McBride Glacier was chosen as the case study for the *SedPlume* Model. McBride Glacier is located at the head of McBride Inlet, $58^\circ\,50'N$ $136^\circ\,00'W$, which is a tributary to Muir Inlet in Glacier Bay National Park, South-East Alaska. A satellite image showing the location of McBride Glacier within Glacier Bay is shown in Figure 5.1. McBride Glacier is a tidewater glacier with a single subglacial tunnel as the dominant source of both meltwater and sediment to the fjord. The glacier is $24\,km$ long and flows from an altitude of $2100\,m$ to terminate at a grounded ice front in the extensive fjord system of Glacier Bay, Alaska. The glacier drainage basin measured from maps published by Brown *et al.* (1982) is $\sim 185\,km^2$, with the area covered by the glacier $\sim 148\,km^2$.

The glacier underwent rapid retreat from 1963 to 1986, to reveal a 90–100 m deep basin, which now forms a tributary fjord leading into Muir Inlet. A map of the position

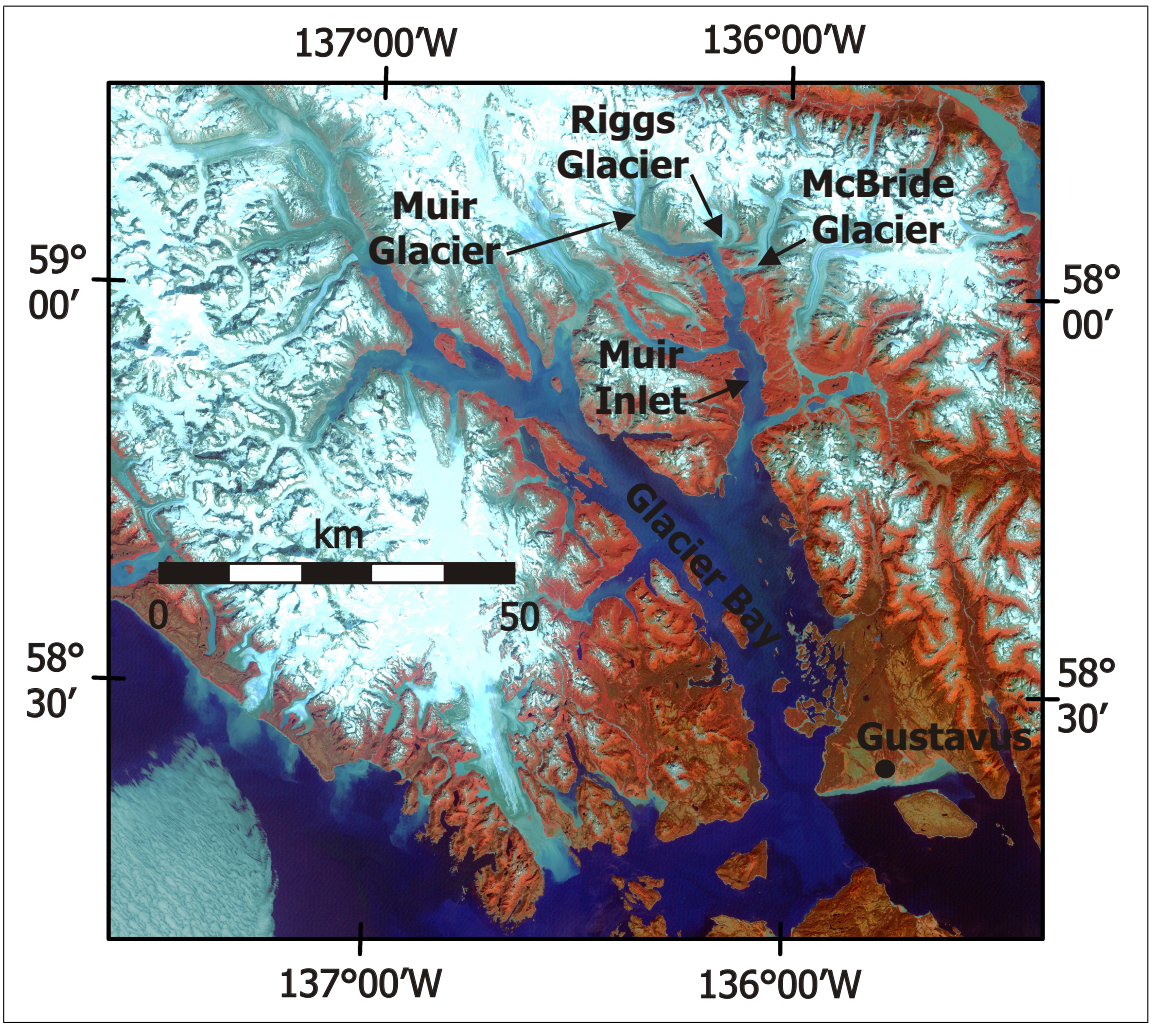

Figure 5.1: *Landsat ETM+ false colour composite image (Bands 4–3–2, Resolution 30 m) of Glacier Bay National Park, showing McBride, Riggs and Muir Glaciers, Muir Inlet, Glacier Bay and Gustavus, the location of a weather station. Source for this data set was the Global Land Cover Facility, www.landcover.org.*

of the glacier terminus from 1946 to 1987, as well as the bathymetry of McBride Inlet in 1987 and the position of the upwelling at the terminus from 1984 to 1987 (from Cowan and Powell, 1991) is shown in Figure 5.2. The subglacial tunnel is estimated to be at a water depth of 40 m and the meltwater plume is observed to surface less than 100 m from the glacier front (Cowan and Powell, 1991). Powell and Cowan (1987) reported that when high stream discharge coincides with low tide, an upwelling can be seen at the surface. During a 4 day period of high discharge in July 1985, a sediment-charged upwelling was observed 0.5 m above the water surface next to the glacier front, which was accompanied by a roaring sound that was heard within 1 km of the glacier.

There is an extensive data set for sediment deposition in McBride Inlet. Ross Powell and Ellen Cowan carried out fieldwork between 1984 and 1987, and during this

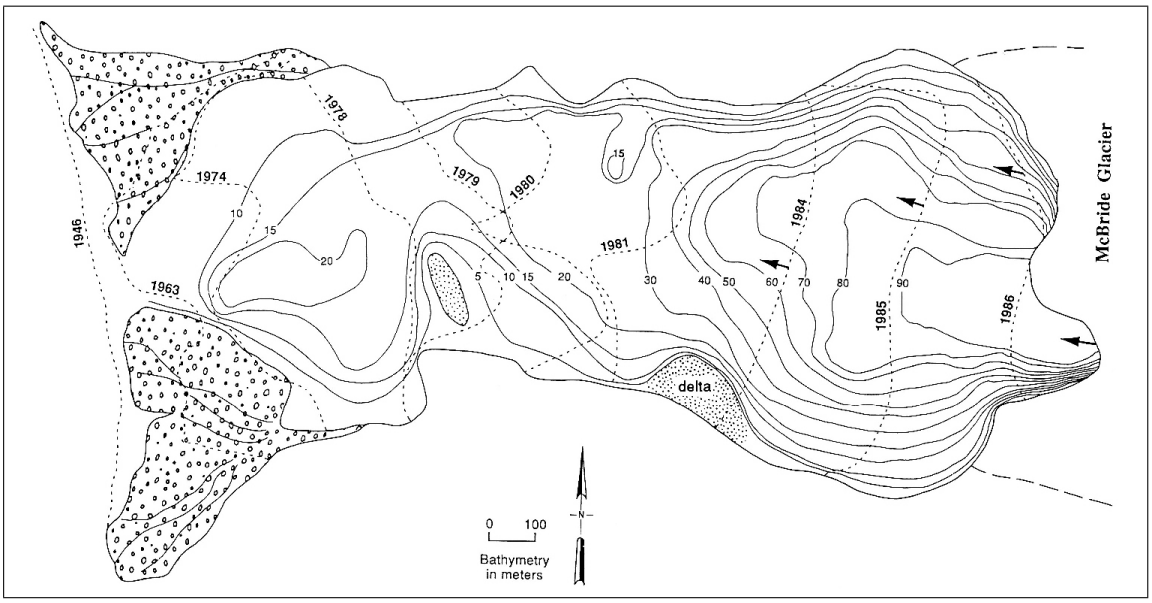

Figure 5.2: *Map of bathymetry in McBride Inlet in 1987, also showing the position of the glacier terminus from 1946 to 1987. The arrows indicate the position of the upwelling at the terminus from 1984 to 1987 (from Cowan and Powell, 1991).*

time a wide range of data was collected including sediment trap measurements, echo sounder profiles, as well as air temperature and precipitation data, which have been comprehensively published in journal articles and conference proceedings. However, it is not possible to measure some of the model input parameters at McBride Glacier for reasons of accessibility, for example the meltwater flux from the subglacial conduit. Values for such parameters are instead estimated from measurements at similar glaciers in the Glacier Bay region where possible. If none exist, then values are inferred from measurements at other glaciers around the world, which have relatively similar characteristics to McBride Glacier.

5.2 Input Parameters

5.2.1 Initial Volume Flux

Since it is not possible to make direct measurements of the flux of water flowing from the submerged subglacial conduit at McBride Glacier, it was necessary to look at measurements collected from other glaciers to deduce a reasonable estimate. In Muir Inlet (see Figure 5.1) Matthews and Quinlan (1975) found that the water emerging from the subglacial tunnel is composed of a mixture of meltwater and rainwater. Total runoff was observed to be subject to daily, seasonal and annual fluctuations, with a peak in spring/summer due to melting and another in autumn due to precipitation. At

the head of Muir Inlet is Muir Glacier, where Mackiewicz *et al.* (1984) observed that glacial melt is the dominant control on meltwater discharge. The flux was found to vary unimodally, with peak discharge in the autumn (October). Diurnal fluctuations were recorded to appear early in summer, when maximum discharges occurred in early evening. During the winter season the meltwater originates from basal sources and Mackiewicz *et al.* (1984) found discharges fell to around 10% compared to summer, with no diurnal fluctuations. In Glacier Bay the melt season varies from year to year, but usually begins in early May and lasts into September (Cowan and Powell, 1990). Large rain storms have been observed to generate high sedimentation rates, during which a large proportion of the annual sedimentation takes place (Denner *et al.*, 1999).

There is frequent and heavy precipitation in the Glacier Bay region of Alaska. Near the entrance to Glacier Bay at Gustavus, annual precipitation for 1985 was $1449\,mm$ at sea level (Cowan *et al.*, 1988). Cowan and Powell (1991) measured rainfall from the end of May until the end of August 1986, when there were episodic storm events with precipitation rates of up to $42\,mm\,day^{-1}$, with August being the wettest month. In 1986, an intense period of sedimentation was observed in McBride Inlet by Cowan *et al.* (1988). It was interpreted to have been induced by a 48 hour rainstorm, which preceded the sedimentation event. The total rainfall for the 48 hour period from the 27^{th} to 28^{th} August was measured to be $61.2\,mm$ at sea level (Cowan *et al.*, 1988) and the rainfall could have been three times this at elevations above $1000\,m$ (Murphy and Schamach, 1966). Sedimentation rates were observed to be five times higher then the previously recorded maximum rate at a distal location on 30^{th} August and three times higher than the previous maximum at a proximal location during the rain event. A sediment trap $5\,m$ above the bottom at a distance of $700\,m$ from the subglacial stream collected $15.4\,cm$ of sediment in 19 hours (from 1755 on 29^{th} August to 1310 on 30^{th} August), which is equivalent to $19.5\,cm\,day^{-1}$, and it is likely that sedimentation occurred at this rate for 3-4 days. By comparison, the annual sediment accumulation at 700 m from the subglacial stream was measured to be approximately $2\,m\,yr^{-1}$ (Cowan and Powell, 1991). The *SedPlume* Model will be run for such an extreme event, since deposition rates at McBride Glacier have been observed to be highly episodic with high rainfall events accounting for a significant proportion of the annual sediment budget (Cowan *et al.*, 1988). As a first approximation, the maximum flux of water flowing from the McBride Glacier subglacial conduit during a storm event can be estimated from the sum of the total melt over the glacier area and the total rainwater run off over the area of the drainage basin.

Since very little snow was present on the ablation zone of the glacier when the 1986 storm occurred on McBride Glacier, the rainwater was able to drain extremely rapidly

through the englacial and subglacial conduits, resulting in high rates of erosion and transport of subglacial sediment. It seems reasonable to draw a comparison with an intense storm-discharge event observed by Denner *et al.* (1999) at Matanuska Glacier in September 1995.

Matanuska Glacier is located in the Chugach Mountains of south-central Alaska. Denner *et al.* (1999) collected stream flow and suspended sediment data at the ice margin and from a stream gauge $500\,m$ from the ice margin, as well as meteorological data. The drainage basin area of Matanuska Glacier is $647\,km^2$, approximately 3.5 times the drainage basin area of McBride Glacier, with the glacier covering an area of $362\,km^2$, 2.5 times that of McBride Glacier. In particular, this study investigated the hydrologic-system response to intense rain events at different times of year.

One of these events occurred over 2 days in September 1995 during which $56\,mm$ of rainfall was measured near the stream gauging station at the glacier front. The instantaneous peak discharge flow at the gauging station was $234\,m^3s^{-1}$ on 22^{nd} September, which is much higher than the previous summer maximum of $143\,m^3s^{-1}$ which occurred on the 6^{th} July. In June 1997 there was another storm, during which $28\,mm$ of rain fell in 48 hours. The response of the glacial stream discharge to this smaller storm event was much less pronounced compared to the September 1995 storm-discharge event.

This study demonstrates the variability of the response of the glacial hydrologic system throughout the annual cycle due to factors such as overlying snow, and the state of the englacial and subglacial drainage system. Of interest to this study, they found that the total specific storm run off for 9 days after the September storm event was equal to the estimated average rainfall over the watershed over the same period, although the precipitation over the basin was based on extrapolation of limited data. Therefore, it is assumed that the total specific run off equals the average rainfall over the watershed as was the case for Matanuska Glacier.

For such a storm event, the rainfall measured by Cowan and Powell (1991) can be taken as representative of the rainfall below $1000\,m$ and three times that value can be taken as the rainfall above $1000\,m$ (Murphy and Schamach, 1966). The drainage basin area measured from maps published by Brown *et al.* (1982) at elevations $< 1000\,m$ was found to be approximately $50\,km^2$ and at elevations greater than $1000\,m$ was found to be approximately $135\,km^2$, giving a total drainage basin area of approximately $185\,km^2$.

If the rainfall values are multiplied by the appropriate drainage basin area above and below $1000\,m$, a rainfall flux of $161\,m^3s^{-1}$ over 2 days is found. To find the resulting stream flow depends on the structure of the hydrologic system and the storage time within the glacier. In the absence of further information, it is assumed that the period of increased discharge due to the storm will be a few days, with a sharp peak, as

for Matanuska Glacier. Suspended sediment concentration profiles were recorded at stations $400\,m$ and $700\,m$ from the ice front on the two days after the event. On the 29^{th} August, a sediment-rich interflow was observed with sediment concentrations up to $6\,kg\,m^{-3}$ at $400\,m$ and $700\,m$ from the glacier. On the 30^{th} August the interflows were replaced with an overflow plume $14\,m$ thick, still with relatively high sediment concentrations between 1.8 to $2.7\,kg\,m^{-3}$ but lower than the peak level. Therefore, if the flood event is assumed to last 2 days, this results in a volume flux from the subglacial conduit of $161\,m^3s^{-1}$ due to rainfall.

In addition, there will be a contribution to the subglacial discharge due to glacier melt. There are measurements of three different glaciers in Alaska, which can be used to estimate of the meltwater flux from McBride Glacier, if the observations are scaled up/down depending on the relative area compared to McBride Glacier.

Measurements of glacial streams from grounded glaciers in Glacier Bay were collected by Phillips *et al.* (1991) in July 1986, who observed the water and sediment fluxes from one of the two glacier-fed meltwater streams on the delta in front of Riggs Glacier. Riggs Glacier is situated adjacent to McBride Glacier to the north. It has a comparable length to McBride Glacier, although it is slightly narrower, so has a slightly smaller surface area. At the beginning of July, the discharge of the South Stream in 1986 was observed to vary between 4 and $12\,m^3s^{-1}$, depending on the tidal cycle. There are two meltwater streams — the North Stream has approximately double the flux of the South Stream. The periods over which the measurements were collected were dry, therefore rainwater did not play an important role in the observed fluxes. However, since the discharge was measured at the stream mouth as the stream entered the fjord, the measurements were strongly affected by tidal fluctuations. Even so, taking the mean of the observed minimum and maximum for the South Stream ($8\,m^3s^{-1}$), gives an approximate value of $24\,m^3s^{-1}$ for the total meltwater discharge from the North and South streams. The meltwater discharge at McBride Glacier is likely to be of this order of magnitude under similar climatic conditions.

Elsewhere in Alaska, Anderson *et al.* (1999) collected measurements at the single outlet stream of Bench Glacier, in the Chugach Mountains, from 12^{th} to the 28^{th} June 1996. The glacier is considerably smaller than McBride Glacier, extending over an area of $9\,km^2$, with a total drainage basin area of $12.5\,km^2$. They found maximum discharges of order $10\,m^3s^{-1}$ as the subglacial drainage system shifted from a distributed system to a more efficient conduit system. They also calculated the meltwater production from snow- and ice-melt contributions, using measurements of snow and ice temperature. They found melt rates fluctuated from zero during freezing nights to approximately $10\,m^3s^{-1}$ on clear days. On cloudy days, the discharge was approximately $2\ m^3s^{-1}$. The measurements of Bench Glacier by Anderson *et al.* (1999) were

collected at the beginning of the melt season, when the hydrological system had not fully developed and the air temperatures were not reported for comparison. Given these complications, the equivalent meltwater discharge for McBride Glacier (which is 16 times as large) would be $32\,m^3s^{-1}$.

The discharge rate of Matanuska Glacier at the end of August to the beginning of September was measured to be approximately $40\,m^3s^{-1}$ in dry conditions (Denner *et al.*, 1999). However, glacier melt rates are strongly dependent on temperature. At the time of the 1986 rainstorm induced sedimentation event, mean daily temperatures were around $8°C$. Temperatures at Matanuska Glacier were around $8°C$ from 17th–31st August 1995, when discharge rates were approximately $65\,m^3s^{-1}$. McBride Glacier is approximately 2.5 times smaller than Matanuska Glacier, so the meltwater production would be approximately $26\,m^3s^{-1}$, under similar conditions.

The three estimates of the discharge due to meltwater for McBride Glacier calculated from measurements of Matanuska, Bench and Riggs Glaciers, are remarkably similar, despite the differences in environmental conditions. A mid-range value for the meltwater discharge of $27\,m^3s^{-1}$ is taken as a reasonable estimate of the meltwater discharge from McBride Glacier.

Therefore, the maximum discharge expected at McBride Glacier after an intense rainfall event, estimated as the sum of rainfall ($161\,m^3s^{-1}$) and meltwater ($27\,m^3s^{-1}$) contributions, is approximately $188\,m^3s^{-1}$. Since a high percentage of the annual sediment accumulation in McBride Inlet occurs in episodic events during and after storms (Cowan *et al.*, 1988), a discharge rate of $188\,m^3s^{-1}$ is taken as representative of the discharge that is responsible for depositing the majority of sediment in the fjord.

5.2.2 Subglacial Conduit Radius

The radius of the subglacial conduit cannot be observed, since it is submerged at the base of the tidewater glacier. However, at other Alaskan glaciers englacial tunnels above the waterline have been observed and the subglacial discharge tunnels of glaciers terminating on land have also been observed. These observations provide an estimated orifice radius for the subglacial tunnel at McBride Glacier of between 1–10 m (Powell, R.D. personal communication, 2007). Fountain and Walder (1998) shows a photograph of a subglacial conduit at the margin of South Cascade Glacier, which has a flattened semicircular cross-section and is $1.5\,m$ high.

An empirical relationship has been constructed between the volume flux and the radius of the conduit for fluid flow through a pipe. The relationship originates from the Manning equation, which describes open channel flow (Chow, 1959). It was originally an empirical relationship, but has recently been derived theoretically by using the

theory of turbulence. The Manning equation is:

$$V_0 = \frac{1}{n_M} R_h^{\frac{2}{3}} S_{ws}^{\frac{1}{2}} \tag{5.1}$$

where V_0 is the flow velocity, n_M is the Manning coefficient of roughness, R_h is the hydraulic radius and S_{ws} is the slope of the water surface. This has been applied to pipe flow by Church and Gilbert (1975), who substituted the continuity equation into equation 5.1 to give a relationship between the volume flux and the subglacial conduit radius. The continuity equation for a pipe is:

$$Q_0 = \pi R_0^2 V_0 \tag{5.2}$$

where Q_0 is the meltwater flux, R_0 is the radius and V_0 is the meltwater velocity from the subglacial conduit. The resulting relationship between the volume flux and the conduit radius is:

$$2R_0 = 2.4 \left[\frac{Q_0 \, n_M}{S_0^{1/2}} \right]^{3/8} \tag{5.3}$$

where R_0 is the subglacial conduit radius, Q_0 is the meltwater flux from the subglacial conduit, n_M is the Manning total flow resistance coefficient, which is $\sim$0.02 for subglacial conduits (Church and Gilbert, 1975) and S_0 is the slope of the subglacial conduit ($\tan\theta_0$, where θ_0 is the angle the conduit makes with the horizontal).

Some examples of values of the subglacial conduit radius, for different subglacial conduit slopes when $Q_0 = 188 m^3 s^{-1}$, calculated using equation 5.3, are shown in Table 5.1

Slope (°)	Radius (m)
5	3.11
10	2.73
25	2.28
45	1.97

Table 5.1: *Subglacial conduit radii calculated for different conduit slopes using equation 5.3.*

5.2.3 Initial Plume Velocity

Water emerging from subglacial tunnels is capable of flowing at much greater velocities than subaerial rivers; for example, in a glacial stream in the Alps, velocities have been recorded as high as $50\,m\,s^{-1}$, (Vivian (1975) in Sugden and John (1977), p. 301). This is because subglacial water flows due to the gradient of excess pressure over

hydrostatic pressure (Sugden and John, 1977), which enables it to achieve far higher velocities than open channel flow. Subglacial water pressures have been measured beneath the Glacier d'Argentière. Winter values were observed to be relatively stable at 9–10 bars, compared to diurnally fluctuating summer values of 3–6 bars, rising to 11–12 bars in the afternoon (Vivian (1970) in Sugden and John (1977), p. 288).

For an initial volume flux, Q_0, of $188\,m^3s^{-1}$, the velocities, calculated using equation 3.7 for different possible values of the slope/radius of the subglacial conduit, are shown in Table 5.2.

Slope (°)	Radius (m)	Velocity ($m\,s^{-1}$)
5	3.11	6.17
10	2.73	8.03
25	2.28	11.56
45	1.97	15.39

Table 5.2: *Initial velocity of water emerging from the subglacial conduit for a volume flux of* $188\,m^3s^{-1}$*, for different conduit slopes and respective conduit radii.*

5.2.4 Initial Sediment Concentration

The sediment concentration in the water flowing from the subglacial conduit beneath McBride Glacier has not been measured directly for the same reason that there are no direct measurements of the volume flux of water, since it would be dangerous to approach the submerged glacier front in order to make measurements. However, measurements of sediment concentration in glacial meltwater streams have been collected around the world at glaciers terminating on land, and a selection of these will be described here to demonstrate the variability of sediment concentration from glacier to glacier in different environmental conditions, as well as seasonal variability and the response to events such as heavy rainfall.

The high velocity and increased water viscosity from low temperatures result in very high sediment-carrying capacity for glacial meltwater streams (Mackiewicz *et al.*, 1984). The effect of the water viscosity at low temperatures is most pronounced for fine-grained sand (80-90 μm) and appears to be relatively unimportant for sediment less than 62 μm and greater than 250 μm (Church and Gilbert, 1975). Since the fjord surface salinities generally exceed $4\,ppt$, flocculation of silts and clays occurs when the sediment concentration is sufficient, as described in Section 3.2.9.2 (Kranck, 1975; Syvitski and Murray, 1981).

There have been a number of studies of sedimentation in Svalbard fjords. Elverhøi *et al.* (1980) calculated the sediment load of meltwater emerging at sea level from a

tunnel at the snout of Kongsvegen in Svalbard. It was assumed that sea water penetrates up the tunnel that the meltwater flows out of, therefore measurements of the salinity of oceanic water entering the meltwater tunnel, the salinity of the brackish water flowing from the tunnel and the sediment load of the same brackish water could be used to calculate the initial sediment concentration in the meltwater. They found the meltwater sediment concentration to be around $2.5\,kg\,m^{-3}$, and the velocity of the meltwater plume to be $50\,cm\,s^{-1}$. Elverhoi *et al.* (1983) estimated that sedimentation rates in the inner basin of Kongsfjorden were 50–100 $mm\,yr^{-1}$, compared to sedimentation rates of 1–20 $m\,yr^{-1}$ in McBride Glacier (Cowan and Powell, 1991).

Elsewhere in Svalbard, Dowdeswell and Cromack (1991) studied the dynamics of a turbid freshwater plume derived from glacier-fed streams. The flux of the stream was measured to be 1.02–1.23 $m^3 s^{-1}$ over a 40 hour period in August, with no precipitation over the period of observation. They observed progressive fining of sediments with distance from the stream outlets of glacially derived meltwater. Proximal sediment was observed to have a coarse laminated nature, probably as a result of underflows and turbidity currents, in contrast with the cyclopels formed in Alaska due to tidally driven fluctuations in the position of glacial plumes (Cowan and Powell, 1990; Mackiewicz *et al.*, 1984). Distal sediments were observed to have a structureless, silty nature, originating from the flocculation and settling of suspended sediments through the water column.

Östrem (1975) studied sediment transport in meltwater streams from Norwegian glaciers, which is worth noting as his study demonstrated the dependence of sediment concentration on stream discharge and the variability over the annual cycle. He found that, in general, a high water discharge will in general carry a larger sediment load than a low discharge. After several years of detailed measurements, sediment concentrations were found to range from a few $g\,m^{-3}$ up to $12\,kg\,m^{-3}$ in meltwater discharging from the front of glaciers. He found that the peak in sediment discharge occurred in advance of the water discharge peak for samples taken near to the glacier terminus. Sediment concentrations in these glacial streams in Norway would be expected to be lower than that at McBride Glacier, since the glaciers studied by Östrem (1975) had areas between 4 and 40 km^2, a fraction of the size of McBride Glacier, with consequently lower discharges.

There have been a number of studies of sedimentation from glaciers in Glacier Bay, and some of these have measured sediment concentration in the glacial stream emerging from glaciers terminating on land, while at tidewater glaciers, sediment concentration has been measured once the plumes have reached the surface of the fjord, at some distance from the glacier front.

Hoskin and Burrell (1972) studied sediment transport and accumulation for over

5 years in Queen Inlet, Glacier Bay. The glacier terminates on land and there is an outwash fan with meltwater streams connecting the glacier with the marine environment of the fjord. They found sediment loads always exceeding $1\,kg\,m^{-3}$ in the surface plume at the inlet head. They measured the suspended-sediment load in the largest meltwater stream in September 1969 and found the average sediment concentration to be $12.8\,kg\,m^{-3}$, at a water temperature of $0.5°C$.

In the study carried out by Denner *et al.* (1999) at Matanuska Glacier in south-central Alaska, the suspended sediment concentration in the glacial discharge stream was measured, as well as the discharge flux as described in Section 5.2.1. After the September 1995 storm, the suspended sediment concentration peaked at $21\,kg\,m^{-3}$, a day in advance of the stream flow peak. While the stream flow dropped to pre-storm levels nine days after the storm began, suspended sediment concentrations remained higher than pre-storm values until the last samples were collected 23 days after the event. The daily mean suspended sediment concentration during the flood was 430% higher than the maximum mean daily concentrations in July, probably due to the subglacial drainage system expanding to new parts of the bed and eroding fresh supplies of sediment there. Another storm event was observed in June 1997, which showed quite a different response in the hydrologic system. The suspended sediment concentration showed high temporal variation before and during the storm from 0.4 to $2.5\,kg\,m^{-3}$, with no defined peak in suspended sediment concentration after the storm. The 2 week average mean concentration after the storm was just 15% higher than the 2 week average before it. It is thought that this was due to the subglacial drainage system being under-developed, with limited access to the large amount of sediment that accumulated over the winter, as well as the presence of a deep snowpack preventing overland erosion.

In McBride Inlet itself, Cowan and Powell (1990) found sediment concentrations up to $1.4\,kg\,m^{-3}$ during late July and early August in the surface plume at a distance of approximately $400\,m$ from the glacier front. This increased to up to $6\,kg\,m^{-3}$ at the same distance from the glacier front during an intense storm event in late August (Cowan *et al.*, 1988). The initial suspended-sediment concentration in the water emerging from the subglacial conduit will be significantly higher than the sediment concentration present in the surface plume at some distance from the glacier front. Therefore, taking this into account and the measurements taken by Denner *et al.* (1999) and Hoskin and Burrell (1972), a reasonable estimate of the range of initial sediment concentration in the water emerging from McBride Glacier during the melt season is 1–$10\,kg\,m^{-3}$, increasing during a storm event to 5–$20\,kg\,m^{-3}$, although the sediment load would be considerably lower than this at times of low discharge.

5.2.5 Grain Size Distribution

Sediment deposited in front of McBride Glacier ranges from gravel to mud (Powell and Cowan, 1987) and is described by Facies Association I in Powell's facies model for tidewater fronts of temperate glaciers (Powell, 1981, 1983). The most common proximal lithofacies is interlaminated sand and mud. Sand is deposited by overflows and underflows formed due to subglacial stream discharges and sediment gravity flows (Mackiewicz *et al.*, 1984). Mud is composed of rock flour, which is deposited from turbid overflows. Gravel originates from iceberg-rafting and from sea ice during the winter.

The grain size distribution was measured by Cowan and Powell from sediment traps (Cowan and Powell, 1990, 1991). The sand size fraction was observed to be highly variable. Cowan and Powell (1991) sampled particles as coarse as medium sand in the upwelling; however, within $500\,m$ of the upwelling sediment collecting in traps was mostly sandy silt and sandy mud and farther away was dominated by muds.

In the *SedPlume* model, three categories of sediment are considered according to grain size: sand, silt and clay. Different initial percentages of each of these grain size categories are specified. It is assumed that within each grain size category, the concentration of sediment is uniformly distributed over the range of grain sizes.

Cowan and Powell (1990) found that the average particle size distribution collected in traps $400\,m$ from the glacier was 10% sand, 75% silt and 15% clay. Histograms of particle size distribution of samples from bottom sediment traps approximately $500\,m$ from the subglacial discharge from the 19^{th}–20^{th} July 1985 were presented by Cowan and Powell (1990). Variations in the particle size distribution were observed due to tidal fluctuations. The mean particle size was also presented. At another location $400\,m$ from the glacier, traps were observed to collect large amounts of very fine sand relative to mud. In the model, it is necessary to define the limits of the sand and clay fraction. Since the sand fraction is mainly very fine, the lower limit is assumed to be $\phi = 3$ on the Udden-Wentworth Scale. The upper limit of the clay fraction is assumed to be $\phi = 9$.

5.2.6 Ambient Density Gradient

During winter and spring the water mass in McBride Inlet is homogeneous (Powell and Cowan, 1987). During summer, the addition of glacial meltwater at the surface leads to the fjord waters being heterogeneous, with strong thermoclines, haloclines and pycnoclines. In Figure 14.2(b) in Powell and Cowan (1987), the difference in density between $1\,m$ and $38\,m$ was 6.08 $kg\,m^{-3}$ in July 1985. In the *SedPlume* model the density gradient is assumed to be linear, and so a suitable linear fit through the

measured values from Figure 14.2(b) is used:

$$\rho = 1012 - \frac{7}{30}z \tag{5.4}$$

where z is depth in m, defined in Figure 3.2, and ρ is the density of the water in $kg\,m^{-3}$.

The measurements collected by Powell and Cowan (1987) on 7th July 1985, along with equation 5.4, which is the density profile used in the model runs, are shown in Figure 5.3.

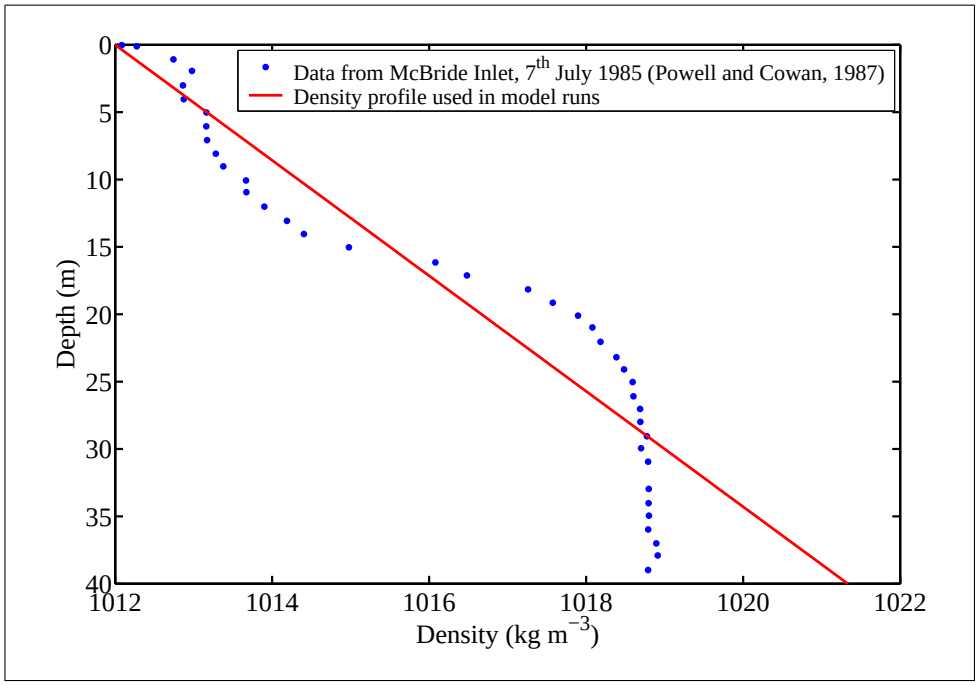

Figure 5.3: *Density profile measured by Powell and Cowan (1987) on 7th July 1985 in McBride Inlet and the density profile used in the model (equation 5.4).*

5.3 Model Output for McBride Glacier

The initial conditions described in the preceding sections are used as inputs for the *SedPlume* Model and the results of the model runs are discussed in this section. The initial volume flux of the plume is taken to be the maximum value, $188\,m^3s^{-1}$, as calculated in Section 5.2.1. Four possible values of the slope of the subglacial conduit are considered: 5°, 10°, 25° and 45°, as explained in Sections 5.2.2 and 5.2.3. The respective values of the conduit radius and initial velocity are shown in Table 5.2, and the initial sediment concentration is in the range 1–20 $kg\,m^{-3}$, as discussed in Section 5.2.4.

The resulting plume trajectories for these four subglacial conduit slopes are shown in Figure 5.4. For all values of the conduit slope, the end point of the plume had to

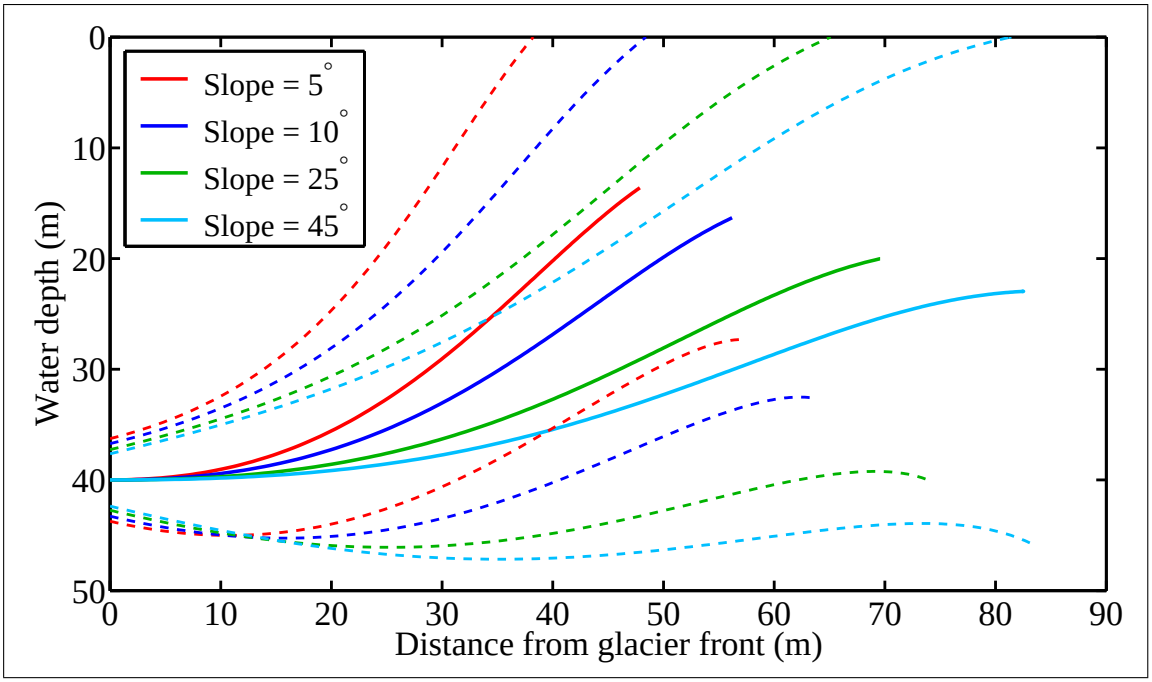

Figure 5.4: *Plume centreline trajectories (solid lines) and plume boundaries (dotted lines) for four possible subglacial conduit slopes (conduit radii and initial velocities defined in Table 5.2).*

be adjusted. In Chapter 3 it was defined that the plume reached the surface when the centreline position passed through the surface plane. However, because of the strongly stratified and relatively low salinity ambient water in McBride Inlet (Figure 5.3), the centreline position never reaches the surface. The plume becomes neutrally buoyant before that occurs, and flows horizontally as an internal density current. In this situation the model will predict an infinite number of oscillations about a level where the centreline density is equal to the ambient density. However, the upper edge of the plume does pass through the surface plane, as shown in Figure 5.4. Therefore, the end point of the integration was taken to be when the upper edge of the plume reaches the surface.

It is probably no coincidence that the plume trajectories plateau off as they reach the surface. The ambient density gradient is created over time by the presence of the freshwater plume, so an equilibrium is established between the plume being able to reach the surface and the steepness of the gradient. If the plume freshens the surface water to the extent that it can no longer reach the surface, it instead forms an interflow, and the surface water is no longer replenished with 'fresh' water. Eventually the surface water becomes more dense than the plume and it is possible for the plume to reach the surface once more. The factors controlling the steepness of the ambient

density gradient are the inflow of saline water from Muir Inlet (tidal currents play an important role), balanced with the introduction of freshwater from the subglacial conduit.

It can be seen that, for a larger subglacial conduit slope, the plume has a faster initial velocity, and reaches the surface further away from the glacier. This is because although all the plumes have the same volume flux, a higher initial velocity results in a higher momentum flux in the horizontal direction, so the plume travels further from the glacier before surfacing.

The density variation with depth for the four different values of the conduit slope, along with the ambient fjord density measured in McBride Inlet on 7th July 1985 by Powell and Cowan (1987), are shown in Figure 5.5. In all four cases, the plumes

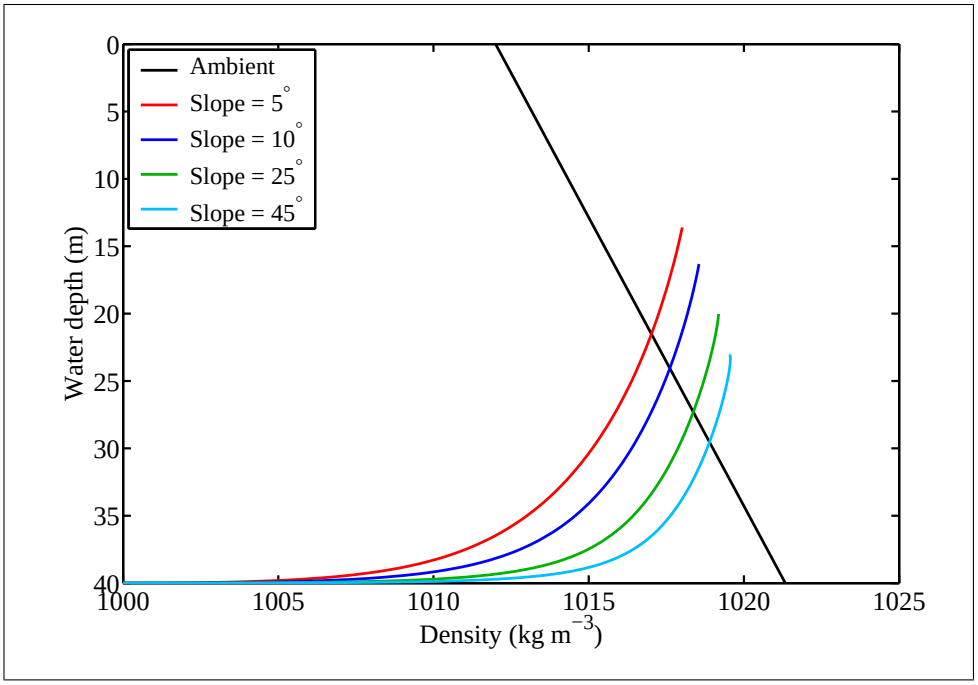

Figure 5.5: *Density of plume changing with depth for four possible subglacial conduit slopes, which result in different conduit radii and initial velocities (Table 5.2), along with the ambient fjord density measured in McBride Inlet on 7th July 1985 by Powell and Cowan (1987).*

become more dense than the ambient fluid as they approach the surface and after this point their trajectories level off. The most mixing (fastest convergence of the plume density to the ambient) occurs as the plume travels horizontally, just after it emerges from the conduit (see Figure 5.4). A higher subglacial conduit slope results in a higher initial plume velocity so the plume travels horizontally for longer enabling more mixing to occur between the plume and the ambient fluid. Therefore the plume density increases more rapidly for higher than for lower subglacial conduit slopes.

Cowan and Powell (1991) measured the sedimentation rate with distance from the

subglacial stream using sediment traps during the summers of 1984 through 1986. They divided their measurements into two groups: traps deployed during the period of peak meltwater discharge and those deployed outside the peak discharge period. They were able to identify the peak discharge period by increased suspended sediment concentrations in water samples and the presence of low salinity surface water. They found that the peak meltwater period lasted approximately 52 days in 1985 and 42 days in 1986. It was estimated that the total melt season is approximately 123 days long, and outside this period meltwater discharge and deposition rate from the glacier is effectively zero.

Cowan and Powell (1990) measured the average particle size distribution of sediment collected in traps $400\,m$ from the glacier to be 10% sand, 75% silt and 15% clay. In the model, the initial fraction of sand, silt and clay is determined by a grid search over the initial fraction of sand and silt (with the clay fraction making up the remainder), so that the fraction of each grain size at $400\,m$ from the glacier is as close as possible to the observations of Cowan and Powell (1990). The initial grain size fractions calculated in this way are shown in Table 5.3.

Slope (°)	Initial Sand Fraction	Initial Silt Fraction	Initial Clay Fraction
5	0.210	0.6423	0.148
10	0.148	0.679	0.173
25	0.0924	0.703	0.205
45	0.0665	0.706	0.227

Table 5.3: *The initial grain size fractions calculated so that the grain size fractions at* $400\,m$ *from* x_s *are 0.1 sand, 0.75 silt and 0.15 clay. Slope refers to the slope of the subglacial conduit from which the meltwater is derived.*

The data collected during the peak discharge period and the modelled deposition rate for four subglacial conduit slopes are shown in Figure 5.6. The initial sediment concentration used as an input for the model is $6\,kg\,m^{-3}$. This produces sedimentation rates of the correct order of magnitude compared to the data. Plumes with lower initial velocity/larger radius have a higher peak deposition rate, but the sedimentation has a smaller spread, so sediment is not carried as far from the glacier margin - lower dispersal distance/higher proximal deposition. On the other hand, plumes with high initial velocity/smaller radius have a lower peak deposition rate and higher rates at larger distances - higher dispersal distance/lower proximal deposition. The area under the curves (total amount of deposition) are the same because the initial sediment fluxes are equal.

The deposition curves are gaussian because the rising plume carries all the initial

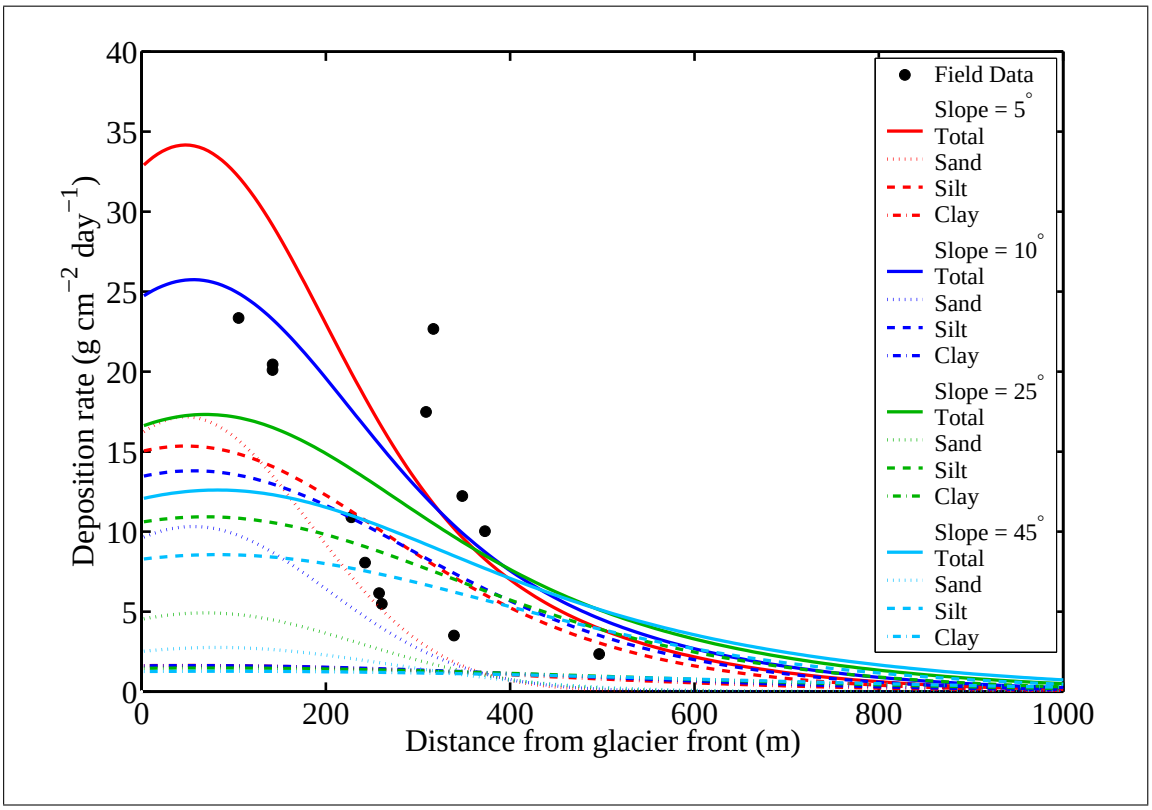

Figure 5.6: *Modelled deposition rate compared to field data during peak discharge season (Cowan and Powell, 1991). Modelled total deposition rate and deposition rate of three particle fractions (Sand:* $3 <= \phi <= 4$*; Silt:* $4 < \phi <= 8$*; Clay:* $8 < \phi <= 9$*) are shown, for four subglacial conduit slopes (conduit radii and initial plume velocities defined in Table 5.2). The initial sediment concentration is* $6\,kg\,m^{-3}$.

sediment load to the surface with deposition only occurring in the gravity current. Using the model, the smallest grain sizes deposited in the rising plume for the different values of the subglacial conduit slope are shown in Table 5.4.

Slope (°)	Minimum grain size deposited in plume (mm)
5	1.569
10	1.444
25	1.366
45	1.357

Table 5.4: *The smallest grain sizes deposited in the rising plume for four values of the slope of the subglacial conduit.*

The grain sizes modelled are up to a maximum size of $\phi = 3$, $d_s = 0.125\,mm$, therefore well below the minimum grain size at which deposition occurs in the plume and all the sediment is carried to the surface, where it is transported in the gravity current.

This is supported by observations of fine sands, which are seen to be transported large distances by glacial meltwater plumes (Powell and Molnia, 1989).

For sediment of a specified grain size, the maximum initial water velocity at which grains of diameter $d_s = 0.125\,mm$ are deposited in the plume for the different values of the subglacial conduit slope are shown in Table 5.5.

Slope (°)	Max initial velocity for $\phi = 3$ deposition in plume ($m\,s^{-1}$)
5	0.2845
10	0.3497
25	0.4662
45	0.5897

Table 5.5: *The smallest grain sizes deposited in the rising plume for four values of the slope of the subglacial conduit.*

These velocities are well below the estimated initial values of the plume velocity investigated with the model (Table 5.2). The initial water velocity from the subglacial conduit would probably only fall to such low values in winter.

The field data can be split roughly into two groups, shown by the filled and unfilled circles in Figure 5.7, to which different gaussian deposition curves can be fitted. One of the determining factors for the magnitude of the deposition rate is the initial sediment concentration. This is not known precisely, but it is likely to range between 1–20 $kg\,m^{-3}$. The value of the sediment concentration producing the best fit to the magnitude of the deposition rate for the lower group of data (filled circles) is found to be $4\,kg\,m^{-3}$, as shown in Figure 5.7. The lowest subglacial conduit slope of 5° shows the best fit to the lower group of data for the gradient of the deposition rate.

The upper group of data (unfilled circles) may be the result of extremely high flux events producing higher suspended sediment concentrations in the glacial plume, although the most likely explanation is that sedimentation from the plume is affected by tidal currents. Cowan (1992) observed that during flood tide the surface layer velocity increased and during ebb tide the surface layer velocity decreased, flowing only due to gravity. Therefore, strong tidal velocities would cause the deposition peak to lie further from the glacier front, and increase the dispersal distance. Each of the sedimentation rate data points was collected over a period of a few days, so the different shaped deposition curves are not the result of observation during a flood tide relative to an ebb tide. However, the upper group of data could have been collected during a spring tide, which drew the glacial plume further down fjord than normal, and the lower group of data could have been collected during less extreme tidal fluctuations. This would explain why the data can be split into two different sedimentation patterns.

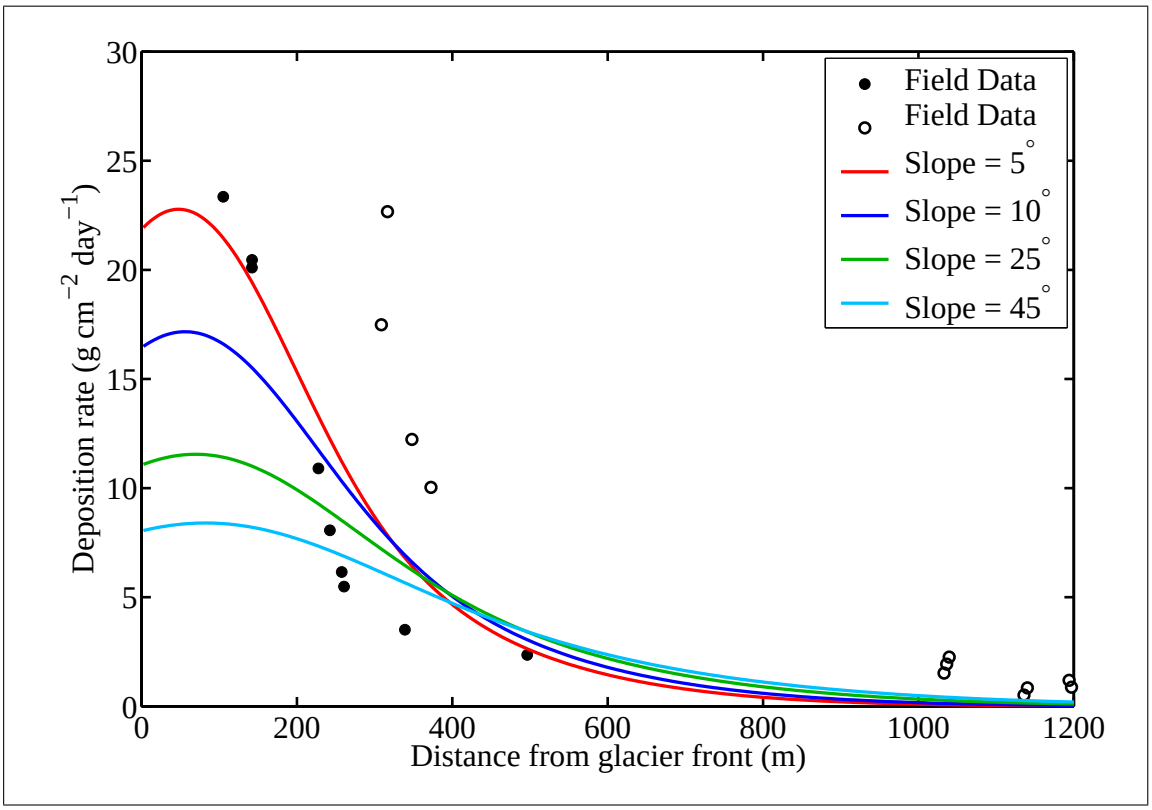

Figure 5.7: *The total modelled deposition rate is compared to field data during peak discharge season (Cowan and Powell, 1991), for four possible subglacial conduit slopes (conduit radii and initial velocities defined in Table 5.2, and initial sediment concentration of* $4\,kg\,m^{-3}$*).*

5.4 Annual Accumulation Rate

The deposition rates simulated by the model in Section 5.3 are representative of high sedimentation events, which are the source of the vast majority of the sediment deposited in McBride Inlet over the annual cycle. Simulated daily sedimentation rates can be extrapolated to represent accumulation over a year by multiplying the appropriate sedimentation rate by the estimated number of days that this rate occurs during the 123–day melt season (Cowan and Powell, 1991). Two sedimentation regimes are assumed to occur during the melt season, which are simulated with the model: a 'storm' and a 'background' accumulation rate. During the 'storm' regime, the discharge is taken to be $Q_0 = 188\,m^3s^{-1}$ and the initial sediment concentration is $6\,kg\,m^{-3}$. During the 'normal' regime, the discharge is assumed to be $Q_0 = 100\,m^3s^{-1}$ and the initial sediment concentration is $6\,kg\,m^{-3}$. The initial grain size fractions are decided as before, by carrying out a grid search over the initial sand and silt fraction to find the closest match to the observations of the size fractions at $400\,m$ by Cowan and Powell (1990). The number of days that more than $10\,mm$ of rain fell in 24 hours from May to September 1986 (Cowan and Powell, 1991) is taken as representative of the number

of days in a year that the 'storm' regime occurs. This results in 28 days per year of the 'storm' sedimentation rate. For the remainder of the melt season (95 days), a 'normal' sedimentation rate is assumed. The density of the sediment once it has been deposited is assumed to be $1700\,kg\,m^{-3}$. The two deposition rates are converted into units of $m\,day^{-1}$, multiplied by the respective number of days when each rate occurs over the course of a year and added together. Using this method, the modelled sedimentation rates are converted into an annual sediment accumulation rate with units of $m\,yr^{-1}$.

Cowan and Powell (1991) multiplied the sediment accumulation from near bottom traps, which were assumed to represent sediment accumulation on the fjord floor, by the number of days that this rate occurred (either during or outside of the peak discharge period) in that particular year. The annual sedimentation rates (during peak discharge period) for McBride Inlet calculated using this method, from Figure 8 in Cowan and Powell (1991), and the modelled annual sediment accumulation are shown in Figure 5.8. As with the daily sedimentation data, there is a considerable spread

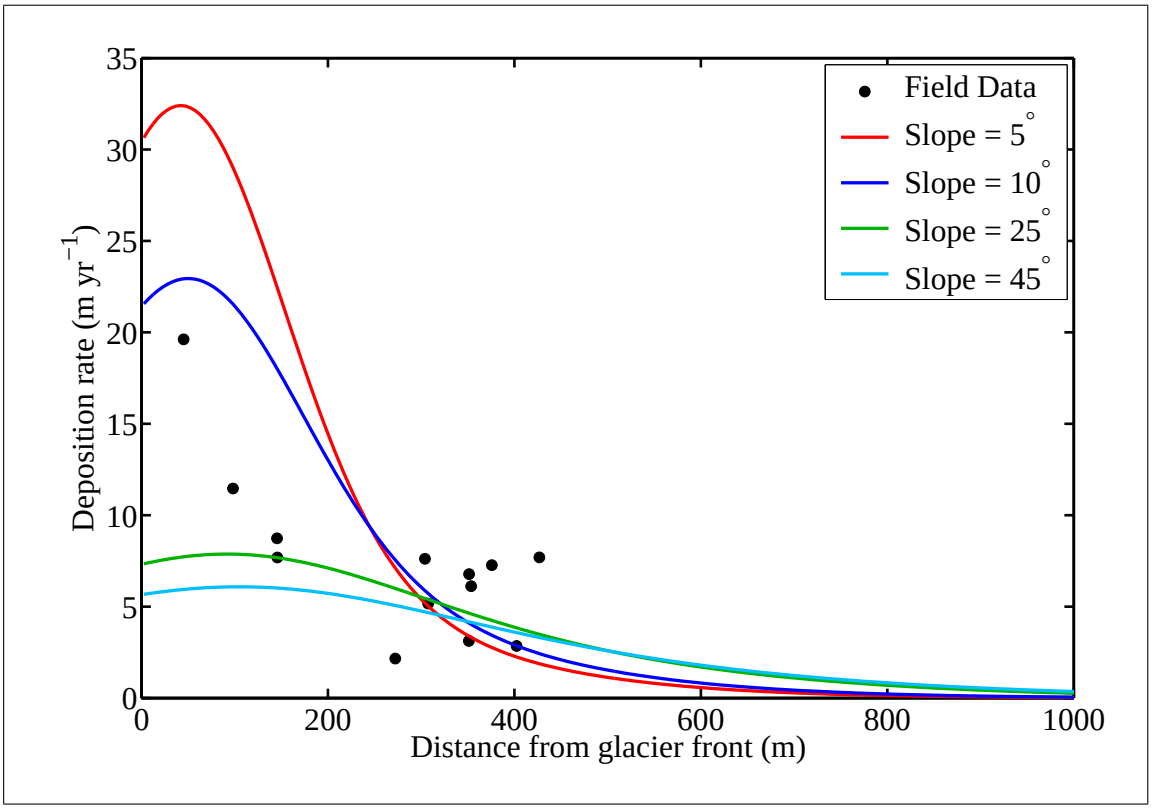

Figure 5.8: *Modelled annual deposition rate for four possible subglacial conduit slopes calculated for 28 days of 'storm' regime per year:* $Q_0 = 188\,m^3 s^{-1}$, *initial sediment concentration* $6\,kg\,m^{-3}$; *and 95 days of 'normal' regime per year:* $Q_0 = 100\,m^3 s^{-1}$, *initial sediment concentration* $6\,kg\,m^{-3}$. *Field data shown were derived from sediment traps deployed during the peak discharge season from 1984–6. The measured sedimentation rate for each trap was multiplied by the estimated number of days that the rate occurred during the 123–day melt season (Cowan and Powell, 1991, Figure 8).*

in the field data for the annual sedimentation rate with distance from the glacier. The modelled annual accumulation rates show a similar magnitude and pattern of deposition to the observed rates. The slope of the subglacial conduit has an important influence on the modelled sedimentation rate, with the 10° slope best reproducing the gradient of the data points. The spread of sedimentation rates for the same distance from the glacier front in the collected data indicates that there were plume fluctuations, possibly caused by changing tidal conditions between the times when the sediment traps were collected.

5.5 Summary

In this chapter, the *SedPlume* Model introduced in Chapter 3 has been applied to McBride Inlet, Alaska. The shape and magnitude of the daily sedimentation rate curves produced by the model compare well to the observations of sedimentation rate by Cowan and Powell (1991). A conduit radius of $3.11\,m$, an initial velocity of $6.17\,m\,s^{-1}$ and an initial sediment concentration of 4–6 $kg\,m^{-3}$ produce the best fit to the measured daily sedimentation rate during peak discharge season.

The modelled annual sedimentation rates (28 days of 'storm' regime: $Q_0 = 188\,m^3 s^{-1}$, $\phi_0 = 6\,kg\,m^{-3}$; and 95 days of 'normal' regime: $Q_0 = 100\,m^3 s^{-1}$, $\phi_0 = 6\,kg\,m^{-3}$) compare well to the annual accumulation rates that were calculated by Cowan and Powell (1991), with peaks of 20–30 $m\,yr^{-1}$ near to the glacier front.

Estimates of the input parameters are made using the available data, which is limited in places. To test the model's performance more thoroughly, better constraints of the initial plume conditions are required. The most important parameters, which are poorly constrained at present, are the radius of the subglacial conduit and the velocity of water emerging from it. These could be measured using a remotely operated vehicle with the ability to venture close to the glacier front (Dowdeswell and Powell, 1996). If a flow meter was located and secured close to the subglacial conduit, this could provide data on the daily fluctuations in the flux of water flowing through the subglacial conduit.

The extremely high sedimentation rates, characteristic of Alaskan fjords (Powell and Molnia, 1989), are generated by the model when suitable values are taken for the input parameters. This is encouraging and provides confidence in utilising the *SedPlume* Model to simulate sediment deposition from glacial plumes.

Chapter 6

Parameter Experiments: *SedBerg* and *SedPlume* Models

6.1 Introduction

In this chapter, experiments investigating the impacts of changing the input parameters on the sedimentation rate calculated by the *SedBerg* and *SedPlume* models are conducted. The purpose of these experiments is to attain an understanding of the influence of various input parameters on the resulting patterns of glacimarine sedimentation in a general context. For the *SedBerg* Model, the parameters studied are the mean iceberg size, the water temperature, the depth of the thermocline and the seeds of the random number generator for water and wind velocities. The parameters examined with the *SedPlume* Model are the initial plume velocity, the subglacial conduit radius, the initial sand fraction and the ambient density gradient. Each section begins with the relevance of the experiment to our understanding of glacimarine environments. Then the model results are presented and finally concluding remarks are made on the consequences for glacimarine sedimentation.

6.2 *SedBerg* Model

6.2.1 Mean Iceberg Size

6.2.1.1 Motivation

The iceberg size distribution calved from a glacier depends on a number of factors including glacier dynamics, bedrock topography, glacier thickness, water depth and climate (Warren, 1992). As discussed in Section 2.3, the shape of the size distribution can usually be approximated by a lognormal distribution because there is a peak in

frequency of icebergs around a certain size and the frequency of larger iceberg sizes drops rapidly.

The expected value of the lognormal iceberg size distribution varies greatly at different locations. In Kongsfjorden, North-West Spitsbergen, Dowdeswell and Forsberg (1992) observed iceberg widths from 0.5 to 30 m. In Scoresby Sund, East Greenland, Dowdeswell *et al.* (1992) recorded the horizontal dimension (length or width, depending on which was facing the ship) and keel depth of a large number of icebergs. The size distribution was lognormal with an expected value of 173.3 m for the horizontal dimension. Around the coast of Antarctica, Dowdeswell and Bamber (2007) calculated mean keel depths between 139 and 577 m from measurements of the ice thickness at the grounding line of calving margins. For these three examples, the mean iceberg size shows considerable variation, which suggests that the mean iceberg size is strongly dependent on conditions at the glacier or ice shelf from which it calved.

The response of icebergs to forcing conditions (equation 2.41) as well as the melt rate due to forced convection (equation 2.20) are affected by their size (defined in Section 2.3). Thus, varying the mean of the lognormal iceberg size distribution is likely to have an impact on the sedimentation rate.

6.2.1.2 Model Inputs

To test the effect of changing the mean of the iceberg size distribution on the sedimentation rate, the *SedBerg* Model is run for different lognormal distributions with a range of mean iceberg sizes. To enable the cross-comparison of varying the mean iceberg size, a common restriction must be placed on all the iceberg size distributions. Consequently, the probability that the realisation of the random variable (iceberg size) is less than or equal to a certain value, L_{max}, is fixed, $F(L_{max})$. It is specified that there is a probability of 0.999 that a randomly drawn iceberg has a size less than or equal to the thickness of glacier front. This was chosen as it is the point where the iceberg thickness is 'censored' to ensure it does not exceed the thickness of the glacier. A grid search is performed on the variance to find the lognormal distribution parameters such that the cumulative distribution function, $F(L_{max})$, equals the specified value. The cumulative distribution function is the integral of the probability density function (equation 2.7) and for the lognormal is:

$$F(L_{max}) = \int_{-\infty}^{L_{max}} f(L_k)\, dL_k = \frac{1}{2} + \frac{1}{2}\mathrm{erf}\left[\frac{\ln(L_{max}) - \mu}{\sigma\sqrt{2}}\right] \tag{6.1}$$

The lognormal distribution parameters are calculated from the expectation (or

mean), $E(L_i)$, and variance, $V(L_i)$, as follows:

$$\mu = \ln\left[E(L_i)\right] - \frac{1}{2}\ln\left[\frac{V(L_i)}{E(L_i)^2} + 1\right] \tag{6.2}$$

$$\sigma = \sqrt{\ln\left[\frac{V(L_i)}{E(L_i)^2} + 1\right]} \tag{6.3}$$

For various values of the expectation $E(L_i)$, the probability that the realisation of the iceberg size is less than or equal to L_{max}, $F\left(L_{max}\right)$, is set equal to 0.999 and the threshold size, L_{max}, is set to be $650\,m$, which is equal to the ice front thickness of Kangerdlugssuaq Gletscher (Chapter 4). Equations 6.2 and 6.3 are substituted into equation 6.1 and solved to find the variance, $V(L_i)$. The six iceberg size distributions calculated using this method are shown in Figure 6.1.

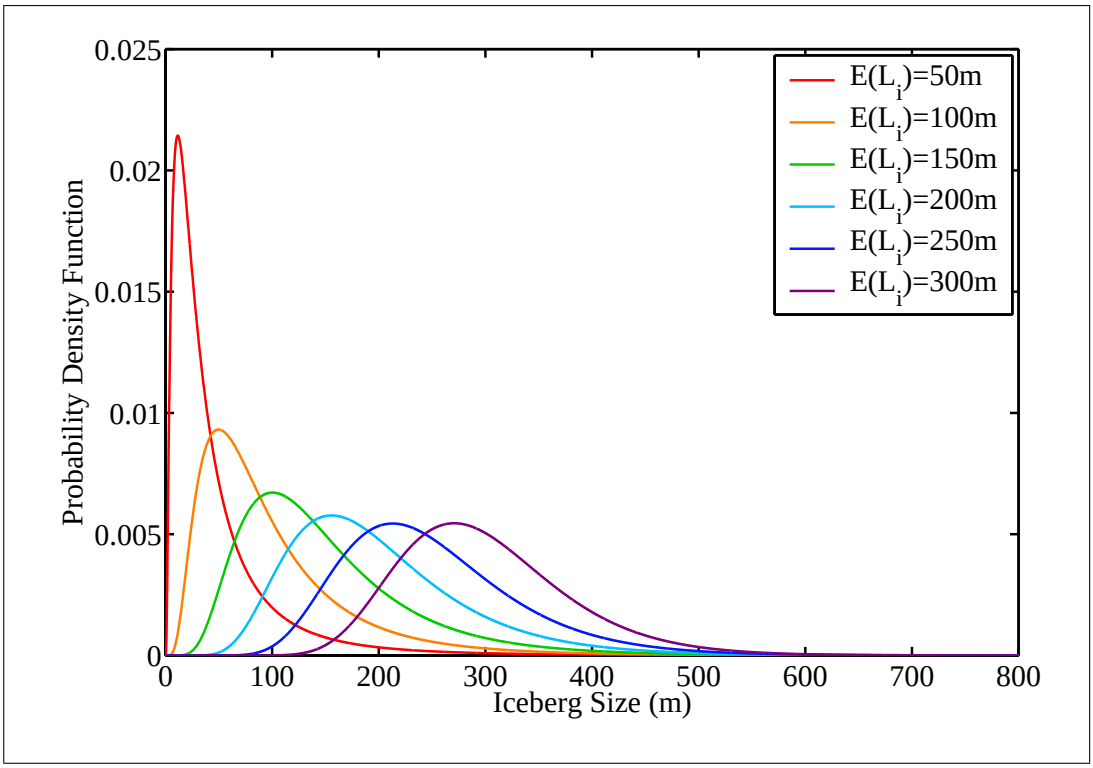

Figure 6.1: *The iceberg size probability density functions used in the* SedBerg *Model runs to test the dependence of sedimentation rate on mean iceberg size.*

In these model experiments, the fjord is assumed to have a similar configuration as Kangerdlugssuaq Fjord, with a length of $80\,km$ and a width of $5\,km$, with a glacier front height of $650\,m$ and width of $4.6\,km$. The water temperature is set to be constant with depth and equal to $1°C$ in summer and -1.358$°C$ in winter. This removes the effect of different sized icebergs being exposed to water of a different temperature and the only variable changing between runs is the expected value of the iceberg

size distribution. The annual volume of icebergs produced is set to $15\,km^3yr^{-1}$ to 2 decimal places. The icebergs are assumed to contain only englacial sediment with a concentration of 0.085 % by volume.

6.2.1.3 Model Outputs

The across-fjord sedimentation rate, averaged over the length of the fjord, is shown for the different mean iceberg sizes in Figure 6.2. The across-fjord transects are used here,

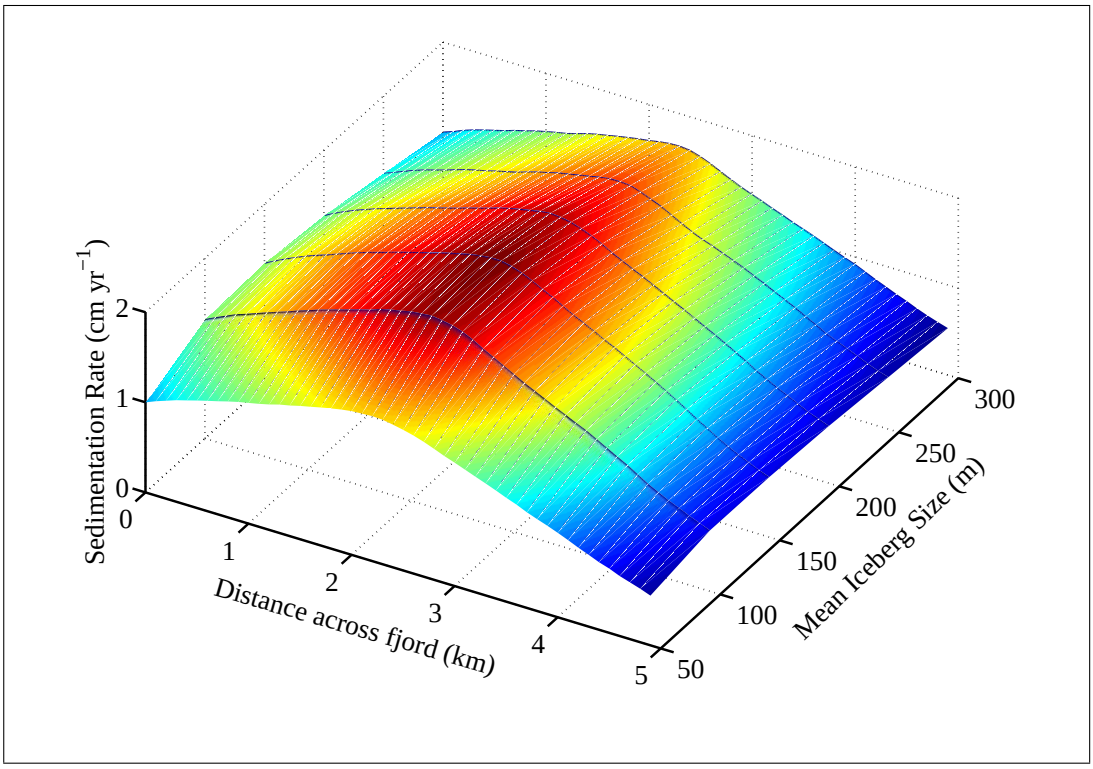

Figure 6.2: *Transects of sedimentation rate across the fjord (averaged along the length of the fjord - 80 km) for the range of mean iceberg sizes corresponding to the probability density functions in Figure 6.1.*

as in Chapter 4, to provide an average rate over the fjord basin. The sedimentation rate shows a maximum at a mean iceberg size of $150\,m$, where the peak rate is $2.18\,cm\,yr^{-1}$. The maximum change in the sedimentation rate over the range of mean iceberg sizes considered is approximately 36%.

There is an interplay of two influences, which causes the variation in sedimentation rate with mean iceberg size in Figure 6.2. One control is the melt rate due to forced convection, the dominant subaqueous melt process, which decreases gradually with increasing iceberg size (equation 2.20). The other factor is that smaller icebergs have a larger surface area to volume ratio (smaller inertia) and therefore are accelerated to higher velocities than larger icebergs. This is demonstrated in Figure 4.24, where the smaller icebergs travel further under the same forcing conditions; in other words,

smaller icebergs travel at velocities closer to the water velocity. The melt rate due to forced convection increases with the difference between the water velocity and the iceberg velocity, therefore, the melt rate increases with iceberg size. The dominant control on the subaqueous melt rate (equation 2.20), and consequently on the sedimentation rate, at small iceberg sizes is the difference between the water and iceberg velocity and at large mean iceberg sizes is the iceberg size.

6.2.1.4 Implications

The *SedBerg* Model results demonstrate that even with the same flux of icebergs from a glacier, iceberg size distributions with different expected values result in a variation in the sedimentation rate in the fjord. Over the range of mean iceberg sizes studied with the model, there is a significant change in the sedimentation rate of approximately 36%.

The relationship between mean iceberg size and the sedimentation rate is more complex than assumed by Matsumoto (1996), who assumes that iceberg life expectancy is proportional to the iceberg mass to a power. However, the *SedBerg* Model outputs in this section show that when modelling the sedimentation rate from a population of icebergs, it is important to include the effect of both iceberg size and iceberg velocity relative to ocean currents on the melt rate.

In the work of Gladstone *et al.* (2001), a single iceberg size distribution was applied to the whole of the Antarctica. However, the observations of Orheim (1987) and Young *et al.* (1998) provide evidence that there are significant variations in the iceberg size distributions around the coast of Antarctica. Orheim (1987) suggested that the reason for the regional differences is the diversity of the calving sites from which the icebergs originate. This conjecture is supported by Dowdeswell and Bamber (2007), who inferred the iceberg keel depths around the coast of Antarctica based on measurements of the thickness of the floating margins from satellite radar altimetry. The *SedBerg* Model output in Figure 6.2 indicates that the sedimentation rate and meltwater flux are influenced by the mean iceberg size used; therefore, it may be beneficial to include a range of iceberg size distributions when modelling the iceberg melt and sedimentation rate in the Southern Ocean.

Since it proves a challenge to estimate even contemporary iceberg size distributions, deducing iceberg size distributions in the past, for example during the Last Glacial Maximum (LGM), is fraught with difficulties. It is therefore reasonable that Death *et al.* (2006) assumed the iceberg size distribution from the Eurasian Ice Sheet during the LGM was the same as it is today in Scoresby Sund from measurements by Dowdeswell *et al.* (1992). However, the effect on the sedimentation rate of variations in

the iceberg size distribution, which have been shown in this section, should be noted. A possible technique to calculate different iceberg size distributions for the various calving margins of the Eurasian Ice Sheet would be to utilise the method developed by Dowdeswell and Bamber (2007) with the ice thickness and calving rate provided by an ice sheet model (e.g. Siegert and Dowdeswell, 2002).

6.2.2 Water Temperature

6.2.2.1 Motivation

Water temperature varies with depth in modern polar oceans, as demonstrated by the CTD profiles collected in 1993 and 2004 in Kangerdlugssuaq Fjord (Figure 4.12). Measurements in the Amundsen Sea by Jenkins (1999), for example, also show a change in temperature with depth, with a thermocline at between 100 and 300 m (depending on the proximity to Pine Island Glacier), which separated a cold surface layer (at approximately -1.5°C) from a warmer deep layer (at approximately 1.5°C). The upwelling of deep water around Antarctica leads to an positive correlation of temperature with depth (Toggweiler and Samuels, 1995)

The water temperature plays an important role in determining iceberg melt rate, because of the temperature dependence of the melt rate due to forced convection and buoyant vertical convection (Section 2.4.1). The *SedBerg* Model differs from previous iceberg models in that a vertical temperature profile is defined and the mean temperature over the keel depth 'felt' by each iceberg is calculated. This means that larger icebergs are influenced by deeper water temperatures.

These model experiments assist in quantifying the influence that past ocean temperature fluctuations may have had on the sedimentation rate due to iceberg rafting. In terms of applications to field study areas, the hydrographic and climatic regime determine the water temperature profile in a fjord. For example, in East Greenland the water temperature profile in the fjord is governed by the relative influence of Atlantic Intermediate Water compared to Polar Water (Jennings and Weiner, 1996; Sutherland and Pickart, 2007).

6.2.2.2 Model Inputs

For these *SedBerg* Model runs, it is assumed that the summer water temperature profile consists of two layers separated by a thermocline. In summer, the water below the thermocline is assumed to have a temperature of 1°C, and the temperature of the upper layer is varied. The temperature of the layer above the thermocline is prescribed, in different experiments, to be colder as well as warmer than the water

below the thermocline. Colder surface water would be caused by abundant glacier and iceberg melt, as observed by Jenkins (1999) in the Southern Ocean, whereas a warmer surface layer could be caused by ocean currents introducing a warmer water mass, such as occurs intermittently in Kangerdlugssuaq Fjord (Section 4.3.5).

Model runs are also performed varying the thickness of the thermocline while the temperature of the upper and lower layers remain the same. This has the effect of altering the number of icebergs that are exposed to the deeper water below the thermocline. Modifying the mean iceberg size while the thermocline depth remains the same would have a similar effect. Since the iceberg size distribution is lognormal, there is a rapid decrease in icebergs above a certain size, so the effect of changing the thermocline depth is likely to reflect this.

The iceberg size distribution used for these runs has an expectation of 170 m and a standard deviation of 90.6 m ($\mu = 5.0108$; $\sigma = 0.5$). The probability density function of the iceberg keel depth is shown in Figure 6.3.

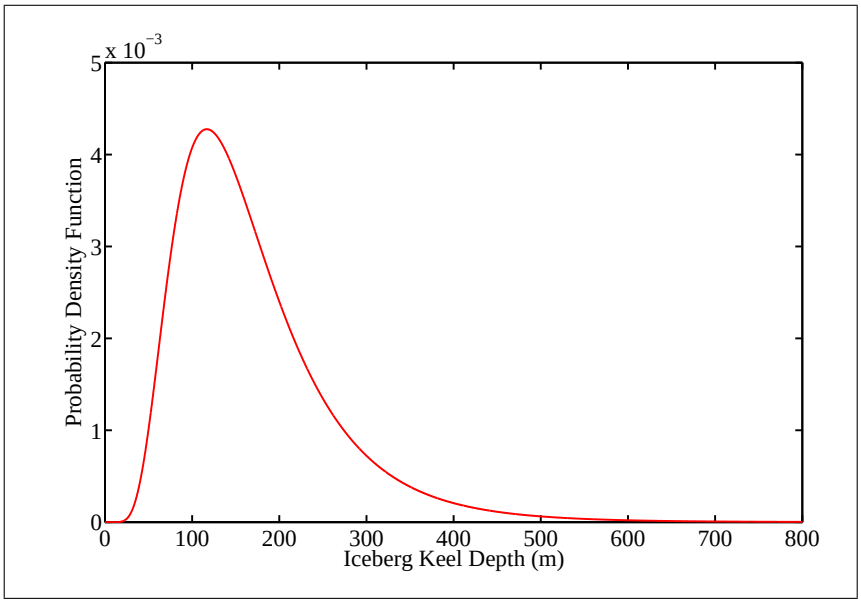

Figure 6.3: *Probability density function of the iceberg keel depth utilised for model runs exploring the effect of water temperature and depth of thermocline on the sedimentation rate.*

The water temperature profiles studied with the model for a thermocline depth of 100 m are shown in Figure 6.4. The winter profile for all the model runs is taken to be -1.358°C above 100 m, increasing linearly to 1°C at 400 m, and a constant at 1°C below this. The air temperature is assumed to be 'Cold' (average at Angmagssalik from 1895–1925, Section 4.3.7). The fjord is assumed to have a similar configuration as Kangerdlugssuaq Fjord (80 km long by 5 km wide), with the annual volume of icebergs produced equal to 15 $km^3 yr^{-1}$ to 2 decimal places and icebergs assumed to contain only englacial sediment, as in Section 6.2.1.

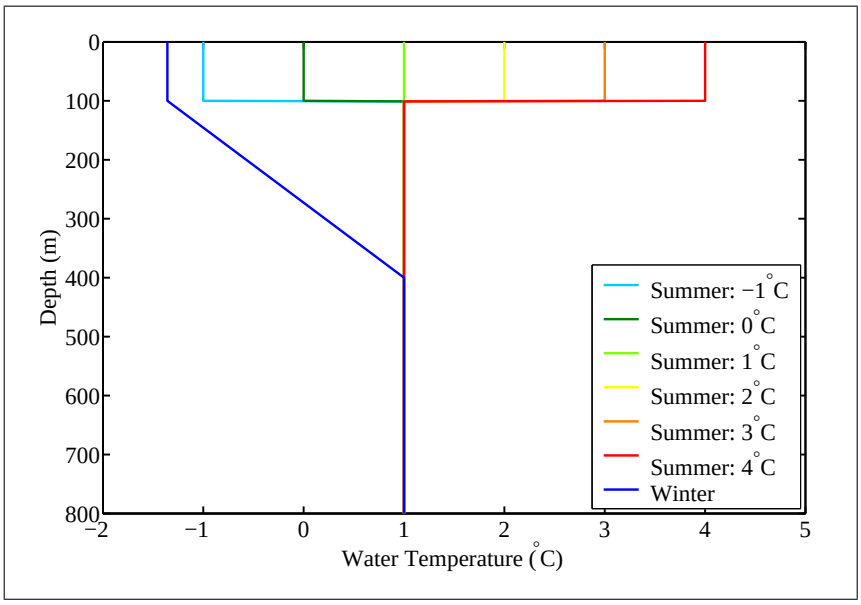

Figure 6.4: *Water temperature profiles used as model inputs for investigating the effect of changing surface layer temperature, for a thermocline depth of 100 m.*

6.2.2.3 Model Outputs

The across-fjord sedimentation rates (mean along whole length of the fjord) for a range of upper layer water temperatures, with the thermocline at 100 m and a constant temperature of 1°C below this, are shown in Figure 6.5. As expected, the sedimentation rate increases with increasing water temperature of the upper 100 m (equations 2.20 and 2.27). The increase in the peak sedimentation rate (near the centre of the fjord), for an upper water layer temperature increase from -1°C to 4°C, is 0.35 $cm\,yr^{-1}$. This is a 17% increase for a 5°C temperature rise. The effect would be much larger for an iceberg size distribution with a peak at lower values because a greater proportion of icebergs would be fully submerged in the surface layer. It can be seen in Figure 6.3 that a large proportion of icebergs have keel depths greater than the thermocline depth and are under the influence of the deeper layer of water at a constant temperature below the thermocline.

The thickness of the thermocline is varied for a surface layer temperature of 4°C, with the water temperature below the thermocline at 1°C. The model results for the across fjord transects of sedimentation rate for different thermocline depths are shown in Figure 6.6. The sedimentation rate increases with the thermocline depth. The difference between a thermocline depth of 50 m and 300 m is 0.4 $cm\,yr^{-1}$, or a 22.2% increase. The response of the sedimentation rate to the changing thermocline depth depends on the iceberg size distribution. For the iceberg size distribution investigated here, the mean iceberg keel depth is 120.6 m, and the proportion of icebergs which are only exposed to the surface layer at different depths of the thermocline can be seen

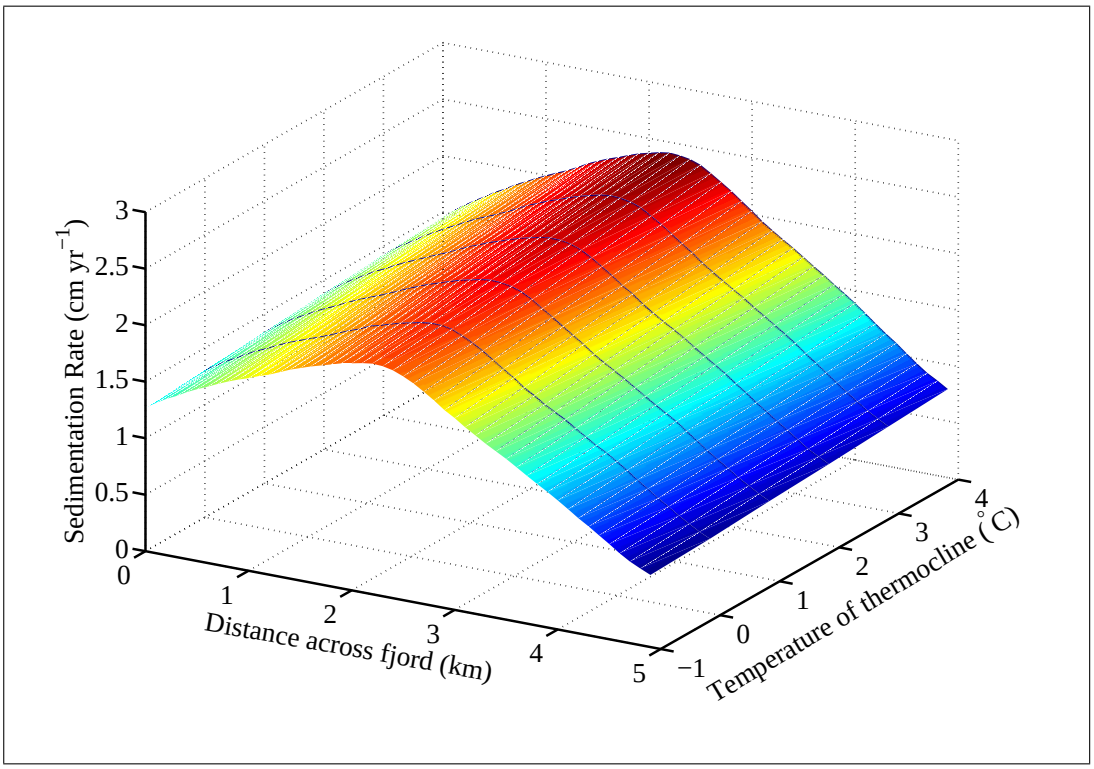

Figure 6.5: *Across fjord transects of sedimentation rate for a range of upper layer water temperatures, with the thermocline at* 100 *m and constant temperatures of* 1°*C below this (temperature profiles shown in Figure 6.4).*

from Figure 6.3.

6.2.2.4 Implications

Previous models of iceberg drift and melt have often excluded the effect of ocean temperature variation with depth; for example, Bigg *et al.* (1997); Løset (1993a) and Matsumoto (1996). The *SedBerg* Model calculates the average water temperature 'felt' by an iceberg over its keel depth to determine the iceberg melt rate of its sides and takes the water temperature at the iceberg base to calculate its basal melt rate. The effect of temperature and the temperature gradient is found to be significant. The influence increases with an increasing proportion of icebergs that are large enough to penetrate into the deeper layer of water, or equivalently a shallower thermocline depth, and with increasing temperature gradients.

It has been inferred from the chloride concentration and the oxygen isotopic composition from Ocean Drilling Program cores in the deep Pacific, Southern, and Atlantic oceans that temperatures during the LGM were relatively homogeneous and close to the freezing point of seawater at the ocean's surface (Adkins *et al.*, 2002). The ocean stratification during glacial periods was instead due to salinity contrasts. Therefore, during glacial intervals the surface temperature is representative of the temperature

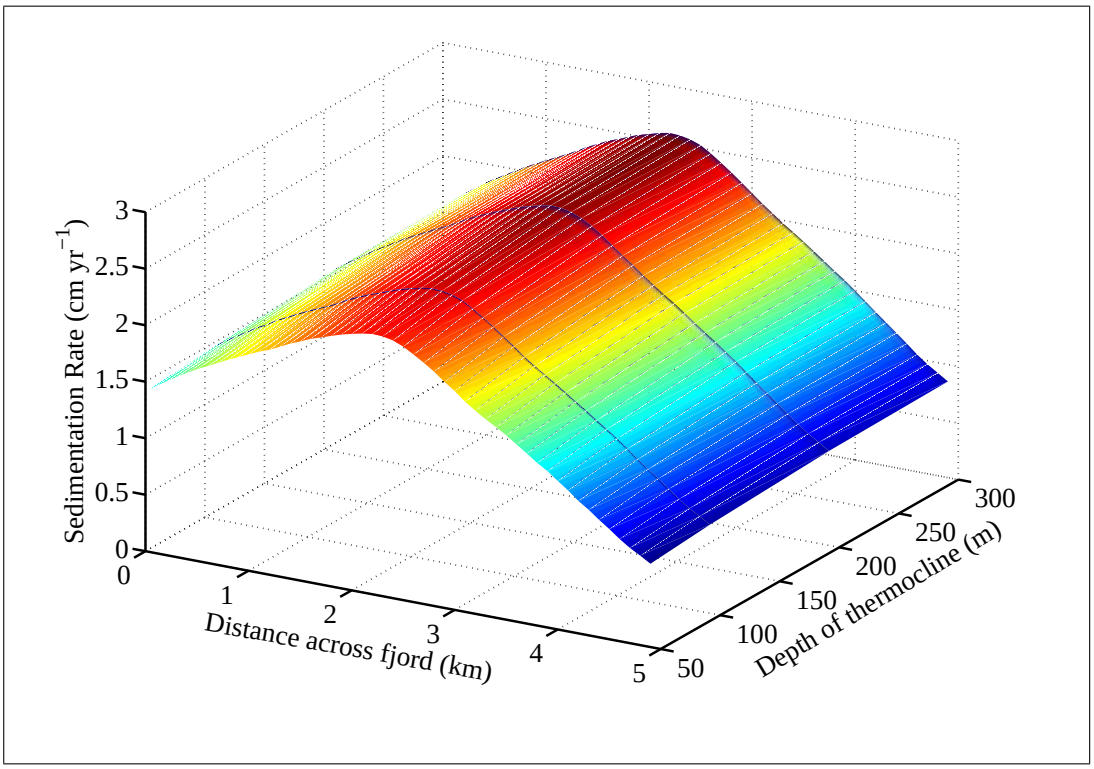

Figure 6.6: *Across fjord transects of sedimentation rates for varying thermocline depths, with the surface layer at a temperature of 4°C.*

of the whole water column.

However, this is not the case in polar oceans during interglacial periods. Variations in the thermocline depth of a few hundred metres and more have occurred during the Holocene in the coastal regions of Greenland. It is not uncommon for a change in temperature of the surface water to accompany a change in depth of the thermocline. For example, in Nansen Fjord during the Medieval Warm Period, warm Atlantic Intermediate Water occupied the fjord floor at a depth of 500 m (Jennings and Weiner, 1996).

Gladstone *et al.* (2001) used the Bigg *et al.* (1997) iceberg model to simulate the meltwater flux from icebergs in the Southern Ocean. The iceberg melt rate was calculated from the surface water temperature only. This is a reasonable assumption for icebergs with keel depths shallower than the thermocline depth. Upwelling in the Southern Ocean causes the ocean temperature to increase with depth. Jenkins (1999) observed a thermocline between 100–300 m near to the coast of Antarctica and Karsten and Marshall (2002) established that the depth of the thermocline at 64°S to be approximately 200 m. The recent work of Dowdeswell and Bamber (2007) estimated the maximum keel depths of icebergs from ice shelves in Antarctica to vary between approximately 160 and 680 m. Therefore, it is likely that the temperature stratification of the ocean will affect the melt rate of larger icebergs, especially near

the coast.

The meltwater injection from icebergs modelled by Gladstone *et al.* (2001) was found to be comparable to the excess of precipitation over evaporation in coastal regions, but small elsewhere. They proposed that giant icebergs, which were not modelled, may last longer and extend the influence of iceberg meltwater to the north. Silva *et al.* (2006) calculated the contribution of giant icebergs to freshwater input in the Southern Ocean. They utilised a database of the trajectories and sizes of giant icebergs (with a long-axis greater than approximately $18\,km$) and modelled their basal melt rates. They took the far-field water temperature to be equal to the layer below the base of the iceberg as calculated by the OCCAM model. The combined estimates of iceberg freshwater flux for both 'normal' and giant icebergs from Gladstone *et al.* (2001) and Silva *et al.* (2006) were found to produce a significant contribution to the freshwater balance of the Southern Ocean.

In light of the satellite radar altimetry investigations of Dowdeswell and Bamber (2007), the maximum 'normal' iceberg thicknesses, excluding giant icebergs, seem likely to exceed the $250\,m$ that was specified by Gladstone *et al.* (2001). If the Dowdeswell and Bamber (2007) iceberg size distributions were applied to the various calving margins around Antarctica, some of the distributions would have larger expected values than was assumed by Gladstone *et al.* (2001). If the influence of warmer water temperatures at depth was included, this would increase iceberg melt rates. However, the experiments in Section 6.2.1 imply that larger icebergs (size greater than approximately $150\,m$) may melt more slowly, due to the inverse relation between the melt rate and iceberg size. Therefore a larger proportion of icebergs may survive for longer and contribute to meltwater injection further away from the coast. It may be worthwhile to investigate the effect of these changes on the modelled spatial distribution of the iceberg freshwater input around Antarctica (see Section 7.4).

6.2.3 Random number seeds: water and wind velocities

6.2.3.1 Motivation

The motion of icebergs is driven by wind and water forcing. In the *SedBerg* Model, four random number sequences are generated to determine the x and y-components of the wind and water velocities. The output of the random number generator depends on the value of the seed used to initialise it. The *SedBerg* Model runs described in this thesis were for 10 model years and, in Chapter 4, the annual sedimentation rate generated over this time was compounded to represent longer time periods. Therefore, it is important to test the variability of the results based on the sequence of random numbers used to generate the iceberg motion, as this provides a measure of

the uncertainty in the model output.

6.2.3.2 Model Inputs

The *SedBerg* Model was run for a mean iceberg size of 173.3 m (size distribution in Section 4.3.3), under 'Cold' conditions as defined in Section 4.4.2. The fjord is assumed to have a similar configuration as Kangerdlugssuaq Fjord, with the annual volume of icebergs produced equal to 15 km^3yr^{-1} to 2 decimal places and icebergs assumed to contain only englacial sediment, as in Section 6.2.1.

6.2.3.3 Model Outputs

The model output of along-fjord sedimentation rates (calculated as the mean of the central 1 km wide section), for different initial seeds of the water and air velocities are shown in Figure 6.7. The fine structure of the along-fjord deposition curve varies for

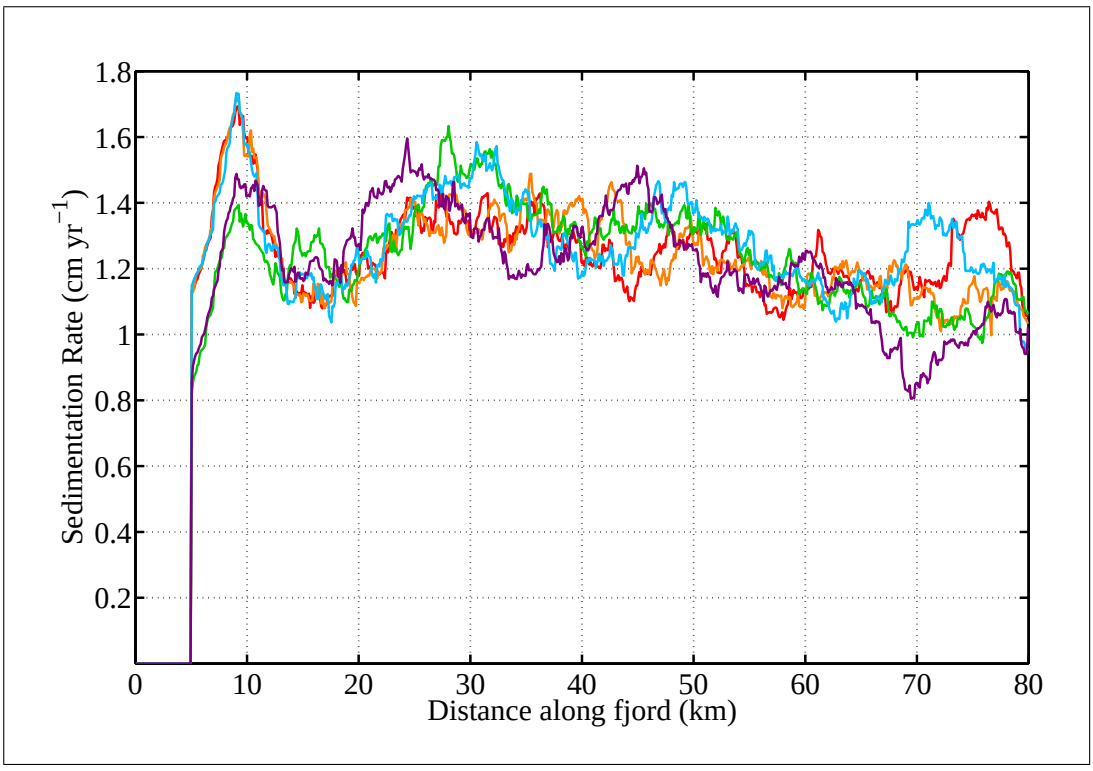

Figure 6.7: *Transects of sedimentation rates along the fjord (mean of central 1 km wide section) for 10 modelled years with different initial seeds for the random number generator for the water and air velocities.*

each of the model runs utilising different seeds. This confirms that these features are due to the random nature of the forcing parameters. The deposition pattern is likely to become smoother for longer model runs.

The model output for the across-fjord transects of sedimentation rate, which demonstrate the integrated effect over the length of the fjord, for different initial seeds of

the water and air velocities, are shown in Figure 6.8. There is a spread in the average

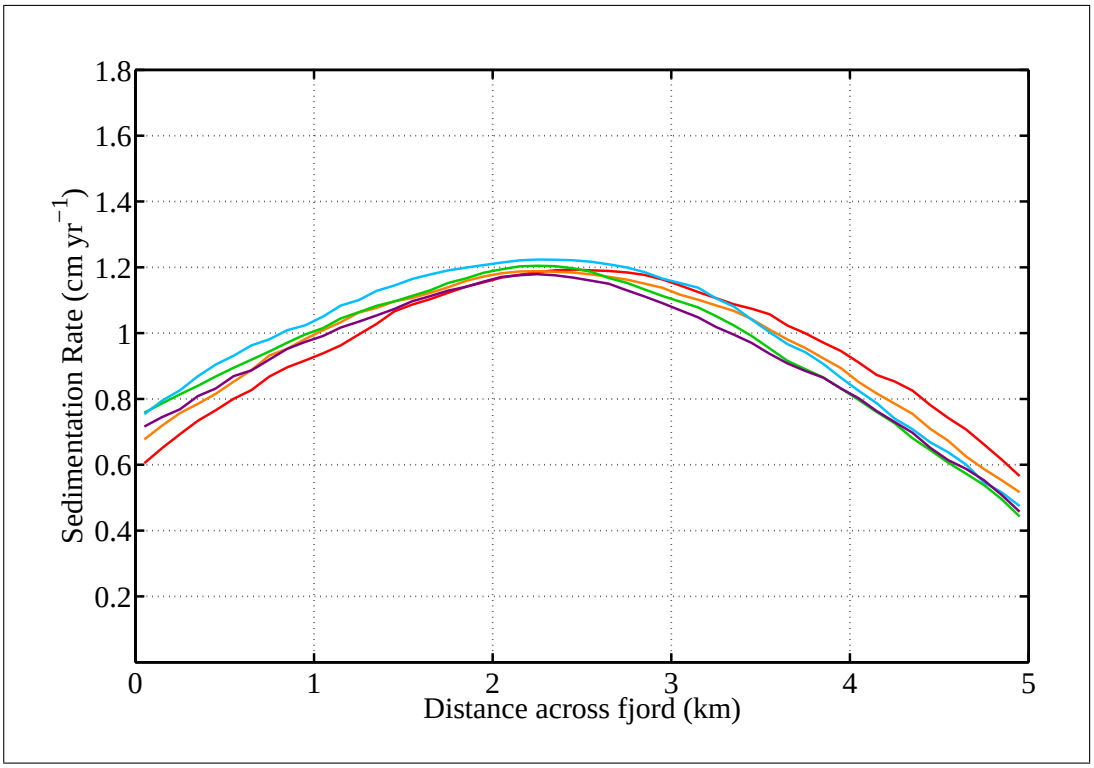

Figure 6.8: *Transects of sedimentation rates across the fjord (mean along whole length) for 10 modelled years with different initial seeds for the random number generator for the water and air velocities.*

peak deposition rate along the length of the fjord of approximately 5% for the different seeds. Therefore, changing the initial values of random number generator seeds governing the wind and water forcing parameters does have a small effect on the rate of deposition in the fjord.

6.2.3.4 Implications

The uncertainty due to the random nature of the forcing that drives the motion of the icebergs is approximately 5% for the mean sedimentation rate along the fjord (across-fjord transect shown in Figure 6.8). The variability observed down the fjord is an artifact of the stochastic parameterisation of the wind and water velocities. If the model is run for long enough time periods, the distribution of sediment over the fjord will converge to the true probability distribution of sedimentation.

6.3 *SedPlume* Model

The parameter experiments carried out with the *SedPlume* Model in this section are for a plume rising from the base of a glacier with the same thickness ($40\,m$) as McBride

Glacier (Chapter 5). For the range of grain sizes investigated ($\phi = 3$ to $\phi = 9$ on the Udden-Wentworth Scale), the whole sediment load is carried to the surface. Therefore all sedimentation occurs from the gravity current and the rate and pattern of deposition is determined by the plume properties at the surface, as well as the initial sediment size fractions. The *SedPlume* Model experiments in this section are organised according to the effect of changing the initial conditions on the surface attributes of the plume (Section 6.3.1) and the consequences of changing the initial sand fraction and the initial plume velocity on the sand fraction deposited by the gravity current (Section 6.3.2). A third section (Section 6.3.3) investigates the impact of varying the ambient density gradient, which may play a role in determining the plume trajectory and the plume properties at the surface.

6.3.1 Plume Properties at the Surface

6.3.1.1 Motivation

Model experiments are performed while varying the initial plume velocity and subglacial meltwater conduit radius to investigate their influence on plume attributes at the surface, which consequently affect the sedimentation rate and pattern. The size of the subglacial conduit at different glaciers depends on environmental and climatic conditions. The principal factor in determining the conduit radius is thought to be the flux of water passing through the glacier (Eyles, 2006; Fountain and Walder, 1998; Ng, 2000). For example, larger conduits will form if there are high precipitation rates and a mild climate. The water discharge, or velocity, emerging from the conduit is subject to daily, as well as seasonal fluctuations (Anderson *et al.*, 1999; Bingham *et al.*, 2005).

6.3.1.2 Model Inputs

The *SedPlume* Model is run for subglacial meltwater conduit radii between 0.2 and $5\,m$ and initial plume velocities between 0.2 and $50\,m\,s^{-1}$, which are realistic extreme limits for glacial meltwater plumes. The maximum velocity of $50\,m\,s^{-1}$ was recorded by Vivian (1975) at a glacial stream in the Alps (Sugden and John, 1977, p. 301). A constant ambient density of $1025\,kg\,m^{-3}$ is assumed.

6.3.1.3 Model Outputs

The plume properties at the surface presented in this section, which influence the pattern and rate of sedimentation in the gravity current, are: the distance that the plume surfaces from the glacier, x_s; the volume flux at the surface, Q_s; the momentum flux at the surface, M_s, and the buoyancy flux at the surface, B_s.

Since all the sediment is carried to the surface and deposited by the gravity current, the distance from the glacier at which the plume surfaces, x_s, determines the position of the peak sediment deposition rate. This distance, x_s, over the two-dimensional parameter space of initial plume velocity and conduit radius, is shown in Figure 6.9. Over the range of values shown, x_s is most sensitive to changes in the plume velocity

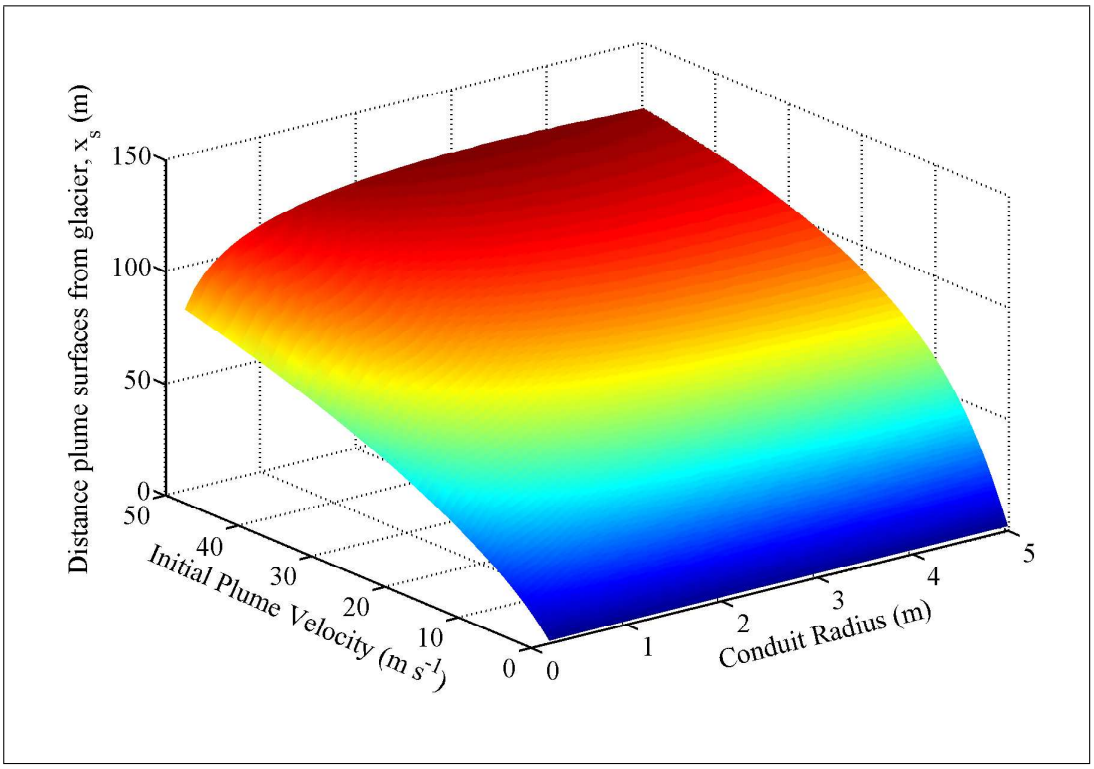

Figure 6.9: *The influence of the initial velocity and conduit radius on the distance that the plume surfaces from the glacier front, x_s over a range of realistic values for glacial plumes.*

and increases with initial velocity, due to the accompanying increase in the initial horizontal momentum flux (equation 3.8). The horizontal momentum flux remains the same as the plume rises as there is no opposing force (equation 3.20).

As the conduit radius is increased, the plume surfaces further from the glacier front. The increase in x_s with conduit radius is due to the associated increase in the horizontal momentum flux. This increase is greatest at small radii and is not as important at larger radii, due to the decrease in the surface area to volume ratio as the conduit radius is increased. The volume of denser ambient fluid entrained compared to the volume of fluid in the buoyant plume is decreased with increasing conduit radii. Therefore, with increasing conduit radii there is an increased upward acceleration of the plume due to buoyancy forces relative to the increase in the horizontal momentum flux, which acts to slow down the increase in the distance the plume surfaces from the glacier front. If the conduit radius is increased to even larger values than those considered here, this effect would eventually result in x_s decreasing with increasing

radius.

The volume flux of the plume when it reaches the surface determines the sediment concentration at the surface of the plume, ϕ_s (equation 3.10), which governs the magnitude of the peak and the spread of the deposition rate from the gravity current (equation 3.59). The volume flux of the plume when it reaches the surface, Q_s, over the two-dimensional parameter space of initial plume velocity and conduit radius, is shown in Figure 6.10. Q_s increases with increasing initial plume velocity, since volume

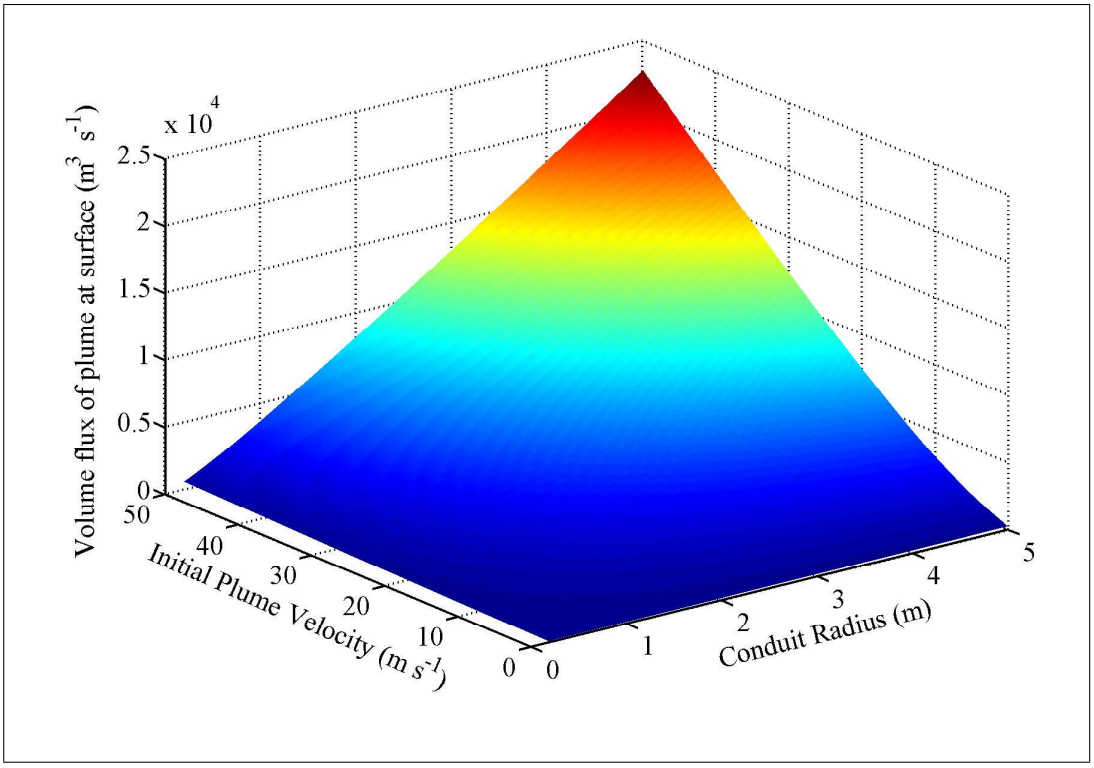

Figure 6.10: *The influence of the initial velocity and conduit radius on the volume flux of the plume when it reaches the surface over a range of realistic values for glacial plumes.*

flux is dependent on velocity (equation 3.7), and a higher initial volume flux results in a higher volume flux at the surface. For the same reason, the plume volume flux at the surface also has a positive trend with conduit radius. The volume flux depends on the square of the radius but is proportional to the velocity (equation 3.7). For this reason the volume flux at the surface is more sensitive to the conduit radius than to the initial velocity. The rate of change of the volume flux is proportional to both the radius and the velocity (equation 3.19), which accounts for the linear relationship between the surface volume flux with both conduit radius and initial velocity.

The momentum flux of the plume when it reaches the surface is strongly linked to the volume flux by definition (equation 3.8). The momentum flux of the plume when it reaches the surface, M_s, over the two-dimensional parameter space of initial plume velocity and conduit radius for values appropriate for glacial plumes, is shown

in Figure 6.11. M_s increases with increasing initial plume velocity and conduit radius.

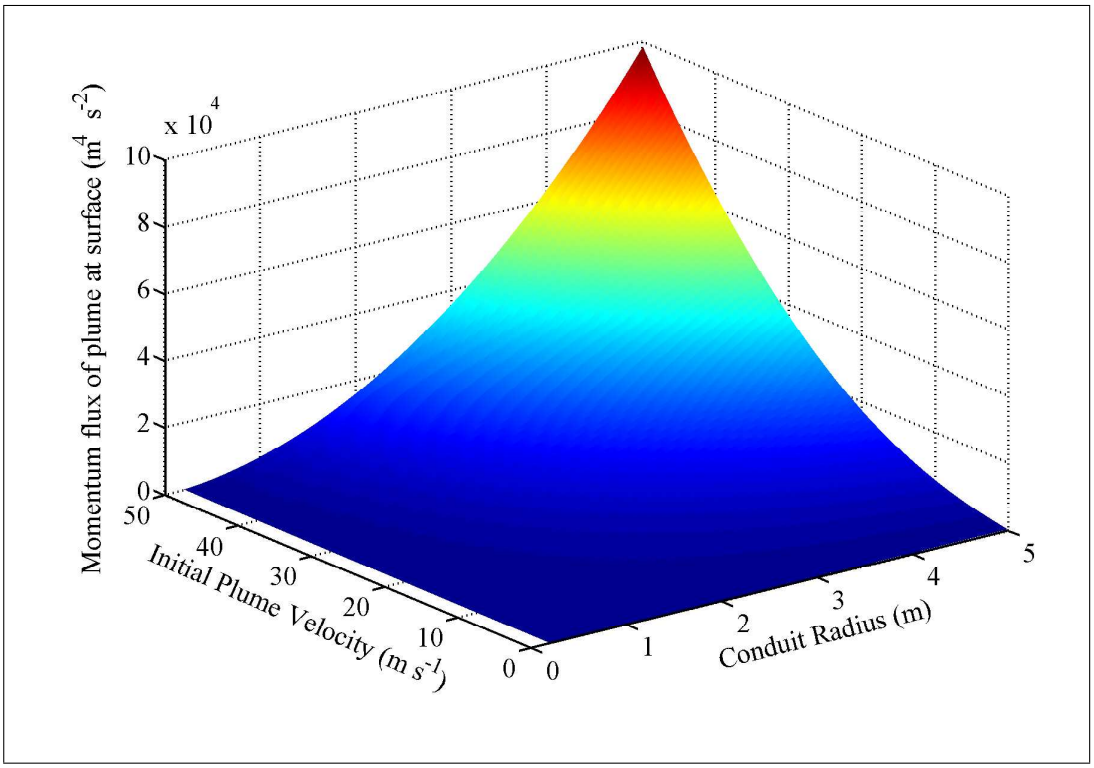

Figure 6.11: *The influence of the initial velocity and conduit radius on the momentum flux of the plume when it reaches the surface over a range of realistic values for glacial plumes.*

The rate of increase in the momentum flux at the surface with initial plume velocity and conduit radius is non-linear and is larger at higher values of initial velocity and radius. This is because the momentum flux is proportional to the square of the velocity and the square of the radius (equation 3.8). However, the rate of increase of the momentum flux is proportional to the square of the radius (equations 3.24), which is the reason that the momentum flux at the surface is more sensitive to the value of the conduit radius than the initial plume velocity.

The buoyancy flux of the plume when it reaches the surface, B_s, is also related to the volume flux by definition (equation 3.9). B_s, over the two-dimensional parameter space of initial plume velocity and conduit radius, is shown in Figure 6.12. The buoyancy flux at the surface increases linearly with initial plume velocity, because the buoyancy and the rate of change of buoyancy are both directly proportional to the velocity (equations 3.9 and 3.26). The relationship between buoyancy flux at the surface and conduit radius is non-linear because the buoyancy flux and the rate of change of the buoyancy flux both depend on the square of the radius (equations 3.9 and 3.26).

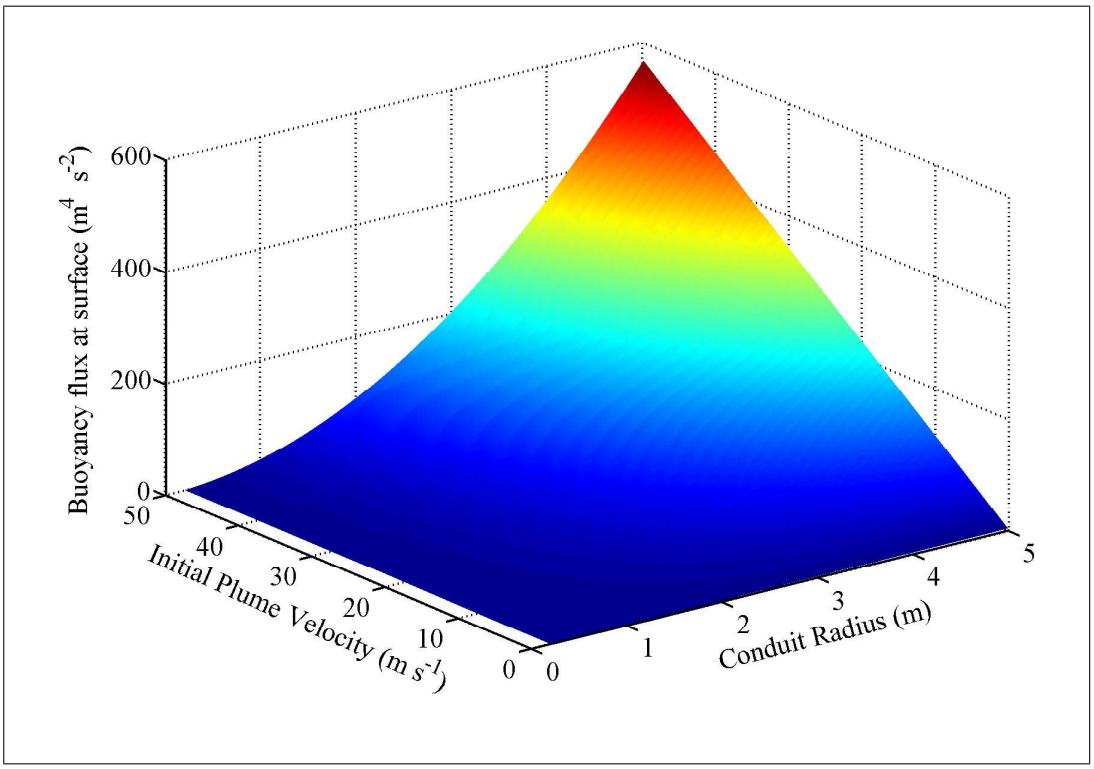

Figure 6.12: *The influence of the initial velocity and conduit radius on the buoyancy flux of the plume when it reaches the surface over a range of realistic values for glacial plumes.*

6.3.1.4 Implications

The dependence of the distance that the plume surfaces from the glacier front, x_s, on the subglacial conduit radius and initial plume velocity, indicates that the peak sediment deposition occurs further from the glacier front for higher initial plume velocities and larger subglacial conduit radii. Increasing the initial plume velocity has the greater influence on x_s over the range of values studied and increasing the subglacial conduit radius above approximately $2\,m$ does have a notable effect on x_s.

Observations at glacier margins show that it is the initial plume velocity that varies most rapidly and over the largest range of values. Humphrey *et al.* (1986) measured water and sediment discharge from Variegated Glacier in Alaska. They observed seasonal trends, weather-related events and diurnal variations. The daily minimum and maximum discharge varied by approximately 20%, with large discharge fluctuations controlled by major storms. Over the melt season, the main stream discharge increased to approximately four times its value in early August compared to mid-May. Typically for most glaciers, flow is low in the early morning, rising rapidly towards the late afternoon with dramatic increases in the early evening (Larson, 1978). During the winter season, when the flow is derived from basal pressure-melting alone, the discharge flow falls to approximately 10% of the summer flow (Embleton and King,

1975). The position of the peak deposition will fluctuate with the plume velocity variations, as modelled in Figure 6.9. Powell (1990) associated the discharge flow rate of the meltwater stream with the formation of different sedimentary fan types at the margin of tidewater glaciers, as shown in Figure 6.13.

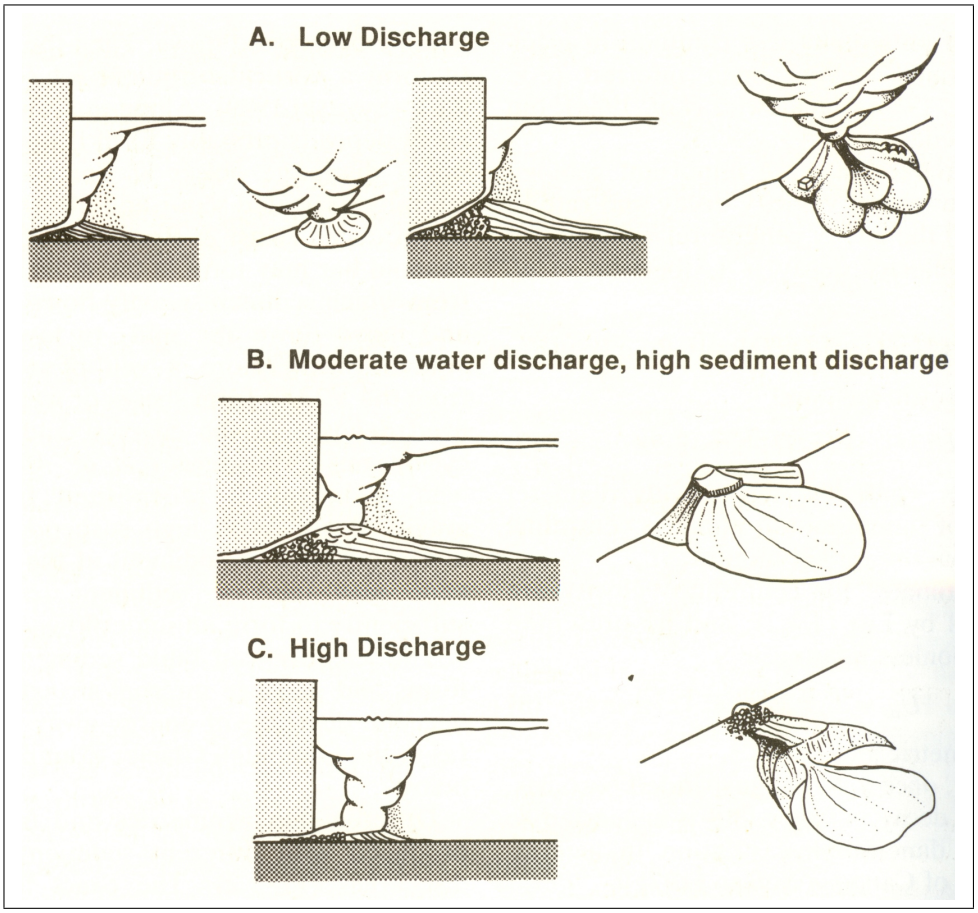

Figure 6.13: *Alternative sedimentary fan types caused by low, moderate and high subglacial meltwater discharges Powell (from 1990).*

The volume flux at the surface determines the pattern of deposition. Higher volume fluxes result in wider dispersal of sediment deposits; lower values produce narrower dispersal (equation 3.59). Therefore, an increase in either the initial velocity or the conduit radius delivers sediment deposition with a wider dispersal. If the plume discharge remains constant for a period of time, then varies rapidly to a different flux, a lobate fan would form (Powell, 1990). This plume behaviour is imitated by the *SedBerg* Model.

The *SedPlume* Model provides a quantitative assessment of the plume trajectory and surface volume flux produced by various initial plume velocities and conduit radii, which determine the cross-sectional profile of ice-marginal glacimarine fan deposits.

6.3.2 Deposited Sand Fraction

6.3.2.1 Motivation

The variation with distance from a glacier front of the grain size fractions deposited by subglacial meltwater discharge produces characteristic lithofacies. Cyclically interlaminated sediment consisting of stratified sandy mud produced by suspension settling from plumes, particularly during periods of high meltwater discharge, have been observed as prominent features in proximal glacial marine settings (Cowan and Powell, 1990; Cowan *et al.*, 1999; Powell and Molnia, 1989). These lithofacies have been termed cyclopsams by Mackiewicz *et al.* (1984).

In the following model experiments, the influence of the initial sand fraction and the initial plume velocity on the sand fraction deposited in the gravity current with distance from x_s is examined.

6.3.2.2 Model Inputs

In this section, the *SedPlume* Model is run for three initial parameter experiments:

1. The initial sand fraction and initial plume velocity are varied to study the sand fraction deposited at x_s and at $300\,m$ from x_s: initial sand fraction is varied between 0 and 0.9, with clay fraction of 0.1 and remaining fraction as silt; the initial plume velocity is varied between 0.2 and $50\,m\,s^{-1}$; subglacial conduit radius is $2.5\,m$; initial sediment concentration is $10\,kg\,m^{-3}$ and ambient density is $1025\,kg\,m^{-3}$.
2. Initial plume velocity and distance from x_s are adjusted to explore the sand fraction deposited with distance from x_s: initial plume velocity is varied between 0.2 and $50\,m\,s^{-1}$; initial grain fractions are 0.1 sand, 0.8 silt and 0.1 clay; subglacial conduit radius is $2.5\,m$; initial sediment concentration is $10\,kg\,m^{-3}$ and ambient density is $1025\,kg\,m^{-3}$.
3. The initial sand fraction and distance from x_s are altered to examine the sand fraction deposited with distance from x_s: initial sand fraction is varied between 0 and 0.9, with clay fraction of 0.1 and remaining fraction as silt; initial velocity is $9.6\,m\,s^{-1}$ and subglacial conduit radius is $2.5\,m$, providing a volume flux of $188\,m^3\,s^{-1}$.

6.3.2.3 Model Outputs

The resulting sand fraction deposited by the gravity current at the point where the plume surfaces, x_s, over the two-dimensional parameter space of initial plume velocity and sand fraction (Experiment 1), is shown in Figure 6.14. Firstly, note that there

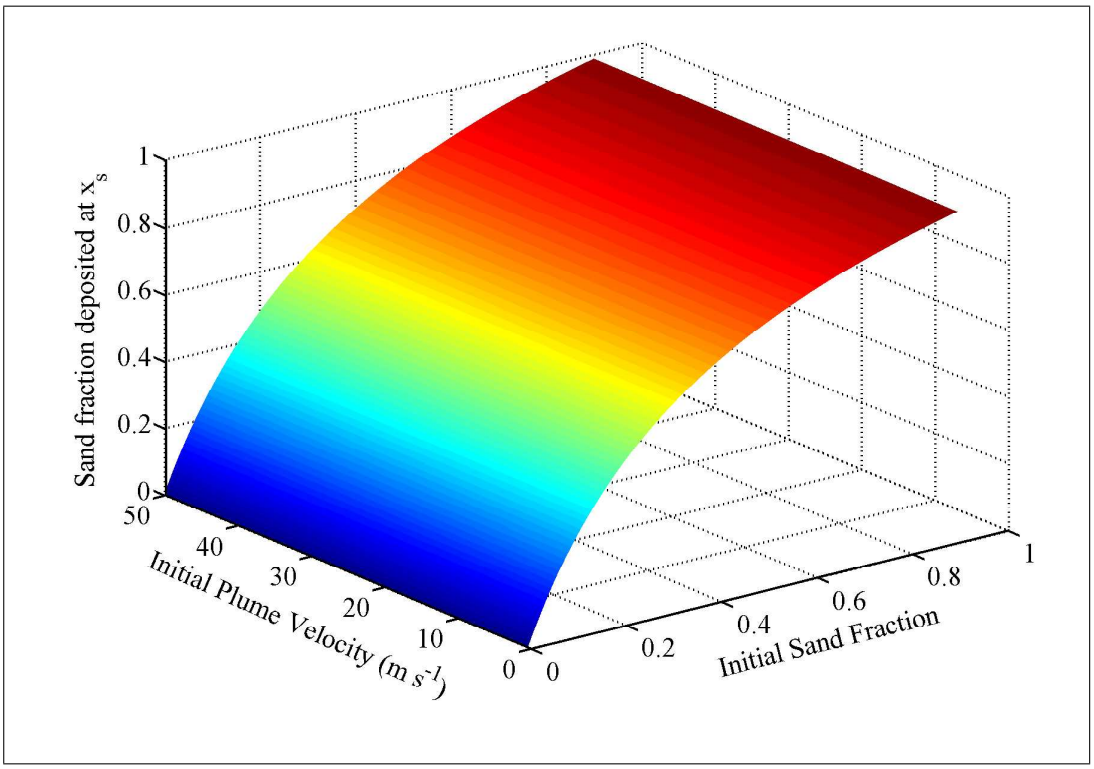

Figure 6.14: *The sand fraction deposited at the point the plume reaches the surface is shown against the initial plume velocity and sand fraction.*

is no effect on the sand fraction deposited at x_s with changing values of the initial plume velocity. This is because the peak deposition rate of each particle fraction only depends on its initial concentration and settling velocity (equation 3.59). The sand fraction deposited at x_s is always greater than the initial sand fraction and increases non-linearly with increasing initial sand fraction, caused by the logarithmic base 2 relation between the size classes of sand, silt and clay with grain diameter, the power law relation between grain size and settling velocity (equations 3.40–3.42) and the exponential nature of equation 3.59 with settling velocity.

The sand fraction deposited by the gravity current at $300\,m$ from the point where the plume surfaces, x_s, over the two-dimensional parameter space of initial plume velocity and sand fraction (Experiment 1), is shown in Figure 6.15. Figures 6.14 and 6.15 show that a lower sand fraction is deposited at $300\,m$ from x_s compared with the sand fraction deposited at x_s. The ratio of sand fraction deposited at x_s to that at $300\,m$ from x_s, decreases with increasing plume velocity. This indicates that with increasing initial plume velocity the deposition of the sand fraction has a higher dispersal. To investigate the effect of initial plume velocity on the dispersal of sand further, the sand fraction deposited with distance from x_s over a range of initial plume velocities (Experiment 2) is shown in Figure 6.16. This confirms that increasing the initial plume velocity increases the dispersal of sand, i.e. a higher proportion of sand is deposited

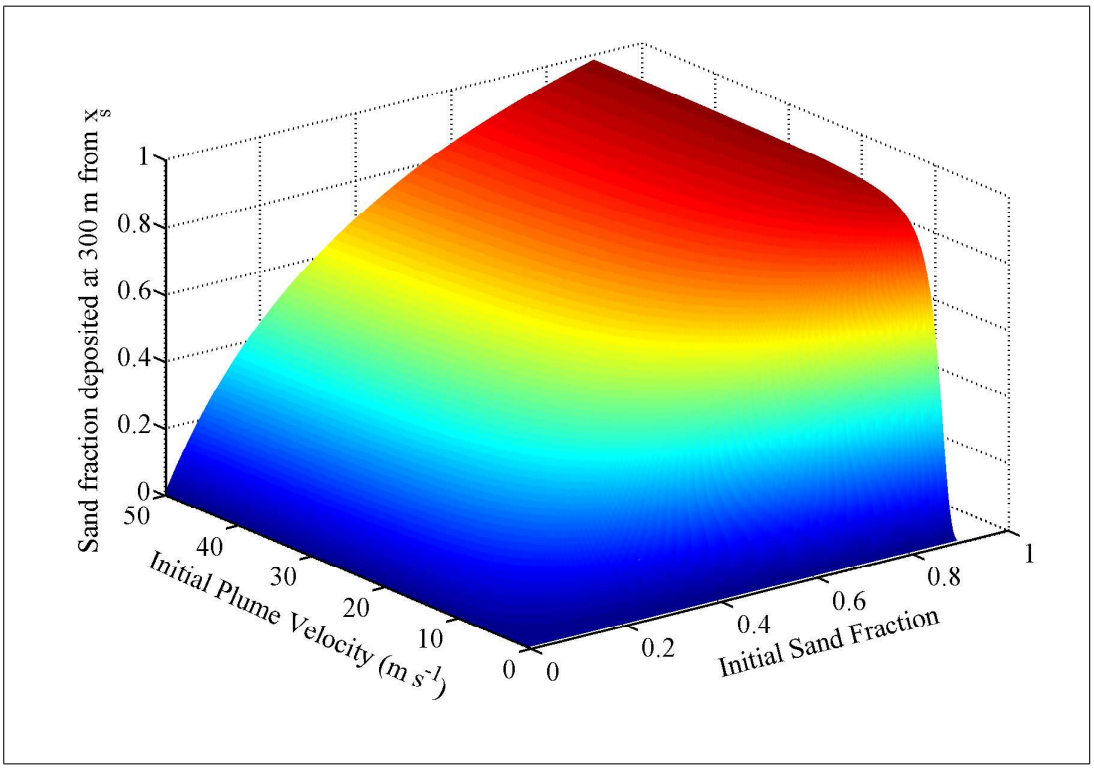

Figure 6.15: *The sand fraction deposited at 300 m from the point the plume reaches the surface is shown against the initial plume velocity and sand fraction.*

at larger distances from x_s. However, there is no change in the peak sand fraction deposited at x_s with initial plume velocity (c.f. Figure 6.14).

The sand fraction deposited with distance from x_s over a range of initial sand fractions (Experiment 3) is shown in Figure 6.17. The volume flux is constant for these model runs, so the total mass flux of sediment also remains constant. As the initial sand fraction is increased, so does the sand fraction deposited, although the relationship is non-linear. The dispersion of the sand fraction also increases with initial sand fraction.

6.3.2.4 Implications

There is a non-linear increase of sand fraction deposited at x_s with initial sand fraction (Figure 6.14), resulting in the steepest gradient at low initial sand fractions. Therefore, for low initial sand fractions, small variations in the initial sand fraction result in large changes in the sand fraction deposited at x_s. The sediment concentration in meltwater streams from modern glaciers has been observed to be extremely variable with diurnal and seasonal fluctuations, as well as variations over the course of discharge events (Thayyen *et al.*, 1999). This is a potential mechanism for the deposition of laminated couplets.

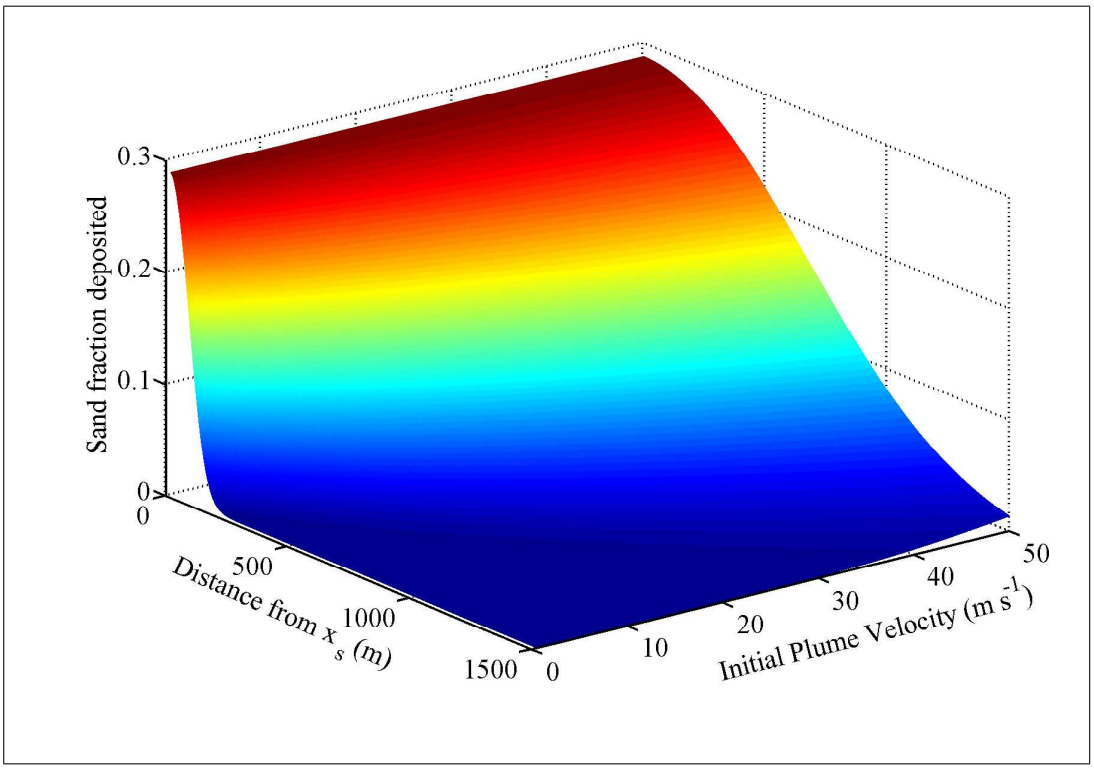

Figure 6.16: *The sand fraction deposited with distance from x_s for a range of initial plume velocities. Initial grain fractions are 0.1 sand, 0.8 silt and 0.1 clay; subglacial conduit radius is 2.5 m; initial sediment concentration is 10 kg m^{-3} and ambient density is 1025 kg m^{-3}.*

Mackiewicz *et al.* (1984) defined the term 'cyclopsams' for interlamination of coarse-grained sand and mud in extreme proximal positions and hypothesised that these couplets may be formed by fluctuations in the meltwater stream discharge. Cyclopsams are common sedimentary features of temperate glacimarine settings (Cowan *et al.*, 1999; Phillips *et al.*, 1991). The positive trend between sand fraction dispersal and initial plume velocity produced by the *SedPlume* Model (Figure 6.16), shows that it is capable of simulating the formation of cyclopsams by fluctuations in the meltwater stream discharge.

The tidal cycle will affect the position of the rising plume, so that it rises closer to the glacier front during flood tide and is pulled further away from the glacier during ebb tide. The deposition from surface gravity currents is affected by tides, as they draw turbid overflows down-fjord. Cyclopels were defined by Mackiewicz *et al.* (1984) as laminated couplets produced by suspension settling of particles from turbid plumes, which are produced at the rate of approximately two per day by the tidal oscillation. Tidal influences may transport grain sizes up to coarse silt over distances of more than 12 *km* from the glacier front (Syvitski *et al.*, 1985). Ambient water velocities are not included in the *SedPlume* Model at present; however, they could be a future addition to the model (see Section 7.4).

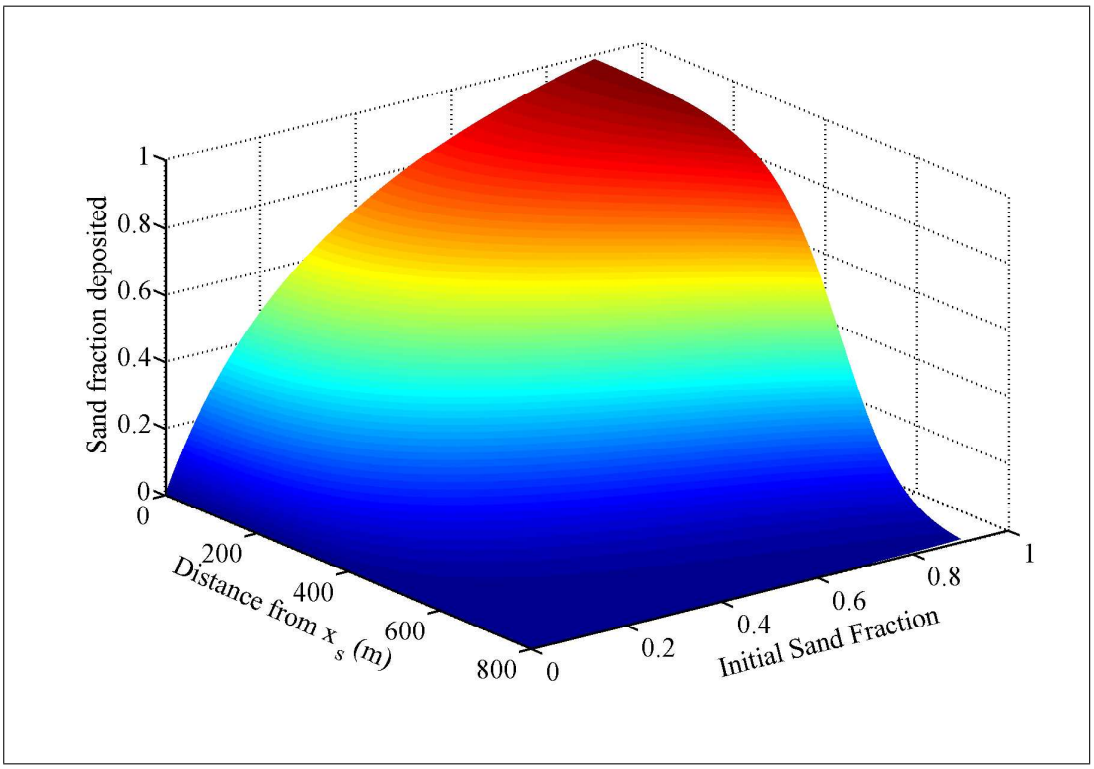

Figure 6.17: *The sand fraction deposited against distance from x_s and the initial sand fraction.*

6.3.3 Ambient Density Gradient

6.3.3.1 Motivation

Powell (1984) suggested that sea water density stratification may control the trajectories of glacial meltwater plumes; therefore, the influence of ambient density gradients, caused by salinity differences, on plume attributes are investigated in this section.

6.3.3.2 Model Inputs

The ambient density gradients explored with the model are shown in Figure 6.18. The density at the depth of the subglacial conduit is held constant at $1025\,kg\,m^{-3}$ and the gradient is varied so that the surface density ranges from 1012 to $1025\,kg\,m^{-3}$. For simplicity, the various ambient density gradients are referred to by their surface water density in the figures in this section.

6.3.3.3 Model Outputs

The distance the plume surfaces from the glacier, x_s, over the two-dimensional parameter space of ambient density gradient and initial plume velocity, is shown in Figure 6.19. There is an almost imperceptible increase in the distance that the plume surfaces from

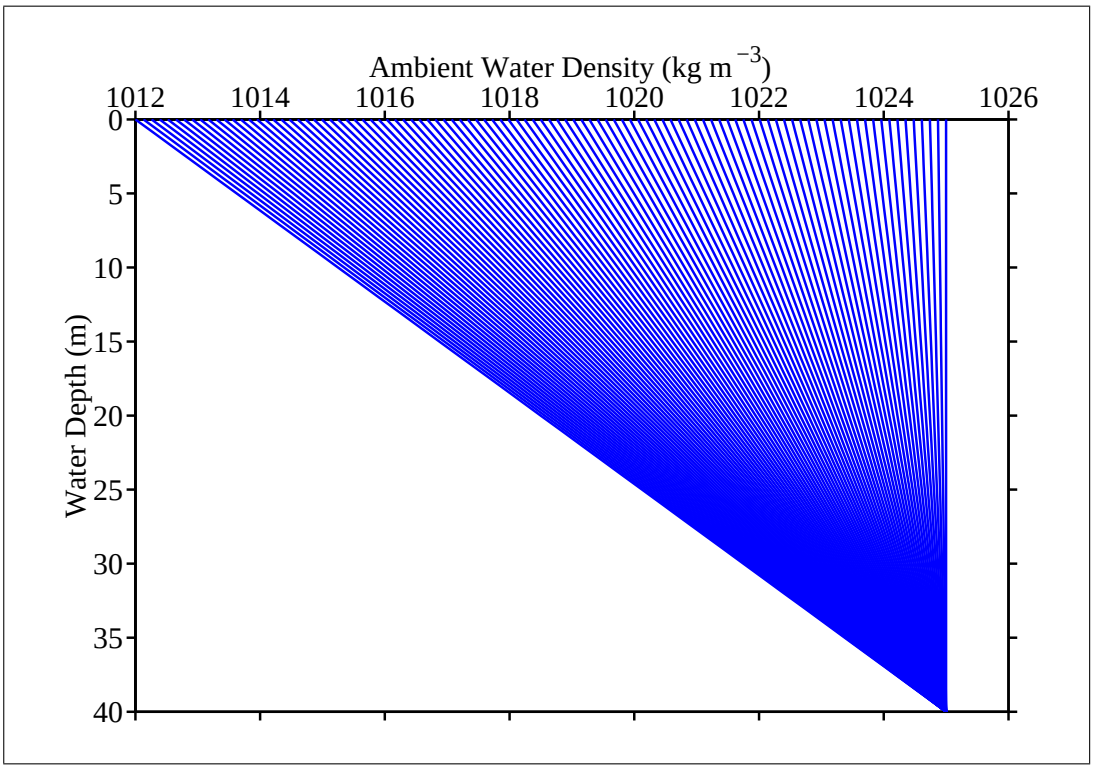

Figure 6.18: *The range of ambient water density gradients used in this section, which for clarity are referred to by their surface density in the other figures.*

the glacier front, x_s, with increasing density gradient (decreasing ambient density at the surface), due to a decrease in the density difference between the plume and the ambient fluid. The reduced vertical acceleration upwards due to the smaller buoyancy difference permits the plume to travel further horizontally before reaching the surface. However, this effect is insignificant compared to the increase in x_s with initial plume velocity, which was discussed in Section 6.3.1

The trajectories of two plumes, with contrasting initial velocities, rising in ambient water, either with a uniform density or with the maximum density gradient shown in Figure 6.18, are shown in Figure 6.20. The change in ambient density does have an effect on the trajectory, but this is overwhelmed by the more dominant influence of the initial plume velocity. The plume with an initial velocity of $1\,m\,s^{-1}$ shows unstable behaviour as it nears the surface because it has become neutrally buoyant. Its velocity decelerates until it begins to descend. As it does so it entrains a large amount of ambient fluid, thus its radius increases very rapidly. Eventually the edge of the plume reaches the surface, at which point the *SedBerg* Model stops the calculation.

The volume flux of the plume at the surface for a conduit radius of $2.5\,m$, over the two-dimensional parameter space of ambient density gradient and initial plume velocity, is shown in Figure 6.21. The ambient density gradient has an almost negligible effect on the volume flux of the plume at the surface; therefore, there is no significant

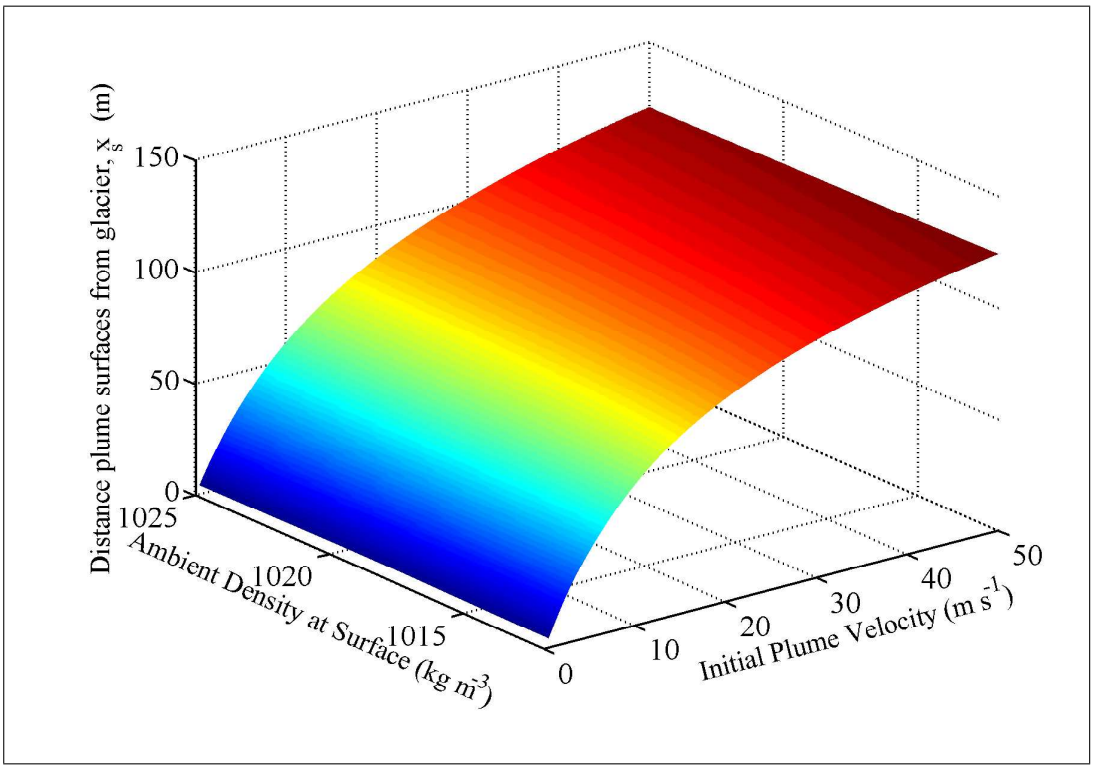

Figure 6.19: *The distance the plume surfaces from the glacier, for a conduit radius of 2.5 m, is shown against the initial plume velocity and the ambient water density at the surface, which corresponds to the gradient of the ambient water (Figure 6.18).*

associated effect on the pattern of sediment deposition. There is a small increase in volume flux at the surface with decreasing ambient density at the surface (increasing

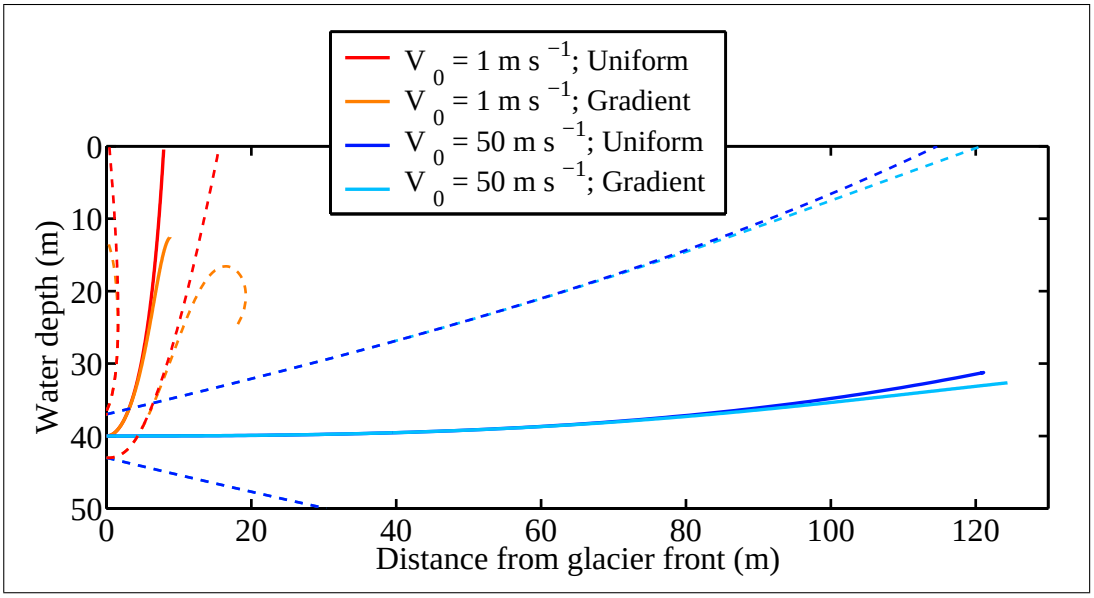

Figure 6.20: *The trajectories of plumes with initial velocities of 1 and 50 m s^{-1} and either a uniform ambient or a density gradient equal to the maximum in Figure 6.18.*

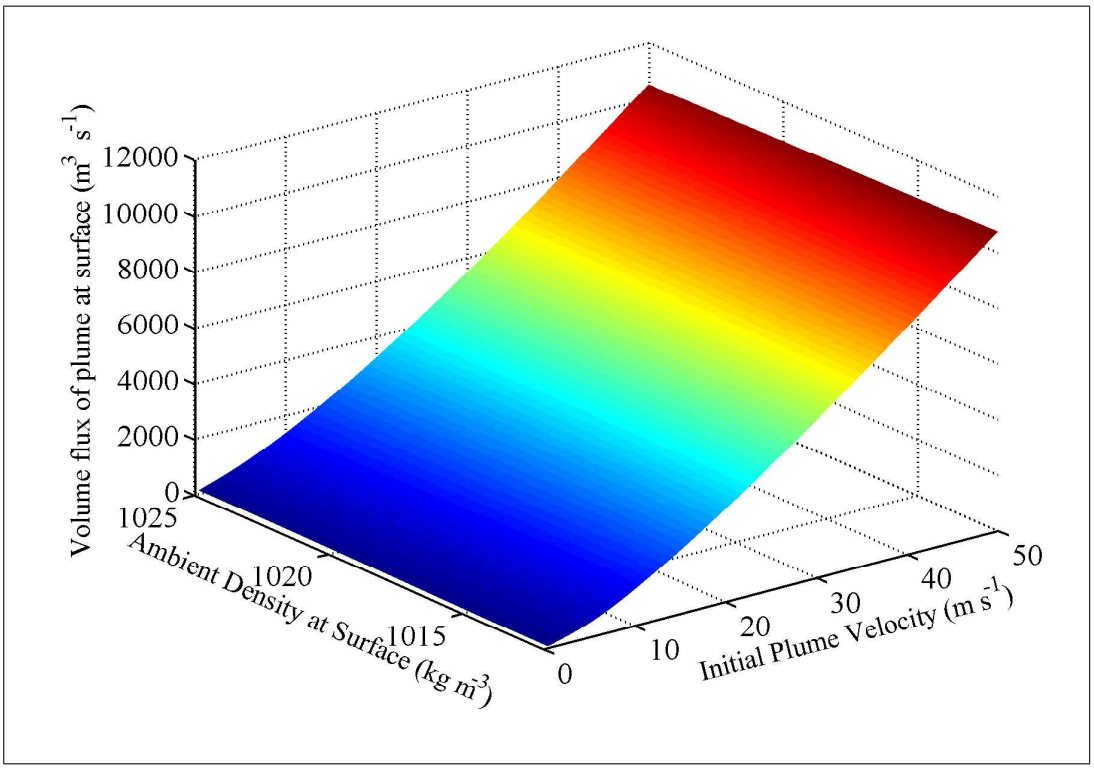

Figure 6.21: *The volume flux of the plume at the surface, for a conduit radius of 2.5 m, is shown against the initial plume velocity and the ambient water density at the surface, which corresponds to the gradient of the ambient water (Figure 6.18).*

ambient density gradient), as shown by the larger plume radii in Figure 6.20. Steeper density gradients produce longer plume trajectories and result in deceleration of plumes near the surface. This provides longer distances and times for plumes to entrain ambient fluid. However, the effect is very small compared with that of varying the initial plume velocity.

The buoyancy flux of the plume at the surface for a conduit radius of $2.5\,m$ over the two-dimensional parameter space of ambient density gradient and initial plume velocity is shown in Figure 6.22. For a uniform ambient (where the ambient density at surface is $1025\,kg\,m^{-3}$), the buoyancy flux behaves in the same way as in Figure 6.12 and increases with increasing initial plume velocity. However, as the ambient density gradient is increased, the buoyancy flux at the surface increases less rapidly with initial plume velocity. For the higher density gradients investigated, the buoyancy flux at the surface becomes negative. This is because the plume entrains denser ambient at depth, which it transports upwards, causing the plume to become more dense than the ambient fluid at shallower depths.

At the highest values of the surface density gradients, the surface buoyancy flux decreases with increasing initial plume velocity as high density gradients. Two factors are responsible. Firstly, the plume trajectory is longer for increasing values of the

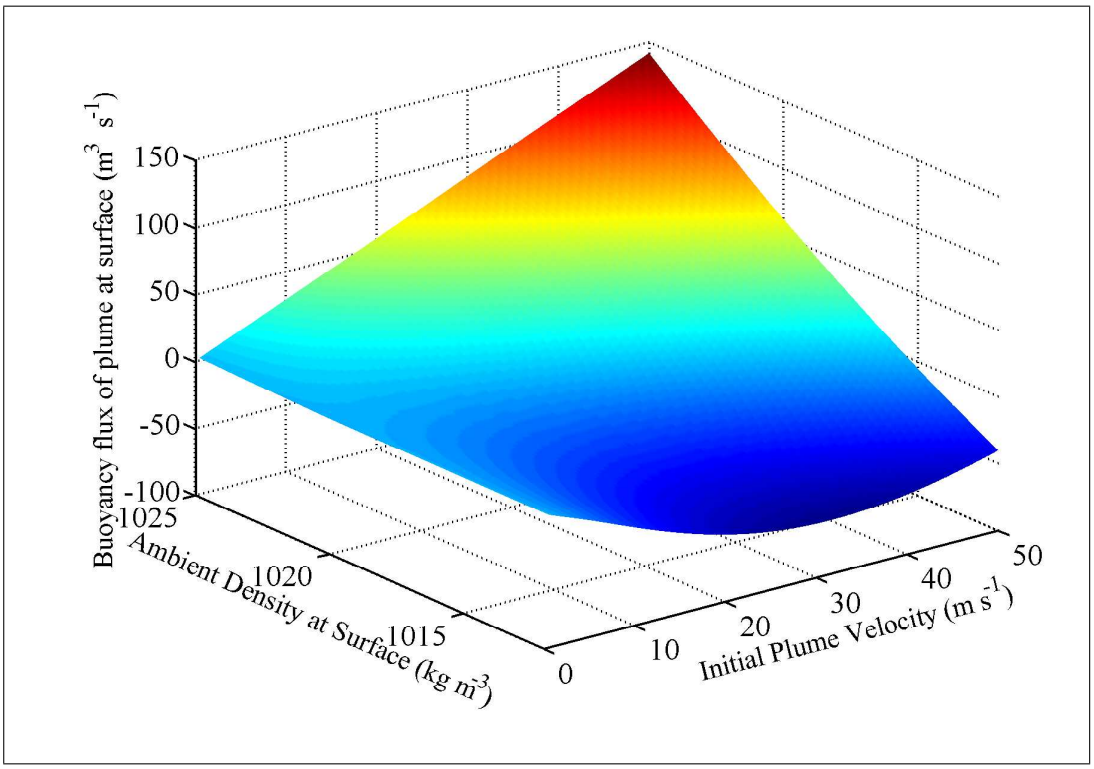

Figure 6.22: *The buoyancy flux of the plume at the surface, for a conduit radius of 2.5 m, is shown against the initial plume velocity and the ambient water density at the surface, which corresponds to the gradient of the ambient water (Figure 6.18).*

initial plume velocity, so there is further distance for the plume to entrain ambient fluid. Secondly, more mixing occurs at higher velocities. Both of these mechanisms lead to more ambient fluid being entrained at depth and carried in the plume to the surface, so the buoyancy flux at the surface becomes more negative (the plume becomes more dense compared to the ambient). As the velocity is increased further, the buoyancy flux of the plume at the surface eventually increases once again. This is because with increasing initial plume velocity, the increase in the length of the plume trajectory diminishes (Figure 6.19), and although the mixing increases, the buoyancy flux and its rate of change both increase as well (Figure 6.12), leading to a gradual increase in the buoyancy flux at the surface.

6.3.3.4 Implications

The ambient density gradient determines the density of water entrained by the plume as it rises; therefore, it does impact on plume trajectory and the plume properties at the surface. However, for the density gradient applied here, the effect is small compared to the influence of varying the initial plume velocity. If the water depths were larger, then density stratification would have a greater impact on the distance the plume surfaces from the glacier. Figure 6.22 demonstrates that, for the steeper density

gradients, the modelled buoyancy flux of the plume at the surface becomes negative. At this point the glacial meltwater would form an interflow. The point where the *SedPlume* Model stops the integration could be adjusted to include cases where the plume becomes negatively buoyant and starts to descend. From this point, the glacial meltwater could be modelled as a radially spreading interflow, such as Cowan and Powell (1990) observed in McBride Inlet.

It was proposed in Section 5.3, with reference to McBride Inlet, that the steepness of the ambient density gradient is controlled by an equilibrium between the inflow of saline water from Muir Inlet and freshwater from the subglacial conduit. If the plume freshens the surface water to the extent that it can no longer reach the surface, it forms an interflow. This means that the surface water is no longer replenished with 'fresh' water and will eventually become more dense than the plume. When this happens, the plume is able to reach the surface once more and so the cycle continues. Therefore, it is concluded that in shallow-silled fjords with high meltwater inputs from subglacial streams, such as McBride Inlet, the steep ambient density gradients which develop may induce the short-lived formation of interflows.

6.4 Summary

This chapter has described the results of model experiments carried out with the *SedBerg* and *SedPlume* models, which have explored the implications of varying environmental and climatic conditions on the sediment deposition rate and pattern produced by tidewater glaciers in fjords.

The experiments performed with *SedBerg* Model indicate that the mean iceberg size of the lognormal distribution may have a significant effect on the sedimentation rate, due to the dependence of the melt rate on iceberg size and iceberg velocity relative to the water (Figure 6.2). This suggests that, in iceberg models that simulate the sedimentation rate and meltwater injection from icebergs, consideration should be given to the appropriate iceberg size distributions that are applied.

By utilising a depth-averaged temperature over the keel depth of each iceberg, it is shown that the temperature of the surface layer and the depth of the thermocline may have significant effects on the sedimentation rate (Figures 6.5 and 6.6). Although additional calculations would be required, it may be beneficial to include the effect of temperature variation with depth in iceberg models, especially for larger icebergs which penetrate into deep water.

Varying the seeds of the random number generator for the water and wind forcing parameters altered the average sedimentation rate along-fjord (across-fjord transect) by up to 5% (Figure 6.8). This is an artifact of the stochastic parameterisation of the

wind and water velocities. The distribution of sediment over the fjord will converge to the true probability distribution of sedimentation if the model is run for long enough time periods.

It should be noted that iceberg calving rates are capable of large temporal variations in response to increases in glacier velocity and/or rate of change of the terminus position (Benn *et al.*, 2007b). The sedimentation rate is proportional to the flux of icebergs calved into the fjord, so the calving rate is extremely influential in determining the sedimentation rate in glaciated fjords.

In Sections 6.3.1 and 6.3.2, the *SedPlume* Model simulated two possible mechanisms for the formation of laminated coarse-sand and mud couplets in proximal glacimarine settings (cyclopsams):

1. Fluctuations in initial plume velocity result in variations in the distance the plume surfaces from the glacier front and the dispersal of sediment deposition: higher initial velocity leads to plume surfacing further from glacier and a higher volume flux at the surface, which causes a wider dispersal (Figures 6.9 and 6.10).
2. The initial plume velocity affects the pattern of sand fraction deposited with distance: higher initial velocity produces wider dispersal of sand fraction (Figure 6.16).

The experiments conducted in Section 6.3.3 with the *SedPlume* Model suggest that short-lived interflows may form in glacimarine environments where there are salinity-induced steep ambient density gradients. However, since the density gradient is controlled by the influx of freshwater from the subglacial stream relative to the inflow of salty water over the sill, the equilibrium would soon adjust so that the meltwater would form an overflow once more.

Chapter 7

Conclusions and Future Work

The focus of this thesis has been two numerical models, *SedBerg* and *SedPlume*, developed to simulate the two dominant processes of marine sedimentation in glaciated fjords: iceberg-rafting and delivery from meltwater plumes. The high sedimentation rates occurring in fjord environments result in high-resolution sedimentary records, providing evidence of glacial and climatic conditions during and since deglaciation (Powell, 1984; Skei, 1983; Syvitski, 1989).

7.1 Numerical Models

The *SedBerg* Model is a Monte Carlo based simulation with a number of underlying parametric probability distributions to capture the stochastic behaviour of iceberg formation and dynamics (Chapter 2). This formulation does not require a full observational data set of wind and water velocities, which are not available for many regions and only exist since historical records began. Instead of utilising results from atmospheric and ocean general circulation models, probability distributions are constructed from the limited data that exist and are used as representative of wind and water velocity behaviour. The rate of iceberg production is dependent on the calving rate from the glacier and the iceberg size distribution parameters. A population of icebergs is produced with a size distribution determined by parameterisation of observations.

The forces governing the iceberg drift trajectories in the *SedBerg* Model are the water drag, wind drag, wave radiation force, Coriolis force and horizontal pressure gradient force. The water velocity is calculated as a tidal oscillation plus a residual outflow velocity towards the mouth of the fjord, which has an additional stochastic variation of $\pm 10\%$. The wind velocity is drawn from a probability distribution (for example, the Laplace distribution was applied for wind velocities in Kangerdlugssuaq Fjord in Chapter 4). Collisions of icebergs with the fjord walls and ice front are modelled using the concept of collision impulse as a rigid body impacts on a plane.

Icebergs are overturned if either horizontal dimension becomes less than a specified fraction of the vertical dimension.

Semi-empirical treatments of subaqueous and subaerial iceberg melt processes are utilised. The subaqueous processes include forced convection and buoyant vertical convection, with wave erosion not significant in the sheltered environments of fjords. The water temperature is calculated as the average over the iceberg keel depth for the melt rate of the iceberg sides and taken as the temperature at the keel depth for the melt rate of the iceberg base. The subaerial processes incorporated are sensible heat exchange (forced convection) and solar radiation, with an empirical modification of the melt rate caused by debris accumulation on the iceberg surface. Debris melted out onto the iceberg surface is dumped when an overturning event occurs.

The icebergs are assumed to be composed of englacial ice with a layer of basal ice present for a proportion of icebergs, calculated to conserve the basal and englacial volumes of ice lost from the glacier with the respective volumes in the icebergs. The concentrations of sediment contained in each layer are taken from field measurements of glacier ice.

The *SedBerg* Model offers a complete system that captures the non-linearity inherent in iceberg-driven sedimentation. The Monte Carlo simulation techniques, coupled with the prescribed iceberg dynamics, provide a feasible and relatively straightforward methodology to model sedimentation in iceberg-dominated fjords, as well as in open ocean environments. The Monte Carlo element relates to the randomness associated with iceberg formation, wind and water velocities. Including this random behaviour allows the incorporation of uncertainties implicit in utilising limited field data to derive empirical relationships.

The *SedPlume* Model simulates the sedimentation rate from subglacial meltwater plumes (Chapter 3). The meltwater discharge is assumed to flow at a constant rate for long enough periods that the plume can be modelled as a steady state. The turbulent plume is assumed to entrain ambient fluid at a rate proportional to the local velocity of the plume. The plume motion is considered in two dimensions: one horizontal dimension (perpendicular to the glacier front) and the vertical dimension. An integral model is formulated for the conservation equations of volume, momentum, buoyancy and sediment flux along the trajectory of the plume. Sedimentation occurs from the plume when the radial component of the sediment fall velocity is greater than the entrainment velocity.

Once the plume rises to the surface, it is treated as a radially spreading gravity current. Analytical solutions have been formulated for sediment deposition from gravity currents formed when a buoyant plume reaches the surface (Bonnecaze *et al.*, 1995; Sparks *et al.*, 1991), and these equations are applied to the glacial plume when it

reaches the surface. Flocculation of silt and clay particles is included by using empirical measurements of particle settling velocities in fjords to adjust the settling velocity of fine-grained sediments by an appropriate amount.

The *SedPlume* Model is, to the author's knowledge, the first attempt to construct a numerical model of sedimentation from glacial meltwater plumes. As such, it provides quantitative simulations of the rates and patterns of deposition in ice-proximal glacimarine environments. It can be utilised to deduce the glacial hydrological conditions necessary to generate observed glacial submarine outwash deposits (Powell and Molnia, 1989).

7.2 Case Studies

A case study was selected for each model. The *SedBerg* Model was applied to Kangerdlugssuaq Fjord in East Greenland (Chapter 4), as an example of a glaciated fjord where iceberg-rafting is the primary sediment transport process from the glacier (Syvitski *et al.*, 1996). The sedimentation rate over the past 1500 years was simulated, encompassing several different climate intervals including the Medieval Warm Period (MWP) and the Little Ice Age (LIA). The modelled sedimentation rate was compared to a long core collected in 1993, which was dated at 1430±60 yr B.P. at the base (Syvitski *et al.*, 1996). From the core log of magnetic susceptibility and organic carbon content, the potential boundaries between the different climate intervals were inferred. Core records from nearby Nansen Fjord, with additional radiocarbon dates (Jennings and Weiner, 1996), were also utilised to interpret the possible influence of variations in climate on environmental conditions in the fjord, which impact on iceberg-rafted sedimentation.

The required model input parameters were estimated from measurements collected during marine geological and geophysical studies in the fjord (1991, 1993 and 2004) and, if no observations were available, data sets from other fjords in the region were used. Where there was uncertainty in the appropriate input parameter to use, the various possibilities were explored to gauge the effect of using different values.

The past 1500 years were divided into five climatic regimes: Pre-Medieval Warm Period, Medieval Warm Period, Transition Period, Little Ice Age and Modern Period. The 10 year model outputs for different climatic scenarios (Figure 4.38) were summed to find sedimentation rates over each of these five intervals. If the estimates of the division of the core record into the respective climate intervals are correct, the implication is that there were high sedimentation rates during the MWP. A mechanism that would cause an increase in sedimentation rates is the break up of the sikussak (multi-year shorefast sea ice) in front of Kangerdlugssuaq Gletscher. In general, when

a sikussak is present, any basal ice contained within icebergs melts out while they are trapped near to the glacier front (Dowdeswell *et al.*, 2000; Syvitski *et al.*, 1996). However, in the absence of a sikussak, icebergs containing basal debris would be able to drift freely in the fjord and deposit higher concentrations of sediment. This hypothesis is supported by evidence in Nansen Fjord, where higher sedimentation rates were observed during the MWP and the foraminiferal record suggests that warm Atlantic Intermediate Water occupied the fjord floor (Jennings and Weiner, 1996).

The sediment accumulation generated when the *SedBerg* Model was applied to each of the five climate intervals (Figure 4.39) compared favourably with the empirical evidence from sediment cores (Figure 4.4). The salient features of the climate intervals were present in the model runs. In particular, the sedimentation rate during the MWP was twice as high (approximately $1.2\,cm\,yr^{-1}$) as during the other intervals (0.6–$0.7\,cm\,yr^{-1}$), which supports the hypothesis that the sikussak in front of Kangerdlugssuaq Fjord was absent during this period.

The *SedPlume* Model was applied to McBride Inlet in Glacier Bay, Alaska (Chapter 5). This is a temperate glaciated fjord where the majority of sedimentation originates from meltwater sources (Cowan and Powell, 1990, 1991). There is a tidewater glacier at the head of the inlet, which has a single subglacial conduit draining water and sediment from the glacier into the fjord. Extensive measurements of sedimentation rates with distance from the glacier were collected by Ross Powell and Ellen Cowan between 1984 and 1987. Air temperature and precipitation, as well as profiles of suspended sediment concentration, current velocity and density were also measured. The flux of meltwater was estimated from the rainfall measurements and the discharge at other glaciers in Glacier Bay. The separation of the flux into the subglacial conduit radius and the initial plume velocity was calculated from an empirical relationship for fluid flow through a pipe, originating from the Manning equation. The initial size fractions of sand, silt and clay were found by performing a grid search on model outputs to match them with the size fractions at $400\,m$ from the glacier front observed by Cowan and Powell (1990).

The plume trajectories produced by the *SedPlume* Model, for the range of possible initial conditions, were 'S' shaped with a progressively flatter gradient as they approached the surface (Figure 5.4). The modelled plume density profiles showed the densities of the plumes at the surface were more dense than the ambient fluid (Figure 5.5). Both of these plume properties are caused by the density gradient of the ambient fluid. Denser fluid is entrained into the plume at depth and carried upwards. Since the ambient density decreases towards the surface, it is possible for the plume to become more dense than the ambient. This causes the plume to decelerate as it rises and results in the 'S'-shaped trajectories.

The modelled annual accumulation rates produced a reasonable fit to the observed data with peak ice-proximal annual sedimentation rates of approximately $22\,m\,yr^{-1}$ (Figure 5.8). The *SedPlume* Model performed well when it was applied to the case study of McBride Inlet and replicated the magnitude of the sedimentation rate, with the initial size fractions adjusted to equal those observed at a certain distance from the glacier by Cowan and Powell (1990). Therefore, the *SedPlume* Model has successfully simulated the rate and pattern of sedimentation from a glacial meltwater plume.

The two case studies illustrated the notable differences in sedimentation from icebergs and meltwater plumes (Dowdeswell *et al.*, 1998). Firstly, the rate of deposition in ice-proximal locations is approximately three orders of magnitude higher for the meltwater plume in McBride Inlet compared with iceberg-rafted sedimentation in Kangerdlugssuaq Fjord. The exceptionally high proximal sedimentation rates from glacial plumes decrease rapidly with distance from the glacier front, although some fine-grained sediment is carried further in the overflow plume (Syvitski *et al.*, 1985, observed coarse silt transported more than $12\,km$). However, iceberg-rafting provides a constant flux of sediment, which is transported extremely large distances from the glacier front (hundreds of kilometres: Dowdeswell *et al.*, 1998). The *SedBerg* and *SedPlume* models highlight the distinct deposits generated in contrasting glacimarine settings.

7.3 Parameter Experiments

The model experiments performed with the *SedBerg* Model investigated the effects of mean iceberg size, water temperature and the depth of the thermocline and the seeds of the random number generator for the water and wind velocities. An experiment varying the mean iceberg size demonstrated that, even with the same iceberg flux, different expected values of the iceberg size distribution impact on the sedimentation rate (Figure 6.2). Therefore, it is important to estimate the iceberg size distribution as accurately as possible. This applies to simulating the iceberg-rafted sedimentation rate, as well as the freshwater flux introduced from icebergs to the ocean. Gladstone *et al.* (2001) assumed a single iceberg size distribution in their work modelling meltwater injection from icebergs in the Southern Ocean and Death *et al.* (2006) applied a single iceberg size distribution to the Eurasian Ice Sheet at the Last Glacial Maximum. Given the known variability of the iceberg size distribution from different calving margins (Dowdeswell and Bamber, 2007; Orheim, 1987), it may be beneficial to include an appropriate range of iceberg size distributions.

The *SedBerg* Model calculates an average water temperature over the keel depth of

each iceberg to determine the melt rate of the iceberg sides and the water temperature at the iceberg base to calculate the basal melt rate. This allows the effect of varying the depth of the thermocline and the temperature of the surface layer to be investigated. The surface water temperature has been used in other iceberg models (Bigg *et al.*, 1997; Løset, 1993a; Matsumoto, 1996) to calculate the melt rate, so this is a unique feature of the *SedBerg* Model.

The temperature and the temperature gradient were both shown to have an influence on the sedimentation rate (Figures 6.5 and 6.6). The sedimentation rate increases with increasing temperature of the water above the thermocline. If the surface layer is warmer than the deep layer, sedimentation rate also increases with depth of the thermocline, since a higher proportion of icebergs are surrounded by the warm surface layer. It has been inferred from deep sediment cores that, during glacial intervals, the ocean temperature was more homogenous than it is today (Adkins *et al.*, 2002), so a single surface temperature is probably representative of the whole water column during these time periods. However, there is often high temperature stratification in fjords and polar oceans during interglacial periods, particularly during the summer months (Figure 4.12; Jenkins, 1999). Therefore, consideration should be given to whether a single surface temperature or an average temperature over the keel depth is representative of the temperature 'felt' by the icebergs for the specific environment under investigation.

The *SedBerg* Model runs, where the seeds for the random number generators of water and wind velocities were varied, provided a measure of the uncertainty of approximately 5% for 10 modelled years, which is an artifact of the stochastic parameterisations applied. If the model were run for long enough time periods, the sediment distribution over the fjord would eventually converge to the true probability distribution.

The parameter experiments carried out with the *SedPlume* Model investigated the implications for the properties of the buoyant plume at the surface, as well as the deposited sand fraction. Increases in the initial plume velocity produce a wider dispersal of sediment as well as increasing the dispersal of the sand fraction, leading to higher deposition rates and higher sand fractions at greater distances from the glacier front. The manifestation of fluctuations in the initial plume velocity on the pattern of deposition is the formation of cyclopsams (cyclically interlaminated couplets of sand and mud), which are common features of temperate glacimarine settings (Cowan *et al.*, 1999; Phillips *et al.*, 1991). Observations at grounded tidewater glacier margins indicate that the flow velocity of subglacial streams varies diurnally, seasonally and due to precipitation-induced events (Humphrey *et al.*, 1986; Larson, 1978). In addition, a dramatic response in the sedimentation rate in front of a tidewater glacier was observed

following a rainstorm event (Cowan *et al.*, 1988).

The effect of the ambient density gradient was explored because it has been proposed that it may influence sedimentation (Powell, 1984). For the range of ambient density gradients investigated, the effects on sedimentation were very small, even though the plume trajectories and the buoyancy of the plumes at the surface were significantly affected. The role of the ambient density gradient may be more important in deeper water. The model experiments demonstrated that high density gradients may lead to the formation of interflows. However, in shallow fjords with high freshwater input and limited access to the ocean, steep ambient density gradients form, for example McBride Inlet (Chapter 5). An equilibrium is established between the ability of the plume to reach the surface and the steepness of the gradient. If the plume freshens the surface water to the extent that it can no longer reach the surface, it forms an interflow for a time, during which the surface water is no longer replenished with 'fresh' water. Eventually the surface water becomes more dense than the plume and it is possible for the plume to reach the surface once more. The factors controlling the steepness of the ambient density gradient are the inflow of saline water from Muir Inlet (tidal currents play an important role), balanced with the introduction of freshwater from the subglacial conduit.

7.4 Future Work

At present the *SedBerg* Model has been designed to be applied to fjords. However, only a small number of modifications would enable it to be applied to wider areas and to assimilate inputs from general circulation models. It could also be utilised to simulate the freshwater injection to the oceans from iceberg melt, as well as sedimentation rates. Since the Bigg *et al.* (1997) model already has these capabilities, it may be more productive to make the following modifications to this model instead. The inclusion of regional differences in the iceberg size distribution and the effect of temperature variation with depth on the iceberg melt rate, for example, may prove important in modelling the freshwater contribution of icebergs in the Southern Ocean (Sections 6.2.1 and 6.2.2).

It would also be of interest to confirm or reject the conjecture made in Chapter 4 that the sikussak in front of Kangerdlugssuaq Gletscher was absent during the Medieval Warm Period, resulting in higher sedimentation rates. If additional core samples were dated, this would clarify the variation in the sedimentation rate over the past 1500 years.

It would be useful to obtain more accurate input parameters for the *SedPlume*

Model: the subglacial conduit radius, the initial velocity of the emerging plume and the suspended sediment concentration. A remotely operated vehicle could be utilised to venture close enough to the glacier to collect these measurements (Dowdeswell and Powell, 1996), and perhaps secure a flow meter and a turbidity meter near to the subglacial conduit, which would record continuously over a period of time. It would be valuable to simultaneously measure the size fraction deposited with distance from the glacier. This would allow a more comprehensive test of the *SedPlume* Model performance for simulating sedimentation rate and pattern.

Some modifications that could be made to the existing *SedPlume* Model are to include the effect of ambient water currents on the meltwater plume, as this would enable the effect of tides on plume deposition to be examined. The *SedPlume* Model could also be altered to include three-dimensions. This would allow the inclusion of the coriolis effect, ambient cross-flow currents and plumes flowing into the fjord at angles other than 90° to the glacier front.

One of the initial aims of this doctoral study was to produce numerical routines for glacimarine sedimentation, which would be integrated into *SedFlux* (Syvitski and Hutton, 2001), a comprehensive stratigraphic simulation model developed by Prof. James Syvitski and his group at the University of Colorado. *SedFlux* includes the effects of sea-level fluctuations, storms, slope instabilities, turbidity currents, debris flows, sediment compaction, tectonic uplift and isostatic subsidence due to sediment load. Suitable versions of the *SedBerg* and *SedPlume* models will be integrated into *SedFlux* in the near future, enabling the simulation of glacially-derived sedimentation by iceberg-rafting and meltwater processes, accompanied by subsequent sediment reworking. The modified *SedFlux* Model could be utilised alongside an ice sheet model to simulate the sediment deposition on a continental margin during ice sheet retreat, for example, during deglaciation following the Last Glacial Maximum.

Finally, the model of glacimarine sedimentation will be applied to other fjord and shelf settings, to aid the understanding of short term processes of glacimarine sedimentation and to investigate the longer term development of sedimentary stratigraphy and the architecture of glacier-influenced continental margins.

References

ACIA (2004), *Impacts of a Warming Arctic: Arctic Climate Impact Assessment*.

Adkins, J. F., McIntyre, K. and Schrag, D. P. (2002), "The salinity, temperature, and δ^{18}O of the glacial deep ocean", *Science*, **298**(5599), 1769–1773.

Alley, R. B., Cuffey, K. M., Evenson, E. B., Strasser, J. C., Lawson, D. E. and Larson, G. J. (1997), "How glaciers entrain and transport basal sediment: Physical constraints", *Quaternary Science Reviews*, **16**(9), 1017–1038.

Alley, R. B., Lawson, D. E., Evenson, E. B., Strasser, J. C. and Larson, G. J. (1998), "Glaciohydraulic supercooling: a freeze-on mechanism to create stratified, debris-rich basal ice: II. Theory", *Journal of Glaciology*, **44**(148), 563–569.

Alley, R. B. and Macayeal, D. R. (1994), "Ice-rafted debris associated with binge purge oscillations of the Laurentide Ice Sheet", *Paleoceanography*, **9**(4), 503–511.

Anderson, S. P., Fernald, K. M. H., Anderson, R. S. and Humphrey, N. F. (1999), "Physical and chemical characterization of a spring flood event, Bench Glacier, Alaska, USA: evidence for water storage", *Journal of Glaciology*, **45**(150), 177–189.

Andrews, J. T. (1998), "Abrupt changes (Heinrich events) in late Quaternary North Atlantic marine environments: a history and review of data and concepts", *Journal of Quaternary Science*, **13**(1), 3–16.

Andrews, J. T., Milliman, J. D., Jennings, A. E., Rynes, N. and Dwyer, J. (1994), "Sediment thicknesses and Holocene glacial marine sedimentation-rates in three East Greenland fjords (ca. 68°N)", *Journal of Geology*, **102**(6), 669–683.

Bailey, R. (1994), "Implications of iceberg dynamics for iceberg stability estimation", *Cold Regions Science and Technology*, **22**(2), 197–203.

Banke, E. G. and Smith, S. D. (1974), "Measurements of towing drag on small icebergs", in: "Proceedings IEEE Ocean 74: International Conference on Engineering in the Ocean Environment", , vol. 1Halifax, Canada, pp. 130–132.

Bass, D. (1980), "Stability of icebergs", *Annals of Glaciology*, **1**, 43–47.

Benn, D. I. and Evans, D. J. A. (1996), "The interpretation and classification of subglacially-deformed materials", *Quaternary Science Reviews*, **15**(1), 23–52.

Benn, D. I. and Evans, D. J. A. (1998), *Glaciers and Glaciation*, Arnold, London.

Benn, D. I., Hulton, N. R. J. and Mottram, R. H. (2007a), "'Calving laws', 'sliding

laws' and the stability of tidewater glaciers", *Annals of Glaciology*, **46**, in press.

Benn, D. I., Warren, C. R. and Mottram, R. H. (2007b), "Calving processes and the dynamics of calving glaciers", *Earth Science Reviews*, **82**(3-4), 143–179.

Bigg, G. R., Wadley, M. R., Stevens, D. P. and Johnson, J. A. (1996), "Prediction of iceberg trajectories for the North Atlantic and Arctic Oceans", *Geophysical Research Letters*, **23**(24), 3587–3590.

Bigg, G. R., Wadley, M. R., Stevens, D. P. and Johnson, J. A. (1997), "Modelling the dynamics and thermodynamics of icebergs", *Cold Regions Science and Technology*, **26**(2), 113–135.

Bingham, R. G., Nienow, P. W., Sharp, M. J. and Boon, S. (2005), "Subglacial drainage processes at a High Arctic polythermal valley glacier", *Journal of Glaciology*, **51**(172), 15–24.

Bonnecaze, R. T., Hallworth, M. A., Huppert, H. E. and Lister, J. R. (1995), "Axisymmetrical particle-driven gravity currents", *Journal of Fluid Mechanics*, **294**, 93–121.

Bonnecaze, R. T., Huppert, H. E. and Lister, J. R. (1993), "Particle-driven gravity currents", *Journal of Fluid Mechanics*, **250**, 339–369.

Boulton, G. S. (1978), "Boulder shapes and grain-size distribution of debris as indicators of transport paths though a glacier and till genesis", *Sedimentology*, **25**, 773–799.

Box, J., Key, J., Maslanik, J. and Serreze, M. (1998), "Arctic Global Radiation (AGR) data set", Boulder, CO: National Snow and Ice Data Center, Digital media.

Braithwaite, R. (1980), "Regional modelling of ablation in West Greenland", *The Geological Survey of Greenland (GGU) Rapport 98*.

Brown, C. S., Meier, M. F. and Post, A. (1982), "Calving speed of Alaska tidewater glaciers with application to Columbia Glacier", *U.S. Geological Survey Professional Paper*, **1258-C**.

Bursik, M. I., Sparks, R. S. J., Gilbert, J. S. and Carey, S. N. (1992), "Sedimentation of tephra by volcanic plumes: I. Theory and its comparison with a study of the Fogo A plinian deposit, Sao Miguel (Azores)", *Bulletin of Volcanology*, **54**(4), 329.

Cardoso, S. S. S. and Zarrebini, M. (2001), "Convection driven by particle settling surrounding a turbulent plume", *Chemical Engineering Science*, **56**(11), 3365–3375.

Cardoso, S. S. S. and Zarrebini, M. (2002), "Sedimentation from surface currents generated by particle-laden jets", *Chemical Engineering Science*, **57**(8), 1425–1437.

Carey, S. N., Sigurdsson, H. and Sparks, R. S. J. (1988), "Experimental studies Of particle-laden plumes", *Journal of Geophysical Research*, **93**(B12), 15,314–15,328.

Chirivella, J. E. and Miller, C. G. (1978), "Hydrodynamics of icebergs in transit", in: Husseiny, A. A. (ed.), "Iceberg Utilization: Proceedings of the First International

Conference, Ames, Iowa, 1977", pp. 315–333.

Chow, V. (1959), *Open-channel hydraulics*, McGraw-Hill, New York.

Christoffersen, P., Tulaczyk, S., Carsey, F. D. and Behar, A. E. (2006), "A quantitative framework for interpretation of basal ice facies formed by ice accretion over subglacial sediment", *Journal of Geophysical Research*, **111**(F1). F01017, doi:10.1029/2005JF000363.

Chu, P. C. K., Lee, J. H. and Chu, V. H. (1999), "Spreading of turbulent round jet in coflow", *Journal of Hydraulic Engineering-ASCE*, **125**(2), 193–204.

Chu, V. H. and Lee, J. H. W. (1996), "General integral formulation of turbulent buoyant jets in cross-flow", *Journal of Hydraulic Engineering-ASCE*, **122**(1), 27–34.

Church, M. and Gilbert, R. (1975), "Proglacial fluvial and lacustrine environments", in: Jopling, A. V. and McDonald, B. C. (eds.), "Glaciofluvial and glaciolacustrine sedimentation", Society of Economic Paleontologists and Mineralogists, pp. 22–100.

Clarke, G. K. and La Prairie, D. I. (2001), "Modelling Iceberg Drift and Ice-Rafted Sedimentation", in: Straughan, B., Greve, R., H., Ehrentraut and Wang, Y. (eds.), "Continuum Mechanics and Applications in Geophysics and the Environment", Springer-Verlag, New York, pp. 183–200.

Cowan, E. A. (1992), "Meltwater and tidal currents: Controls on circulation in a small glacial fjord", *Estuarine, Coastal and Shelf Science*, **34**(4), 381–392.

Cowan, E. A., Cai, J., Powell, R. D., Seramur, K. C. and Spurgeon, V. L. (1998), "Modern tidal rhythmites deposited in a deep-water estuary", *Geo-Marine Letters*, **18**(1), 40.

Cowan, E. A. and Powell, R. D. (1990), "Suspended sediment transport and deposition of cyclically interlaminated sediment in a temperate glacial fjord, Alaska, U.S.A.", in: Dowdeswell, J. A. and Scourse, J. D. (eds.), "Glacimarine environments: processes and sediments", Geological Society of London Special Publication No. 53, pp. 75–89.

Cowan, E. A. and Powell, R. D. (1991), "Ice-proximal sediment accumulation rates in a temperate glacial fjord, southeastern Alaska", in: Anderson, J. and Ashley, G. M. (eds.), "Glacial marine sedimentation; Paleoclimatic significance", Geological Society of America Special Paper 261, pp. 61–73.

Cowan, E. A., Powell, R. D. and Smith, N. D. (1988), "Rainstorm-induced event sedimentation at the tidewater front of a temperate glacier", *Geology*, **16**(5), 409–412.

Cowan, E. A., Seramur, K. C., Cai, J. K. and Powell, R. D. (1999), "Cyclic sedimentation produced by fluctuations in meltwater discharge, tides and marine productivity in an Alaskan fjord", *Sedimentology*, **46**(6), 1109–1126.

Crapper, P. F. (1977), "Forced plume characteristics", *Tellus*, **29**, 470–475.

Csathó, B., Bolzan, J., Van der Veen, C., Schenk, A. and Lee, D.-C. (1999), "Surface velocities of a Greenland outlet glacier from high-resolution visible satellite", *Polar Geography*, **23**(1), 71–82.

Curran, K. J., Hill, P. S., Milligan, T. G., Cowan, E. A., Syvitski, J. P. M. and Konings, S. M. (2004), "Fine-grained sediment flocculation below the Hubbard Glacier meltwater plume, Disenchantment Bay, Alaska", *Marine Geology*, **203**(1-2), 83–94.

Dahl-Jensen, D., Mosegaard, K., Gundestrup, N., Clow, G. D., Johnsen, S. J., Hansen, A. W. and Balling, N. (1998), "Past temperatures directly from the Greenland Ice Sheet", *Science*, **282**(5387), 268–271.

Death, R., Siegert, M. J., Bigg, G. R. and Wadley, M. R. (2006), "Modelling iceberg trajectories, sedimentation rates and meltwater input to the ocean from the Eurasian Ice Sheet at the Last Glacial Maximum", *Palaeogeography Palaeoclimatology Palaeoecology*, **236**(1-2), 135–150.

Denner, J. C., Lawson, D. E., Larson, G. J., Evenson, E. B., Alley, R. B., Strasser, J. C. and Kopczynski, S. (1999), "Seasonal variability in hydrologic-system response to intense rain events, Matanuska Glacier, Alaska, USA", *Journal of Glaciology*, **28**, 267–271.

Dowdeswell, J. A. (1986), "The distribution and character of sediments in a tidewater glacier, Southern Baffin Island, N.W.T., Canada", *Arctic and Alpine Research*, **18**(1), 45–56.

Dowdeswell, J. A. (1987), "Processes of glacimarine sedimentation", *Progress in Physical Geography*, **11**, 52–90.

Dowdeswell, J. A. and Bamber, J. L. (2007), "Keel depths of modern Antarctic icebergs and implications for sea-floor scouring in the geological record", *Marine Geology*, **243**, 120–131.

Dowdeswell, J. A. and Cromack, M. (1991), "Behavior Of A Glacier-Derived Suspended Sediment Plume In A Small Arctic Inlet", *Journal Of Geology*, **99**(1), 111–123.

Dowdeswell, J. A. and Dowdeswell, E. (1989), "Debris in icebergs and rates of glacimarine sedimentation; observations from Spitsbergen and a simple model", *Journal of Geology*, **97**, 221–231.

Dowdeswell, J. A., Elverhoi, A. and Spielhagen, R. (1998), "Glacimarine sedimentary processes and facies on the Polar North Atlantic margins", *Quaternary Science Reviews*, **17**(1-3), 243–272.

Dowdeswell, J. A. and Forsberg, C. F. (1992), "The size and frequency of icebergs and bergy bits derived from tidewater glaciers in Kongsfjorden, northwest Spitsbergen", *Polar Research*, **11**(2), 81–91.

Dowdeswell, J. A. and Murray, T. (1990), "Modelling rates of sedimentation from icebergs", in: Dowdeswell, J. and Scourse, J. (eds.), "Glacimarine Environments: Processes and Sediments", , vol. 53 of *Geological Society of London Special Publication*pp. 121–137.

Dowdeswell, J. A. and Ó Cofaigh, C. (2002), "Glacier-influenced sedimentation on high-latitude continental margins: Introduction and overview", in: Dowdeswell, J. A. and ÓCofaigh, C. (eds.), "Glacier-Influenced Sedimentation on High-Latitude Continental Margins", Geological Society of London Special Publication No. 203, pp. 1–9.

Dowdeswell, J. A. and Powell, R. D. (1996), "Submersible remotely operated vehicles (ROVs) for investigations of the glacier ocean-sediment interface", *Journal of Glaciology*, **42**(140), 176–183.

Dowdeswell, J. A., Uenzelmannneben, G., Whittington, R. J. and Marienfeld, P. (1994a), "The Late Quaternary sedimentary record in Scoresby Sund, East Greenland", *Boreas*, **23**(4), 294–310.

Dowdeswell, J. A., Whittington, R. J. and Hodgkins, R. (1992), "The sizes, frequencies, and freeboards of East Greenland icebergs observed using ship radar and sextant", *Journal of Geophysical Research*, **97**(C3), 3515–3528.

Dowdeswell, J. A., Whittington, R. J., Jennings, A. E., Andrews, J. T., Mackensen, A. and Marienfeld, P. (2000), "An origin for laminated glacimarine sediments through sea-ice build-up and suppressed iceberg rafting", *Sedimentology*, **47**(3), 557–576.

Dowdeswell, J. A., Whittington, R. J. and Marienfeld, P. (1994b), "The origin of massive diamicton facies by iceberg rafting and scouring, Scoresby Sund, East Greenland", *Sedimentology*, **41**(1), 21–35.

Duthinh, D. and Fuglem, M. K. (1988), "Iceberg-structure interaction: force, energy and probability", in: Saeki, H. and Hirayama, K. (eds.), "IAHR 9th International Symposium on Ice, vol. 1", Sapporo Japan, pp. 324–340.

Duthinh, D., Klein, K., Regrettier, J.-F., Guichard, A. and Engler, M. (1990), "Full scale iceberg impact: a pilot experiment in Antarctica", in: "IAHR 10th International Symposium on Ice, vol. 2", Espoo, Finland, pp. 890–901.

Duthinh, D. and Marsden, S. (1986), "Iceberg impact load on a gravity based structure", in: Ryan, W. L. (ed.), "Fourth International Conference in Cold regions Engineering", Anchorage, Alaska, pp. 82–92.

Dwyer, J. L. (1993), *Monitoring characteristics of glaciation in the Kangerdlugssuaq Fjord region, East Greenland, using digital LANDSAT MSS and TM Data*, Ph.D. thesis, University of Colorado, Boulder.

Dwyer, J. L. (1995), "Mapping tide-water glacier dynamics in East Greenland using Landsat data", *Journal of Glaciology*, **41**(139), 584–595.

Eijpen, K. J., Warren, C. R. and Benn, D. I. (2003), "Subaqueous melt rates at calving

termini: a laboratory approach", *Annals of Glaciology*, **36**, 179–183.

El-Tahan, M., Vankatesh, S. and El-Tahan, H. (1987), "Validation and quantitative assessment of the deterioration mechanisms of arctic icebergs", *Journal of Offshore Mechanics and Arctic Engineering*, **109**, 102–108.

Ellison, T. H. and Turner, J. S. (1959), "Turbulent entrainment in stratified flows", *Journal of Fluid Mechanics*, **6**, 423–448.

Elverhøi, A., Liestøl, O. and Nagy, J. (1980), "Glacial erosion, sedimentation and microfauna in the inner part of Kongsfjorden, Spitsbergen", *Norsk Polarinstitutt Skrifter*, **172**, 33–61.

Elverhoi, A., Lonne, O. and Seland, R. (1983), "Glaciomarine sedimentation in a modern fjord environment, Spitsbergen", *Polar Research*, **1**, 127–149.

Embleton, C. and King, C. A. M. (1975), *Glacial Geomorphology*, Edward Arnold, 573 pp.

Ernst, G. G. J., Sparks, R. S. J., Carey, S. N. and Bursik, M. I. (1996), "Sedimentation from turbulent jets and plumes", *Journal of Geophysical Research*, **101**(B3), 5575–5589.

Eyles, N. (2006), "The role of meltwater in glacial processes", *Sedimentary Geology*, **190**(1-4), 257–268.

Eyles, N., Eyles, C. H. and Miall, A. D. (1983), "Lithofacies types and vertical profile models; an alternative approach to the description and environmental interpretation of glacial diamict and diamictite sequences", *Sedimentology*, **30**(3), 393–410.

Fofonoff, P. and Millard, R. (1983), "Algorithms for computation of fundamental properties of seawater", *UNESCO Technical Papers in Marine Science*, **44**, 53pp.

Foster, T. D. and Carmack, E. C. (1976), "Temperature and salinity structure in the Weddell Sea", *Journal of Physical Oceanography*, **6**(1), 36–44.

Fountain, A. G. and Walder, J. S. (1998), "Water flow through temperate glaciers", *Reviews of Geophysics*, **36**(3), 299–328.

Frankenstein, S. and Shen, H. (1997), "Laboratory observations of ice-floe processes made during long-term drift and collision experiments", *Antarctic Journal of the United States*, **32**(4), 13–16.

German, C. R. and Sparks, R. S. J. (1993), "Particle Recycling In The TAG Hydrothermal Plume", *Earth and Planetary Science Letters*, **116**(1-4), 129–134.

Gilbert, R. (1982), "Contemporary Sedimentary Environments On Baffin Island, Nwt, Canada - Glaciomarine Processes In Fiords Of Eastern Cumberland Peninsula", *Arctic and Alpine Research*, **14**(1), 1–12.

Gilbert, R. (1983), "Sedimentary processes of Canadian Arctic fjords", *Sedimentary Geology*, **36**(2-4), 147–175.

Gilbert, R. (1985), "Quaternary Glaciomarine Sedimentation Interpreted from Seismic

Surveys of Fjords on Baffin Island, Nwt", *Arctic*, **38**(4), 271–280.

Gill, A. E. (1982), *Atmosphere-Ocean Dynamics*, Academic Press, New York, 662 pp.

Gladstone, R. M., Bigg, G. R. and Nicholls, K. W. (2001), "Iceberg trajectory modeling and meltwater injection in the Southern Ocean", *Journal of Geophysical Research*, **106**(C9), 19,903–19,915.

Hallermeier, R. J. (1981), "Terminal settling velocity of commonly occurring sand grains", *Sedimentology*, **28**(6), 859–865.

Heinrich, H. (1988), "Origin and consequences of cyclic ice rafting in the Northeast Atlantic Ocean during the past 130,000 years", *Quaternary Research*, **29**(2), 142–152.

Hill, P. S., Syvitski, J. P., Cowan, E. A. and Powell, R. D. (1998), "In situ observations of floc settling velocities in Glacier Bay, Alaska", *Marine Geology*, **145**(1-2), 85–94.

Hopkins, M. A. and Shen, H. H. (2001), "Simulation of pancake-ice dynamics in a wave field", *Annals of Glaciology*, **33**, 355–360.

Hoskin, C. and Burrell, D. (1972), "Sediment transport and accumulation in a fjord basin, Glacier Bay, Alaska", *Journal of Geology*, **80**, 539–551.

Howat, I. M., Joughin, I. and Scambos, T. A. (2007), "Rapid changes in ice discharge from Greenland outlet glaciers", *Science*, **315**(5818), 1559–1561.

Hubbard, B. and Sharp, M. (1993), "Weertman regulation, multiple refreezing events and the isotopic evolution of the basal ice layer", *Journal of Glaciology*, **39**(132), 275–291.

Hubbard, B. and Sharp, M. (1995), "Basal ice facies and their formation in the western Alps", *Arctic and Alpine Research*, **27**(4), 301–310.

Hughes, T. (1992), "Theoretical calving rates from glaciers along ice walls grounded in water of variable depths", *Journal of Glaciology*, **38**(129), 282–294.

Hughes, T. (2002), "Calving bays", *Quaternary Science Reviews*, **21**(1-3), 267–282.

Humphrey, N., Raymond, C. and Harrison, W. (1986), "Discharges of turbid water during mini-surges of Variegated Glacier, Alaska, U.S.A.", *Journal of Glaciology*, **32**(111), 195–207.

Hunter, L. E., Powell, R. D. and Lawson, D. E. (1996), "Flux of debris transported by ice at three Alaskan tidewater glaciers", *Journal of Glaciology*, **42**(140), 123–135.

Huppert, H. E. and Josberger, E. G. (1980), "The melting of ice in cold stratified water", *Journal of Physical Oceanography*, **10**(6), 953–960.

Huppert, H. E. and Turner, J. S. (1978), "On melting icebergs", *Nature*, **271**(5640), 46–48.

Huppert, H. E. and Turner, J. S. (1980), "Ice blocks melting into a salinity gradient", *Journal of Fluid Mechanics*, **100**, 367–384.

IPCC (2007), *IPCC Fourth Assessment Report: The Physical Science Basis*, Cambridge University Press.

Iverson, N. R. (1993), "Regelation of ice through debris at glacier beds: Implications for sediment transport", *Geology*, **21**(6), 559–562.

Iverson, N. R. (2000), "Sediment entrainment by a soft-bedded glacier: A model based on regelation into the bed", *Earth Surface Processes And Landforms*, **25**(8), 881–893.

Jenkins, A. (1999), "The impact of melting ice on ocean waters", *Journal of Physical Oceanography*, **29**(9), 2370–2381.

Jennings, A. E. and Weiner, N. J. (1996), "Environmental change in eastern Greenland during the last 1300 years: Evidence from foraminifera and lithofacies in Nansen Fjord, 68°N", *Holocene*, **6**(2), 179–191. 0959-6836.

Jensen, K. G., Kuijpers, A., Koc, N. and Heinemeier, J. (2004), "Diatom evidence of hydrographic changes and ice conditions in Igaliku Fjord, South Greenland, during the past 1500 years", *Holocene*, **14**(2), 152–164.

Jirka, G. H. (2004), "Integral model for turbulent buoyant jets in unbounded stratified flows. Part 1: single round jet", *Environmental Fluid Mechanics*, **4**, 1–56.

Johnsen, S. J., Clausen, H. B., Dansgaard, W., Gundestrup, N. S., Nansson, M., Johnsson, P., Steffensen, J. P. and Sveinbjornsdottir, A. E. (1992), "A "deep" ice core from East Greenland", *Meddelelser om Grønland. Geoscience*, **29**, 1–22.

Josberger, E. (1978), "A laboratory and field study of iceberg deterioration", in: Husseiny, A. A. (ed.), "Iceberg Utilization: Proceedings of the First International Conference, Ames, Iowa, 1977", pp. 245–264.

Kamb, B. (1987), "Glacier surge mechanism based on linked cavity configuration of the basal water conduit system", *Journal of Geophysical Research*, **92**(B9), 9083–9100.

Karsten, R. H. and Marshall, J. (2002), "Testing theories of the vertical stratification of the ACC against observations", *Dynamics of Atmospheres and Oceans*, **36**(1-3), 233–246.

Kneller, B. and Buckee, C. (2000), "The structure and fluid mechanics of turbidity currents: a review of some recent studies and their geological implications", *Sedimentology*, **47**, 62–94.

Knight, P. G. (1997), "The basal ice layer of glaciers and ice sheets", *Quaternary Science Reviews*, **16**(9), 975–993.

Kranck, K. (1973), "Flocculation of suspended sediment in the sea", *Nature*, **246**(5432), 348–350.

Kranck, K. (1975), "Sediment deposition from flocculated suspensions", *Sedimentology*, **22**(1), 111–123.

Kranck, K. (1980), "Experiments on the significance of flocculation in the settling of

fine-grained sediment in still water", *Canadian Journal of Earth Sciences*, **17**(11), 1517–1526.

Kranck, K. (1981), "Particulate matter grain-size characteristics and flocculation in a partially mixed estuary", *Sedimentology*, **28**(1), 107–114.

Kristensen, M. (1983), "Iceberg calving and deterioration in Antarctica", *Progress in Physical Geography*, **7**(3), 313–328. 0309-1333.

Kristensen, M., Squire, V. A. and Moore, S. C. (1982), "Tabular icebergs in ocean waves", *Nature*, **297**(5868), 669–670.

Lane-Serff, G. F. and Moran, T. J. (2005), "Sedimentation from buoyant jets", *Journal of Hydraulic Engineering-ASCE*, **131**(3), 166–174.

Larson, G. L. (1978), "Meltwater storage in a temperate glacier, Burroughs Glacier, Southeast Alaska", Tech. Rep. 66, Institute of Polar Studies, Ohio State University.

Lawson, D. E. (1979), "Sedimentological analysis of the western terminus region of Matanuska Glacier, Alaska", Tech. Rep. 79-9, Cold Regions Research and Engineering Laboratory.

Lide, D. R. (ed.) (2000), *CRC Handbook of Chemistry and Physics: A Ready-Reference Book of Chemical and Physical Data*, 81st ed., Boca Raton, Fla: CRC Press.

List, E. (1982), "Turbulent jets and plumes", *Annual Reviews of Fluid Mechanics*, **14**, 189–212.

List, E. J. and Imberger, J. (1973), "Turbulent entrainment in buoyant jets and plumes", *Journal of the Hydraulics Division-ASCE*, **99**(HY9), 1461–1474.

List, E. J. and Imberger, J. (1975), "Closure of discussion to: Turbulent entrainment in buoyant jets and plumes", *Journal of the Hydraulics Division-ASCE*, **101**(HY5), 617–620.

Løset, S. (1992), "Heat exchange at the air exposed surface of icebergs", in: "IAHR 92: 11th International Symposium on Ice, Banff, Alberta", pp. 735–746.

Løset, S. (1993a), "Numerical modeling of the temperature distribution in tabular icebergs", *Cold Regions Science and Technology*, **21**(2), 103–115.

Løset, S. (1993b), "Thermal energy conservation in icebergs and tracking by temperature", *Journal of Geophysical Research*, **98**(C6), 10,001–10,012.

Luckman, A., Murray, T., de Lange, R. and Hanna, E. (2006), "Rapid and synchronous ice-dynamic changes in East Greenland", *Geophysical Research Letters*, **33**(3), L03,503.

Mackiewicz, N. E., Powell, R. D., Carlson, P. R. and Molnia, B. F. (1984), "Interlaminated ice-proximal glacimarine sediments in Muir Inlet, Alaska", *Marine Geology*, **57**(1-4), 113–147.

Mangor, K. and Zorn, R. (1983), "Iceberg conditions offshore Greenland", *Iceberg Research*, **4**, 4–20.

Martin, S., Josberger, E. and Kauffman, P. (1978), "Wave-induced heat transfer to an iceberg", in: Husseiny, A. A. (ed.), "Iceberg Utilization: Proceedings of the First International Conference, Ames, Iowa, 1977", pp. 260–264.

Matskevitch, D. G. (1997), "Eccentric impact of an ice feature: linearizes model", *Cold Regions Science and Technology*, **25**, 159–171.

Matsumoto, K. (1996), "An iceberg drift and decay model to compute the ice-rafted debris and iceberg meltwater flux: application to the interglacial North Atlantic", *Paleoceanography*, **11**(6), 729–742.

Matsumoto, K. (1997), "Modeled glacial North Atlantic ice-rafted debris pattern and its sensitivity to various boundary conditions", *Paleoceanography*, **12**(2), 271–280.

Matthews, J. B. and Quinlan, A. V. (1975), "Seasonal characteristics of water masses in Muir Inlet, a fjord with tidewater glaciers", *Journal of the Fisheries Research Board of Canada*, **32**(10), 1693–1703.

Mattson, L., Gardner, J. S. and Young, G. J. (1993), "Ablation on debris covered glaciers: an example from the Rakhiot glacier, Punjab, Himalaya", in: Young, G. J. (ed.), "Snow and glacier hydrology (Proceedings of the Kathmandu Symposium, November 1992)", IAHS Publication No. 218, pp. 289–296.

Mauviel, F. (1980), "Iceberg dynamical modelling", *Annals of Glaciology*, **1**, 123–127.

Maxworthy, T. (1999), "The dynamics of sedimenting surface gravity currents", *Journal of Fluid Mechanics*, **392**, 27–44.

Middleton, J. H. (1979), "Times of rise for turbulent forced plumes", *Tellus*, **31**, 82–88.

Morgan, V. I. and Budd, W. F. (1978), "The distribution, movement and melt rates of Antarctic icebergs", in: Husseiny, A. A. (ed.), "Iceberg Utilization: Proceedings of the First International Conference, Ames, Iowa, 1977", pp. 220–228.

Morton, B. (1959), "Forced plumes", *Journal of Fluid Mechanics*, **5**, 151–163.

Morton, B. (1971), "The choice of conservation equations for plume models", *Journal of Geophysical Research*, **76**(30), 7409–7416.

Morton, B. R., Taylor, G. and Turner, J. S. (1956), "Turbulent gravitational convection from maintained and instantaneous sources", *Proceedings of the Royal Society of London. Series A*, **234**, 1–23.

Motyka, R. J., Hunter, L., Echelmeyer, K. A. and Connor, C. (2003), "Submarine melting at the terminus of a temperate tidewater glacier, LeConte Glacier, Alaska, USA", *Annals of Glaciology*, **36**, 57–65.

Mountain, D. G. (1980), "On predicting iceberg drift", *Cold Regions Science and Technology*, **1**(3-4), 273–282.

Mugford, R. and Lane-Serff, G. F. (2007), "Errata for "Sedimentation from buoyant jets" by Gregory F. Lane-Serff and Terry J. Moran", *Journal of Hydraulic Engineering-ASCE*, **133**(4), 462.

Mulder, T. and Syvitski, J. P. M. (1995), "Turbidity currents generated at river mouths during exceptional discharges to the world oceans", *Journal of Geology*, **103**(3), 285–299.

Murphy, T. D. and Schamach, S. (1966), "Mountain versus sea level rainfall measurements during storms at Juneau, Alaska", *Journal of Hydrology*, **4**, 12–20.

Neshyba, S. and Josberger, E. G. (1980), "On the estimation of Antarctic iceberg melt rate", *Journal of Physical Oceanography*, **10**(10), 1681–1685.

Ng, F. S. L. (2000), "Canals under sediment-based ice sheets", *Annals of Glaciology*, **30**, 146–152.

Nicholson, L. and Benn, D. I. (2006), "Calculating ice melt beneath a debris layer using meteorological data", *Journal of Glaciology*, **52**(178), 463–470.

Nye, J. (1973), "Water at the bed of a glacier", in: "Symposium on the hydrology of glaciers", IAHS Publication No. 95, pp. 189–194.

Ó Cofaigh, C. and Dowdeswell, J. A. (2001), "Laminated sediments in glacimarine environments: diagnostic criteria for their interpretation", *Quaternary Science Reviews*, **20**(13), 1411–1436.

Orheim, O. (1980), "Physical characteristics and life expectancy of tabular Antarctic icebergs", *Annals of Glaciology*, **1**, 11–18.

Orheim, O. (1987), "Icebergs in the Southern Ocean", *Annals of Glaciology*, **9**, 241–242.

Orheim, O., Wadhams, P. and Kristensen, M. (1982), "Iceberg response to sea state", *Iceberg Research*, **1**, 10–15.

Östrem, G. (1959), "Ice melting under a thin layer of moraine and the existence of ice cores in moraine ridges", *Geografiska Annaler. Series A. Physical Geography*, **41**(4), 228–230.

Östrem, G. (1975), "Sediment transport in glacial meltwater streams", in: Jopling, A. V. and McDonald, B. C. (eds.), "Glaciofluvial and glaciolacustrine sedimentation", Society of Economic Paleontologists and Mineralogists, pp. 101–122.

Ottesen, D. and Dowdeswell, J. A. (2006), "Assemblages of submarine landforms produced by tidewater glaciers in Svalbard", *Journal of Geophysical Research*, **111**. F01016, doi:10.1029/2005JF000330.

Overpeck, J., Hughen, K., Hardy, D., Bradley, R., Case, R., Douglas, M., Finney, B., Gajewski, K., Jacoby, G., Jennings, A., Lamoureux, S., Lasca, A., MacDonald, G., Moore, J., Retelle, M., Smith, S., Wolfe, A. and Zielinski, G. (1997), "Arctic environmental change of the last four centuries", *Science*, **278**(5341), 1251–1256.

Pelto, M. S. and Warren, C. R. (1991), "Relationship between tidewater glacier calving velocity and water depth at the calving front", *Annals of Glaciology*, **15**, 115–118.

Peterson, T. and Vose, R. (1997), "An overview of the Global Historical Climatology

Network temperature database", *Bulletin of the American Meteorological Society*, **78**(12), 2837–2849.

Peterson, T., Vose, R., Schmoyer, R. and Razuvaev, V. (1998), "Global Historical Climatology Network (GHCN) quality control of monthly temperature data", *International Journal of Climatology*, **18**(11), 1169–1179.

Phillips, A. C., Smith, N. D. and Powell, R. D. (1991), "Laminated sediments in prodeltaic deposits, Glacier Bay, Alaska", in: Anderson, J. and Ashley, G. M. (eds.), "Glacial marine sedimentation; Paleoclimatic significance", Geological Society of America Special Paper 261, pp. 51–60.

Powell, R. D. (1981), "A model for sedimentation by tidewater glaciers", *Annals of glaciology*, **2**, 129–134.

Powell, R. D. (1983), "Glacial-marine sedimentation processes and lithofacies of temperate tidewater glaciers, Glacier Bay, Alaska", in: Molnia, B. F. (ed.), "Glacial-marine sedimentation", Plenum Press, pp. 185–232.

Powell, R. D. (1984), "Glacimarine Processes And Inductive Lithofacies Modeling Of Ice Shelf And Tidewater Glacier Sediments Based On Quaternary Examples", *Marine Geology*, **57**(1-4), 1–52.

Powell, R. D. (1990), "Glacimarine processes at grounding-line fans and their growth to ice-contact deltas", in: Dowdeswell, J. A. and Scourse, J. D. (eds.), "Glacimarine environments: processes and sediments", Geological Society London Special Publication No. 53, pp. 53–73.

Powell, R. D. and Cowan, E. A. (1987), "Depositional processes at McBride Inlet and Riggs Glacier", in: Anderson, P. G., Goldthwait, R. P. and McKenzie, G. D. (eds.), "Observed processes of glacial deposition in Glacier Bay, Alaska", Misc. Publication No. 236, Byrd Polar Research Center, pp. 140–156.

Powell, R. D. and Molnia, B. F. (1989), "Glacimarine sedimentary processes, facies and morphology of the South-Southeast Alaska shelf and fjords", *Marine Geology*, **85**(2-4), 359–390.

Press, W. H., Teukolsky, S. A., Vetterling, W. T. and Flannery, B. P. (2002), *Numerical Recipes in C: The Art of Scientific Computing*, 2nd ed., Cambridge University Press, Cambridge.

Priestley, C. H. B. and Ball, F. K. (1955), "Continuous convection from an isolated source of heat", *Quarterly Journal of the Royal Meteorological Society*, **81**, 144–157.

Rao, A. V. (2006), *Dynamics of particles and rigid bodies: A systematic approach*, Cambridge University Press.

Reeh, N. (1984), "Greenland ice-sheet mass balance and sea-level change", in: "Glaciers, ice sheets, and sea level: effect of a CO2-induced climatic change", United States Department of Energy, Seattle, Washington, pp. 155–171.

Reeh, N. (2004), "Holocene climate and fjord glaciations in Northeast Greenland: implications for IRD deposition in the North Atlantic", *Sedimentary Geology*, **165**(3-4), 333–342.

Reeh, N., Mayer, C., Miller, H., Thomsen, H. H. and Weidick, A. (1999), "Present and past climate control on fjord glaciations in Greenland: Implications for IRD-deposition in the sea", *Geophysical Research Letters*, **26**(8), 1039–1042.

Riggs, N., Thangam Babu, P., Sullivan, M. A. and Russell, W. E. (1980), "Iceberg drift observations in Lancaster Sound", *Cold Regions Science and Technology*, **1**(3-4), 283–291.

Rignot, E. (1996), "Tidal motion, ice velocity and melt rate of Petermann Gletscher, Greenland, measured from radar interferometry", *Journal of Glaciology*, **42**(142), 476–485.

Rignot, E., Braaten, D., Gogineni, S. P., Krabill, W. B. and McConnell, J. R. (2004), "Rapid ice discharge from southeast Greenland glaciers", *Geophysical Research Letters*, **31**(10). L10401.

Rignot, E. and Kanagaratnam, P. (2006), "Changes in the velocity structure of the Greenland ice sheet", *Science*, **311**(5763), 986–990.

Rodi, W. (ed.) (1982), *Turbulent Buoyant Jets and Plumes*, Pergamon Press.

Röthlisberger, H. (1972), "Water pressure in intra- and subglacial channels", *Journal of Glaciology*, **11**, 177–203.

Röthlisberger, H. and Lang, H. (1987), "Glacial hydrology", in: Gurnell, A. M. and Clark, M. J. (eds.), "Glacio-fluvial Sediment Transfer", Wiley, New York, pp. 207–284.

Rouse, H., Yih, C. and Humphreys, H. (1952), "Gravitational convection from a boundary source", *Tellus*, **4**, 201–210.

Ruddiman, W. F. and Wright, H. E. (1987), *North America and adjacent oceans during the last deglaciation.*, vol. K-3 of *The geology of North America, vol. K-3*, Geological Society of America.

Russell, W. E., Riggs, N. P. and Robe, R. Q. (1977), "Local iceberg motion - a comparison of field and model studies", in: Muggeridge, D. B. (ed.), "Proceedings of POAC 77: Fourth International Conference on Port and Ocean Engineering under Arctic Conditions, vol. 2", St. John's, Canada, pp. 784–798.

Russell-Head, D. (1980), "The melting of free-drifting icebergs", *Annals of Glaciology*, **1**, 119–122.

Shirasawa, K., Riggs, N. and Muggeridge, D. (1984), "The drift of a number of idealized model icebergs", *Cold Regions Science and Technology*, **10**(1), 19–30.

Siegert, M. J. and Dowdeswell, J. A. (2002), "Late Weichselian iceberg, surface-melt and sediment production from the Eurasian Ice Sheet: results from numerical ice-

sheet modelling", *Marine Geology*, **188**(1-2), 109–127.

Silva, T. A. M., Bigg, G. R. and Nicholls, K. W. (2006), "Contribution of giant icebergs to the Southern Ocean freshwater flux", *Journal of Geophysical Research*, **111**. C03004, doi: 10.1029/2004JC002843.

Skei, J. (1983), "Why Sedimentologists Are Interested In Fjords", *Sedimentary Geology*, **36**(2-4), 75–80.

Smith, L. M. and Andrews, J. T. (2000), "Sediment characteristics in iceberg dominated fjords, Kangerlussuaq region, East Greenland", *Sedimentary Geology*, **130**(1-2), 11.

Smith, N. D., Phillips, A. C. and Powell, R. D. (1990), "Tidal drawdown - A mechanism for producing cyclic sediment laminations in glaciomarine deltas", *Geology*, **18**(1), 10–13.

Smith, S. D. (1993), "Hindcasting iceberg drift using current profiles and winds", *Cold Regions Science and Technology*, **22**(1), 33–45.

Smith, S. D. and Banke, E. G. (1983), "The influence of winds, currents and towing forces on the drift of icebergs", *Cold Regions Science and Technology*, **6**(3), 241–255.

Sohn, H. G., Jezek, K. C. and van der Veen, C. J. (1998), "Jakobshavn Glacier, West Greenland: 30 years of spaceborne observations", *Geophysical Research Letters*, **25**(14), 2699–2702.

Sparks, R. S. J., Bonnecaze, R. T., Huppert, H. E., Lister, J. R., Hallworth, M. A., Mader, H. and Phillips, J. (1993), "Sediment-laden gravity currents with reversing buoyancy", *Earth and Planetary Science Letters*, **114**(2-3), 243–257.

Sparks, R. S. J., Carey, S. N. and Sigurdsson, H. (1991), "Sedimentation from gravity currents generated by turbulent plumes", *Sedimentology*, **38**(5), 839–856.

Sugden, D. E. and John, B. S. (1977), *Glaciers and landscape: a geomorphological approach*, Edward Arnold (Publishers) Ltd.

Sutherland, D. and Pickart, R. (2007), "The East Greenland Coastal Current: Structure, variability and forcing", *submitted to Progress in Oceanography*.

Syvitski, J. (1989), "On the deposition of sediment within glacier-influenced fjords: oceanographic controls", *Marine Geology*, **85**, 301–329.

Syvitski, J. and Murray, J. (1981), "Particle interaction in fjord suspended sediment", *Marine Geology*, **39**, 215–242.

Syvitski, J. P., Burrell, D. C. and Skei, J. M. (1987), *Fjords: Processes and Products*, Springer, New York.

Syvitski, J. P. M., Andrews, J. T. and Dowdeswell, J. A. (1996), "Sediment deposition in an iceberg-dominated glacimarine environment, East Greenland: basin fill implications", *Global and Planetary Change*, **12**, 251–270.

Syvitski, J. P. M., Asprey, K. W., Clattenburg, D. A. and Hodge, G. D. (1985), "The

prodelta environment of a fjord - suspended particle dynamics", *Sedimentology*, **32**(1), 83–107.

Syvitski, J. P. M., Asprey, K. W. and Leblanc, K. W. G. (1995), "In-Situ Characteristics Of Particles Settling Within A Deep-Water Estuary", *Deep-Sea Research Part II: Topical Studies in Oceanography*, **42**(1), 223–256.

Syvitski, J. P. M. and Hutton, E. W. H. (2001), "2D SEDFLUX 1.0C: an advanced process-response numerical model for the fill of marine sedimentary basins", *Computers and Geosciences*, **27**, 731–753.

Thayyen, R. J., Gergan, J. T. and Dobhal, D. P. (1999), "Particle size characteristics of suspended sediments and subglacial hydrology of Dokriani Glacier, Garhwal Himalaya, India", *Hydrological Sciences Journal-Journal des Sciences Hydrologiques*, **44**(1), 47–61.

Thomas, R. H., Abdalati, W., Akins, T. L., Csatho, B. M., Frederick, E. B., Gogineni, S. P., Krabill, W. B., Manizade, S. S. and Rignot, E. J. (2000), "Substantial thinning of a major east Greenland outlet glacier", *Geophysical Research Letters*, **27**(9), 1291–1294.

Toggweiler, J. R. and Samuels, B. (1995), "Effect of Drake Passage on the global thermohaline circulation", *Deep-Sea Research Part I: Oceanographic Research Papers*, **42**(4), 477–500.

Turner, J. S. (1979), *Buoyancy Effects in Fluids*, Cambridge University Press.

Turner, J. S. (1986), "Turbulent entrainment: the development of the entrainment assumption, and its application to geophysical flows", *Journal of Fluid Mechanics*, **173**, 431–471.

Van der Veen, C. J. (1996), "Tidewater calving", *Journal of Glaciology*, **42**(141), 375–385.

Van der Veen, C. J. (2002), "Calving glaciers", *Progress in Physical Geography*, **26**(1), 96–122.

Veitch, G. and Woods, A. W. (2000), "Particle recycling and oscillations of volcanic eruption columns", *Journal of Geophysical Research*, **105**(B2), 2829–2842.

Veitch, G. and Woods, A. W. (2002), "Particle recycling in volcanic plumes", *Bulletin of Volcanology*, **64**(1), 31–39.

Venkatesh, S., Murphy, D. and Wright, G. (1994), "On the deterioration of icebergs in the marginal ice zone", *Atmosphere-Ocean*, **32**(2), 469–484.

Vieli, A., Funk, M. and Blatter, H. (2001), "Flow dynamics of tidewater glaciers: a numerical modelling approach", *Journal of Glaciology*, **47**(159), 595–606.

Vinje, T. (1989), "Icebergs in the Barents Sea", in: Sinha, N. K., Sodhi, D. S. and Chung, J. S. (eds.), "Eighth International Conference on Offshore Mechanics and Arctic Engineering", pp. 139–145.

Wadhams, P. (1988), "Winter observations of iceberg frequencies and sizes in the South Atlantic Ocean", *Journal of Geophysical Research*, **93**(C4), 3583–3590.

Wagner, B., Melles, M., Hahne, J., Niessen, F. and Hubberten, H. W. (2000), "Holocene climate history of Geographical Society O, East Greenland - evidence from lake sediments", *Palaeogeography, Palaeoclimatology, Palaeoecology*, **160**(1-2), 45–68.

Warren, C. R. (1992), "Iceberg calving And the glacioclimatic record", *Progress in Physical Geography*, **16**(3), 253–282.

Weeks, W. and Mellor, M. (1978a), "Some elements of iceberg technology", Tech. Rep. 78-2, Cold Regions Research and Engineering Laboratory.

Weeks, W. F. and Campbell, W. J. (1973), "Icebergs as a fresh-water source; an appraisal", *Journal of Glaciology*, **12**(65), 207–233.

Weeks, W. F. and Mellor, M. (1978b), "Some elements of iceberg technology", in: Husseiny, A. A. (ed.), "Iceberg Utilization: Proceedings of the First International Conference, Ames, Iowa, 1977", pp. 45–98.

Weertman, J. (1972), "General theory of water flow at the base of a glacier or ice sheet", *Reviews of Geophysics*, **10**(1), 287–333.

White, F. M., Spaulding, M. L. and Gominho, L. (1980), "Estimates of the various mechanisms involved in iceberg deterioration in the open ocean environment", Tech. Rep. CG-D-62-80, U.S. Coast Guard Report.

Williamson, S. N., Sharp, M. J., Dowdeswell, J. A. and Benham, T. J. (2007), "Iceberg calving rates from northern Ellesmere Island ice caps, 1999-2003", *submitted to Journal of Glaciology*.

Young, N. W., Turner, D., Hyland, G. and Williams, R. N. (1998), "Near-coastal iceberg distributions in East Antarctica, 50–145°E", *Annals of Glaciology*, **27**, 68–74.

Zarrebini, M. and Cardoso, S. S. S. (2000), "Patterns of sedimentation from surface currents generated by turbulent plumes", *American Institute of Chemical Engineers Journal*, **46**(10), 1947–1956.